Turbulent stresses and non-zonal transition in electromagnetic ion-temperature-gradient turbulence

Yujia Zhang

A thesis submitted for the degree of Doctor of Philosophy

University of Oxford

December 2025

Supervised by: Michael Barnes and Alexander A. Schekochihin

Abstract

The performance of magnetic-confinement fusion devices is strongly influenced by turbulent transport driven by micro-instabilities. While finite plasma beta (β) is often associated with reduced ion-temperature-gradient (ITG) turbulence through electromagnetic stabilisation, recent gyrokinetic studies have identified a transition to high-transport states at sufficiently large beta. Understanding the physical mechanisms underlying this transition is essential for assessing the prospects of high-beta operation in future fusion devices.

This thesis investigates electromagnetic ITG turbulence using a combination of gyrokinetic simulations and reduced fluid models. First, a detailed derivation of the implicit advance scheme employed in the gyrokinetic code stella is presented. The numerical framework is then used to analyse nonlinear electromagnetic turbulence in realistic tokamak equilibria representative of conventional and spherical tokamaks. By deriving expressions for Reynolds, Maxwell and diamagnetic turbulent stresses and the associated energy transfers, it is shown that increasing β modifies the balance of momentum transport responsible for sustaining zonal flows. Near the transition to high-transport states, Maxwell stresses increasingly oppose the Reynolds-stress drive of zonal flows, leading to a reduction of zonal-flow regulation and the emergence of turbulence dominated by non-zonal fluctuations. The scaling of the stress balance with plasma beta is quantified, and convergence studies are performed to establish the robustness of the results.

To gain further physical insight, a reduced fluid model describing electromagnetic ITG turbulence is derived from gyrokinetics by carrying out subsidiary expansion in small electron-to-ion mass-ratio and cold-ion limit. The model captures the essential competition between Reynolds, Maxwell and diamagnetic stresses while remaining sufficiently simple to permit analytical investigation. Linear stability analysis recovers the electrostatic ITG limit, finite-β stabilisation, Alfvénic dynamics and the high-β interchange regime. Nonlinear simulations of the reduced model reproduce the transition from zonal-flow-dominated turbulence to high-transport states observed in the gyrokinetic calculations. The transition is interpreted as a consequence of a changing the balance between turbulent stresses rather than the onset of a distinct linear instability.

Together, these results provide a unified picture of the non-zonal transition in electromagnetic ITG turbulence. They demonstrate that finite-β effects alter turbulent self-

organisation through Maxwell and diamagnetic stresses, thereby weakening zonal-flow regulation and enabling enhanced transport. The findings may potentially contribute to the broader understanding of transport limits in magnetically confined fusion plasmas.

Acknowledgements

First and foremost, I would like to express my sincere gratitude to my supervisors, Michael Barnes and Alexander Scheckochihin, whose expertise, understanding and generous support have made this thesis possible. I first met Michael during my college interview eight years ago. Then, in my second year of undergraduate study, I attended his lectures on statistical mechanics and was struck by how clear and rigorously presented they were. I was extremely surprised, when later, the department assigned him to supervise my master's project – working with him is my fate it seems. His patient guidance and encouragement inspired me to pursue a PhD in magnetic-confinement fusion. Throughout my PhD I ran into countless problems about physics, numerics and even personal life, and his thoughtful ideas and advice were always indispensable. My other supervisor, Alexander Scheckoshihin, has a very unique and charming character – I really appreciate the numerous jokes he came up with during our weekly seminars and out-of-physics times. He undoubtedly possesses extensive knowledge in plasma physics and has profoundly shaped my understanding of reduced models that describe complex physical phenomena in fusion. Besides, in the college dinners and fusion conferences we attended together, I really enjoyed the conversations we had about world history and politics. I have benefited so much from the difference between my supervisors: Michael is more practically minded when it comes to giving advice, which taught me how to present results that resonate with a larger fraction of the fusion community. Alex, on the other hand, pushed my theoretical thinking and helped me present the physical picture clearly – both to engage readers and to gain personal satisfaction in understanding the subject. I have always believed that working with both Alex and Michael is an experience that is only offered to the most privileged PhD student in fusion.

I am deeply grateful for the financial support provided by Tokamak Energy Ltd. and the Simons Foundation; without it this work would not have been possible. Staff at Tokamak Energy generously supported me during my visits to the company. In particular, I would like to thank Michele Romanelli, my external supervisor, for his warm welcome when I first became involved with the company during my master's and for his help in securing funding. Former employees at Tokamak Energy Salomon Janhunen, Michael Hardman and Michail Anastopoulos Tzanis, and current employees Peter Buxton, Alexandra Dudkovskaia, Filip Janky and Alsu Sladkomedova, have assisted me with the projects and their insights into the subject were invaluable. My thanks also go to Bill Dorland and Felix Parra Diaz for providing computing resources from Princeton, and to Richard Nies for the fruitful discussions in several occasions.

Many thanks to the colleagues at Oxford who supported me throughout these four years as a PhD student. I especially enjoyed working with Plamen Ivanov and Toby Adkins who are the smartest individuals I have ever met. To me, they were my informal supervisors. I am also thankful for the challenges, lovely office chats and the enjoyable moments shared with my cohort colleagues William Clarke and Michael Nastac. My thanks also go to others who have been part of the Oxford community, including Mantas Abazorius, Georgia Acton, Robbie Ewart, Juan Ruiz Ruiz, and Leonard-Petru Turica — and to many others unnamed, with whom I shared many memorable moments.

This thesis would not have progressed smoothly without the assistance from Benjamin Chapman-Oplopoiou, Daniel Kennedy and Sarah Newton during my job search. I especially enjoyed working with Daniel, who has been very responsive and actively contributed to my project. I would also like to thank Colin Roach and Dmitri Uzdensky for tolerating my presentation for Confirmation of Status and offering their useful advice on my work.

I would like to thank Fabrizio Caola for his trust and for inviting me to teach at Wadham College. Teaching there has been a genuine joy, and I feel fortunate to continue teaching after my PhD. I am also very grateful to college advisor Jeffrey Tseng for his kindness and support throughout the term times.

I greatly enjoyed training as a kickboxer during the first two years of my PhD. Many thanks to the Oxford University Kickboxing Club and my coach, Jan, for teaching me physical and mental resilience. Co-coaching classes also helped me become a considerably more confident person.

On a personal note, I wish to thank my family for their unconditional love and encouragement. The infinite amount of care and support I received in my early years gave me the strength and confidence to endure the ups and downs of this long process and ultimately to earn this PhD. My life outside physics would have been much poorer without the many wonderful times I shared with my friends from high school, Tianyuan Zhao and Jiayao Shao. Finally, to my wife, Chen Wang: Thank you for all the love and beautiful memories you shared with me. Many people would agree that the story of how we first met reads like the plot of a movie which is still far from ending. Asking you to leave your job and relocate to the UK was a big challenge. I feel somewhat guilty about all the fuss you have to ensure, but I am also profoundly grateful that you have agreed to explore new opportunities with me. Let us build an exciting path forward, and allow me repay that trust by being a caring and responsible partner.

Contents

List of Figures

List of Tables

Chapter 1

Introduction

So now you want us to drop everything we are doing and start worrying about what the big questions are?!

— Ian Abel, Oxford plasma seminars and Vienna meetings

This thesis is concerned with the issue of turbulent transport in tokamak plasmas with thermal energy densities that are non-negligible compared to the magnetic field energy density. In this chapter, I introduce the key concepts needed by the reader, including the magnetic geometry of tokamaks, curvature-mediated, ion-temperature-gradient (cITG) instabilities, zonal flows and the framework of gyrokinetics.

1.1 Magnetic confinement fusion

1.1.1 Fusion plasmas in tokamaks

Fusion reactions, which occur routinely in the cores of stars, release an enormous amount of energy. To harness this energy on Earth, the fusion fuel – isotopes of hydrogen – must be heated to temperatures of up to hundreds of millions of degrees. At such extreme conditions, the fuel turns into plasma—a state of matter consisting of a mixture of positively charged ions and free electrons. No solid-container material can withstand direct contact with plasma at these temperatures, as it would instantly melt or vaporize. Because plasmas consist of charged particles, their motion can be effectively controlled by external magnetic fields. Thus, the most widely used method for confining high-temperature plasmas is magnetic confinement, where strong magnetic fields (typically several teslas) are used to trap ions and electrons inside a solid device, allowing separation between the hottest part of the plasma and the inner wall. While the plasma is magnetically confined, external heating methods are applied until fusion reactions are initiated and self-sustained by the power they produce. One of the most widely adopted configurations for magnetic confinement is the tokamak, which has, to date, demonstrated a strong capability to sustain relatively long-duration confinement of fusion plasmas [Wesson, 2011]. In this thesis, we focus on tokamaks and the associated challenges on the pathway to terrestrial fusion.

1.1.2 Energy loss due to turbulent transport

One way to measure the steady-state performance of a tokamak is to use the fusion power gain, parameterised via the Q-factor, which is defined as

$$Q \equiv \frac{P_{\mathrm{fu}}}{P_{\mathrm{h}}} = \frac{P_{\mathrm{fu}}}{P_{\mathrm{loss}} - fP_{\mathrm{fu}}}, \tag{1.1}$$

where P_{fu} is the power produced by the fusion reactions and P_{h} is the external heating power absorbed by the plasma to maintain the steady-state temperature, which is the difference between the power lost to the surroundings P_{loss} via various transport mechanisms that carry heat out of the tokamak[1] and the power that the plasma gains from the fusion reactions fP_{fu}. The factor $0 < f < 1$ represents the fraction of fusion energy that remains inside the plasma, since the fusion energy carried by the neutrons can freely leave the device. For our purposes, P_{h} is only meaningful when it is positive. Consider that the plasma has reached a certain temperature that fixes P_{fu}. If P_{loss} is reduced by suppressing transport, P_h will decrease, lifting the Q-factor. Notice that the Q-factor approaches infinity when P_{loss} completely balances the power gain fP_{fu}, allowing the plasma to self-sustain its temperature without any external heating.

To date, the record Q-factor achieved by tokamaks is about 0.66, which was set by the Joint European Torus (JET) in 1998 [Gibson and the JET Team, 1998][2]. It is still far from the ultimate goal of the fusion community ($Q \gg 1$). One of the main challenges is reducing P_{loss} since inappropriate plasma conditions – such as excessively steep pressure gradients – can trigger various types of instabilities and the associated transport events. The most dangerous of these are magneto-hydrodynamic (MHD) instabilities, which are system-sized disturbances that can grow rapidly and cause disruptions that lead to the complete loss of plasma confinement. Great care is thus taken to develop equilibria that are MHD stable.

However, even when MHD stability is ensured, micro-instabilities can still arise, causing turbulent mixing and limiting the energy confinement. In some tokamaks, the applied magnetic fields are strong and the plasma pressure is sufficiently weak that the turbulent fluctuations are often well-approximated as electrostatic in nature. While not all aspects

[1] Including turbulence, neoclassical transport, radiation, etc.

[2] In the experiment, the plasma stored energy was still increasing, meaning the discharge had not yet reached true steady-state. Because a portion of the absorbed power was being used to raise the plasma energy rather than maintain it, the measured $Q \approx 0.66$ underestimates the performance achievable in steady conditions. If this transient energy increase is removed from P_{h}, the inferred steady-state value is estimated to be $Q \approx 0.8$.

of these electrostatic turbulence fluctuations are fully understood, many of their basic properties have been identified. In particular, the turbulence is usually driven by one of a number of instabilities with a characteristic wavelength comparable to the ion or electron gyro-radius and feeds off a combination of gradients in the plasma density, flow and temperature. These gradients are inevitable because the pressure must be sufficiently high in the plasma core to sustain fusion reactions, while remaining low enough near the wall to prevent structural damage. The archetypal example of these gradient-driven instabilities is the curvature-ITG instability [Horton et al., 1981, Waltz, 1988, Romanelli, 1989, Kotschenreuther et al., 1995a, Evensen et al., 1998, Zocco et al., 2018], which has been observed experimentally to dominate turbulent transport in a range of scenarios [Citrin et al., 2017, Van Wyk et al., 2017]. It has been extensively characterised by solving the gyrokinetic-Poisson system of equations, most commonly via numerical simulations [Dimits et al., 2007, Saarelma et al., 2012, Bañón Navarro et al., 2020, Mazzi et al., 2022], but also via analytical calculations in a handful of simplified limits [Anderson et al., 2002, Ivanov et al., 2020, 2022]. Since the curvature branch of the ITG instability is the main focus of this thesis, the shorthand 'ITG', whenever it is used, refers to 'curvature-ITG' throughout the remainder of the thesis.

Despite the confinement degradation posed by electrostatic ITG turbulence, a growing number of current experiments, as well as many proposed fusion-reactor plasmas, reach large enough plasma pressures for the confining magnetic fields to be modified significantly. In such cases, the magnetic fluctuations can qualitatively change the turbulence and associated transport levels. The quantity that parameterises the relative importance of magnetic field fluctuations is the plasma beta, β, defined as the ratio of plasma pressure to magnetic pressure. Previous studies have shown that the inclusion of finite-β (electromagnetic) effects can lead to stabilisation of the linear ITG instability [Kim et al., 1993, Jarmën et al., 1998, Kim and Han, 2019] and to nonlinear suppression of turbulence [Snyder, 1999, Chen et al., 2003, Pueschel and Jenko, 2010, Citrin et al., 2013, 2014, Whelan et al., 2018], even for β values on the order of a percent. This makes physical sense: The bending of field lines by turbulent fluctuations produces a restoring force that resists the motions induced by the fluctuations. Consequently, it has been proposed that going to higher beta via increasing both thermal plasma pressure and by introducing high-energy, or fast, particles into the plasma could improve confinement [Pueschel and Jenko, 2010, Citrin et al., 2014, Sama et al., 2024]. These results seem encouraging. Provided that MHD stability can be maintained, operating at higher beta values could significantly improve cost-effectiveness for a given heating power, as the fusion power output scales with plasma pressure, whereas the cost of tokamak operation is largely governed by the magnetic field strength.

There is, however, an emerging body of evidence from gyrofluid [Scott, 2006] and gyrokinetic [Giacomin et al., 2024, Waltz, 2010, Pueschel et al., 2013c, Rath and Peeters, 2022] simulations that at even higher β values, there is an abrupt transition from a state with modest heat flux to a state with very large heat flux. The calculated heat fluxes are orders of magnitude larger than the gyro-Bohm estimate in some cases [Giacomin et al., 2024], and in others the turbulence does not appear to saturate at all [Waltz, 2010, Pueschel et al., 2013c, Rath and Peeters, 2022]. This is found across a wide range of plasma parameters and simulation codes, and therefore, is unlikely to be a numerical artifact. Past explanations for these high (or diverging) fluxes are varied and will be discussed in more detail in Subsection 1.4.3.

The high-flux turbulent states present a significant challenge, as they hinder fusion devices from operating at higher beta values. Understanding the high-flux cases is crucial, as they indicate whether additional measures are necessary to enable operation at high beta. For instance, Giacomin et al. [2024], Anastopoulos Tzanis et al. [2025] demonstrated that incorporating the shearing effect arising from the equilibrium $\boldsymbol{E} \times \boldsymbol{B}$ rotation of the plasma allows the electromagnetic turbulence to saturate at much lower levels in gyrokinetic simulations. These rotation flows occur primarily in the toroidal direction due to the axisymmetric geometry of the device. It is perhaps fortunate that plasma rotation naturally arises in real tokamak devices such as JET, MAST-U, ST40, ASDEX Upgrade, NSTX, etc, as a result of heating by neutral beam injection (NBI) [Stix, 1972]. In addition, intrinsic rotation — spontaneous plasma flows that arise without any external momentum input — have also been studied [Parra and Barnes, 2015] and observed [Rice et al., 2007, Grierson et al., 2017].

However, not all tokamaks possess dedicated systems for driving toroidal rotation that is large enough for turbulence suppression, such as the STEP Programme, where external momentum input is expected to be quite limited, and it is therefore essential to assess whether external momentum input is fundamentally required for achieving good confinement and stability in the high-beta scenarios. Thus, this thesis is motivated by the need to develop a physical understanding of the high-flux phenomena observed in simulations of finite-beta turbulence. In the remaining part of the introduction, we will explain the tools for studying turbulence in tokamaks.

1.2 Magnetic geometry of a tokamak

Ions and electrons follow the magnetic field lines in helical trajectories. Because they can stream relatively freely along these field lines, an appropriate magnetic topology is required to confine the plasma within the device. In addition, the ITG instabilities rely on magnetic curvature – abundant in tokamak geometry – to become unstable. For these reasons, understanding the magnetic geometry of tokamaks and the methods used to model it is essential.

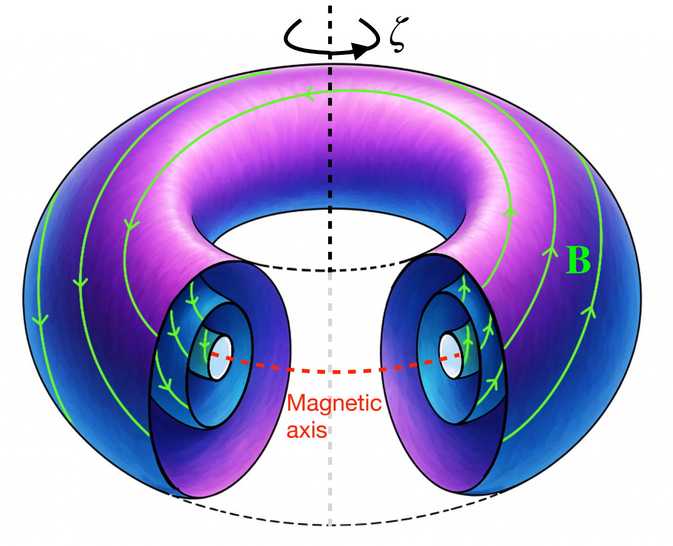

Figure 1.1: Nested flux-surfaces of a tokamak with axisymmetric magnetic field configuration. The green lines are magnetic field lines with arrows indicating local magnetic field vectors. The red dashed line is the magnetic axis, and ζ is the toroidal angle.

1.2.1 Flux surfaces

The magnetic field configuration of tokamaks is predominantly axisymmetric. The magnetic field lines form nested 'flux' surfaces in the shape of torii, with the magnetic field vectors tangent to each surface (see Fig. 1.1 for an illustration). The innermost flux surface is effectively a single closed field line called the magnetic axis. The toroidal shape is chosen because it is the only geometry in which magnetic field lines can be traced continuously around a closed surface. This is crucial since the particles could rapidly escape, leading to a loss of plasma confinement if the field lines were to extend beyond the intended confinement surface.

A common practical definition of a flux surface uses the poloidal (short way around the torus) magnetic flux: Choose a cross-section at a given toroidal (long way around the torus) angle ζ such as the one shown in Fig. 1.2, and draw a line on the cross-section connecting the magnetic axis and a point of interest (shown as a red dashed line in the same figure). The point of interest has coordinates (R,Z), where R is the distance from the axis of symmetry and Z is the height above the magnetic axis. Sweep the line around in ζ to form a ribbon. The flux label ψ is then defined as the poloidal flux through that ribbon per radian in ζ,

$$\psi = \frac{1}{2\pi} \int_{S_p} \boldsymbol{B} \cdot \mathrm{d}\boldsymbol{S_p}, \tag{1.2}$$

where $\boldsymbol{B}$ is the magnetic field vector, and S_p is the area of the ribbon. Contours with constant ψ are identified as the flux surfaces.

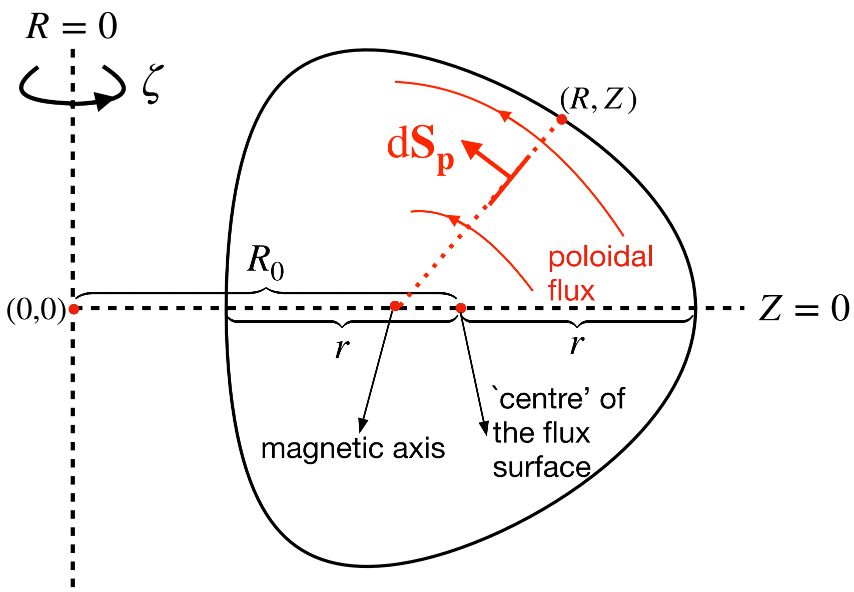

Figure 1.2: A sample cross-section at a given toroidal angle ζ, whose shape is determined by Miller parametrisation.

1.2.2 The Grad-Shafranov equation

To characterise the allowed flux-surface shapes in an axisymmetric MHD equilibrium, we consider ideal MHD force balance:

$$\boldsymbol{J} \times \boldsymbol{B} = c\nabla p, \tag{1.3}$$

where $\boldsymbol{J}$ is the plasma current density, c is the speed of light and p is the pressure of the plasma. The current density $\boldsymbol{J}$ is related to $\boldsymbol{B}$ via the low-frequency version of Ampère's law[3]:

$$\nabla \times \boldsymbol{B} = \frac{4\pi}{c}\boldsymbol{J}. \tag{1.4}$$

Together with the divergence free condition $\nabla \cdot \boldsymbol{B} = 0$, one obtains the Grad-Shafranov equation [Grad and Rubin, 1958, Shafranov, 1966] written in cylindrical coordinates:

$$\frac{\partial^2\psi}{\partial Z^2} - \frac{1}{R}\frac{\partial\psi}{\partial R} + \frac{\partial^2\psi}{\partial R^2} = -R^2\frac{\mathrm{d}p}{\mathrm{d}\psi} - RB_\zeta\frac{\mathrm{d}(RB_\zeta)}{\mathrm{d}\psi}, \tag{1.5}$$

where $B_\zeta = \boldsymbol{B} \cdot \hat{\boldsymbol{\zeta}}$ is the toroidal component of the magnetic field. Solving this equation with appropriate boundary conditions yields the flux surfaces as level surfaces of ψ. Note that $p = p(\psi)$ is a flux function, meaning that the plasma pressure is constant on a flux surface. Generally speaking, the pressure is highest in the core region (in the vicinity of the magnetic axis) and falls off as one moves radially outward (in the direction of

[3]The displacement current is negligible, unless particles are relativistic which is generally not the case for fusion plasmas.

increasing ψ) across flux surfaces. The force balance equation (1.3) then indicates that the flux surfaces can only be maintained if the magnetic force is strong enough to balance the pressure force that attempts to push the plasma radially outwards. Notice that the plasma current density $\boldsymbol{J}$ is required for generating the magnetic force. Hence, a stable plasma current is essential for the operation of tokamaks. In pulsed tokamak operation, the magnetic field from the central solenoid (located at the $R = 0$ axis) is ramped up until it reaches its maximum, inducing a toroidal plasma current during this process. For steady-state operation, however, external current drive methods — such as neutral beam injection (NBI) and radiofrequency (RF) waves — or self-generated bootstrap currents [Bickerton et al., 1971, Cordey et al., 1988] are required.

The equilibrium force balance (1.3) can also be expressed in a form that makes the underlying physics more transparent:

$$\begin{aligned} (\nabla \times \boldsymbol{B}) \times \boldsymbol{B} &= 4\pi \nabla p, \\ \longrightarrow (\boldsymbol{B} \cdot \nabla B)\, \hat{\boldsymbol{b}} + B\, (\boldsymbol{B} \cdot \nabla)\, \hat{\boldsymbol{b}} - B \nabla B &= 4\pi \nabla p, \end{aligned} \tag{1.6}$$

where we used (1.4) and $\hat{\boldsymbol{b}} = \boldsymbol{B}/B$. Extracting the radial component of (1.6), we get

$$\left[\left(\hat{\boldsymbol{b}} \cdot \nabla \right) \hat{\boldsymbol{b}} \right] \cdot \hat{\boldsymbol{n}}_\psi = \frac{\beta}{2} \nabla \ln p + \nabla \ln B \cdot \hat{\boldsymbol{n}}_\psi, \tag{1.7}$$

where $\hat{\boldsymbol{n}}_\psi = \nabla\psi/|\nabla\psi|$, $\beta = 8\pi p/B^2$ is the plasma beta, and $\left(\hat{\boldsymbol{b}} \cdot \nabla \right) \hat{\boldsymbol{b}}$ is the curvature vector. (1.7) tells us that, in the radial direction, the magnetic tension force must balance with the combined pressure force due to plasma and magnetic field strength. At low enough β, we can ignore the plasma pressure and simply have

$$\left(\hat{\boldsymbol{b}} \cdot \nabla \right) \hat{\boldsymbol{b}} = \nabla \ln B. \tag{1.8}$$

1.2.3 Approximate solutions to the Grad-Shafranov equation – Miller parametrization

In practice, we commonly use a family of flux-surface shapes that are only local solutions to the Grad-Shafranov equation. The shapes of those surfaces are described by the Miller parametrization [Miller et al., 1998, Stacey, 2008]. Each cross-section at fixed ζ (see Fig. 1.2) is described by the cylindrical coordinates (R,Z) parametrised as

$$R(r, \vartheta) = R_0(r) + r \cos\Big(\vartheta + \sin(\vartheta) \arcsin(\delta(r)) \Big), \tag{1.9}$$

$$Z(r, \vartheta) = \kappa(r) r \sin(\vartheta), \tag{1.10}$$

where the flux surface label r is the half-diameter of the flux surface at the height of the magnetic axis and ϑ is a poloidal angle[4]. R_0 is the distance between the axis of symmetry and the 'centre' of the flux surface. The parameters δ and κ control the triangularity and elongation of the plasma, respectively. Fig. 1.2 illustrates a sample cross-section with $\delta = 0.4$ and $\kappa = 1.1$.

The magnetic field lines on a flux surface are in general helical: they wind both toroidally and poloidally. The degree of helicity, i.e., the pitch of the field lines, is expressed by the safety factor

$$q(\psi) = \frac{\mathrm{d}\zeta}{\mathrm{d}\vartheta_s}, \tag{1.11}$$

where ϑ_s is the straight-field-line poloidal angle and is in general a function of ψ, ζ and ϑ. It is called a straight-field-line angle because ζ appears as a linear function of ϑ_s as the angles vary by following the field line. By contrast, this property does not generally hold for the ϑ used in the Miller parametrisation.

In the limit of large aspect ratio ($R_0 \gg r$) and circular cross-section ($\delta = 0$ and $\kappa = 1$), the safety factor has an approximate expression given by

$$q(\psi) = \frac{rB_\zeta}{RB_p}, \tag{1.12}$$

where $B_p = \boldsymbol{B} \cdot \nabla\vartheta / |\nabla\vartheta|$ is the poloidal component of the magnetic field vector. Physically, specifying q determines how many times a field line circles toroidally for each poloidal circuit. The name 'safety factor' reflects its importance in equilibrium MHD stability.

1.2.4 Flux tube coordinates

As mentioned in Subsection 1.1.2, the energy confinement of a tokamak is often impaired by the turbulence driven by ITG instabilities with a characteristic wavelength comparable to the ion gyro-radius ρ_i. Since the plasma is strongly magnetised, ρ_i is typically small compared with macroscopic length scales such as the tokamak major radius. For these reasons, we adopt the local, flux-tube approximation [Beer et al., 1995], modeling ion-scale instabilities in a flux tube rather than across the entire plasma volume. A flux tube is a three-dimensional region that follows a magnetic field line on one chosen flux surface. Its cross-section perpendicular to the field is taken to have linear dimensions that are small compared with the size of the tokamak, yet large enough to ensure that turbulent fluctuations at the ends of the domain are decorrelated. This local treatment of turbulence takes advantage of the spatial scale separation between the fluctuations and

[4] Note that ϑ is not the same as the angle, denoted by θ, between the $Z = 0$ axis and the line joining $(R = R_0, Z = 0)$ and an arbitrary point (R,Z). A simple way to see this is to consider $\vartheta = 90°$, which corresponds to the maximum value of Z. However, this does not occur at $\theta = 90°$.

the equilibrium, and greatly simplifies analysis while retaining the essential physics.

Inside a flux tube, the equilibrium magnetic field is described using the Clebsch representation $\boldsymbol{B} = \nabla\alpha \times \nabla\psi$, in which ψ labels flux-surfaces as defined previously, and α is a function that labels different field lines. In axisymmetric configurations, it is related to the usual toroidal and straight-field-line poloidal angles ζ and ϑ_s, respectively, by $\alpha = \zeta - q\,(\psi)\,\vartheta_s$. Along a field line α is constant, and $\mathrm{d}\zeta = q\,(\psi)\,\mathrm{d}\vartheta_s$, which is consistent with the definition of q (1.11).

The quantity used to label position along the field line is not unique. Here, we simply denote it by z, which may represent any convenient choice, such as the poloidal angle ϑ, the toroidal angle ζ, or even the distance along the field line. We take $z = 0$ to correspond to the out-board mid-plane of the device ($Z = 0$, $R = R_0 + r$ on Fig. 1.2). Given that we are interested in working in the local, flux-tube approximation, we find it convenient to, at this stage, specialise to field-aligned, flux-tube coordinates (x,y,z) [Beer et al., 1995, Highcock, 2012] in which

$$x = \left(\frac{\mathrm{d}x}{\mathrm{d}\psi}\right)_{\psi_0} (\psi - \psi_0)\,,\ y = \left(\frac{\mathrm{d}y}{\mathrm{d}\alpha}\right)_{\alpha_0} (\alpha - \alpha_0)\,, \tag{1.13}$$

are, respectively, the radial and binormal coordinates, while z remains the coordinate along the magnetic field. Here, the constants ψ_0 and α_0 are the values of ψ and α at the centre of the flux-tube, and the constant derivatives $\mathrm{d}x/\mathrm{d}\psi$ and $\mathrm{d}y/\mathrm{d}\alpha$, which are also evaluated at the centre of the flux-tube, are chosen so that both x and y have dimensions of length. In this work, we define z such that $\boldsymbol{B} \cdot \nabla z > 0$, so $\nabla\alpha \times \nabla\psi \cdot \nabla z > 0$ or $\nabla y \times \nabla x \cdot \nabla z > 0$. Note that the (x,y,z) coordinate system is defined here to be left-handed. This follows from the convention used in several gyrokinetic codes, such as GS2 [Kotschenreuther et al., 1995b]. In terms of x and y, the magnetic field can be written as

$$\frac{\boldsymbol{B}}{B_0} = \nabla y \times \nabla x, \tag{1.14}$$

where $B_0 = (\mathrm{d}x/\mathrm{d}\psi)^{-1}\,(\mathrm{d}y/\mathrm{d}\alpha)^{-1}$. Note that, in general, ∇x and ∇y are not orthogonal to each other as a result of magnetic shear and shaping of the flux-surface:

$$\begin{aligned}\nabla x \cdot \nabla y &= \frac{1}{B_0}\nabla\psi \cdot \nabla\alpha \\ &= \frac{1}{B_0}\nabla\psi \cdot \left(\nabla\zeta - \frac{\mathrm{d}q}{\mathrm{d}\psi}\vartheta_s\nabla\psi - q\nabla\vartheta_s\right) \\ &= -\frac{|\nabla\psi|^2}{B_0}\frac{\mathrm{d}q}{\mathrm{d}\psi}\vartheta_s - \frac{q}{B_0}\nabla\psi \cdot \nabla\vartheta_s \\ &= -\frac{|\nabla\psi|^2}{B_0}\frac{\mathrm{d}\ln r}{\mathrm{d}\psi}q\hat{s}\vartheta_s - \frac{q}{B_0}\nabla\psi \cdot \nabla\vartheta_s,\end{aligned} \tag{1.15}$$

where r is the flux surface label used in the Miller parametrisation introduced in Subsection 1.2.3, and $\hat{s} = \mathrm{d}\ln q/\mathrm{d}\ln r$ is the magnetic shear, which measures the rate of change of q in the radial direction. The first term on the right-hand-side of (1.15) vanishes at $\vartheta_s = 0$ ($z = 0$) or on the out-board mid-plane. For Miller-parametrised surfaces, $\nabla\psi \cdot \nabla\vartheta_s \approx 0$ in the case of large-aspect ratio ($R_0/r \gg 1$), circular flux surfaces ($\delta = 0, \kappa = 1$). Thus, the out-board mid-plane is a special location where (∇x,∇y,∇z) can form an orthogonal basis in certain magnetic geometry.

1.3 Gyrokinetics

We shall now introduce a widely used tool for studying ITG turbulence – gyrokinetics. As we have argued, the physics of the ITG instability and its associated turbulence can be described by the flux-tube approximation. The turbulent fluctuations are then described by the gyrokinetic–Maxwell system of equations [Frieman and Chen, 1982, Abel et al., 2013][5], which are obtained by imposing the so-called gyrokinetic ordering on the Vlasov–Fokker–Planck–Maxwell equations. The gyrokinetic ordering takes the size of the ion-scale fluctuations perpendicular to the equilibrium magnetic field to be of the order of the ion thermal gyro-radius ρ_i and $\rho_i/L \ll 1$, where $L \sim L_B \sim L_T \sim L_n$ with L_B, L_T, and L_n the magnetic-field, temperature, and density gradient scale lengths, respectively, defined by $L_\alpha = |\nabla \ln \alpha|^{-1}$. Additionally, particles stream relatively freely along magnetic field lines but are constrained in the perpendicular direction by their Larmor motion, the turbulent structures tend to be strongly elongated along the field, i.e., $k_\parallel/k_\perp \ll 1$, where $k_\parallel$ and $k_\perp$ are the wavenumbers parallel and perpendicular to the magnetic field, respectively. Moreover, the time scale associated with the turbulent fluctuations is assumed to be much shorter than the confinement time during which the equilibrium magnetic and pressure profiles evolve, but is still much longer than $1/\Omega_i$, with Ω_i the ion cyclotron frequency. Finally, the δf-gyrokinetics, which concerns only the turbulent fluctuations on a fixed background equilibrium, also assumes that the turbulent fluctuations are small in size compared to the equilibrium quantities. The resulting ordering for the δf-gyrokinetics is

$$\frac{k_\parallel}{k_\perp} \sim \frac{\rho_s}{L} \sim \frac{|\delta \boldsymbol{B}|}{B} \sim \frac{e\phi}{T_e} \sim \frac{\delta f_s}{f_s} \sim \frac{\omega}{\Omega_s} \sim \rho_* \ll 1, \tag{1.16}$$

where $\delta\boldsymbol{B}$ is the magnetic field fluctuation, ρ_s is the Larmor radius of species s, e is the proton charge, ϕ is the electrostatic potential fluctuation, T_s is the equilibrium temperature of species s, f_s is the particle distribution function for species s, δf_s is its fluctuating component, ω is the characteristic frequency of the turbulent fluctuations, Ω_s is the Larmor frequency of species s, and $\rho_* \sim \rho_s/L$ is a small expansion parameter. The resulting

[5] Although gyrokinetics is not limited to the local approximation.

gyrokinetic equation is:

$$\frac{\partial h_s}{\partial t} + v_\parallel \hat{\boldsymbol{b}} \cdot \nabla z \left(\frac{\partial h_s}{\partial z} \right) + \boldsymbol{v}_{Ms} \cdot \nabla_\perp h_s - \frac{\mu}{m_s} \hat{\boldsymbol{b}} \cdot \nabla B \frac{\partial h_s}{\partial v_\parallel} + \langle \boldsymbol{v}_\chi \rangle_{\boldsymbol{R}_s} \cdot \nabla_\perp h_s$$
$$+ \langle \boldsymbol{v}_\chi \rangle_{\boldsymbol{R}_s} \cdot \nabla F_s = \frac{Z_s e}{T_s} F_s \frac{\partial \langle \chi \rangle_{\boldsymbol{R}_s}}{\partial t} + \langle C\left[h_s\right] \rangle_{\boldsymbol{R}_s}, \tag{1.17}$$

which describes the time-evolution of the non-Boltzmann part of δf_s, i.e.,

$$\delta f_s = -\frac{Z_s e \phi}{T_s} F_s + h_s, \quad F_s\left(\boldsymbol{R}_s, v\right) = \frac{n_s}{\pi^{3/2} v_{\text{ths}}^3} \exp\left(-\frac{v^2}{v_{\text{ths}}^2} \right), \tag{1.18}$$

where Z_s is the atomic number (-1 for electrons), n_s is the equilibrium density of species s, $v_{\text{ths}} = \sqrt{2T_s/m_s}$ is the thermal speed with m_s the particle mass. (1.17) includes the magnetic drifts:

$$\boldsymbol{v}_{Ms} = \frac{\hat{\boldsymbol{b}}}{\Omega_s} \times \left[v_\parallel^2 \left(\hat{\boldsymbol{b}} \cdot \nabla \right) \hat{\boldsymbol{b}} + \frac{v_\perp^2}{2} \nabla \ln B \right] \tag{1.19}$$

Using (1.6), we obtain an alternative form for (1.19), given by

$$\boldsymbol{v}_{Ms} = \frac{\hat{\boldsymbol{b}}}{\Omega_s} \times \left[\left(v_\parallel^2 + \frac{v_\perp^2}{2} \right) \nabla \ln B + \frac{\beta}{2} v_\parallel^2 \nabla \ln p \right]. \tag{1.20}$$

(1.17) also includes drifts due to the fluctuating electromagnetic fields:

$$\langle \boldsymbol{v}_\chi \rangle_{\boldsymbol{R}_s} = \frac{c}{B} \hat{\boldsymbol{b}} \times \frac{\partial \langle \chi \rangle_{\boldsymbol{R}_s}}{\partial \boldsymbol{R}_s}, \tag{1.21}$$

$$\chi = \phi - \frac{\boldsymbol{v} \cdot \boldsymbol{A}}{c}, \tag{1.22}$$

where $\langle\rangle_{\boldsymbol{R}_s}$ denotes gyroaverage at fixed guiding centre position $\boldsymbol{R}_s$, $\boldsymbol{v}$ is the velocity vector of the particle and $\boldsymbol{A}$ is the magnetic vector potential. $\langle C\left[h_s\right] \rangle_{\boldsymbol{R}_s}$ is the gyroaveraged Landau collision operator. Unless stated otherwise, the distribution functions h_s and F_s are functions of $\boldsymbol{R}_s$, the velocity component parallel to the equilibrium magnetic field $v_\parallel$, and the magnetic moment $\mu = m_s v_\perp^2/2B$ with $v_\perp$ the velocity component perpendicular to the equilibrium magnetic field. The electrostatic potential ϕ and the magnetic vector potential $\boldsymbol{A}$ are functions of the real space coordinates $\boldsymbol{r} = (x, y, z)$ introduced in Subsection 1.2.4. The perpendicular derivative $\nabla_\perp$ is defined in the flux-tube coordinates as

$$\nabla_\perp = \nabla x \frac{\partial}{\partial x} + \nabla y \frac{\partial}{\partial y}. \tag{1.23}$$

The gyrokinetic equations determine the evolution of the perturbed distribution functions h_s for each species given the electromagnetic fields they produce. To close the set of equations, we also need the field equations for ϕ and $\boldsymbol{A}$. The quasineutrality constraint of the plasma gives an equation for ϕ:

$$0 = \sum_s Z_s \delta n_s = \sum_s Z_s \left[-\frac{Z_s e \phi}{T_s} n_s + \int \mathrm{d}^3\boldsymbol{v} \; \langle h_s \rangle_{\boldsymbol{r}} \right], \tag{1.24}$$

where δn_s is the density fluctuation of species s, $\langle\rangle_{\boldsymbol{r}}$ denotes gyroaverage about $\boldsymbol{r}$ and the velocity space integral is defined as

$$\int \mathrm{d}^3\boldsymbol{v} = \int_0^{2\pi} \mathrm{d}\sigma \int_{-\infty}^{\infty} \mathrm{d}v_\parallel \int_0^{\infty} \frac{B}{m_s} \mathrm{d}\mu \tag{1.25}$$

with σ the gyro-angle. The parallel component of the magnetic vector potential $A_\parallel$ is calculated from the parallel Ampère's law:

$$\nabla_\perp^2 A_\parallel = -\frac{4\pi}{c} \sum_s Z_s e \int d^3\boldsymbol{v} \, v_\parallel \, \langle h_s \rangle_{\boldsymbol{r}}, \tag{1.26}$$

The perpendicular component of the magnetic vector potential $\boldsymbol{A}_\perp$ is related to the field-strength fluctuation $B_\parallel = \delta\boldsymbol{B} \cdot \hat{\boldsymbol{b}}$ by

$$B_\parallel = \hat{\boldsymbol{b}} \cdot (\nabla_\perp \times \boldsymbol{A}_\perp), \tag{1.27}$$

which is obtained from the perpendicular part of Ampère's law:

$$\nabla_\perp^2 B_\parallel = -\frac{4\pi}{c} \hat{\boldsymbol{b}} \cdot \left[\nabla_\perp \times \sum_s Z_s e \int d^3\boldsymbol{v} \; \langle \boldsymbol{v}_\perp h_s \rangle_{\boldsymbol{r}} \right]. \tag{1.28}$$

Since the field equations are linear, we can write them in Fourier space to facilitate evaluation of the gyroaverages, which are local operation in Fourier space. The resulting expressions will prove to be useful later. Writing $\phi = \sum_{\boldsymbol{k}} \phi_{\boldsymbol{k}} \exp(i\boldsymbol{k} \cdot \boldsymbol{r})$ and $h_s = \sum_{\boldsymbol{k}} h_{s,\boldsymbol{k}} \exp(i\boldsymbol{k} \cdot \boldsymbol{R}_s)$, the quasineutrality constraint (1.24) becomes

$$\sum_{\boldsymbol{k}} e^{i\boldsymbol{k}\cdot\boldsymbol{r}} \sum_s \frac{Z_s^2 e \phi_{\boldsymbol{k}}}{T_s} n_s = \sum_{\boldsymbol{k}} e^{i\boldsymbol{k}\cdot\boldsymbol{r}} \sum_s Z_s \int \mathrm{d}^3\boldsymbol{v} \left\langle \exp\left(i\boldsymbol{k} \cdot \frac{\boldsymbol{v}_\perp \times \hat{\boldsymbol{b}}}{\Omega_s} \right) \right\rangle_{\boldsymbol{r}} h_{s,\boldsymbol{k}}. \tag{1.29}$$

The gyroaverage appearing on the right-hand side of the equation can be recognised as the Bessel function

$$\left\langle \exp\left(i\boldsymbol{k} \cdot \frac{\boldsymbol{v}_\perp \times \hat{\boldsymbol{b}}}{\Omega_s} \right) \right\rangle_{\boldsymbol{r}} = J_0(a_s), \tag{1.30}$$

where $a_s = k_\perp v_\perp / \Omega_s$. Hence, the Fourier component $\phi_{\boldsymbol{k}}$ is calculated by

$$\sum_s \frac{Z_s^2 e \phi_{\boldsymbol{k}}}{T_s} n_s = \sum_s Z_s \int \mathrm{d}^3\boldsymbol{v} \; J_0(a_s) h_{s,\boldsymbol{k}}. \tag{1.31}$$

Similarly, the parallel component of Ampère's law is written in Fourier space as

$$A_{\|,\boldsymbol{k}} = \frac{4\pi e}{k_\perp^2 c} \sum_s Z_s \int \mathrm{d}^3\boldsymbol{v}\, J_0(a_s) v_\| h_{s,\boldsymbol{k}}. \tag{1.32}$$

Finally, Fourier decomposing perpendicular component of Ampère's law leads to

$$B_{\|,\boldsymbol{k}} = \frac{4\pi e}{k_\perp^2 c} i\hat{\boldsymbol{b}} \cdot \boldsymbol{k}_\perp \times \sum_s Z_s \int \mathrm{d}^3\boldsymbol{v} \left\langle \boldsymbol{v}_\perp \exp\left(i\boldsymbol{k} \cdot \frac{\boldsymbol{v}_\perp \times \hat{\boldsymbol{b}}}{\Omega_s} \right) \right\rangle_{\boldsymbol{r}} h_{s,\boldsymbol{k}}, \tag{1.33}$$

where the gyroaverage is written as

$$\left\langle \boldsymbol{v}_\perp \exp\left(i\boldsymbol{k} \cdot \frac{\boldsymbol{v}_\perp \times \hat{\boldsymbol{b}}}{\Omega_s} \right) \right\rangle_{\boldsymbol{r}} = i \frac{v_\perp}{k_\perp} \hat{\boldsymbol{b}} \times \boldsymbol{k}_\perp J_1(a_s) \tag{1.34}$$

with J_1 a Bessel function. Using $\boldsymbol{k}_\perp \times (\hat{\boldsymbol{b}} \times \boldsymbol{k}_\perp) = k_\perp^2 \hat{\boldsymbol{b}}$, (1.33) becomes

$$B_{\|,\boldsymbol{k}} = -\frac{4\pi e}{c} \sum_s Z_s \int \mathrm{d}^3\boldsymbol{v}\, \frac{v_\perp^2}{\Omega_s} \frac{J_1(a_s)}{a_s} h_{s,\boldsymbol{k}} = -\frac{4\pi}{B} \sum_s \int \mathrm{d}^3\boldsymbol{v}\, m_s v_\perp^2 \frac{J_1(a_s)}{a_s} h_{s,\boldsymbol{k}}. \tag{1.35}$$

Once h_s is known, one obtains ϕ, $A_\|$ and $B_\|$ from the above field equations. The fields are then fed back to (1.17) through $\langle \chi \rangle_{\boldsymbol{R}_s}$ to evolve the distribution functions:

$$\langle \chi \rangle_{\boldsymbol{R}_s} = \sum_{\boldsymbol{k}} e^{i\boldsymbol{k}\cdot\boldsymbol{R}_s} \left[J_0(a_s) \left(\phi_{\boldsymbol{k}} - \frac{v_\| A_{\|,\boldsymbol{k}}}{c} \right) + \frac{T_s}{Z_s e} \frac{2v_\perp^2}{v_{\mathrm{th}s}^2} \frac{J_1(a_s)}{a_s} \frac{B_{\|,\boldsymbol{k}}}{B} \right]. \tag{1.36}$$

The gyrokinetic-Maxwell system of equations evolve only the perturbations h_s, ϕ and $\boldsymbol{A}$. By contrast, the equilibrium (background) quantities – e.g. B, n_s and T_s – are prescribed and held fixed when solving (1.17). This reflects the separation of spatial and temporal scales between the turbulent fluctuations and the evolution of equilibrium profiles. Hence, in solving (1.17), one needs to specify the magnetic geometry, various plasma parameters such as density and temperature and their corresponding gradients.

For the turbulent fluctuations, statistical periodicity is assumed in the domain perpendicular to the equilibrium magnetic field. However, this property does not generally hold in the direction parallel to the magnetic field, except for certain simple geometries such as a Z-pinch, which we will discuss in Chapter 4. The spatial coordinates are then represented using a pseudo-spectral method, with Fourier transforms applied in the perpendicular (x,y) plane and finite differences used along z. Thus, we can expand any fluctuating quantity $g(\boldsymbol{r})$ as

$$g(\boldsymbol{r}) = \sum_{\boldsymbol{k}_\perp} g_{\boldsymbol{k}_\perp}(z) e^{i\boldsymbol{k}_\perp\cdot\boldsymbol{r}} = \sum_{\boldsymbol{k}_\perp} g_{\boldsymbol{k}_\perp}(z)\, e^{ik_x x + ik_y y}, \tag{1.37}$$

which is the representation commonly used in gyrokinetic codes. The Fourier components $\phi_{\boldsymbol{k}}$, $A_{\parallel,\boldsymbol{k}}$ and $B_{\parallel,\boldsymbol{k}}$ and $h_{s,\boldsymbol{k}}$ appearing in field equations (1.31), (1.32) and (1.35) should therefore be regarded as functions of z in the general case[6].

As the quantity $k_\perp$ appears in the Bessel functions J_0 and J_1, we need to obtain the relation between the magnitude of the perpendicular wavenumber $k_\perp$ and $(k_x,\, k_y)$. This is achieved by considering the Laplacian operator acting on $g\,(\boldsymbol{r})$:

$$
\begin{aligned}
\nabla_\perp^2 g\,(\boldsymbol{r}) &= \sum_{\boldsymbol{k}_\perp} g_{\boldsymbol{k}_\perp}(z) \left(\nabla x \frac{\partial}{\partial x} + \nabla y \frac{\partial}{\partial y}\right)^2 e^{ik_x x + ik_y y} \\
&= -\sum_{\boldsymbol{k}_\perp} g_{\boldsymbol{k}_\perp}(z) \left(|\nabla x|^2 k_x^2 + |\nabla y|^2 k_y^2 + 2\nabla x \cdot \nabla y k_x k_y\right) e^{ik_x x + ik_y y},
\end{aligned} \tag{1.38}
$$

where $|\nabla x|$, $|\nabla y|$ and $\nabla x \cdot \nabla y$ are, in general, functions of z. Thus, given a set of k_x and k_y, the corresponding $k_\perp = \left(|\nabla x|^2 k_x^2 + |\nabla y|^2 k_y^2 + 2\nabla x \cdot \nabla y k_x k_y\right)^{1/2}$.

1.4 ITG turbulence

In this Section, we describe the characteristics of the ITG instability and the corresponding ITG turbulence.

1.4.1 ITG instability

We start by presenting a simplified physical picture for the driving mechanism of the ITG instability. Consider a cross-section of a flux tube (the grey box on the left-hand-side of Fig. 1.3) located on the out-board side of a flux-surface. The box is chosen to be small enough that the background gradients, including the ion temperature gradient ∇T, the magnetic field strength gradient ∇B and the curvature vector $(\hat{\boldsymbol{b}} \cdot \nabla)\hat{\boldsymbol{b}}$, are assumed to stay constant inside. In the out-board region considered, the plasma gets hotter as one moves radially inward, so $\nabla T \propto -\hat{\boldsymbol{x}}$. Both ∇B and $(\hat{\boldsymbol{b}} \cdot \nabla)\hat{\boldsymbol{b}}$ point in the same direction as ∇T, since B increases towards the $R = 0$ axis. Note that, in order for ∇B and $(\hat{\boldsymbol{b}} \cdot \nabla)\hat{\boldsymbol{b}}$ to be aligned, the plasma beta has to be assumed low (see (1.8)). $\boldsymbol{B}$ is perpendicular to the box and is pointing into the page on the right-hand-side of Fig. 1.3.

Now consider an initial mixing between the hot and cold regions of the plasma separated by the green boundary as shown in Fig. 1.3 (The fluctuation varies in the $\hat{\boldsymbol{y}}$-direction). The positive ions undergo magnetic drifts – curvature drift $\boldsymbol{v}_c$ and ∇B-drift $\boldsymbol{v}_{\nabla B}$ given by

$$
\boldsymbol{v}_c = \frac{v_\parallel^2}{\Omega_i} \hat{\boldsymbol{b}} \times (\hat{\boldsymbol{b}} \cdot \nabla \hat{\boldsymbol{b}}) \quad \text{and} \quad \boldsymbol{v}_{\nabla B} = \frac{v_\perp^2}{2\Omega_i} \hat{\boldsymbol{b}} \times \nabla \ln B, \tag{1.39}
$$

[6] We will allow Fourier decomposition along z later when discussing the fluid model. See Chapter 4.

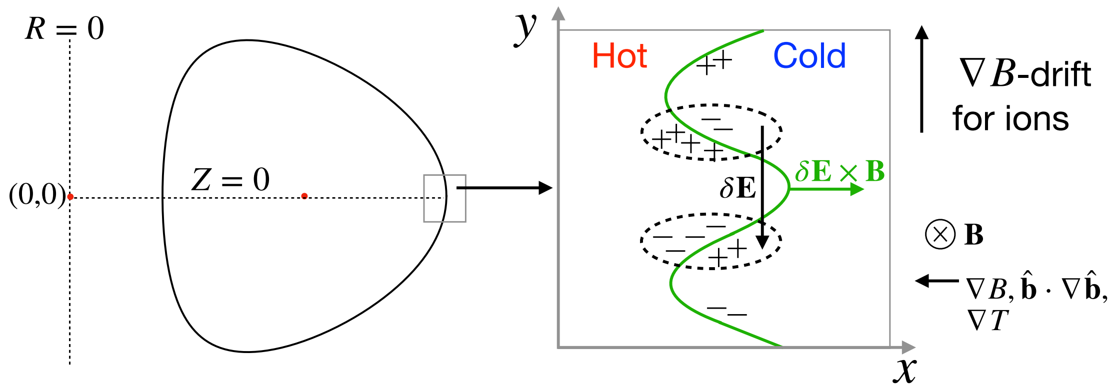

Figure 1.3: Illustration of the positive feedback loop that drives the ITG instability.

respectively. In our case, both $\boldsymbol{v}_c$ and $\boldsymbol{v}_{\nabla B}$ point in the $\hat{\boldsymbol{y}}$-direction. Since the magnetic drift velocity scales with the kinetic energy of the ions, the ions in the hot region drift faster on average than those in the cold region. As a result, positive ions tend to pile up at some portions of the green boundary and become depleted at others, producing a spatial charge imbalance and therefore an electrostatic perturbation $\delta\boldsymbol{E}$ between those regions. That self-generated $\delta\boldsymbol{E}$ then drives $\boldsymbol{E}\times\boldsymbol{B}$ motion which can amplify the initial perturbation and temperature mixing. It is this positive-feedback mechanism that drives the ITG instability.

For the positive-feedback mechanism to operate, we require ∇T and ∇B to be mostly aligned. This condition holds on the out-board side of the flux surface ($z \approx 0$), so the ITG drive there is the strongest. As one moves poloidally around the flux surface, the alignment deteriorates. In particular, in the in-board side of the flux surface ($z \approx \pi$), ∇T and ∇B are approximately anti-aligned, which tends to stabilise the ITG instability. Therefore, one expects the ITG instability to acquire non-trivial mode structure along the field line.

The spatial scales of the fluctuations also play a role in their stability. According to the physical mechanism above, the growth rate of the instability depends on the rate of charge separation. Using the expression for the curvature drift $\boldsymbol{v}_c$ (1.39), the charge separation can be estimated to occur at a rate $\sim k_y\rho_i v_{\mathrm{th}i}/R$ ('$\sim$'means 'on the order of' throughout the thesis), where k_y is the y-component of the wavenumber and $R = |\hat{\boldsymbol{b}}\cdot\nabla\hat{\boldsymbol{b}}|^{-1}$ is the radius of curvature. Physically, $k_y\rho_i v_{\mathrm{th}i}/R$ represents the inverse of the time it takes for the ions to drift a distance comparable to the perpendicular wavelength of the perturbation and thereby build up a net charge across the fluctuation. At $k_y\rho_i \ll 1$, this crossing time is long, so ions produce charge separation very slowly and the instability drive is weak. Naively one might therefore expect the growth rate to keep increasing with $k_y\rho_i$. However, in the opposite limit of $k_y\rho_i \gg 1$, the instability drive is weakened by the finite-Larmor-radius (FLR) effect: because the ion gyro-orbit spans many fluctuation wavelengths, the ions sample (and average) the fluctuating electric field $\delta\boldsymbol{E}$ around their orbit. Overall, the ions experience almost no net $\delta\boldsymbol{E}$, preventing the $\boldsymbol{E}\times\boldsymbol{B}$ drift from further amplifying the perturbation. Hence, the ITG drive is strongest when $k_y\rho_i \sim 1$, which provides a justification for the use of gyrokinetics.

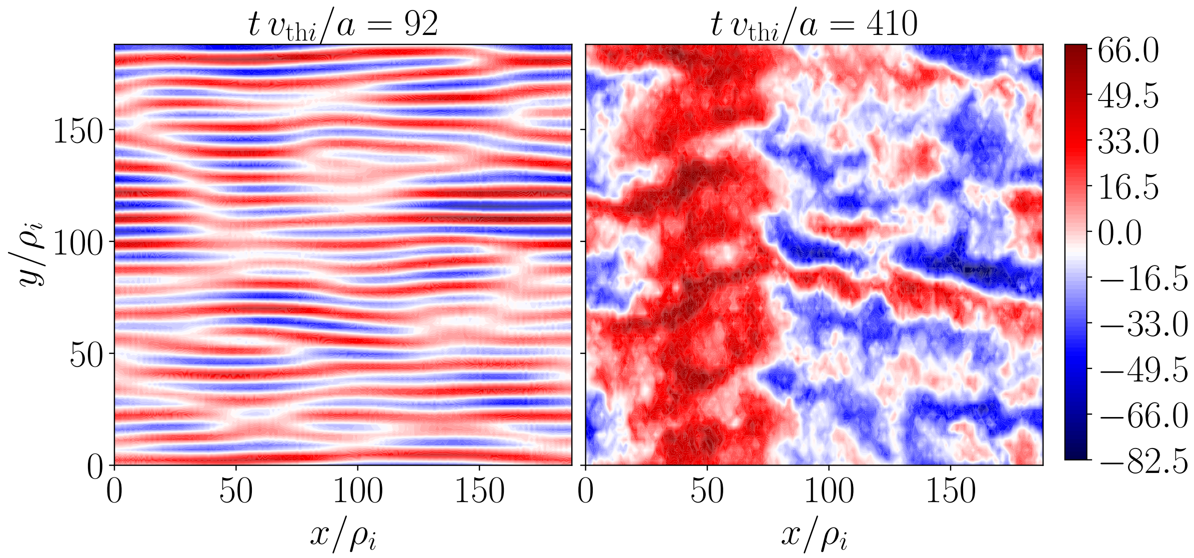

Figure 1.4: Snapshots of electrostatic fluctuations ϕ in (x,y) plane at $z = 0$ obtained from a low-beta gyrokinetic simulation [Barnes et al., 2019]. In this simulation, the ITG turbulence generates strong zonal flows that suppress the transport.

A typical snapshot of the spatial structure in the (x,y)-plane for the ITG instability is shown in the left panel of Fig. 1.4. This snapshot, which shows contours of the electrostatic potential, is taken from a gyrokinetic simulation. The simulation is run for ITG turbulence at sufficiently low plasma beta that the magnetic fluctuations have negligible impact on the qualitative properties of the instabilities. As expected from the physical picture shown in Fig. 1.3, perturbations grow exponentially in the early phase ($tv_{\mathrm{th}i}/a = 92$ with a being the flux label r of the last closed flux surface), and ϕ varies mostly along y, forming alternating, straight red and blue bands that span radially along x. This is because the contour plot only reveals modes with the largest growth rates, which are typically modes with $k_y\rho_i \sim 1$ and $k_x\rho_i = 0$, where k_x is the x-component of the wavenumber. They are also referred to as streamer modes as they appear to be elongated radially. Modes with non-zero k_x typically have smaller growth rates due to FLR damping and collisional dissipation. At a later time ($tv_{\mathrm{th}i}/a = 410$), which is shown on the right panel of Fig. 1.4, nonlinear coupling to the large-amplitude streamers eventually lifts up other, linearly-stable modes and drives the system into a saturated turbulent state that transports particles and energy across flux surfaces. Notice that the spatial scale in the $\hat{\boldsymbol{y}}$-direction of the turbulence is typically larger than the fastest growing modes, and there appears to be band structures oriented in the $\hat{\boldsymbol{y}}$-direction. The red, vertical bands, corresponding to 'zonal' flows, dominates over the streamer modes. These zonal structures play a crucial role in saturating ITG turbulence, as discussed below.

1.4.2 Zonal flow suppression

In the flux-tube coordinates, the zonal flow velocity v_Z is written as

$$v_Z = -\left\langle \frac{c|\nabla x|}{B}\frac{\partial \phi}{\partial x}\right\rangle_{yz}, \tag{1.40}$$

where the flux-surface average $\langle \cdots \rangle_{yz}$ is defined as

$$\langle \cdots \rangle_{yz} \equiv \frac{\int \mathrm{d}z\, J \,\langle \cdots \rangle_y}{\int \mathrm{d}z\, J}, \tag{1.41}$$

where $J = [(\boldsymbol{B}\cdot\nabla z)(\mathrm{d}y/d\alpha)(\mathrm{d}x/\mathrm{d}\psi)]^{-1}$ is the volume Jacobian and $\langle\rangle_y = 1/L_y \int \mathrm{d}y$ with L_y the box size in y of the flux tube. Note that we have made use of the local approximation to ignore the slow (x,y) variation of J. Thus, all zonal quantities refer to those that have undergone the average (1.41), after which they become functions purely of x.

The structure of the zonal electrostatic potential, $\langle\phi\rangle_{yz}$, which approximately indicates the zonal flow strength, is largely visible on the right-hand side of Fig. 1.4, even though the total ϕ is plotted: Near the edges of the red vertical band in Fig. 1.4, the gradient $\mathrm{d}\langle\phi\rangle_{yz}/\mathrm{d}x$, and hence the magnitude of the radial electric field, is the largest, creating the strongest zonal flow along y. On the other hand, at local extrema of $\langle\phi\rangle_{yz}$, the zonal flow velocity is negligible. This radial variation of zonal flow velocity is an essential property, since it produces a zonal-flow shear that decorrelates the long, radially elongated streamers. If the zonal shear is large enough (roughly when the shearing rate is comparable to the linear growth rate or nonlinear decorrelation rate of the dominant modes), the streamers are broken up. This process extracts energy from the large-scale turbulent structures, which are very effective in transporting energy, and redirects it toward smaller scales, ultimately depositing it at viscous scales where the energy is dissipated. Thus, a state with strong zonal flows often results in reduced transport. If zonal flows are weak or strongly damped, streamers persist and turbulence saturates at much higher transport levels.

Zonal-flow dynamics play a central role in determining the so-called Dimits shift [Dimits et al., 2000] for electrostatic ITG turbulence. The Dimits shift denotes the difference between two thresholds: the linear threshold, above which the ITG instability becomes linearly unstable, and the nonlinear threshold (also called the Dimits threshold), beyond which the turbulent transport increases rapidly with the driving temperature gradient. Early expectations assumed these thresholds would coincide, since linear instabilities seed turbulence. However, numerical and theoretical studies showed that the Dimits threshold often sits at a larger temperature gradient than the linear one — the Dimits shift — implying a window of gradients where linear growth exists but nonlinear transport is strongly suppressed.

This suppression is attributed to the self-generated zonal flows, whose shearing disrupts turbulence and keeps transport anomalously low. Below the Dimits threshold, the zonal flows are strong enough to produce predator–prey dynamics [Diamond et al., 2005, Ricci et al., 2006, Kobayashi and Rogers, 2012]: the zonal shear suppresses turbulence and is itself eroded slowly by dissipation, so turbulence remains at a low level. When the zonal shear decays sufficiently, turbulence grows, which in turn drives stronger zonal flows that re-suppress the turbulence. This cycle then repeats.

Crossing the Dimits threshold produces a qualitative change in how zonal flows are generated, resulting in comparatively weaker zonal flows. The predator-prey dynamics is then lost, and the turbulence saturates via a critically balanced energy cascade [Barnes et al., 2011, Nies et al., 2024] far above the threshold. Because zonal shearing has less impact on the turbulence, the turbulent amplitudes track the linear instability drive more closely. As a result, turbulent transport increases rapidly above the threshold and its dependence on the temperature gradient strengthens. Nevertheless, the zonal flows are still important in regulating the turbulence, allowing it to saturate at reasonable levels.

As the turbulence enters the electromagnetic regime (when plasma β is finite), the presence of strong magnetic fluctuations can significantly impair zonal flow generation. The zonal flows sometimes become so weak that the turbulence is observed to produce divergent transport levels in the numerical simulations[7]. In the next Subsection, we discuss the adverse effect of magnetic fluctuations on zonal flow generation.

1.4.3 Non-zonal transition

As finite-β effects are included, the ITG turbulence is modified. At sufficiently large values of β, the turbulence is observed numerically to produce much higher transport than in the electrostatic limit, as discussed briefly in Subsection 1.1.2. One possible explanation is that it is due to the presence of electromagnetic instabilities (instabilities that intrinsically require magnetic fluctuations). For example, the turbulence driven by kinetic ballooning modes (KBMs) have been observed to drive large transport via their interaction with tearing-parity modes, even when the KBM growth rates are subdominant to other electrostatic instabilities [Mulholland et al., 2024]. There are also cases where the linear instability exhibits characteristics of both electrostatic and electromagnetic modes [Kennedy et al., 2023, Giacomin et al., 2024], leading to transport levels significantly

[7]The heat fluxes we obtain from those simulations sometimes grow indefinitely. However, in reality, heat fluxes cannot be infinite. Thus, the practical implication of the divergent fluxes is that the equilibrium profiles are significantly modified by the turbulence, including decrease in plasma beta and pressure gradients.

higher than those of practical relevance.

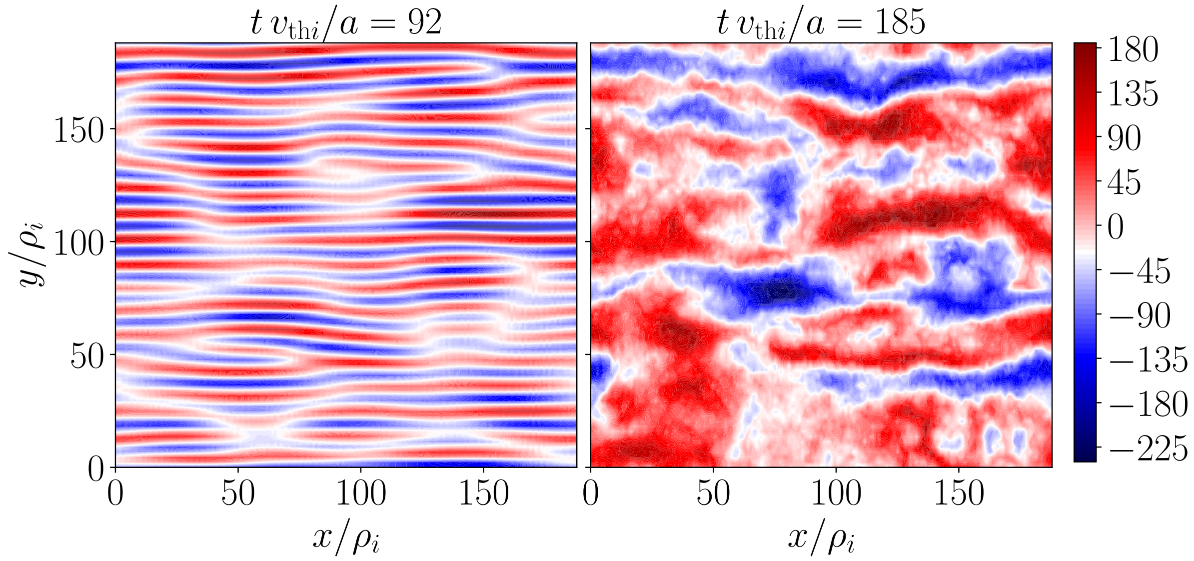

Figure 1.5: Snapshots of electrostatic fluctuations ϕ in the (x,y) plane at $z = 0$ obtained from a `stella` gyrokinetic simulation with higher beta than the one in Fig. 1.4. In this simulation, the ITG turbulence is incapable of generating strong zonal flows. Instead, large streamer structures persist, leading to extremely high transport.

However, it is not clear if the electromagnetic instabilities are the root cause of the observed high transport levels. A number of studies have found that the onset of electromagnetic instabilities does not necessarily imply extreme transport: Some gyrokinetic simulations of KBM-unstable plasmas can achieve well-saturated turbulence, [Pueschel et al., 2008, Maeyama et al., 2014, Kumar et al., 2021, Najlaoui et al., 2025] and some demonstrate heat fluxes considerably lower than the corresponding electrostatic cases [McKinney et al., 2021]. The KBM turbulence may have a different saturation mechanism from ITG turbulence as pointed out by Maeyama et al. [2014], and it was observed there that even when the growth rates of ITG and KBM instabilities are similar, the KBM turbulence produces lower transport, despite weaker zonal flows.

Conversely, in the absence of purely electromagnetic instabilities, ITG turbulence may still enter a regime of 'high-β runaway', characterized by extreme transport levels [Waltz, 2010, Pueschel et al., 2013b, Rath and Peeters, 2022, Giacomin et al., 2024]. This runaway behaviour is associated with the emergence of streamers – radially-elongated, coherent structures – that efficiently transport heat across the system once the plasma beta exceeds a critical value. The transition occurring at this critical beta is often referred to as a 'non-zonal' transition [Pueschel et al., 2013b] to reflect both the corresponding suppression of zonal flow and to distinguish it from the electromagnetic linear instability threshold. In this work, we shall be using the term *non-zonal* to describe states with large (or divergent) turbulent transport and zonal fluctuation amplitudes comparable to or smaller than the non-zonal counterparts.

The absence of a clear zonal structure beyond the non-zonal threshold is illustrated in Fig. 1.5, where the snapshots are analogous to those in Fig. 1.4 but correspond to a gyrokinetic simulation with a higher plasma beta. The ITG instabilities that develop during the early phase appear qualitatively similar to those in the low-beta case. However, as seen by comparing the right-hand sides of Fig. 1.4 and Fig. 1.5, the flux-surface-averaged potential, $\langle\phi\rangle_{yz}$, is far less dominant in the latter, and prominent streamer structures are clearly visible.

Numerical evidence indicates that the non-zonal transition has a stronger influence on ITG turbulence, where transport suppression relies on zonal flows. Several explanations have been proposed for the non-zonal transition. Waltz [2010] proposed that the zonal structures are unstable to tertiary excitation of electromagnetic instabilities, such as MHD modes or KBMs. The tertiary modes could then grow to amplitudes larger than the zonal modes. However, it was later shown that zonal amplitudes generated by turbulence are insufficient to excite KBMs under typical conditions [Pueschel et al., 2013a]. Instead, Pueschel et al. [2013b, 2014] argues that the transition arises from increased magnetic stochasticity at higher β, which is accompanied by fast electron streaming along the radially perturbed field lines. As a result, the zonal structures are effectively 'short-circuited'. The presence of magnetic stochasticity – and its β^2 scaling in electromagnetic ITG turbulence – has been discussed previously [Nevins et al., 2011] in contexts separate from the non-zonal transition. Nevertheless, Pueschel et al. [2013b] proposes a new physical insight: while the tearing-parity magnetic perturbations dominate magnetic stochasticity below the non-zonal threshold, twisting-parity magnetic perturbations begin to contribute significantly at the threshold, leading to a discontinuous elevation of the magnetic stochasticity level. This change in twisting-parity behaviour is attributed to the radial excursions of field lines exceeding the turbulence's radial correlation length. Consequently, above the threshold, stochasticity may exhibit a stronger scaling with magnetic energy due to contributions from modes of both parities. However, more recent work [Rath and Peeters, 2022] finds no evidence for this stronger stochasticty scaling with magnetic energy above the non-zonal threshold. An alternative explanation proposed there is that, at the non-zonal threshold, the Reynolds stress – which normally drives zonal flows – is completely canceled by the Maxwell stress.

In this thesis, we focus primarily on the stress-based picture. This approach is physically intuitive: if the high or divergent transport states result from weakened zonal flows, then directly analysing the evolution of zonal flows should reveal the underlying physics, where turbulent stresses emerge naturally as the relevant quantities. We will show later that the evolution of zonal flows is controlled by the competition between a combination of linear and nonlinear stresses. Combined with an empirical scaling for the stresses, we then demonstrate that the threshold for the non-zonal transition can be predicted from a single, effectively electrostatic, nonlinear simulation. Since this work involves numerical simulations performed with the gyrokinetic code `stella`, its numerical schemes are introduced in Chapter 2. Readers already familiar with the code, or those primarily interested in the results, may skip this chapter.

Chapter 2

Gyrokinetic code – `stella`

To solve the kinetic equation on a mesh, you really need to know what you are doing. That's why, historically, people haven't.
— Rafael Bailo, Oxford plasma seminars and Vienna meetings

There are various gyrokinetic codes that perform local flux-tube gyrokinetic simulations such as `GS2` [Kotschenreuther et al., 1995b], `GENE` [Jenko et al., 2000], `stella` [Barnes et al., 2019], `CGYRO` [Candy et al., 2016, 2020] and `GX` [Mandell et al., 2024]. Since the majority of the numerical work presented in this thesis is performed using the gyrokinetic code `stella`, we will introduce the algorithm in this chapter. The electrostatic version of `stella` has been thoroughly introduced in Barnes et al. [2019]. Thus, we will focus on the changes in the algorithm as we include magnetic perturbations.

2.1 Normalised gyrokinetic equation

`stella` is a pseudo-spectral code, meaning that we solve the Fourier transformed version of (1.17), where the Fourier transform is only performed in the (x, y) plane perpendicular to the equilibrium magnetic field. Fourier transforming (1.17), we obtain:

$$\frac{\partial h_{s,\boldsymbol{k}}}{\partial t} + v_\parallel(\hat{\boldsymbol{b}}\cdot\nabla z)\frac{\partial h_{s,\boldsymbol{k}}}{\partial z} + i\omega_{d,s,\boldsymbol{k}}h_{s,\boldsymbol{k}} - \frac{\mu}{m_s}(\hat{\boldsymbol{b}}\cdot\nabla B)\frac{\partial h_{s,\boldsymbol{k}}}{\partial v_\parallel} + \mathcal{N}_{\boldsymbol{k}} + ik_y c\frac{\mathrm{d}y}{\mathrm{d}\alpha}\frac{\mathrm{d}F_s}{\mathrm{d}\psi}\left\langle\chi\right\rangle_{\boldsymbol{R}_s,\boldsymbol{k}} = \frac{Z_s e}{T_s}F_s\frac{\partial\left\langle\chi\right\rangle_{\boldsymbol{R}_s,\boldsymbol{k}}}{\partial t}, \tag{2.1}$$

where the subscript $\boldsymbol{k}$ refers to the corresponding Fourier mode. We will not discuss the collisional term here. The magnetic drift frequency is

$$\omega_{d,s,\boldsymbol{k}} = \frac{\hat{\boldsymbol{b}}}{\Omega_s}\times\left[\left(v_\parallel^2 + \frac{B\mu}{m_s}\right)\nabla\ln B + \frac{\beta}{2}v_\parallel^2\nabla\ln p\right]\cdot\left(k_x\nabla x + k_y\nabla y\right), \tag{2.2}$$

where we have used $\mu = m_s v_\perp^2/2B$ and (1.23) to rewrite (1.20). $\mathcal{N}_{\boldsymbol{k}}$ is the Fourier transformed nonlinearity:

$$\frac{c}{B}(\hat{\boldsymbol{b}} \times \nabla x \cdot \nabla y)\boldsymbol{\mathcal{F}}_{\boldsymbol{k}} \left[\boldsymbol{\mathcal{F}}_{\boldsymbol{k}}^{-1}[ik_x \langle \chi \rangle_{\boldsymbol{R}_s,\boldsymbol{k}}]\boldsymbol{\mathcal{F}}_{\boldsymbol{k}}^{-1}[ik_y h_{s,\boldsymbol{k}}] - \boldsymbol{\mathcal{F}}_{\boldsymbol{k}}^{-1}[ik_y \langle \chi \rangle_{\boldsymbol{R}_s,\boldsymbol{k}}]\boldsymbol{\mathcal{F}}_{\boldsymbol{k}}^{-1}[ik_x h_{s,\boldsymbol{k}}]\right], \tag{2.3}$$

where $\boldsymbol{\mathcal{F}}_{\boldsymbol{k}}$ represents the forward Fourier transform from position space to wavenumber space that outputs a Fourier mode with wavenumber $\boldsymbol{k}$, and $\boldsymbol{\mathcal{F}}_{\boldsymbol{k}}^{-1}$ denotes the inverse transform. Next, we rewrite (2.1) in a dimensionless form with a set of normalisations

$v_r = \sqrt{\frac{2T_r}{m_r}}$	$\tilde{m}_s = \frac{m_s}{m_r}$
$\rho_r = \frac{v_r}{\Omega_r}$	$\tilde{T}_s = \frac{T_s}{T_r}$
$\Omega_r = \frac{eB_r}{m_r c}$	$\tilde{n}_s = \frac{n_s}{n_r}$
$\tilde{t} = t\frac{v_r}{a}$	$\tilde{B} = \frac{B}{B_r}$
$\tilde{\nabla} = a\nabla$	$\tilde{h}_{s,\boldsymbol{k}} = \frac{h_{s,\boldsymbol{k}}}{F_s e^{\tilde{v}^2}}\frac{a}{\rho_r}$
$\tilde{v} = \frac{v}{v_{\mathrm{th}s}}$	$\tilde{\phi}_{\boldsymbol{k}} = \frac{e\phi_{\boldsymbol{k}}}{T_r}\frac{a}{\rho_r}$
$\tilde{v}_\parallel = \frac{v_\parallel}{v_{\mathrm{th}s}}$	$\tilde{A}_{\parallel,\boldsymbol{k}} = \frac{A_{\parallel,\boldsymbol{k}}}{\rho_r B_r}\frac{a}{\rho_r}$
$\tilde{\mu} = \frac{\mu B_r}{2T_s}$	$\tilde{B}_{\parallel,\boldsymbol{k}} = \frac{B_{\parallel,\boldsymbol{k}}}{B_r}\frac{a}{\rho_r}$

Table 2.1: Reference and normalised quantities used in `stella`. The subscript 'r' stands for the reference quantity and the tilde denotes the normalised quantities. Here, a is the reference length for the equilibrium scale lengths, which is often taken to be the half-diameter of the last closed flux-surface at the height of the magnetic axis. Note that the normalisation of ∇ does not apply to ∇x or ∇y since $\nabla x \sim \nabla y \sim 1$.

listed in Tab. 2.1. The normalised equation is

$$\frac{\partial \tilde{h}_{s,\boldsymbol{k}}}{\partial \tilde{t}} + \frac{v_{\mathrm{th}s}}{v_r}\tilde{v}_\parallel(\hat{\boldsymbol{b}} \cdot \tilde{\nabla} z)\frac{\partial \tilde{h}_{s,\boldsymbol{k}}}{\partial z} + i\tilde{\omega}_{d,s,\boldsymbol{k}}\tilde{h}_{s,\boldsymbol{k}} - \frac{v_{\mathrm{th}s}}{v_r}\tilde{\mu}(\hat{\boldsymbol{b}} \cdot \tilde{\nabla}\tilde{B})\frac{\partial \tilde{h}_{s,\boldsymbol{k}}}{\partial \tilde{v}_\parallel} + \tilde{\mathcal{N}}_{\boldsymbol{k}} + i\tilde{\omega}_{*,s,\boldsymbol{k}} \langle \tilde{\chi} \rangle_{\boldsymbol{R}_s,\boldsymbol{k}} = \frac{Z_s}{\tilde{T}_s}e^{-\tilde{v}^2}\frac{\partial \langle \tilde{\chi} \rangle_{\boldsymbol{R}_s,\boldsymbol{k}}}{\partial \tilde{t}}, \tag{2.4}$$

which includes the normalised magnetic drift frequency

$$\tilde{\omega}_{d,s,\boldsymbol{k}} = \frac{\tilde{T}_s}{Z_s \tilde{B}} \hat{\boldsymbol{b}} \times \left[\left(\tilde{v}_\parallel^2 + \tilde{B}\tilde{\mu} \right) \tilde{\nabla} \ln \tilde{B} + \frac{\beta_r \tilde{n}_s \tilde{T}_s}{2\tilde{B}^2} \tilde{v}_\parallel^2 \tilde{\nabla} \ln \tilde{p} \right] \cdot \left(k_x \rho_r \nabla x + k_y \rho_r \nabla y \right), \tag{2.5}$$

with $\beta_r = 8\pi n_r T_r / B_r^2$ the reference plasma beta, the energy injection frequency

$$\tilde{\omega}_{*,s,\boldsymbol{k}} = \frac{B_r a}{2} e^{-\tilde{v}^2} k_y \rho_r \frac{\mathrm{d}y}{\mathrm{d}\alpha} \frac{\mathrm{d} \ln F_s}{\mathrm{d}\psi}, \tag{2.6}$$

the Fourier component of the normalised nonlinearity $\tilde{\mathcal{N}}_{\boldsymbol{k}}$ given by

$$\frac{\boldsymbol{b} \times \nabla x \cdot \nabla y}{2\tilde{B}} \boldsymbol{\mathcal{F}}_{\boldsymbol{k}} \left[\boldsymbol{\mathcal{F}}_{\boldsymbol{k}}^{-1} [i k_x \rho_r \langle \tilde{\chi} \rangle_{\boldsymbol{R}_s,\boldsymbol{k}}] \boldsymbol{\mathcal{F}}_{\boldsymbol{k}}^{-1} [i k_y \rho_r \tilde{h}_{s,\boldsymbol{k}}] - \boldsymbol{\mathcal{F}}_{\boldsymbol{k}}^{-1} [i k_y \rho_r \langle \tilde{\chi} \rangle_{\boldsymbol{R}_s,\boldsymbol{k}}] \boldsymbol{\mathcal{F}}_{\boldsymbol{k}}^{-1} [i k_x \rho_r \tilde{h}_{s,\boldsymbol{k}}] \right], \tag{2.7}$$

and the normalised, gyroaveraged potential $\langle \tilde{\chi} \rangle_{\boldsymbol{R}_s,\boldsymbol{k}}$

$$\langle \tilde{\chi} \rangle_{\boldsymbol{R}_s,\boldsymbol{k}} = J_0(a_s) \left(\tilde{\phi}_{\boldsymbol{k}} - 2\tilde{v}_\parallel \frac{v_{\mathrm{th}s}}{v_r} \tilde{A}_{\parallel,\boldsymbol{k}} \right) + 4\tilde{\mu} \frac{\tilde{T}_s}{Z_s} \frac{J_1(a_s)}{a_s} \tilde{B}_{\parallel,\boldsymbol{k}}, \tag{2.8}$$

where a_s can be written in terms of the normalised quantities as

$$a_s = \frac{k_\perp v_\perp}{\Omega_s} = \sqrt{\frac{2\tilde{m}_s \tilde{T}_s}{Z_s^2 \tilde{B}}} k_\perp \rho_r \sqrt{\tilde{\mu}}. \tag{2.9}$$

The equation (2.4) contains time derivatives of both $\tilde{h}_{s,\boldsymbol{k}}$ and $\langle \tilde{\chi} \rangle_{\boldsymbol{R}_s,\boldsymbol{k}}$, which complicates the numerical implementation. Hence, we define two new functions:

$$\tilde{g}_{s,\boldsymbol{k}} = \tilde{h}_{s,\boldsymbol{k}} - \left(\frac{Z_s}{\tilde{T}_s} J_0(a_s) \tilde{\phi}_{\boldsymbol{k}} + 4\tilde{\mu} \frac{J_1(a_s)}{a_s} \tilde{B}_{\parallel,\boldsymbol{k}} \right) e^{-\tilde{v}^2}, \tag{2.10}$$

$$\bar{\tilde{g}}_{s,\boldsymbol{k}} = \tilde{h}_{s,\boldsymbol{k}} - \frac{Z_s}{\tilde{T}_s} \langle \tilde{\chi} \rangle_{\boldsymbol{R}_s,\boldsymbol{k}} e^{-\tilde{v}^2} = \tilde{g}_{s,\boldsymbol{k}} + 2\frac{Z_s}{\tilde{T}_s} J_0(a_s) \tilde{v}_\parallel \frac{v_{\mathrm{th}s}}{v_r} \tilde{A}_{\parallel,\boldsymbol{k}} e^{-\tilde{v}^2}. \tag{2.11}$$

We then write (2.4) in a form that is solved by `stella`:

$$\begin{aligned} &\frac{\partial \bar{\tilde{g}}_{s,\boldsymbol{k}}}{\partial \tilde{t}} + \frac{v_{\mathrm{th}s}}{v_r} \tilde{v}_\parallel (\hat{\boldsymbol{b}} \cdot \tilde{\nabla} z) \frac{\partial}{\partial z} \left[\tilde{g}_{s,\boldsymbol{k}} + \left(\frac{Z_s}{\tilde{T}_s} J_0(a_s) \tilde{\phi}_{\boldsymbol{k}} + 4\tilde{\mu} \frac{J_1(a_s)}{a_s} \tilde{B}_{\parallel,\boldsymbol{k}} \right) e^{-\tilde{v}^2} \right] \\ &+ i\tilde{\omega}_{d,s,\boldsymbol{k}} \left[\tilde{g}_{s,\boldsymbol{k}} + \left(\frac{Z_s}{\tilde{T}_s} J_0(a_s) \tilde{\phi}_{\boldsymbol{k}} + 4\tilde{\mu} \frac{J_1(a_s)}{a_s} \tilde{B}_{\parallel,\boldsymbol{k}} \right) e^{-\tilde{v}^2} \right] - \frac{v_{\mathrm{th}s}}{v_r} \tilde{\mu} (\hat{\boldsymbol{b}} \cdot \tilde{\nabla} \tilde{B}) \frac{\partial \tilde{g}_{s,\boldsymbol{k}}}{\partial \tilde{v}_\parallel} \\ &+ \tilde{\mathcal{N}}_{\boldsymbol{k}} + i\tilde{\omega}_{*,s,\boldsymbol{k}} \langle \tilde{\chi} \rangle_{\boldsymbol{R}_s,\boldsymbol{k}} = 0. \end{aligned} \tag{2.12}$$

Note that the equation is not purely written in terms of $\bar{\tilde{g}}_{s,\boldsymbol{k}}$. This is because writing the mirror term with $\bar{\tilde{g}}_{s,\boldsymbol{k}}$ produces a term which is $\propto (v_{\text{th}s}/v_r)^2$:

$$\frac{v_{\text{th}s}}{v_r}\tilde{\mu}\left(\hat{\boldsymbol{b}}\cdot\tilde{\nabla}\tilde{B}\right)\frac{\partial\tilde{h}_{s,\boldsymbol{k}}}{\partial\tilde{v}_\parallel} = \frac{v_{\text{th}s}}{v_r}\tilde{\mu}\left(\hat{\boldsymbol{b}}\cdot\tilde{\nabla}\tilde{B}\right)\frac{\partial\bar{\tilde{g}}_{s,\boldsymbol{k}}}{\partial\tilde{v}_\parallel} + 2\frac{Z_s}{\tilde{T}_s}J_0(a_s)\left(\frac{v_{\text{th}s}}{v_r}\right)^2\tilde{\mu}\left(\hat{\boldsymbol{b}}\cdot\tilde{\nabla}\tilde{B}\right)\tilde{A}_{\parallel,\boldsymbol{k}}e^{-\tilde{v}^2}. \tag{2.13}$$

In the electron gyrokinetic equation, the second term on the right-hand side of (2.13) includes a factor of $(v_{\text{th}e}/v_r)^2$. Since it is common to choose $v_{\text{th}i} \approx v_r$, $(v_{\text{th}e}/v_r)^2 \approx 3600$ for deuterium–electron plasmas, which imposes a stringent constraint on the timestep for numerical simulations. To maintain stability while using realistic timestep sizes, `stella` advances $\bar{\tilde{g}}_{s,\boldsymbol{k}}$ by including $\tilde{g}_{s,\boldsymbol{k}}$ in the linear terms, while the nonlinear term $\tilde{\mathcal{N}}_{\boldsymbol{k}}$ is evaluated using $\tilde{h}_{s,\boldsymbol{k}}$. Since this scheme requires frequent conversion among $\tilde{h}_{s,\boldsymbol{k}}$, $\tilde{g}_{s,\boldsymbol{k}}$, and $\bar{\tilde{g}}_{s,\boldsymbol{k}}$, `stella` provides dedicated routines to transform between these functions using (2.10) and (2.11).

To solve for the fields, we couple (2.12) with the Maxwell equations (written in terms of $\tilde{g}_{s,\boldsymbol{k}}$). Using (1.31) and

$$\int \mathrm{d}^3\boldsymbol{v} = 2\pi\tilde{B}v_{\text{th}s}^3\int_0^\infty \mathrm{d}\tilde{\mu}\int_{-\infty}^\infty \mathrm{d}\tilde{v}_\parallel, \tag{2.14}$$

we obtain the normalised quasineutrality condition

$$\begin{aligned}\sum_s \frac{Z_s^2\tilde{n}_s}{\tilde{T}_s}\left[1-\Gamma_0(\alpha_s)\right]\tilde{\phi}_{\boldsymbol{k}} - \sum_s \frac{Z_s\tilde{n}_s}{\tilde{B}}\Gamma_1(\alpha_s)\tilde{B}_{\parallel,\boldsymbol{k}}&\\ = \sum_s Z_s\tilde{n}_s\frac{2\tilde{B}}{\sqrt{\pi}}\int_0^\infty \mathrm{d}\tilde{\mu}\int_{-\infty}^\infty \mathrm{d}\tilde{v}_\parallel\, J_0(a_s)\tilde{g}_{s,\boldsymbol{k}} = \hat{Q}\tilde{g}_{s,\boldsymbol{k}},&\end{aligned} \tag{2.15}$$

where

$$\alpha_s = \frac{k_\perp^2\rho_s^2}{2} = \frac{\tilde{m}_s\tilde{T}_s}{2Z_s^2\tilde{B}^2}k_\perp^2\rho_r^2. \tag{2.16}$$

(1.32) leads to the normalised parallel Ampère's law

$$\tilde{A}_{\parallel,\boldsymbol{k}} = \frac{\beta_r}{k_\perp^2\rho_r^2}\sum_s Z_s\tilde{n}_s\left(\frac{v_{\text{th}s}}{v_r}\right)\frac{2\tilde{B}}{\sqrt{\pi}}\int_0^\infty \mathrm{d}\tilde{\mu}\int_{-\infty}^\infty \mathrm{d}\,\tilde{v}_\parallel J_0\left(a_s\right)\tilde{v}_\parallel\tilde{g}_{s,\boldsymbol{k}} = \hat{P}_\parallel\tilde{g}_{s,\boldsymbol{k}}, \tag{2.17}$$

and (1.35) leads to the normalised perpendicular Ampère's law

$$\begin{aligned}\left[1+\frac{\beta_r}{\tilde{B}^2}\sum_s \tilde{n}_s\tilde{T}_s\Gamma_1(\alpha_s)\right]\tilde{B}_{\parallel,\boldsymbol{k}} + \frac{\beta_r}{2\tilde{B}}\left[\sum_s Z_s\tilde{n}_s\Gamma_1(\alpha_s)\right]\tilde{\phi}_{\boldsymbol{k}}&\\ = -2\beta_r\sum_s \tilde{n}_s\tilde{T}_s\frac{2\tilde{B}}{\sqrt{\pi}}\int_0^\infty \mathrm{d}\tilde{\mu}\int_{-\infty}^\infty \mathrm{d}\tilde{v}_\parallel\tilde{\mu}\frac{J_1(a_s)}{a_s}\tilde{g}_{s,\boldsymbol{k}} = \hat{P}_\perp\tilde{g}_{s,\boldsymbol{k}}.&\end{aligned} \tag{2.18}$$

We define the integral operators $\hat{Q}$, $\hat{P}_\parallel$ and $\hat{P}_\perp$ in (2.15), (2.17) and (2.18), respectively, which will be useful later. The Γ functions are calculated with the following integrals:

$$\Gamma_0(\alpha_s) = \frac{1}{n_s}\int \mathrm{d}^3\boldsymbol{v}\,[J_0(a_s)]^2 F_s = \frac{2\tilde{B}}{\sqrt{\pi}}\int_0^\infty \mathrm{d}\tilde{\mu}\int_{-\infty}^{\infty}\mathrm{d}\tilde{v}_\parallel\,[J_0(a_s)]^2 e^{-\tilde{v}^2}, \tag{2.19}$$

$$\Gamma_1(\alpha_s) = \frac{1}{n_s}\int \mathrm{d}^3\boldsymbol{v}\,\frac{2v_\perp^2}{v_{\mathrm{th}s}^2}J_0(a_s)\frac{J_1(a_s)}{a_s}F_s = \frac{8\tilde{B}^2}{\sqrt{\pi}}\int_0^\infty \mathrm{d}\tilde{\mu}\int_{-\infty}^{\infty}\mathrm{d}\tilde{v}_\parallel\,\tilde{\mu}\frac{J_0(a_s)J_1(a_s)}{a_s}e^{-\tilde{v}^2}. \tag{2.20}$$

An alternative definition of Γ_1 is

$$\Gamma_1(\alpha_s) = \frac{1}{2n_s}\int \mathrm{d}^3\boldsymbol{v}\left[\frac{2v_\perp^2}{v_{\mathrm{th}s}^2}\frac{J_1(a_s)}{a_s}\right]^2 F_s = \frac{16\tilde{B}^3}{\sqrt{\pi}}\int_0^\infty \mathrm{d}\tilde{\mu}\int_{-\infty}^{\infty}\mathrm{d}\tilde{v}_\parallel\,\tilde{\mu}^2\left[\frac{J_1(a_s)}{a_s}\right]^2 e^{-\tilde{v}^2}. \tag{2.21}$$

(2.20) is used for deriving (2.15), while (2.21) is used for deriving (2.18).

2.2 Operator splitting

For electrons, parallel streaming and mirror terms carry a factor of v_{the}/v_r, making the numerical treatment challenging. Thus, as described by Barnes et al. [2019], we employ operator splitting to separate fast streaming and mirror dynamics from the rest. The idea is to split equation (2.12) into three pieces:

$$\frac{\partial\bar{\tilde{g}}_{s,\boldsymbol{k}}}{\partial\tilde{t}} = \left(\frac{\partial\bar{\tilde{g}}_{s,\boldsymbol{k}}}{\partial\tilde{t}}\right)_1 + \left(\frac{\partial\bar{\tilde{g}}_{s,\boldsymbol{k}}}{\partial\tilde{t}}\right)_2 + \left(\frac{\partial\bar{\tilde{g}}_{s,\boldsymbol{k}}}{\partial\tilde{t}}\right)_3, \tag{2.22}$$

where the terms on the right-hand side of the equation satisfy

$$\left(\frac{\partial\bar{\tilde{g}}_{s,\boldsymbol{k}}}{\partial\tilde{t}}\right)_1 + i\tilde{\omega}_{d,s,\boldsymbol{k}}\left[\tilde{g}_{s,\boldsymbol{k}} + \left(\frac{Z_s}{\tilde{T}_s}J_0(a_s)\tilde{\phi}_{\boldsymbol{k}} + 4\tilde{\mu}\frac{J_1(a_s)}{a_s}\tilde{B}_{\parallel,\boldsymbol{k}}\right)e^{-\tilde{v}^2}\right] + \tilde{\mathcal{N}}_{\boldsymbol{k}} + i\tilde{\omega}_{*,s,\boldsymbol{k}}\left\langle\tilde{\chi}\right\rangle_{\boldsymbol{R}_s,\boldsymbol{k}} = 0, \tag{2.23}$$

$$\left(\frac{\partial\bar{\tilde{g}}_{s,\boldsymbol{k}}}{\partial\tilde{t}}\right)_2 - \frac{v_{\mathrm{th}s}}{v_r}\tilde{\mu}(\hat{\boldsymbol{b}}\cdot\tilde{\nabla}\tilde{B})\frac{\partial\tilde{g}_{s,\boldsymbol{k}}}{\partial\tilde{v}_\parallel} = 0, \tag{2.24}$$

$$\left(\frac{\partial\bar{\tilde{g}}_{s,\boldsymbol{k}}}{\partial\tilde{t}}\right)_3 + \frac{v_{\mathrm{th}s}}{v_r}\tilde{v}_\parallel(\hat{\boldsymbol{b}}\cdot\tilde{\nabla}z)\frac{\partial}{\partial z}\left[\tilde{g}_{s,\boldsymbol{k}} + \left(\frac{Z_s}{\tilde{T}_s}J_0(a_s)\tilde{\phi}_{\boldsymbol{k}} + 4\tilde{\mu}\frac{J_1(a_s)}{a_s}\tilde{B}_{\parallel,\boldsymbol{k}}\right)e^{-\tilde{v}^2}\right] = 0. \tag{2.25}$$

The splitting introduced here is mostly identical to that of Barnes et al. [2019] except in the electromagnetic version we have $\bar{\tilde{g}}_{s,\boldsymbol{k}}$ and $\tilde{B}_{\parallel,\boldsymbol{k}}$ terms. Symbolically, we can write (2.12) as

$$\frac{\partial\bar{\boldsymbol{g}}}{\partial\tilde{t}} = \mathcal{A}[\boldsymbol{g}] + (\mathcal{B}+\mathcal{C})\,\boldsymbol{g}, \tag{2.26}$$

where $\bar{\boldsymbol{g}}$ and $\boldsymbol{g}$ are vectors constructed from $\bar{\tilde{g}}_{s,\boldsymbol{k}}$ and $\tilde{g}_{s,\boldsymbol{k}}$ evaluated at various species and phase space coordinates. $\mathcal{A}$ is the nonlinear operator defined by (2.23), $\mathcal{B}$ and $\mathcal{C}$ are linear operators defined by (2.24) and (2.25), respectively. The electromagnetic fields are not explicitly mentioned in (2.26) since they can be written as integral operators acting on $\tilde{g}_{s,\boldsymbol{k}}$. Operator splitting means that we solve (2.26) in three sequential steps:

$$\bar{\boldsymbol{g}}_1^n = \bar{\boldsymbol{g}}^n + \Delta\tilde{t}\,\mathcal{A}\left[\boldsymbol{g}^n\right], \tag{2.27}$$

$$\bar{\boldsymbol{g}}_2^n = \bar{\boldsymbol{g}}_1^n + \Delta\tilde{t}\,\mathcal{B}\boldsymbol{g}_1^n, \tag{2.28}$$

$$\bar{\boldsymbol{g}}^{n+1} = \bar{\boldsymbol{g}}_2^n + \Delta\tilde{t}\,\mathcal{C}\boldsymbol{g}_2^n, \tag{2.29}$$

where we have used time discretisation with n the timestep label and $\Delta\tilde{t} = \tilde{t}^{n+1} - \tilde{t}^n$. Note that the conversion between $\bar{\boldsymbol{g}}$ and $\boldsymbol{g}$ is required in moving from one step to the next, which is easily achieved by using (2.11). $\bar{\boldsymbol{g}}_1^n$, $\boldsymbol{g}_1^n$, $\bar{\boldsymbol{g}}_2^n$ and $\boldsymbol{g}_2^n$ are intermediate functions during the time advance. In `stella`, we use a 'flip-flop' version in which the order of operations is reversed at every timestep. For example, after the sequence in (2.27)–(2.29) is applied at timestep n, the $(n+1)$th step begins with $\mathcal{C}$, followed by $\mathcal{B}$ and finally $\mathcal{A}$. This alternating ordering ensures second-order accuracy in $\Delta\tilde{t}$ for the linear calculations. However, when the nonlinearity is included in $\mathcal{A}$, the overall scheme retains only first-order accuracy.

2.3 Implicit scheme

In the code, `stella` offers options to advance all the linear terms either explicitly or implicitly in time (the nonlinear term is always advanced explicitly). However, in most practical implementations, $\mathcal{B}$ and $\mathcal{C}$ are treated implicitly. This is because, to ensure numerical stability in an explicit advance, we need to impose stringent timestep constraints for the electrons due to terms $\propto (v_{\mathrm{th}e}/v_r)$. Therefore, in this Section we focus on the implicit treatment of $\mathcal{B}$ and $\mathcal{C}$, which are also the components of the algorithm that require the most modification when magnetic fluctuations are included.

2.3.1 Discretisation

Discretisation of the mirror equation

We first discuss the discretisation of the mirror equation given by (2.24). All species and phase space indices except those of $\tilde{v}_\parallel$ are suppressed for notational simplicity. In the absence of magnetic perturbations, the mirror term can be treated with the Semi-Lagrange method [Barnes et al., 2019]. However, this approach is not currently implemented for electromagnetic simulations, as the inclusion of $\tilde{A}_{\parallel,\boldsymbol{k}}$ significantly complicates the method. We therefore restrict our attention to the standard implicit method with finite differencing to approximate the derivatives.

In (2.24), a two-point stencil is used to discretise the time derivative:

$$\frac{\partial \bar{\tilde{g}}}{\partial \tilde{t}} = \frac{\bar{\tilde{g}}^{n+1} - \bar{\tilde{g}}^{n}}{\Delta \tilde{t}}. \tag{2.30}$$

The time derivatives are evaluated at intermediate times to control the degree of implicitness. For instance, applying this time discretisation to an equation of the form

$$\frac{\partial f}{\partial \tilde{t}} + G(\tilde{t}) = 0, \tag{2.31}$$

where f and G are generic functions, yields

$$\frac{f^{n+1} - f^{n}}{\Delta \tilde{t}} + G\left(\frac{1-u_t}{2}\tilde{t}^{n} + \frac{1+u_t}{2}\tilde{t}^{n+1}\right) = 0, \tag{2.32}$$

where u_t is the time-upwinding parameter: $u_t = 0$ corresponds to a centred (second-order accurate) scheme, while $u_t = 1$ produces a fully implicit (first order accurate) scheme. Using the discretisation rule (2.32), (2.24) becomes

$$\bar{\tilde{g}}^{n+1} - \Delta\tilde{t}\frac{1+u_t}{2}\frac{v_{\mathrm{ths}}}{v_r}\tilde{\mu}\left(\hat{\boldsymbol{b}}\cdot\tilde{\nabla}\tilde{B}\right)\frac{\partial \tilde{g}^{n+1}}{\partial \tilde{v}_{\parallel}} = \bar{\tilde{g}}^{n} + \Delta\tilde{t}\frac{1-u_t}{2}\frac{v_{\mathrm{ths}}}{v_r}\tilde{\mu}\left(\hat{\boldsymbol{b}}\cdot\tilde{\nabla}\tilde{B}\right)\frac{\partial \tilde{g}^{n}}{\partial \tilde{v}_{\parallel}}. \tag{2.33}$$

The $\tilde{v}_{\parallel}$-derivative in (2.24) is discretised in an analogous way. We approximate the derivative with

$$\frac{\partial \tilde{g}}{\partial \tilde{v}_{\parallel}} = \frac{\tilde{g}_{i+1} - \tilde{g}_{i}}{\Delta \tilde{v}_{\parallel}}, \tag{2.34}$$

where i is the $\tilde{v}_{\parallel}$-grid index and $\Delta\tilde{v}_{\parallel} = \tilde{v}_{\parallel i+1} - \tilde{v}_{\parallel i}$. A $\tilde{v}_{\parallel}$-upwinding parameter u_v is introduced so that a generic equation

$$\frac{\partial f}{\partial \tilde{v}_{\parallel}} + G(\tilde{v}_{\parallel}) = 0 \tag{2.35}$$

is discretised as

$$\frac{f_{i+1} - f_{i}}{\Delta \tilde{v}_{\parallel}} + G\left(\frac{1\mp u_v}{2}\tilde{v}_{\parallel i} + \frac{1\pm u_v}{2}\tilde{v}_{\parallel i+1}\right) = 0, \tag{2.36}$$

where the top (bottom) signs correspond to positive (negative) parallel acceleration. For example, positive parallel acceleration corresponds to $\hat{\boldsymbol{b}}\cdot\tilde{\nabla}\tilde{B} < 0$ in (2.24). The $\tilde{v}_{\parallel}$-upwinding parameter u_v is often chosen between 0 (centred differencing in $\tilde{v}_{\parallel}$-space) and 1 (fully upwinded). The former provides second-order accuracy in $\tilde{v}_{\parallel}$, whereas the latter is only first-order accurate and introduces numerical diffusion, but it offers improved numerical stability. Using the discretisation rule (2.36) in (2.33) leads to

$$\begin{aligned}&\frac{1\mp u_v}{2}\bar{\tilde{g}}_i^{n+1}+\frac{1\pm u_v}{2}\bar{\tilde{g}}_{i+1}^{n+1}-\frac{\Delta\tilde{t}}{\Delta\tilde{v}_\parallel}\frac{1+u_t}{2}\frac{v_{\text{ths}}}{v_r}\tilde{\mu}\left(\hat{\boldsymbol{b}}\cdot\tilde{\nabla}\tilde{B}\right)\left(\tilde{g}_{i+1}^{n+1}-\tilde{g}_i^{n+1}\right)\\&\quad=\frac{1\mp u_v}{2}\bar{\tilde{g}}_i^{n}+\frac{1\pm u_v}{2}\bar{\tilde{g}}_{i+1}^{n}+\frac{\Delta\tilde{t}}{\Delta\tilde{v}_\parallel}\frac{1-u_t}{2}\frac{v_{\text{ths}}}{v_r}\tilde{\mu}\left(\hat{\boldsymbol{b}}\cdot\tilde{\nabla}\tilde{B}\right)\left(\tilde{g}_{i+1}^{n}-\tilde{g}_i^{n}\right).\end{aligned}\tag{2.37}$$

For implicit solves, it will prove more convenient to express the terms at $(n+1)$th timestep directly in terms of $\tilde{g}$. Converting $\bar{\tilde{g}}^{n+1}$ to $\tilde{g}^{n+1}$ changes (2.37) to

$$\begin{aligned}&\frac{1\mp u_v}{2}\left(\tilde{g}_i^{n+1}+2\frac{Z}{\tilde{T}}J_0\tilde{v}_{\parallel i}\frac{v_{\text{ths}}}{v_r}\tilde{A}_\parallel^{n+1}e^{-\tilde{v}_i^2}\right)+\frac{1\pm u_v}{2}\left(\tilde{g}_{i+1}^{n+1}+2\frac{Z}{\tilde{T}}J_0\tilde{v}_{\parallel i+1}\frac{v_{\text{ths}}}{v_r}\tilde{A}_\parallel^{n+1}e^{-\tilde{v}_{i+1}^2}\right)\\&\quad-\frac{\Delta\tilde{t}}{\Delta\tilde{v}_\parallel}\frac{1+u_t}{2}\frac{v_{\text{ths}}}{v_r}\tilde{\mu}\left(\hat{\boldsymbol{b}}\cdot\tilde{\nabla}\tilde{B}\right)\left(\tilde{g}_{i+1}^{n+1}-\tilde{g}_i^{n+1}\right)=\frac{1\mp u_v}{2}\left(\tilde{g}_i^{n}+2\frac{Z}{\tilde{T}}J_0\tilde{v}_{\parallel i}\frac{v_{\text{ths}}}{v_r}\tilde{A}_\parallel^{n}e^{-\tilde{v}_i^2}\right)\\&+\frac{1\pm u_v}{2}\left(\tilde{g}_{i+1}^{n}+2\frac{Z}{\tilde{T}}J_0\tilde{v}_{\parallel i+1}\frac{v_{\text{ths}}}{v_r}\tilde{A}_\parallel^{n}e^{-\tilde{v}_{i+1}^2}\right)+\frac{\Delta\tilde{t}}{\Delta\tilde{v}_\parallel}\frac{1-u_t}{2}\frac{v_{\text{ths}}}{v_r}\tilde{\mu}\left(\boldsymbol{b}\cdot\tilde{\nabla}\tilde{B}\right)\left(\tilde{g}_{i+1}^{n}-\tilde{g}_i^{n}\right).\end{aligned}\tag{2.38}$$

Discretisation of the parallel streaming equation

The discretisation of (2.25) proceeds in a similar manner. We now retain only the z index and suppress all the other phase space indices. The time discretisation is the same as (2.32). The z-derivative is approximated by

$$\frac{\partial\tilde{g}}{\partial z}=\frac{\tilde{g}_{j+1}-\tilde{g}_j}{\Delta z},\tag{2.39}$$

where j is the z-grid index and $\Delta z=z_{j+1}-z_j$. The discretisation rule is

$$\frac{\partial f}{\partial z}+G\left(z\right)=0\longrightarrow\frac{f_{j+1}-f_j}{\Delta z}+G\left(\frac{1\mp u_z}{2}z_j+\frac{1\pm u_z}{2}z_{j+1}\right)=0,\tag{2.40}$$

where u_z is the z-upwinding parameter which works in the same way as u_v. The top (bottom) signs correspond to positive (negative) parallel advection velocity. Using the discretisation rules (2.32) and (2.40) on (2.25), we obtain

$$
\begin{aligned}
&\frac{1\mp u_z}{2}\left(\tilde{g}_j^{n+1}+2\frac{Z}{\tilde{T}}J_{0,j}\tilde{v}_\parallel\frac{v_{\rm ths}}{v_r}\tilde{A}_{\parallel j}^{n+1}e^{-\tilde{v}_j^2}\right)+\frac{1\pm u_z}{2}\left(\tilde{g}_{j+1}^{n+1}+2\frac{Z}{\tilde{T}}J_{0,j+1}\tilde{v}_\parallel\frac{v_{\rm ths}}{v_r}\tilde{A}_{\parallel j+1}^{n+1}e^{-\tilde{v}_{j+1}^2}\right)\\
&+\frac{\Delta\tilde{t}}{\Delta z}\frac{1+u_t}{2}\frac{v_{\rm ths}}{v_r}\tilde{v}_\parallel\left[\frac{1\mp u_z}{2}\left(\hat{\boldsymbol{b}}\cdot\tilde{\nabla}z\right)_j+\frac{1\pm u_z}{2}\left(\hat{\boldsymbol{b}}\cdot\tilde{\nabla}z\right)_{j+1}\right]\left[\tilde{g}_{j+1}^{n+1}-\tilde{g}_j^{n+1}+\right.\\
&\left.\left(\frac{Z}{\tilde{T}}J_{0,j+1}\tilde{\phi}_{j+1}^{n+1}+4\tilde{\mu}\frac{J_{1,j+1}}{a_{j+1}}\tilde{B}_{\parallel j+1}^{n+1}\right)e^{-\tilde{v}_{j+1}^2}-\left(\frac{Z}{\tilde{T}}J_{0,j}\tilde{\phi}_j^{n+1}+4\tilde{\mu}\frac{J_{1,j}}{a_j}\tilde{B}_{\parallel j}^{n+1}\right)e^{-\tilde{v}_j^2}\right]\\
&=\frac{1\mp u_z}{2}\bar{\tilde{g}}_j^n+\frac{1\pm u_z}{2}\bar{\tilde{g}}_{j+1}^n\\
&-\frac{\Delta\tilde{t}}{\Delta z}\frac{1-u_t}{2}\frac{v_{\rm ths}}{v_r}\tilde{v}_\parallel\left[\frac{1\mp u_z}{2}\left(\hat{\boldsymbol{b}}\cdot\tilde{\nabla}z\right)_j+\frac{1\pm u_z}{2}\left(\hat{\boldsymbol{b}}\cdot\tilde{\nabla}z\right)_{j+1}\right]\left[\tilde{g}_{j+1}^{n}-\tilde{g}_j^{n}+\right.\\
&\left.\left(\frac{Z}{\tilde{T}}J_{0,j+1}\tilde{\phi}_{j+1}^{n}+4\tilde{\mu}\frac{J_{1,j+1}}{a_{j+1}}\tilde{B}_{\parallel j+1}^{n}\right)e^{-\tilde{v}_{j+1}^2}-\left(\frac{Z}{\tilde{T}}J_{0,j}\tilde{\phi}_j^{n}+4\tilde{\mu}\frac{J_{1,j}}{a_j}\tilde{B}_{\parallel j}^{n}\right)e^{-\tilde{v}_j^2}\right],
\end{aligned}
\tag{2.41}
$$

where we have used (2.11) to replace $\bar{\tilde{g}}^{n+1}$ by $\tilde{g}^{n+1}$.

2.3.2 Green's function method

To solve the equations (2.38) and (2.41), we employ a Green's function approach [Kotschenreuther et al., 1995b]. Since the method is identical for solving both equations, we will illustrate the procedure by solving (2.41). Schematically, we express (2.41) as

$$
\boldsymbol{M}_g\boldsymbol{g}^{n+1}+\boldsymbol{M}_\phi\boldsymbol{\phi}^{n+1}+\boldsymbol{M}_A\boldsymbol{A}_\parallel^{n+1}+\boldsymbol{M}_B\boldsymbol{B}_\parallel^{n+1}=\boldsymbol{V}\left(\bar{\tilde{g}}^n,\tilde{g}^n,\phi^n,A_\parallel^n,B_\parallel^n\right),
\tag{2.42}
$$

where $\boldsymbol{g}^{n+1}$, $\boldsymbol{\phi}^{n+1}$, $\boldsymbol{A}_\parallel^{n+1}$, $\boldsymbol{B}_\parallel^{n+1}$ are vectors whose components are values of $\tilde{g}^{n+1}$, $\tilde{\phi}^{n+1}$, $\tilde{A}_\parallel^{n+1}$ and $\tilde{B}_\parallel^{n+1}$ evaluated at various z-grid points. The z-grids here are grids on an extended z-domain due to the 'twist-and-shift' boundary condition [Beer et al., 1995]. Thus, the vector lengths are $(N_z\times N_{\rm seg})$ with $N_{\rm seg}$ the number of connected segments. $\boldsymbol{V}$ is a vector of the same dimension and it depends on the values of the distribution functions and fields at step n. $\boldsymbol{M}_g$, $\boldsymbol{M}_\phi$, $\boldsymbol{M}_A$ and $\boldsymbol{M}_B$ are square matrices with dimensions $(N_z\times N_{\rm seg})^2$. We remind the reader that (2.42) holds true for each species s, wavenumber $\boldsymbol{k}$, $\tilde{v}_\parallel$ and $\tilde{\mu}$, despite the indices being suppressed for brevity.

Since (2.42) is linear in $\boldsymbol{g}^{n+1}$, we decompose $\boldsymbol{g}^{n+1}$ into homogeneous and inhomogeneous components: $\boldsymbol{g}^{n+1}=\boldsymbol{g}_h^{n+1}+\boldsymbol{g}_{inh}^{n+1}$. These two components satisfy the following equations:

$$
\boldsymbol{M}_g\boldsymbol{g}_h^{n+1}+\boldsymbol{M}_\phi\boldsymbol{\phi}^{n+1}+\boldsymbol{M}_A\boldsymbol{A}_\parallel^{n+1}+\boldsymbol{M}_B\boldsymbol{B}_\parallel^{n+1}=0,
\tag{2.43}
$$

$$
\boldsymbol{M}_g\boldsymbol{g}_{inh}^{n+1}=\boldsymbol{V}\left(\bar{\tilde{g}}^n,\tilde{g}^n,\phi^n,A_\parallel^n,B_\parallel^n\right).
\tag{2.44}
$$

The inhomogeneous solution $\boldsymbol{g}_{inh}^{n+1}$ is found straightforwardly by

$$
\boldsymbol{g}_{inh}^{n+1}=\boldsymbol{M}_g^{-1}\boldsymbol{V}\left(\bar{\tilde{g}}^n,\tilde{g}^n,\phi^n,A_\parallel^n,B_\parallel^n\right),
\tag{2.45}
$$

using the known distribution function and fields at step n. For the homogeneous solution $\boldsymbol{g}_h^{n+1}$, we determine the corresponding Green's function. Consider

$$\boldsymbol{g}^{n+1} = \boldsymbol{g}_h^{n+1} + \boldsymbol{g}_{inh}^{n+1} = \left(\frac{\boldsymbol{\delta g}}{\boldsymbol{\delta \phi}}\right)\boldsymbol{\phi}^{n+1} + \left(\frac{\boldsymbol{\delta g}}{\boldsymbol{\delta A}_\parallel}\right)\boldsymbol{A}_\parallel^{n+1} + \left(\frac{\boldsymbol{\delta g}}{\boldsymbol{\delta B}_\parallel}\right)\boldsymbol{B}_\parallel^{n+1} + \boldsymbol{g}_{inh}^{n+1}, \tag{2.46}$$

where $(\boldsymbol{\delta g}/\boldsymbol{\delta \phi})$, $(\boldsymbol{\delta g}/\boldsymbol{\delta A}_\parallel)$ and $(\boldsymbol{\delta g}/\boldsymbol{\delta B}_\parallel)$ are the response matrices to be determined. $(\boldsymbol{\delta g}/\boldsymbol{\delta \phi})_{ij}$ is derived from the response of $(\boldsymbol{g}_h^{n+1})_i$ to a unit impulse at $(\boldsymbol{\phi}^{n+1})_j$, with all other field fluctuations set to zero, i.e.,

$$\left(\frac{\boldsymbol{\delta g}}{\boldsymbol{\delta \phi}}\right)_{ij} = -\left(\boldsymbol{M}_g^{-1}\boldsymbol{M}_\phi\right)_{ij}, \tag{2.47}$$

where we have used (2.43). In similar ways, we can compute $(\boldsymbol{\delta g}/\boldsymbol{\delta A}_\parallel)$ and $(\boldsymbol{\delta g}/\boldsymbol{\delta B}_\parallel)$. These response matrices are precomputed at the start of the simulation and updated only if the timestep $\Delta\tilde{t}$ changes due to CFL constraints.

Once the response matrices are known, (2.46) becomes an expression relating $\boldsymbol{g}^{n+1}$ to the three electromagnetic fields. In the next step, we solve first for the fields and subsequently evaluate $\boldsymbol{g}^{n+1}$. To obtain the three fields required, we apply the integral operators $\hat{Q}$, $\hat{P}_\parallel$, and $\hat{P}_\perp$, defined in (2.15)–(2.18), to (2.46). This procedure yields a set of three coupled equations, which we express in a matrix form as

$$\left[\begin{array}{c|c|c}
\hat{Q}\left(\frac{\boldsymbol{\delta g}}{\boldsymbol{\delta \phi}}\right) + \boldsymbol{\Gamma}_{11} & \hat{Q}\left(\frac{\boldsymbol{\delta g}}{\boldsymbol{\delta A}_\parallel}\right) & \hat{Q}\left(\frac{\boldsymbol{\delta g}}{\boldsymbol{\delta B}_\parallel}\right) + \boldsymbol{\Gamma}_{13} \\ \hline
\hat{P}_\parallel\left(\frac{\boldsymbol{\delta g}}{\boldsymbol{\delta \phi}}\right) & \hat{P}_\parallel\left(\frac{\boldsymbol{\delta g}}{\boldsymbol{\delta A}_\parallel}\right) - \boldsymbol{I} & \hat{P}_\parallel\left(\frac{\boldsymbol{\delta g}}{\boldsymbol{\delta B}_\parallel}\right) \\ \hline
\hat{P}_\perp\left(\frac{\boldsymbol{\delta g}}{\boldsymbol{\delta \phi}}\right) + \boldsymbol{\Gamma}_{31} & \hat{P}_\perp\left(\frac{\boldsymbol{\delta g}}{\boldsymbol{\delta A}_\parallel}\right) & \hat{P}_\perp\left(\frac{\boldsymbol{\delta g}}{\boldsymbol{\delta B}_\parallel}\right) + \boldsymbol{\Gamma}_{33}
\end{array}\right]
\left[\begin{array}{c}
\boldsymbol{\phi}^{n+1} \\ \hline
\boldsymbol{A}_\parallel^{n+1} \\ \hline
\boldsymbol{B}_\parallel^{n+1}
\end{array}\right]
=
\left[\begin{array}{c}
-\hat{Q}\boldsymbol{g}_{inh}^{n+1} \\ \hline
-\hat{P}_\parallel\boldsymbol{g}_{inh}^{n+1} \\ \hline
-\hat{P}_\perp\boldsymbol{g}_{inh}^{n+1}
\end{array}\right] \tag{2.48}$$

with $\boldsymbol{I}$ the identity matrix with dimensions $(N_z \times N_{\rm seg})^2$, and

$$(\boldsymbol{\Gamma}_{11})_{mn} = \delta_{mn}\sum_s \frac{Z_s^2\tilde{n}_s}{\tilde{T}_s}\left[\Gamma_0(\alpha_s) - 1\right], \tag{2.49}$$

$$(\boldsymbol{\Gamma}_{13})_{mn} = \delta_{mn}\sum_s \frac{Z_s\tilde{n}_s}{\tilde{B}}\Gamma_1(\alpha_s), \tag{2.50}$$

$$(\boldsymbol{\Gamma}_{31})_{mn} = -\delta_{mn}\frac{\beta_r}{2\tilde{B}}\sum_s Z_s\tilde{n}_s\Gamma_1(\alpha_s), \tag{2.51}$$

$$(\mathbf{\Gamma}_{33})_{mn} = -\delta_{mn}\left[1 + \frac{\beta_r}{\tilde{B}^2}\sum_s \tilde{n}_s \tilde{T}_s \Gamma_1(\alpha_s)\right], \tag{2.52}$$

where δ_{mn} denotes the Kronecker delta the indices (m, n) span the extended z-domain. The updated fields $\boldsymbol{\phi}^{n+1}$, $\boldsymbol{A}_{\parallel}^{n+1}$, and $\boldsymbol{B}_{\parallel}^{n+1}$ are calculated by inverting the block matrix (2.48)[1]. The fields are then substituted into (2.43) to compute $\boldsymbol{g}_h^{n+1}$, and the full solution $\boldsymbol{g}^{n+1}$ is obtained by combining $\boldsymbol{g}_h^{n+1}$ and $\boldsymbol{g}_{inh}^{n+1}$.

2.3.3 Summary of the implicit advance scheme

To summarise, the steps for implicitly solving $\boldsymbol{g}^{n+1}$ with parallel streaming terms in (2.25) (and similarly with accelerations term in (2.24)) are as follows:

1. Compute the response matrices $(\boldsymbol{\delta g}/\boldsymbol{\delta \phi})$, $(\boldsymbol{\delta g}/\boldsymbol{\delta A}_{\parallel})$, and $(\boldsymbol{\delta g}/\boldsymbol{\delta B}_{\parallel})$ (performed once at initialisation and updated only if Δt changes) using (2.43):

$$\left(\frac{\boldsymbol{\delta g}}{\boldsymbol{\delta \phi}}\right)_{ij} = -\left(\boldsymbol{M}_g^{-1}\boldsymbol{M}_\phi\right)_{ij}, \tag{2.53}$$

$$\left(\frac{\boldsymbol{\delta g}}{\boldsymbol{\delta A}_{\parallel}}\right)_{ij} = -\left(\boldsymbol{M}_g^{-1}\boldsymbol{M}_A\right)_{ij}, \tag{2.54}$$

$$\left(\frac{\boldsymbol{\delta g}}{\boldsymbol{\delta B}_{\parallel}}\right)_{ij} = -\left(\boldsymbol{M}_g^{-1}\boldsymbol{M}_B\right)_{ij}. \tag{2.55}$$

2. Calculate the inhomogeneous solution $\boldsymbol{g}_{inh}^{n+1}$ via (2.44):

$$\boldsymbol{g}_{inh}^{n+1} = \boldsymbol{M}_g^{-1}\boldsymbol{V}\left(\bar{\tilde{g}}^n, \tilde{g}^n, \phi^n, A_{\parallel}^n, B_{\parallel}^n\right). \tag{2.56}$$

3. Apply the integral operators $\hat{Q}$, $\hat{P}_{\parallel}$, and $\hat{P}_{\perp}$ to (2.46) to derive a closed system of equations for the fields (written in block matrix form (2.48)).

4. Solve for $\boldsymbol{\phi}^{n+1}$, $\boldsymbol{A}_{\parallel}^{n+1}$, and $\boldsymbol{B}_{\parallel}^{n+1}$ by inverting the block matrix in (2.48).

5. Substitute the updated fields into (2.43) to determine $\boldsymbol{g}_h^{n+1}$.

6. Construct the full solution $\boldsymbol{g}^{n+1} = \boldsymbol{g}_h^{n+1} + \boldsymbol{g}_{inh}^{n+1}$.

7. Repeat steps 2 - 6 at every timestep. If $\Delta\tilde{t}$ reduces due to CFL constraint, redo step 1.

[1] This is only correct schematically. In the code, the equation is in fact solved by LU decomposition instead of direct matrix inversion which can easily cause numerical problems.

Chapter 3

Gyrokinetic turbulent stresses

We don't do the calculation because we don't know the answer, we do it because we have a conscience.

— Bryan Taylor, Oxford plasma seminars and Vienna meetings

3.1 Expressions of turbulent stresses and the associated energy transfers

To gain insight into the physical origin of the non-zonal transitions observed in finite-β plasmas, we now turn our attention to the evolution of the zonal components of the electrostatic field that is responsible for the generation of zonal flows within axisymmetric toroidal geometries. We will derive the time-evolution equation for the zonal velocity v_Z and the expressions for the turbulent stresses which drives or damps v_Z.

To obtain the time evolution for v_Z, we first take the time derivative of the quasineutrality constraint (1.24) and apply the flux-surface average (1.41) to get

$$\frac{\partial}{\partial t}\sum_s \frac{Z_s^2 e}{T_s} n_s \left\langle \phi \right\rangle_{yz} = \left\langle \sum_s Z_s \int \mathrm{d}^3\boldsymbol{v}\, \frac{\partial \left\langle h_s \right\rangle_{\boldsymbol{r}}}{\partial t} \right\rangle_{yz} . \tag{3.1}$$

We proceed by replacing $\partial \left\langle h_s \right\rangle_{\boldsymbol{r}} / \partial t$ on the right-hand side of (3.1), by using the gyroaveraged version of (1.17):

$$
\frac{\partial}{\partial t}\sum_s \frac{Z_s^2 e}{T_s} n_s \langle\phi\rangle_{yz} = \underbrace{-\sum_s Z_s \left\langle \int \mathrm{d}^3\boldsymbol{v}\, v_\parallel (\hat{\boldsymbol{b}}\cdot\nabla z)\frac{\partial \langle h_s\rangle_{\boldsymbol{r}}}{\partial z}\right\rangle_{yz}}_{①}
$$

$$
\underbrace{-\sum_s Z_s \left\langle \int \mathrm{d}^3\boldsymbol{v}\, \boldsymbol{v}_{Ms}\cdot\nabla_\perp \langle h_s\rangle_{\boldsymbol{r}}\right\rangle_{yz}}_{②} + \underbrace{\sum_s Z_s \left\langle \int \mathrm{d}^3\boldsymbol{v}\, \frac{\mu}{m_s}(\hat{\boldsymbol{b}}\cdot\nabla B)\frac{\partial \langle h_s\rangle_{\boldsymbol{r}}}{\partial v_\parallel}\right\rangle_{yz}}_{③}
$$

$$
\underbrace{-\sum_s Z_s \left\langle \int \mathrm{d}^3\boldsymbol{v}\, \left\langle \langle \boldsymbol{v}_\chi\rangle_{\boldsymbol{R}_s}\cdot\nabla_\perp h_s\right\rangle_{\boldsymbol{r}}\right\rangle_{yz}}_{④} \underbrace{-\sum_s Z_s \left\langle \int \mathrm{d}^3\boldsymbol{v}\, \left\langle \langle \boldsymbol{v}_\chi\rangle_{\boldsymbol{R}_s}\right\rangle_{\boldsymbol{r}}\cdot\nabla F_s\right\rangle_{yz}}_{⑤}
$$

$$
= \underbrace{\sum_s \frac{Z_s^2 e}{T_s}\left\langle \int \mathrm{d}^3\boldsymbol{v} F_s \frac{\partial \left\langle \langle\chi\rangle_{\boldsymbol{R}_s}\right\rangle_{\boldsymbol{r}}}{\partial t}\right\rangle_{yz}}_{⑥} + \underbrace{\sum_s Z_s \left\langle \int \mathrm{d}^3\boldsymbol{v}\, \left\langle \langle C[h_s]\rangle_{\boldsymbol{R}_s}\right\rangle_{\boldsymbol{r}}\right\rangle_{yz}}_{⑦}. \tag{3.2}
$$

Let us now calculate the right-hand side of the equation term by term.
Term 1 : the parallel streaming contribution is in principle zero because

$$
\begin{aligned}
\left\langle \int \mathrm{d}^3\boldsymbol{v}\, v_\parallel (\hat{\boldsymbol{b}}\cdot\nabla z)\frac{\partial \langle h_s\rangle_{\boldsymbol{r}}}{\partial z}\right\rangle_{yz} &\propto \int \mathrm{d}y\,\mathrm{d}z\, \frac{\hat{\boldsymbol{b}}\cdot\nabla z}{|\boldsymbol{B}\cdot\nabla z|}\int \mathrm{d}v_\parallel\,\mathrm{d}\mu \frac{2\pi B}{m_s} v_\parallel \frac{\partial \langle h_s\rangle_{\boldsymbol{r}}}{\partial z},\\
&\propto \int \mathrm{d}y\,\mathrm{d}z \int \mathrm{d}v_\parallel\,\mathrm{d}\mu\, v_\parallel \frac{\partial \langle h_s\rangle_{\boldsymbol{r}}}{\partial z},\\
&\propto \int \mathrm{d}z\, \frac{\partial}{\partial z}\left(\int \mathrm{d}y \int \mathrm{d}v_\parallel\,\mathrm{d}\mu\, v_\parallel \langle h_s\rangle_{\boldsymbol{r}}\right),
\end{aligned} \tag{3.3}
$$

where we have used (1.25), (1.41), and the fact that $(\mathrm{d}y/\mathrm{d}\alpha)(\mathrm{d}x/\mathrm{d}\psi)$ is constant along the field line. The term inside the bracket on the last line involves an average over y, implying periodicity in z[1]. Hence, the z-integral evaluates to zero.
Term 2 : the magnetic drift term can be decomposed into two parts:

$$
\boldsymbol{v}_{Ms}\cdot\nabla_\perp \langle h_s\rangle_{\boldsymbol{r}} = (\boldsymbol{v}_{Ms}\cdot\nabla x)\frac{\partial \langle h_s\rangle_{\boldsymbol{r}}}{\partial x} + (\boldsymbol{v}_{Ms}\cdot\nabla y)\frac{\partial \langle h_s\rangle_{\boldsymbol{r}}}{\partial y}, \tag{3.4}
$$

where the first term on the right is the radial magnetic drift and the second term is the poloidal magnetic drift. It is easy to see that the poloidal drift vanishes after flux-surface averaging using (1.41), since $\langle h_s\rangle_{\boldsymbol{r}}$ is periodic in y and $(\boldsymbol{v}_{Ms}\cdot\nabla y)$ is independent of y.

[1] In contrast, the twist-and-shift boundary condition needs to be applied to fluctuations with non-zero variation along y.

So, the magnetic drift contribution is

$$\sum_s Z_s \left\langle \int \mathrm{d}^3\boldsymbol{v}\, \boldsymbol{v}_{Ms} \cdot \nabla_\perp \langle h_s \rangle_{\boldsymbol{r}} \right\rangle_{yz} = \sum_s Z_s \left\langle \int \mathrm{d}^3\boldsymbol{v}\, (\boldsymbol{v}_{Ms} \cdot \nabla x) \frac{\partial \langle h_s \rangle_{\boldsymbol{r}}}{\partial x} \right\rangle_{yz}. \tag{3.5}$$

Term (3) : the mirror contribution contains a total derivative of $v_\parallel$. Thus, it vanishes due to the $v_\parallel$-integral, assuming that h_s decays to zero as $v_\parallel \to \infty$.

Term (4) : we start by writing the nonlinearity in terms of Poisson brackets:

$$\begin{aligned}
\langle \boldsymbol{v}_\chi \rangle_{\boldsymbol{R}_s} \cdot \nabla_\perp h_s &= \frac{c}{B} \hat{\boldsymbol{b}} \times \frac{\partial \langle \chi \rangle_{\boldsymbol{R}_s}}{\partial R_s} \cdot \nabla_\perp h_s, \\
&= \frac{c}{B} \hat{\boldsymbol{b}} \times \left(\nabla x \frac{\partial \langle \chi \rangle_{\boldsymbol{R}_s}}{\partial x} + \nabla y \frac{\partial \langle \chi \rangle_{\boldsymbol{R}_s}}{\partial y} \right) \cdot \left(\nabla x \frac{\partial h_s}{\partial x} + \nabla y \frac{\partial h_s}{\partial y} \right) \\
&= \frac{c}{B} (\hat{\boldsymbol{b}} \times \nabla x \cdot \nabla y) \left\{ \langle \chi \rangle_{\boldsymbol{R}_s}, h_s \right\}, \\
&= \frac{c}{B} (\hat{\boldsymbol{b}} \times \nabla x \cdot \nabla y) \left\{ \left\langle \phi - \frac{v_\parallel A_\parallel}{c} - \frac{\boldsymbol{v}_\perp \cdot \boldsymbol{A}_\perp}{c} \right\rangle_{\boldsymbol{R}_s}, h_s \right\},
\end{aligned} \tag{3.6}$$

where we have used (1.21), (1.22), (1.23), and the definition of the Poisson bracket

$$\{f, g\} \equiv \frac{\partial f}{\partial x}\frac{\partial g}{\partial y} - \frac{\partial f}{\partial y}\frac{\partial g}{\partial x}. \tag{3.7}$$

Thus, the nonlinear contribution to the zonal flow equation is

$$\begin{aligned}
&\sum_s Z_s \left\langle \int \mathrm{d}^3\boldsymbol{v}\, \left\langle \langle \boldsymbol{v}_\chi \rangle_{\boldsymbol{R}_s} \cdot \nabla_\perp h_s \right\rangle_{\boldsymbol{r}} \right\rangle_{yz} \\
&= \sum_s Z_s \left\langle \frac{c}{B} (\hat{\boldsymbol{b}} \times \nabla x \cdot \nabla y) \int \mathrm{d}^3\boldsymbol{v}\, \left\langle \{ \langle \phi \rangle_{\boldsymbol{R}_s}, h_s \} \right\rangle_{\boldsymbol{r}} \right\rangle_{yz} \\
&- \sum_s Z_s \left\langle \frac{1}{B} (\hat{\boldsymbol{b}} \times \nabla x \cdot \nabla y) \int \mathrm{d}^3\boldsymbol{v}\, v_\parallel \left\langle \left\{ \langle A_\parallel \rangle_{\boldsymbol{R}_s}, h_s \right\} \right\rangle_{\boldsymbol{r}} \right\rangle_{yz} \\
&- \sum_s Z_s \left\langle \frac{1}{B} (\hat{\boldsymbol{b}} \times \nabla x \cdot \nabla y) \int \mathrm{d}^3\boldsymbol{v}\, \left\langle \{ \langle \boldsymbol{v}_\perp \cdot \boldsymbol{A}_\perp \rangle_{\boldsymbol{R}_s}, h_s \} \right\rangle_{\boldsymbol{r}} \right\rangle_{yz}.
\end{aligned} \tag{3.8}$$

Term (5) : rewriting the energy injection term using the flux-tube coordinates:

$$\begin{aligned}
\left\langle \langle \boldsymbol{v}_\chi \rangle_{\boldsymbol{R}_s} \right\rangle_{\boldsymbol{r}} \cdot \nabla F_s = &\frac{c}{B} \left[\frac{(\nabla y \times \nabla x)}{|\nabla x||\nabla y|} \times \nabla x \frac{\partial \left\langle \langle \chi \rangle_{\boldsymbol{R}_s} \right\rangle_{\boldsymbol{r}}}{\partial x} \right] \cdot \nabla x \frac{\mathrm{d}F_s}{\mathrm{d}x} \\
&+ \frac{c}{B} \left[\frac{(\nabla y \times \nabla x)}{|\nabla x||\nabla y|} \times \nabla y \frac{\partial \left\langle \langle \chi \rangle_{\boldsymbol{R}_s} \right\rangle_{\boldsymbol{r}}}{\partial y} \right] \cdot \nabla x \frac{\mathrm{d}F_s}{\mathrm{d}x},
\end{aligned} \tag{3.9}$$

where we have used

$$\hat{\boldsymbol{b}} = \frac{\nabla y \times \nabla x}{|\nabla x||\nabla y|} \quad \text{and} \quad \nabla F_s = \nabla x \frac{\mathrm{d}F_s}{\mathrm{d}x}. \tag{3.10}$$

The first term on the right-hand side of (3.9) is zero. The second term can be written as a total derivative of y since only $\left\langle \langle \chi \rangle_{\boldsymbol{R}_s} \right\rangle_{\boldsymbol{r}}$ varies in y. Hence, the free-energy injection contribution vanishes under flux-surface averaging.

Term (6) :

$$\sum_s \frac{Z_s^2 e}{T_s} \left\langle \int \mathrm{d}^3\boldsymbol{v}\, F_s \frac{\partial \left\langle \langle \chi \rangle_{\boldsymbol{R}_s} \right\rangle_{\boldsymbol{r}}}{\partial t} \right\rangle_{yz} = \frac{\partial}{\partial t} \sum_s \frac{Z_s^2 e}{T_s} \left\langle \int \mathrm{d}^3\boldsymbol{v}\, F_s \left\langle \langle \phi \rangle_{\boldsymbol{R}_s} \right\rangle_{\boldsymbol{r}} \right\rangle_{yz}$$
$$- \frac{\partial}{\partial t} \sum_s \frac{Z_s^2 e}{c T_s} \left\langle \int \mathrm{d}^3\boldsymbol{v}\, v_\parallel F_s \left\langle \langle A_\parallel \rangle_{\boldsymbol{R}_s} \right\rangle_{\boldsymbol{r}} \right\rangle_{yz} - \frac{\partial}{\partial t} \sum_s \frac{Z_s^2 e}{c T_s} \left\langle \int \mathrm{d}^3\boldsymbol{v}\, F_s \left\langle \langle \boldsymbol{v}_\perp \cdot \boldsymbol{A}_\perp \rangle_{\boldsymbol{R}_s} \right\rangle_{\boldsymbol{r}} \right\rangle_{yz}. \tag{3.11}$$

The second term on the right-hand side of the equation is zero since the integrand is odd in $v_\parallel$.

Term (7) : We leave the collisional term unchanged.

Collecting all the terms (3.5), (3.8), (3.11), the collisional contribution, and writing n_s on the left-hand side of (3.2) as $\int \mathrm{d}^3\boldsymbol{v}\, F_s$, we obtain the final form of the zonal flow equation:

$$\frac{\partial}{\partial t} \sum_s \frac{Z_s^2 e}{T_s} \left\langle \int \mathrm{d}^3\boldsymbol{v}\, F_s \left(\phi - \left\langle \langle \phi \rangle_{\boldsymbol{R}_s} \right\rangle_{\boldsymbol{r}} \right) \right\rangle_{yz} = \Pi_{\mathrm{lin}} + \Pi_\phi + \Pi_{A_\parallel} + \Pi_{B_\parallel} + \Pi_{\mathrm{coll}}, \tag{3.12}$$

where

$$\Pi_{\mathrm{lin}} = - \left\langle \sum_s Z_s \int \mathrm{d}^3\boldsymbol{v}\, \left(\boldsymbol{v}_{Ms,x} \cdot \nabla x \right) \frac{\partial \langle h_s \rangle_{\boldsymbol{r}}}{\partial x} \right\rangle_{yz}$$
$$- \frac{\partial}{\partial t} \sum_s \frac{Z_s^2 e}{T_s} \left\langle \int \mathrm{d}^3\boldsymbol{v}\, F_s \frac{\left\langle \langle \boldsymbol{v}_\perp \cdot \boldsymbol{A}_\perp \rangle_{\boldsymbol{R}_s} \right\rangle_{\boldsymbol{r}}}{c} \right\rangle_{yz}, \tag{3.13}$$

$$\Pi_\phi = - \left\langle \frac{c}{B} (\hat{\boldsymbol{b}} \times \nabla x \cdot \nabla y) \sum_s Z_s \int \mathrm{d}^3\boldsymbol{v}\, \left\langle \left\{ \langle \phi \rangle_{\boldsymbol{R}_s}, h_s \right\} \right\rangle_{\boldsymbol{r}} \right\rangle_{yz}, \tag{3.14}$$

$$\Pi_{A_\parallel} = \left\langle \frac{1}{B} (\hat{\boldsymbol{b}} \times \nabla x \cdot \nabla y) \sum_s Z_s \int \mathrm{d}^3\boldsymbol{v}\, v_\parallel \left\langle \left\{ \langle A_\parallel \rangle_{\boldsymbol{R}_s}, h_s \right\} \right\rangle_{\boldsymbol{r}} \right\rangle_{yz}, \tag{3.15}$$

$$\Pi_{B_\parallel} = \left\langle \frac{1}{B} (\hat{\boldsymbol{b}} \times \nabla x \cdot \nabla y) \sum_s Z_s \int \mathrm{d}^3\boldsymbol{v}\, \left\langle \left\{ \langle \boldsymbol{v}_\perp \cdot \boldsymbol{A}_\perp \rangle_{\boldsymbol{R}_s}, h_s \right\} \right\rangle_{\boldsymbol{r}} \right\rangle_{yz}, \tag{3.16}$$

and

$$\Pi_{\mathrm{coll}} = \left\langle \sum_s Z_s \int \mathrm{d}^3\boldsymbol{v}\, \left\langle \langle C[h_s] \rangle_{\boldsymbol{R}_s} \right\rangle_{\boldsymbol{r}} \right\rangle_{yz} \tag{3.17}$$

are the linear stress, the nonlinear stresses arising from ϕ, $A_\parallel$ and $B_\parallel$, and the collisional damping, respectively. Both sides now have the dimension of particle density divided by time.

We now discuss the physics behind (3.12). In particular, we would like to show that (3.12) is indeed an evolution equation for v_Z. In the remaining part of this Subsection, we focus on a plasma of two species – ions with atomic number Z and electrons. Consider the evolution of zonal flows whose radial wavelength is much larger than the ion Larmor radius. These 'large scale' flows play an important role in the saturation and suppression of turbulence. In this limit, the left-hand side of (3.12) simplifies to

$$-\frac{Z^2 e n_i}{2T_i}|\nabla x|^2 \rho_i^2 \frac{\partial}{\partial t}\frac{\partial^2 \langle\phi\rangle_{yz}}{\partial x^2} = \Pi_{\mathrm{lin}} + \Pi_\phi + \Pi_{A_\parallel} + \Pi_{B_\parallel}, \tag{3.18}$$

where $|\nabla x|$ and B (hence ρ_i) are assumed to be approximately independent of z for the magnetic geometry we are considering. Multiply both sides of (3.18) by $\langle\phi\rangle_{yz}$ and average over the x-domain:

$$\begin{aligned}
\frac{Z^2 e n_i}{4T_i}|\nabla x|^2 \rho_i^2 \frac{\partial}{\partial t}\left\langle\left(\frac{\partial\langle\phi\rangle_{yz}}{\partial x}\right)^2\right\rangle_x &= \left\langle\langle\phi\rangle_{yz}\Pi_{\mathrm{lin}}\right\rangle_x + \left\langle\langle\phi\rangle_{yz}\Pi_\phi\right\rangle_x + \left\langle\langle\phi\rangle_{yz}\Pi_{A_\parallel}\right\rangle_x \\
&\quad + \left\langle\langle\phi\rangle_{yz}\Pi_{B_\parallel}\right\rangle_x, \\
\longrightarrow \left\langle\frac{\partial}{\partial t}\frac{n_i m_i}{2}v_Z^2\right\rangle_x &= \left\langle\langle e\phi\rangle_{yz}\Pi_{\mathrm{lin}}\right\rangle_x + \left\langle\langle e\phi\rangle_{yz}\Pi_\phi\right\rangle_x + \left\langle\langle e\phi\rangle_{yz}\Pi_{A_\parallel}\right\rangle_x \\
&\quad + \left\langle\langle e\phi\rangle_{yz}\Pi_{B_\parallel}\right\rangle_x,
\end{aligned} \tag{3.19}$$

where $\langle\rangle_x \equiv L_x^{-1}\int \mathrm{d}x$ with L_x the flux-tube width in x, the factor $|\nabla x|/B$ has been moved into the flux-surface average, and we have used the definition of v_Z (1.40). (3.19) describes the time evolution of the box-averaged zonal-flow kinetic energy. In the more general case where FLR effects are retained and both $|\nabla x|$ and B vary with z, the zonal-flow evolution must instead be obtained from (3.12), for which the physical interpretation is less transparent.

Equation (3.19) shows that the stresses either inject energy into or extract energy from the zonal flows, depending on the sign of the correlation functions on the right-hand side of (3.19). In previous studies of electrostatic ITG turbulence, it was found that Π_ϕ, or the Reynolds stress, always acts as a drive for zonal flows [Dimits et al., 2007, Ivanov et al., 2020]. Conversely, the Maxwell stress $\Pi_{A_\parallel}$, has been observed to act as an energy sink for the zonal flow [Scott, 2005, Diamond et al., 2005, Rath and Peeters, 2022]. The competition between the Reynolds and Maxwell stresses, which skews in favour of the Maxwell stress as β increases, could lead to net erosion of zonal flow energy and has thus been a hypothesised as the driver behind the transition to non-zonal states in electromagnetic simulations [Rath and Peeters, 2022].

Parameter	CBC	ST40
$\tilde{r} = r/a$	0.5	0.51
$\tilde{R} = R_0/a$	3.0	1.82
$\mathrm{d}\tilde{R}/\mathrm{d}\tilde{r}$	0	-0.16
$\hat{s} = \mathrm{d}\ln q/\mathrm{d}\ln r$	0.8	1.18
κ	1.0	1.36
$\mathrm{d}\kappa/\mathrm{d}\tilde{r}$	0	0.42
δ	0	0.025
$\mathrm{d}\delta/\mathrm{d}\tilde{r}$	0	0.11
B_r	$B_\zeta(R_0)$	2.41 T
n_i/n_r	1	1
n_e/n_r	1	1
T_i/T_r	1	1
T_e/T_r	1	0.75
Z_i	1	1
m_i/m_r	1	1
m_e/m_r	0.00027	0.00054
$-\mathrm{d}\ln n_i/\mathrm{d}\tilde{r}$	0.733	1.06
$-\mathrm{d}\ln n_e/\mathrm{d}\tilde{r}$	0.733	1.06
$-\mathrm{d}\ln T_i/\mathrm{d}\tilde{r}$	2.3	2.09
$-\mathrm{d}\ln T_e/\mathrm{d}\tilde{r}$	2.3	1.54

Table 3.1: Equilibrium parameters for the CBC and ST40 pulse 314.

Resolution	L_y/ρ_r	L_x/ρ_r	$k_{x,\max}\rho_r$	$k_{y,\max}\rho_r$
R1	94	94	2.8	1.4
R2	141	141	2.8	1.4
R3	188	188	2.8	1.4
R4	188	188	2.8	1.4
R5	94	94	5.7	2.8
ST	126	118	3.3	1.6

Table 3.2: Simulation resolutions. $\rho_r = m_r v_r c/eB_r$ is the reference Larmor radius with $v_r = \sqrt{2T_r/m_r}$. *R1-5* are resolutions used for the CBCs and *ST* is used for the ST40 cases. $N_z = 32$ and $N_{v_\parallel} = 48$ for all the simulations. $N_\mu = 16$ for *R1-5* and $N_\mu = 12$ for *ST*.

3.2 Computational study

In this Section, we will be presenting numerical results from gyrokinetic simulations to investigate the effects of turbulent stresses on the zonal flows. The gyrokinetic code employed is `stella`. The spatial coordinates used in `stella` are (k_x,k_y,z) and the velocity space coordinates are ($v_\parallel$,μ). Therefore, the resolution inputs for the simulations include L_x and L_y, the box-sizes in x and y respectively (The z-domain is limited to $[-\pi,\pi]$ in our simulations but it can be extended in principle.); N_{k_x}, the number of k_x Fourier modes; N_{k_y}, the number of k_y modes excluding the negative ones as the k_y-domain is limited by the reality condition; N_z, the number of z-grid points; $N_{v_\parallel}$, the number of $v_\parallel$ grid points and N_μ, the number of μ grid points (see Tab. 3.2 for all the resolutions used in this work).

For all the simulations, physical Coulomb collisions are neglected. To avoid spectral pile-up, hyper-viscosity is employed, whose form is

$$\frac{\partial h_{s,\boldsymbol{k}_\perp}}{\partial t} = -D_{\mathrm{hyper}}\frac{k_\perp^4}{k_{\perp,\max}^4}h_{s,\boldsymbol{k}_\perp}, \tag{3.20}$$

with D_{hyper} the hyper-viscosity coefficient and $h_{s,\boldsymbol{k}_\perp}$ the $\boldsymbol{k}_\perp$ mode of the distribution function for species s. The subscript 'max' stands for the maximum of the corresponding quantity.

We perform the calculations for two different magnetic equilibria, both parametrised in terms of the Miller local parameters. The first equilibrium corresponds to the Cyclone-Base-Case (CBC), which has circular concentric flux surfaces and is widely used for benchmark studies (e.g. Dimits et al. [2000]). The other equilibrium is taken from ST40 (Tokamak Energy Ltd [2025]) pulse number 314, ASTRA RUN102 at time = 450ms. The Miller parameters for both equilibria are provided in Tab. 3.1.

3.2.1 Non-zonal transitions in CBC and ST40

Data from a (q,β_e) parameter scan is given in Fig. 3.1 for both the CBC (top panel) and ST40 (bottom panel) cases, showing various important boundaries in the (q,β_e) parameter space. We conduct a parameter scan over (q,β_e) with ions (deuterium for CBCs and proton for ST40) and electrons. The ratio β_i/β_e is kept fixed as β_e is varied. For the CBC runs, we set $\beta' \equiv (4\pi/B_r^2)dp/d\tilde{r} = 0$[2], where $p = \sum_s n_s T_s$. The $B_\parallel$ fluctuation is ignored and $D_{\text{hyper}} = 0.2$. We use resolution *R1* (see Tab. 3.2) for $q = 1.4$, 1.5, and 1.8, resolution *R2* for $q = 2.0$, 2.2, and 2.4, and resolution *R3* for $q = 2.6$, 2.8, and 3.0. This corresponds to an increase in the x and y box sizes with q, needed to account for the shift in outer scale with q [Barnes et al., 2011, Nies et al., 2024]. For the ST40 runs, we retain β' (consistent with other parameters) and $B_\parallel$, and fix $D_{\text{hyper}} = 2.0$. A single resolution (*ST* in Tab. 3.2) is used for all the ST40 runs, which is sufficient to resolve the outer scales in those runs.

In Fig. 3.1, the non-zonal transition boundary lies within the spacing between the blue and red crosses, which represent saturated and divergent flux states, respectively. For both CBC and ST40 cases, the transition boundary is given roughly by $q^2\beta_e = C_{\text{nl}}$, where C_{nl} is a constant. To probe the role played by linear instabilities, we also performed a series of linear simulations to calculate the instability thresholds of KBMs and ideal ballooning modes (IBMs). The data shows that the KBM linear stability threshold, shown as a purple line in the top panel and purple triangles in both panels, satisfies $q^2\beta_e = C_{\text{KBM}}$. For the CBC, the IBM linear stability threshold, shown as a grey line, also satisfies $q^2\beta_e = C_{\text{IBM}}$, while the same trend holds true for the lower IBM boundary for ST40[3]. For both CBC and ST40 cases, it is clear that $C_{\text{nl}} < C_{\text{KBM}} < C_{\text{IBM}}$, suggesting that the subdominant KBMs are not responsible for triggering the non-zonal transitions. On more practical grounds, the linear stability thresholds follow approximately the same

[2] In `stella`, β' is related to other parameters as $\beta' = (\beta_r/2)\sum_s \tilde{n}_s\tilde{T}_s(-\mathrm{d}\ln n_s/d\tilde{r} - \mathrm{d}\ln T_s/\tilde{r})$. In many other codes, this quantity is defined to be a factor of two larger.

[3] In principle there also exists an upper IBM boundary for the CBC. However, since $\beta' = 0$ in the corresponding nonlinear runs, this boundary is never accessed.

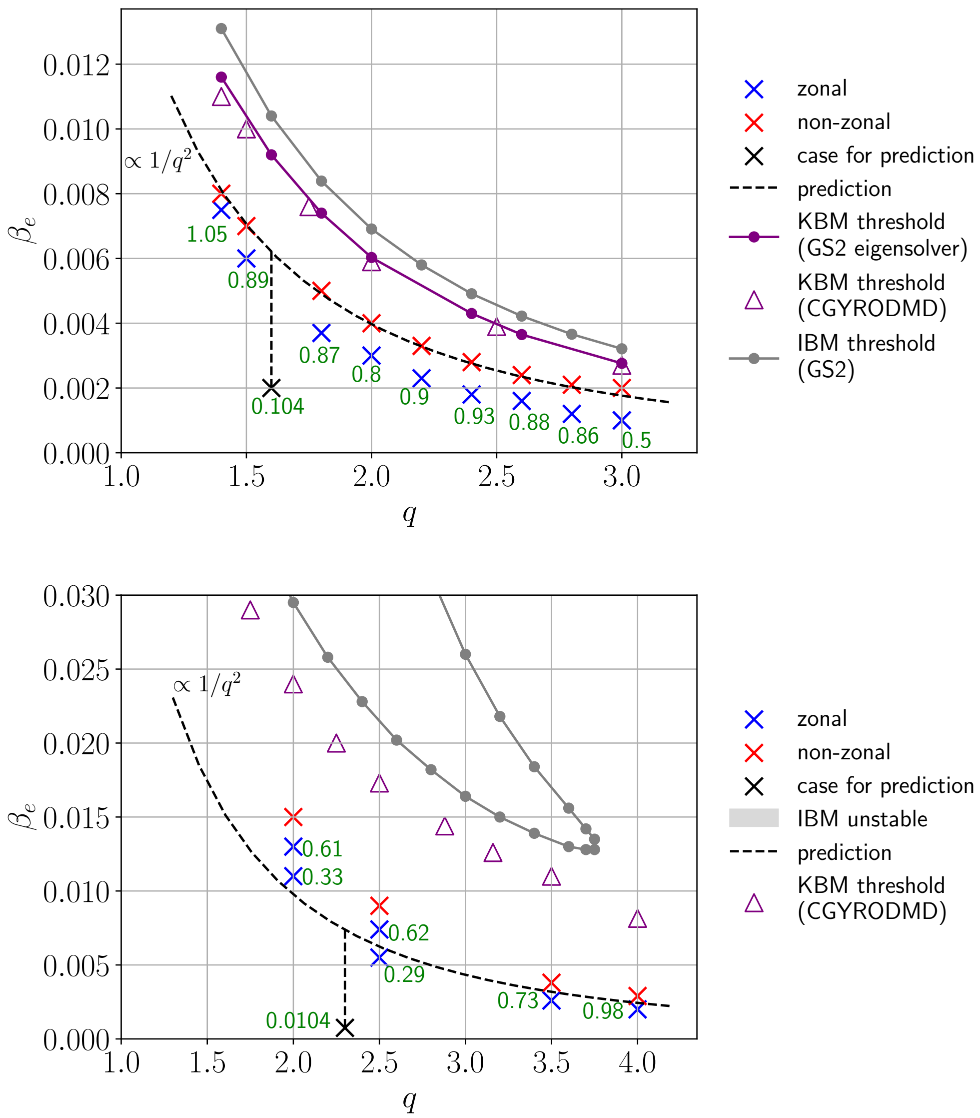

Figure 3.1: Non-zonal transition and linear stability boundaries of KBMs and IBMs in the (q,β_e) parameter space for the CBC (top) and ST40 (bottom) equilibria. The blue crosses represent cases with strong zonal flows and modest heat fluxes, and red crosses represent cases with weak zonal flows and divergent heat fluxes. The corresponding values of $|\langle T_{A_\parallel}\rangle_t / \langle T_\phi \rangle_t|$ for saturated cases are given in green. The curved, dashed black lines satisfy $\beta_e \propto 1/q^2$. **Top panel**: The grey line is the linear stability boundary of IBMs, and the purple line is the linear stability boundary of KBMs obtained from the `GS2` eigenvalue solver. The purple triangles are KBM thresholds obtained from `CGYRODMD` [Dudkovskaia et al., 2025]. The dashed black line is a predicted non-zonal transition boundary based on a single low-$q^2\beta_e$ simulation at $q = 1.6$, $\beta_e = 0.002$ (shown as a black cross). **Bottom panel**: The grey area represents the IBM-unstable region and the purple triangles represent the linear stability thresholds of KBMs. The dashed black line is a predicted non-zonal transition boundary based on a single low-$q^2\beta_e$ simulation at $q = 2.3$, $\beta_e = 0.00075$ (shown also as a black cross).

(q,β_e) scaling as the non-zonal transition boundary, but with an offset that limits their ability as prediction of the boundary location.

3.2.2 The turbulent transfers

We now investigate the zonal drives directly by calculating the turbulent stresses. In particular, we focus on the effect of turbulent stresses on the large-scale zonal flows. We first write the approximate evolution equation for the large-scale, zonal potential (3.18) in Fourier space:

$$\frac{\partial}{\partial t}\frac{Z^2 e n_i}{T_i}|\nabla x|^2\frac{k_x^2\rho_i^2}{2}\langle\phi\rangle_{yz,k_x} = \Pi_{\mathrm{lin},k_x} + \Pi_{\phi,k_x} + \Pi_{A_\parallel,k_x} + \Pi_{B_\parallel,k_x}, \tag{3.21}$$

where Π_{α,k_x} is the k_x-component of the stress contribution from the field α, and we have again assumed that $|\nabla x|$ and B remain roughly constant along z. To obtain an equation for the scale-by-scale energy transfer, we multiply both sides of (3.21) by the complex conjugate of the zonal potential $\langle\phi\rangle^*_{yz,k_x}$ and add to the resulting equation its own complex conjugate. The resulting evolution equation for a zonal flow 'energy' at wavenumber k_x is

$$\frac{\partial}{\partial t}\left[\frac{n_i m_i}{2}\left|v_{Z,k_x}\right|^2\right] = T_{\mathrm{lin},k_x} + T_{\phi,k_x} + T_{A_\parallel,k_x} + T_{B_\parallel,k_x}, \tag{3.22}$$

where

$$v_{Z,k_x} = -\left\langle\frac{c|\nabla x|k_x}{B}\phi_{\boldsymbol{k}}\right\rangle_{yz,k_x}, \tag{3.23}$$

and we have defined the energy transfers from the turbulence to the zonal flows $T_{\mathrm{lin},k_x} = \mathrm{Re}(\langle e\phi\rangle^*_{yz,k_x}\Pi_{\mathrm{lin},k_x})$, $T_{\phi,k_x} = \mathrm{Re}(\langle e\phi\rangle^*_{yz,k_x}\Pi_{\phi,k_x})$, $T_{A_\parallel,k_x} = \mathrm{Re}(\langle e\phi\rangle^*_{yz,k_x}\Pi_{A_\parallel,k_x})$ and $T_{B_\parallel,k_x} = \mathrm{Re}(\langle e\phi\rangle^*_{yz,k_x}\Pi_{B_\parallel,k_x})$. Notice that the left-hand side has become a time derivative of a positive definite quantity. We define the large-scale transfer T_α as

$$T_\alpha = \sum_{k_x\geq -k_y^o}^{k_x\leq k_y^o} T_{\alpha,k_x}, \tag{3.24}$$

where k_y^o is the k_y corresponding to the outer scale of the turbulence, which we take here to be the peak of the heat-flux spectrum in k_y (see the left panel of Fig. 3.4 for a sample spectrum). We focus on these 'large-scale' contributions because they are primarily responsible for regulating the turbulence saturation.

We plot the time traces of the large-scale nonlinear transfers for two representative cases in Fig. 3.2. The left panel corresponds to a CBC simulation with $(q = 1.4, \beta_e = 0.007)$, and the right panel corresponds to an ST40 simulation with $(q = 3.5, \beta_e = 0.00345)$. Both cases are only slightly below the non-zonal transition thresholds, as can be seen from Fig. 3.1. The red and blue curves show the transfers $T_{A_\parallel}$ and T_ϕ, respectively.

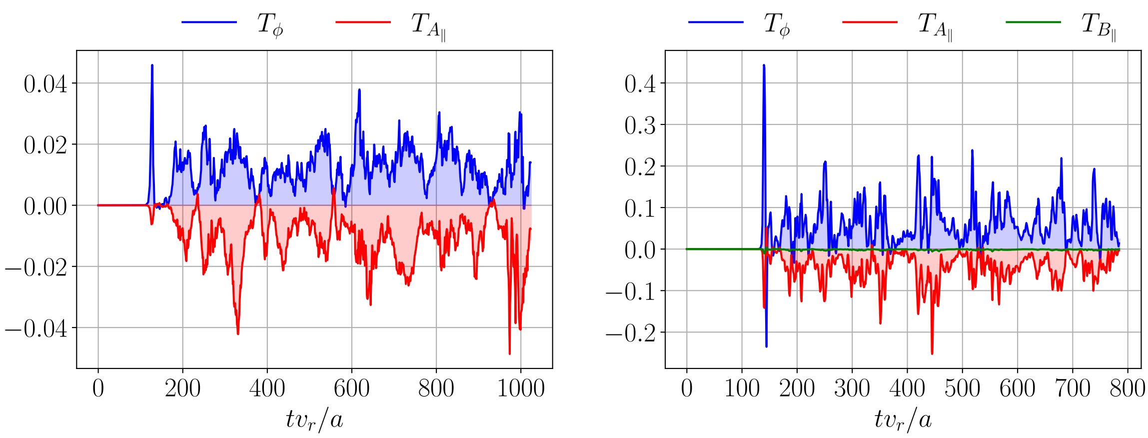

Figure 3.2: Time traces of large-scale, nonlinear transfers normalised by $n_r T_r v_r \rho_r^2/a^3$ for the CBC (*R1* resolution) and ST40 runs just below the non-zonal transition thresholds. The red and blue curves show the transfers $T_{A_\parallel}$ and T_ϕ, respectively. The ratio of red area to blue area represents the ratio between time-averaged transfers r_{MR}. **Left panel**: CBC, $q = 1.4, \beta_e = 0.007$, $r_{MR} \approx 0.81$. **Right panel**: ST40, $q = 3.5, \beta_e = 0.00345$, $r_{MR} \approx 0.79$.

Notice that, on average, $T_\phi > 0$ acts as a zonal-flow drive while $T_{A_\parallel} < 0$ tends to damp the zonal flows. The $T_{B_\parallel}$ contribution in the ST40 run, where it is retained, is negligible compared to the other nonlinear transfers. Consequently, the main competition is between the negative Maxwell-stress transfer and the positive Reynolds-stress transfer. To study how the Reynolds-Maxwell stress balance correlates with the non-zonal transition, we consider the Maxwell-to-Reynolds transfer ratio $r_{MR} \equiv |\langle T_{A_\parallel} \rangle_t / \langle T_\phi \rangle_t|$, which is the absolute value of the ratio between time-averaged transfers (shown as the ratio of red area to blue area in Fig. 3.2), where the time-average $\langle\rangle_t$ is performed over the saturation period of the turbulence. The effects from the Reynolds and Maxwell transfers become comparable just below the non-zonal transition threshold, and for $q^2\beta_e$ values beyond the threshold, the net effect of the nonlinear energy transfer is damping of the zonal modes and a lack of turbulence saturation. The transfer ratio for each saturated simulation is labeled on Fig. 3.1 as green numbers. As expected, the transfer ratio approaches unity near the non-zonal transition boundary.

To further justify the approach of taking the large-scale transfers using (3.24), we study the energy transfer at each k_x to the zonal mode due to turbulent stresses as given by the right-hand side of (3.22). After the system develops into a saturated state, we calculate the time-averaged transfer spectrum in the k_x-space (see Fig. 3.3), revealing how different scales contribute to zonal flow dynamics. In the left panel, we present data from the CBC with $q = 1.4$, $\beta_e = 0.007$ and resolution *R1*. While the Reynolds transfer T_{ϕ,k_x} remains positive at small k_x, indicating a zonal drive at large scales, it turns negative at higher k_x. There even appears to be resonant behaviour near $k_x \sim 1$.

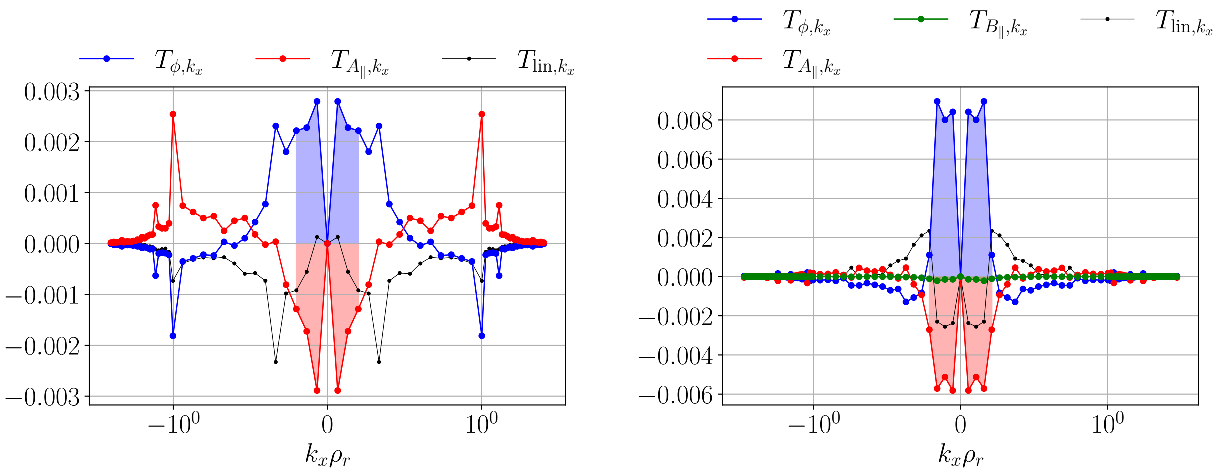

Figure 3.3: k_x-spectra of time-averaged transfers normalised by $n_rT_rv_r\rho_r^2/a^3$. The blue and red regions show the large-scale ($|k_x| <= k_y^o$) transfers due to T_{ϕ,k_x} and $T_{A_\parallel,k_x}$, respectively. **Left panel**: CBC with $q = 1.4$, $\beta_e = 0.007$ and resolution *R1*. **Right panel**: ST40 case with $q = 3.5$, $\beta_e = 0.00345$.

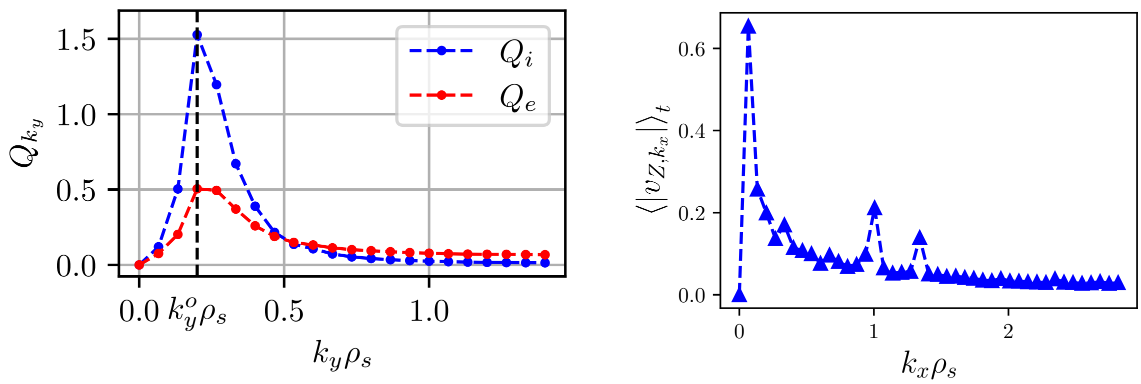

Figure 3.4: **Left panel**: Time-averaged k_y-spectrum normalised by $Q_{gB} = n_rT_rv_r\rho_r^2/a^2$ of the ion (Q_i) and electron (Q_e) heat fluxes for the CBC with $q = 1.4$, $\beta_e = 0.007$ and resolution *R1*. Each point is obtained by first averaging over z, then summing over k_x and averaging over the saturated period. The peak location is labeled as k_y^o. **Right panel**: Time-averaged k_x-spectrum normalised by cT_r/B_rea of the zonal-flow velocity.

These resonant structures are sensitive to numerical resolution and normally disappear when the resolution improves, as shown later in Subsection 3.2.4. In the right panel, we show data from the ST40 simulation with $q = 3.5$, $\beta_e = 0.00345$. There, the large-scale transfers are clearly the dominant contribution, with the signs of Reynolds (positive) and Maxwell (negative) transfers matching the expectations. It appears that the large-scale transfers at low k_x are more robust and one may argue they are more relevant since the zonal flows are predominantly active at those scales. This is illustrated on the right panel of Fig. 3.4, which shows that the time-averaged, zonal flow spectrum peaks at large scales for the CBC discussed above[4].

The large-scale zonal flows discussed so far typically satisfy $k_x\rho_r \lesssim 0.1$. However, as shown by Nies et al. [2024], in certain regimes the saturation level of electrostatic ITG turbulence can instead be predominantly controlled by zonal modes at smaller spatial scales, with $k_x\rho_r \sim 0.5$. These smaller-scale zonal modes propagate radially due to the radial component of the magnetic drift. The result in Nies et al. [2024] was obtained in the context of electrostatic ITG turbulence with electrons assumed to follow an adiabatic response [Hammett et al., 1993, Rogers et al., 2000], i.e.,

$$\delta f_e = \frac{e}{T_e}\left(\phi - \langle\phi\rangle_{yz}\right) F_e. \tag{3.25}$$

This approximation exploits the small electron-to-ion mass ratio, $\sqrt{m_e/m_i}$. What remains to be thoroughly investigated is whether the inclusion of electromagnetic effects, or simply treating electrons kinetically inevitably alters the characteristic scales of the propagating zonal modes. Below, we present two simulations of electromagnetic ITG turbulence where the propagating zonal structures are examined.

The first nonlinear simulation uses the same parameters as those used by the CBCs in Subsection 3.2.1, and with resolution *R1*, $q = 1.4$, $\beta_e = 0.0045$. The second uses a similar parameter set, except for $\tilde{R} = 2.78$, $\beta_e = 0.0015$, $-\mathrm{d}\ln(n_{i,e})/\mathrm{d}\tilde{r} = 0.8$, $-\mathrm{d}\ln(T_{i,e})/\mathrm{d}\tilde{r} = 5.0$ and $D_{\mathrm{hyper}} = 1.0$, with resolutions $N_{v_\parallel} = 48$, $N_\mu = 12$, $L_x = L_y = 188\rho_r$, $k_{x,\max}\rho_r = 2.1$ and $k_{y,\max}\rho_r = 1.4$. The major difference is that the temperature gradients are much higher in the latter. Note that the second set of parameters are only used in the current Subsection. So the word 'CBC' refers to those with parameters given in Tab. 3.1 in the rest of the thesis.

The resulting zonal structures in the saturated turbulence are shown in Fig. 3.5 and Fig. 3.6. Each figure contains two panels: the left shows the zonal velocity v_Z versus (x,t), while the right shows the modulus of its Fourier transform versus (k_x, ω). Compared to the lower-temperature-gradient case in Fig. 3.5, the higher-temperature case in Fig. 3.6 exhibits much clearer signatures of propagating zonal flows. In particular, the left panel of Fig. 3.6 shows small-scale zonal flows propagating radially on top of a large-scale

[4] The corresponding plot for the ST40 case is similar.

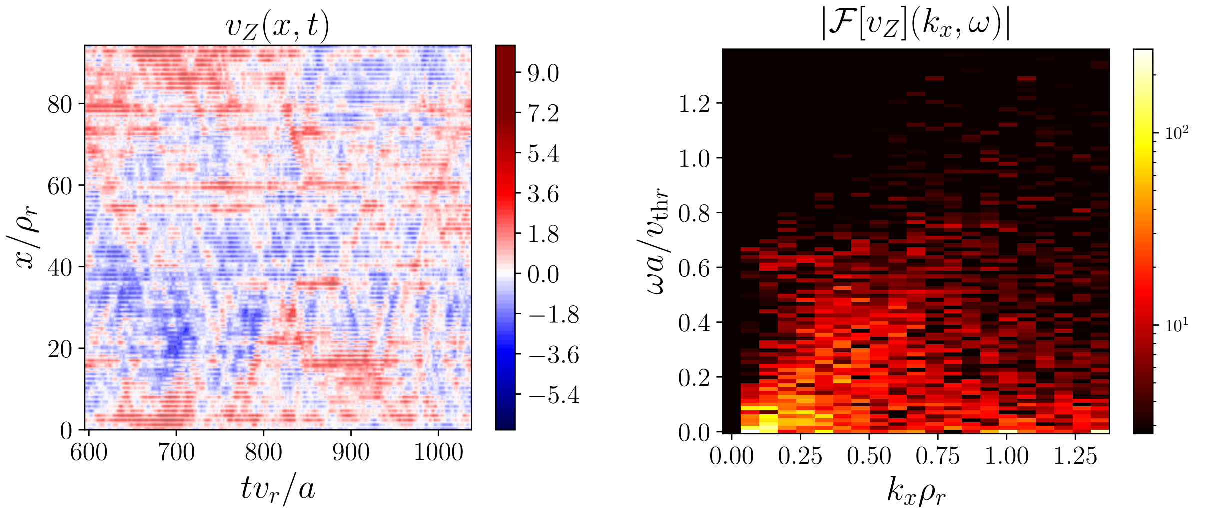

Figure 3.5: Structure of the zonal flow velocity normalised by $cT_r/B_r ea$ obtained from the CBC simulation with lower temperature gradients ($-\mathrm{d}\ln T_{i,e}/\mathrm{d}\tilde{r} = 2.3$), $q = 1.4$ and $\beta_e = 0.0045$. **Left panel**: Zonal velocity v_Z versus (x,t). Propagating, small-scale zonal flows seem to exist but are not obvious. **Right panel**: Modulus of the Fourier transformed v_Z versus (k_x,ω).

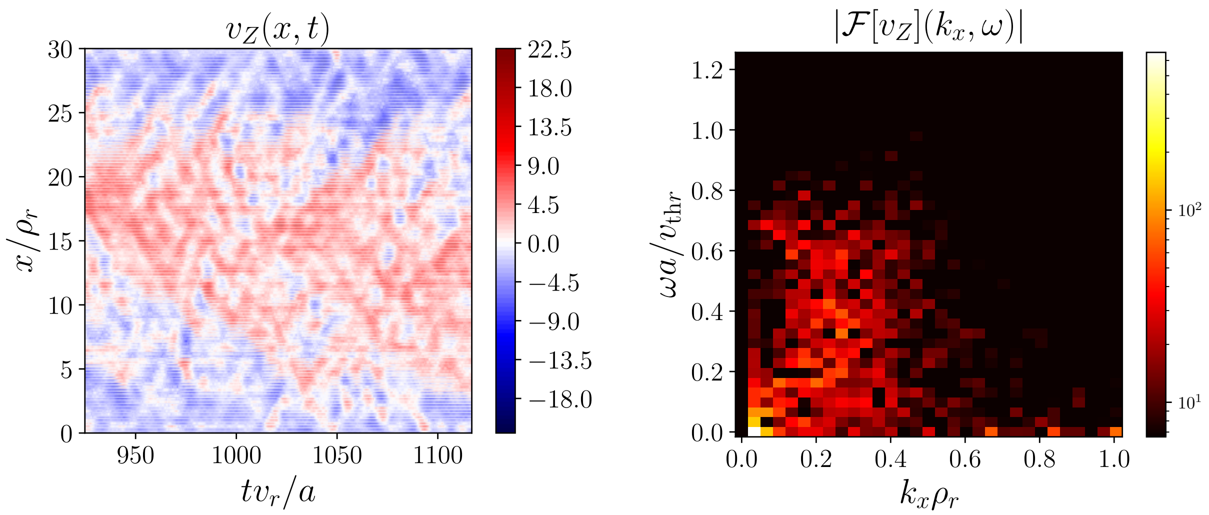

Figure 3.6: Structure of the zonal flow velocity normalised by $cT_r/B_r ea$ obtained from the CBC simulation with higher temperature gradients ($-\mathrm{d}\ln T_{i,e}/\mathrm{d}\tilde{r} = 5.0$), $q = 1.4$ and $\beta_e = 0.0015$. **Left panel**: Zonal velocity v_Z versus (x,t). Propagating, small-scale zonal flows appear on top of a large-scale background of stationary zonal flows. **Right panel**: Modulus of the Fourier transformed v_Z versus (k_x,ω).

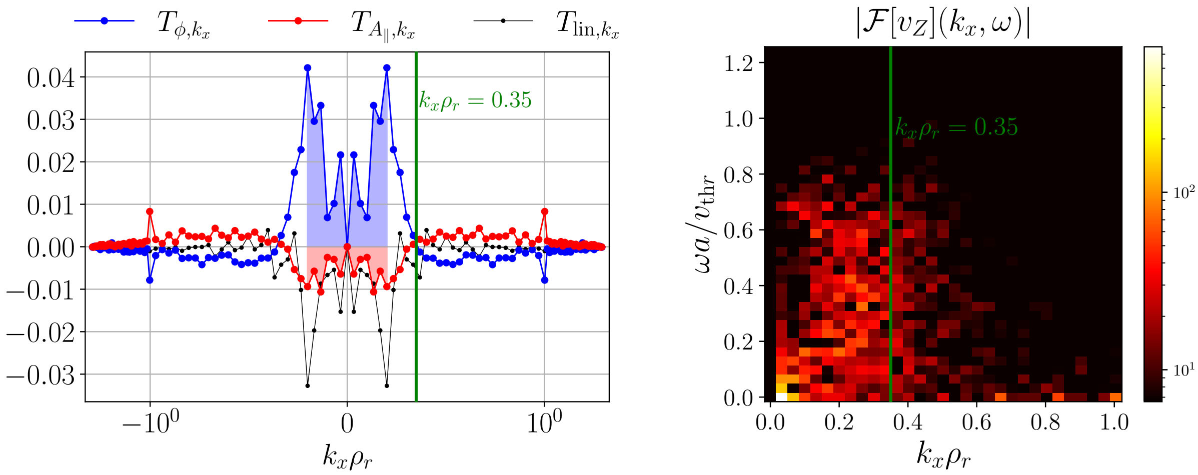

Figure 3.7: **Left panel**: k_x-spectrum of time-averaged transfers normalised by $n_r T_r v_r \rho_r^2/a^3$ for the CBC corresponding to the case in Fig. 3.6. The blue and red regions ($|k_x| <= k_y^o \approx 0.2/\rho_r$) show the large-scale transfers due to T_{ϕ,k_x} and $T_{A_\parallel,k_x}$, respectively. The green line at $k_x\rho_r = 0.35$ marks the location where the transfers first decay to nearly zero. **Right panel**: The same plot as the right panel of Fig. 3.6 except now a green line at $k_x\rho_r = 0.35$ is added for comparison with the left panel of the current figure.

background of stationary zonal flows. This observation can be further confirmed by the right panel of Fig. 3.6, where, even though the dominant peak is located at low k_x and $\omega = 0$ (stationary zonal flows), a propagating branch with frequency $\omega \approx (4/3)\, k_x\rho_r v_{\mathrm{thr}}/a$ is also clearly visible. These propagating components are precisely the ones that Nies et al. [2024] identified as potentially playing a crucial role in setting the saturation level of electrostatic ITG turbulence, leading to the concept of 'grand' critical balance. In the electromagnetic simulations considered here, however, the stationary zonal flows dominate in amplitude over the propagating branch, in contrast to the electrostatic cases with Boltzmann electrons reported in Nies et al. [2024], where the propagating branch was found to be dominant. Consequently, it remains unclear whether the propagating branch plays a decisive role in turbulence saturation in the electromagnetic regime, and, more importantly, whether it controls the non-zonal transition boundary.

Nevertheless, we present the transfer spectrum (see the left panel of Fig. 3.7) corresponding to the case in Fig. 3.6 to examine whether the large-scale transfer defined by (3.24) captures the feature of the propagating zonal flows. As shown by the spectrum, both the Reynolds and Maxwell transfers are dominated by low-k_x contributions and decrease to nearly zero around $k_x\rho_r \approx 0.35$. From the right panel of Fig. 3.7, this wavenumber corresponds approximately to the cut-off scale for the propagating zonal flows. We also note that the outer scale $k_y^o\rho_r \approx 0.2$, defined by the peak of the heat-flux spectrum, is smaller than this cut-off scale. However, computing r_{MR} using the large-scale transfer definition in (3.24) yields a value of 0.263, which is very similar to the value

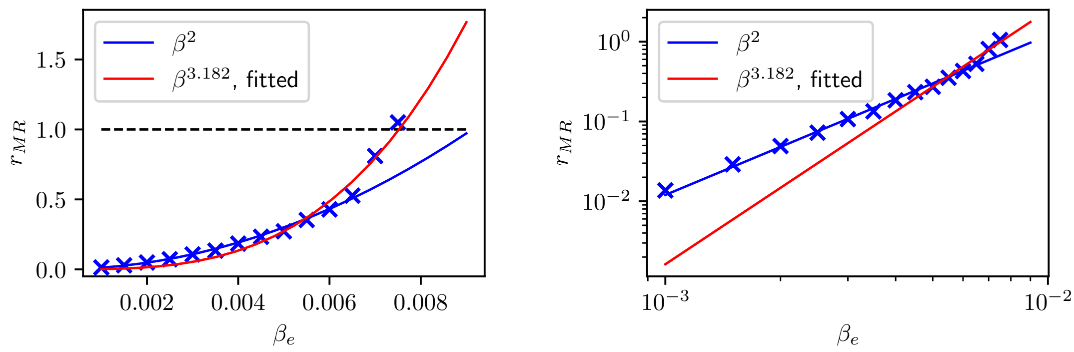

Figure 3.8: Transfer ratio r_{MR} scaling with β_e for the CBC with $q = 1.4$ and resolution *R1*. Right panel is the log-log version of the left one. The blue crosses are the data points and the blue solid line is $\propto \beta_e^2$. The fitted red line is $\propto \beta_e^{3.182}$.

of 0.261 obtained when extending the summation domain up to $k_x\rho_r = 0.35$. Therefore, at least for the CBC cases considered here, the large-scale transfer prescription (3.24) should remain valid for predicting non-zonal transitions, even when smaller-scale zonal modes contribute appreciably to the overall zonal structure.

3.2.3 β_e-scaling of the turbulent transfers

In this Subsection, we consider the scaling of the ratio r_{MR} with q and β_e for electromagnetic ITG turbulence. Armed with this scaling and the ansatz that the non-zonal transition occurs when the Reynolds and Maxwell stresses balance, i.e., when $r_{MR} \approx 1$, one can predict the transition boundary in the (q,β_e) plane from a single nonlinear simulation. In particular, we can calculate r_{MR} from an approximately electrostatic simulation at small (q,β_e) and use the scaling law to extrapolate the transition at $r_{MR} \approx 1$. Such a simulation is much cheaper computationally than the equivalent simulation near the transition boundary, where fast electron motion along the perturbed magnetic field lines leads to a strong constraint on the timestep size allowed for the numerical stability.

In Appendix B, we obtain a heuristic scaling $r_{MR} \propto q^2\beta_e$ by balancing terms in the linear gyrokinetic equations. Combined with the observation that $r_{MR} \approx 1$ near the transition threshold, this scaling is at least consistent with the trend $q^2\beta_e = C_{\mathrm{nl}}$. However, the nonlinear simulation results presented below indicate a stronger dependence, $r_{MR} \propto (q^2\beta_e)^2$, suggesting that the heuristic argument omits key nonlinear physics.

Fig. 3.8 illustrates the transfer ratio scaling with β_e obtained from simulations for the CBC with $q = 1.4$. Two curve fits are applied to both panels. For most of the data points, a β_e^2 scaling (blue solid line) provides an excellent fit. However, as β_e approaches the non-zonal transition threshold at $\beta_e \approx 0.8\%$, this quadratic scaling begins to deviate from the data. When fitting a single curve to the entire dataset, the result is a steeper scaling (red solid line), which captures the behaviour near the transition but fails to accurately represent the lower-β_e regime. Since our goal is to predict non-zonal transition based on low-β_e simulations, the β_e^2 scaling is preferable for extrapolation purposes, as it better captures the trend in the low-β_e regime. As we have seen in Fig. 3.1, the non-zonal transition boundary closely follows the $q^2\beta_e = C_{\rm nl}$ curve for both the CBC and ST40 runs, except that, for ST40, noticeable deviations occur only at relatively small values of q. Hence, we conjecture that the overall scaling law is approximately given by $r_{MR} \propto (q^2\beta_e)^2$.

To demonstrate the predictive power of this scaling law, we perform two simulations – one for the CBC and the other for ST40 – at low $q^2\beta_e$ and calculate the resultant transfer ratio r_{MR}. These two cases are represented in Fig. 3.1 as black crosses, with the corresponding r_{MR} provided in green. Applying the scaling $r_{MR} \propto (q^2\beta_e)^2$ to both cases, we obtain that r_{MR} crosses unity along the black dashed lines in Fig. 3.1. The predicted transition boundaries show excellent agreement with the simulation results in the CBC. For the ST40 cases, the agreement remains good at higher values of q but progressively deviates at lower values of q.

3.2.4 Convergence study

In this Subsection, we conduct convergence studies for the CBC case with $q = 1.4$ and $\beta_e = 0.007$ from Subsection 3.2.1, by either doubling the simulation box dimensions in both the x and y directions, or doubling the number of wavenumbers (k_x,k_y).

Box size convergence

Using the resolution *R4*, we obtain the transfer spectrum (left of Fig. 3.9) and the time trace of the large-scale transfer (right of Fig. 3.9). There are a few notable observations. First, the transfer spectrum now appears significantly cleaner compared to the low resolution case: Most of the transfer activity is concentrated at large scales, where the Reynolds and Maxwell stresses compete. In contrast, the complex small-scale structures observed in Fig. 3.3 seem to play a much less important role. The second observation is that the transfer ratio r_{MR} decreases with time after an initial period of saturation. This is consistent with the findings in [Rath and Peeters, 2022], where the Maxwell stress plays a diminished role as the box-size zonal flow gradually grows and suppresses turbulence.

In the left panel of Fig. 3.10, we show the time traces of the heat fluxes for the CBC case with ($q = 1.4$, $\beta_e = 0.007$) at two different resolutions. In the *R1* simulation, the heat flux reaches a steady level shortly after saturation. In contrast, the *R4* simulation requires a significantly longer time to settle and ultimately saturates at a lower level. This delayed relaxation is caused by the slow, long-term growth of the box-size zonal mode in the *R4* case. The right panel of Fig. 3.10 shows the corresponding time traces of

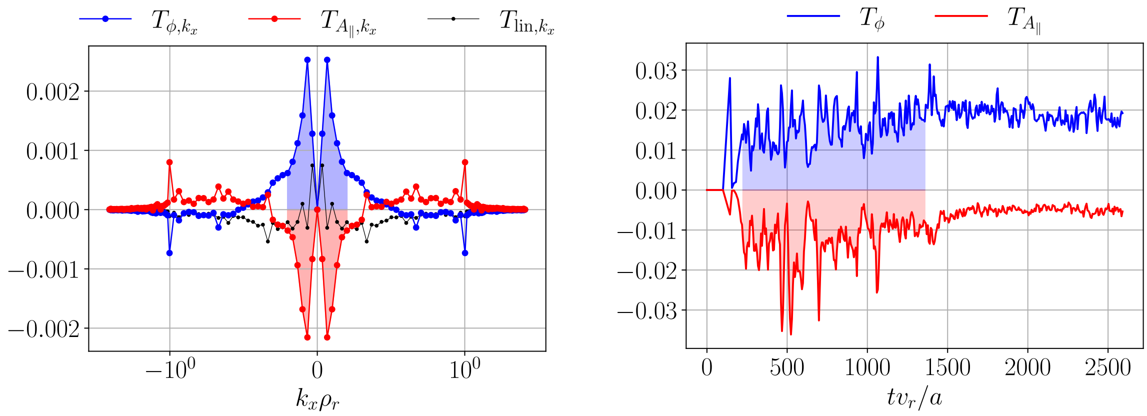

Figure 3.9: The same case as in the left panel of Fig. 3.3 except here the resolution is *R4*. **Left panel**: k_x-spectrum normalised by $n_rT_rv_r\rho_r^2/a^3$ of time-averaged transfers. The blue and red regions show the large-scale ($|k_x| < k_y^o$) transfers due to T_{ϕ,k_x} and $T_{A_\parallel,k_x}$, respectively. **Right panel**: Time traces of large-scale transfers normalised by $n_rT_rv_r\rho_r^2/a^3$. During the steady period indicated by the shadings, $r_{MR} \approx 0.81$.

the zonal electrostatic potential. Compared with the *R1* case, the box-size zonal mode in the *R4* simulation continues to grow over a much longer timescale and eventually reaches a much larger amplitude, leading to a stronger suppression of turbulence and hence a reduced heat flux. During this prolonged growth phase, the ratio r_{MR} decreases, as seen in the right panel of Fig. 3.9. This reduction establishes a positive feedback loop: the weakening of the Maxwell stress allows the zonal flow to grow more strongly, and the resulting enhancement of the box-size zonal flow further suppresses the Maxwell stress, an observation first made by Rath and Peeters [2022].

This positive feedback loop suggests that electromagnetic fluctuations are suppressed by the large scale zonal flows more effectively than their electrostatic counterparts. As a result, saturation might be achieved even for cases slightly above the transition threshold – provided the system is restarted from a state in which the box-size zonal flow has already developed to a level where the Maxwell stress becomes subdominant relative to the Reynolds stress, leading to a transport hysteresis [Rath and Peeters, 2022].

Here, we perform the same test. Fig. 3.11 shows the time traces of the total heat flux for two restart simulations. Both runs begin with parameters ($q = 1.4$, $\beta_e = 0.007$) and are later restarted with a higher value, $\beta_e = 0.01$, at the times indicated by the red stars. In the left panel, corresponding to resolution *R1*, the heat flux rapidly diverges following the restart. In contrast, the right panel shows that, for resolution *R4*, the heat flux remains saturated for a considerably longer interval and persists in a quasi-steady state until the end of the simulation. It is worth noting that if the *R4* simulation is instead initialised with noise, the heat flux diverges[5], indicating that turbulence saturation depends on the

[5]This happens to all the 'non-zonal' cases shown in Fig.3.1, where the simulations are initialised with

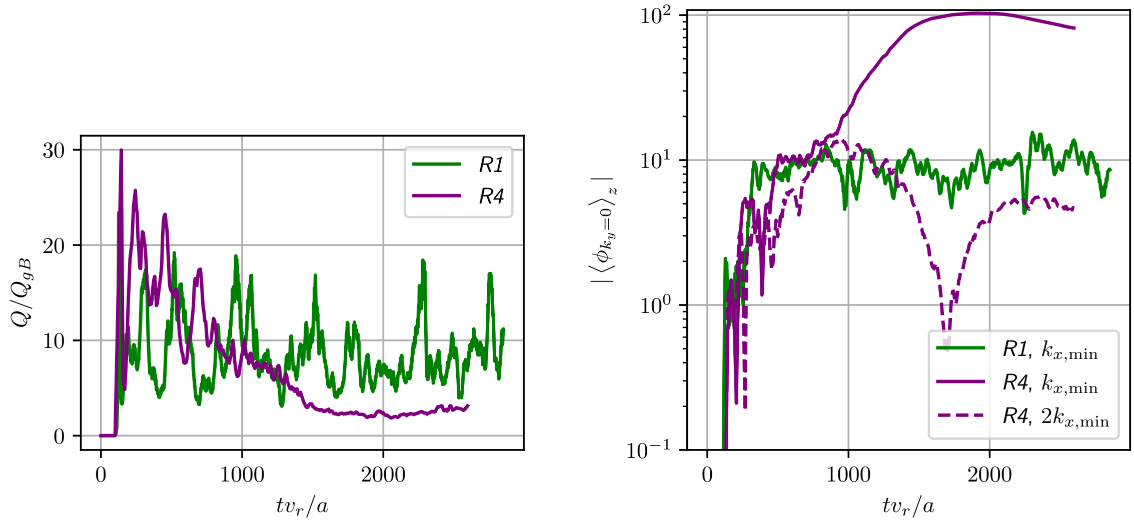

Figure 3.10: **Left panel**: Time trace of the total heat fluxes normalised by $Q_{gB} = n_r T_r v_r \rho_r^2/a^2$ for the CBC with $(q = 1.4, \beta_e = 0.007)$. The data from the simulation with resolution *R1* is shown in green, and that with resolution *R4* is shown in purple. **Right panel**: Time trace of the zonal modes $|\langle\phi_{k_y=0}\rangle_z|$ normalised by $T_r\rho_r/ea$, corresponding to the simulations on the left panel. The box-size zonal mode from the simulation with resolution *R1* is shown in solid green, while the corresponding box-size mode from the *R4* simulation is shown in solid purple. The second-lowest zonal mode from the *R4* simulation (*R4*, $2k_{x,\min}$) – which is equal to the box-size mode in the *R1* simulation (*R1*, $k_{x,\min}$) – is shown in dashed purple.

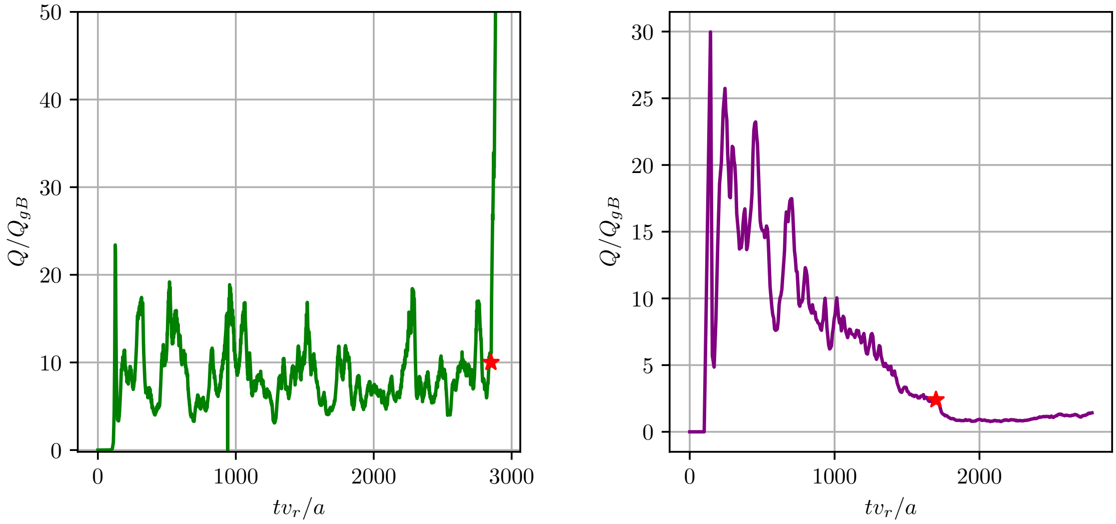

Figure 3.11: Time traces of the total heat fluxes, normalised by $Q_{gB} = n_r T_r v_r \rho_r^2/a^2$, for the CBC simulations with $q = 1.4$. Initially, $\beta_e = 0.007$ for both simulations. When the simulations are restarted at the times marked by the red stars, the value of β_e is increased to 0.01. **Left panel**: Resolution *R1*. **Right panel**: Resolution *R4*.

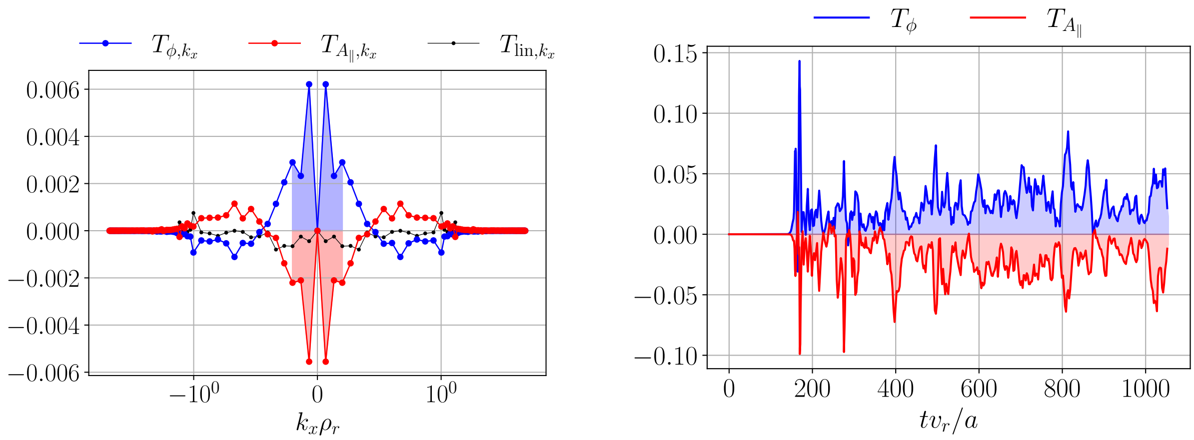

Figure 3.12: The same case as in Fig. 3.3 except here the resolution is *R5*. **Left panel**: k_x-spectrum normalised by $n_r T_r v_r \rho_r^2/a^3$ of time-averaged transfers. The blue and red regions show the large-scale ($|k_x| < k_y^o$) transfers due to T_{ϕ,k_x} and $T_{\parallel,k_x}$, respectively. **Right panel**: Time traces of large-scale transfers normalised by $n_r T_r v_r \rho_r^2/a^3$. During the saturation period indicated by the shading, $r_{MR} \approx 0.86$.

initial zonal structure, particularly the presence of large-scale zonal flows. Therefore, this behaviour is consistent with the transport hysteresis reported by Rath and Peeters [2022].

The transport hysteresis observed shows that the competition between Reynolds and Maxwell stresses determines the saturation only during the transit in which the Maxwell stress stays relatively important. For the simulation with resolution *R4* shown in Fig. 3.9, $r_{MR} \approx 0.81$ during that transit period, which lies close to the value obtained from the case with resolution *R1*.

Resolution convergence

We now perform the transfer calculations using resolution *R5*. The results are presented in Fig. 3.12. As shown in the figure, the transfer spectrum at higher wavenumber resolution remains dominated by large-scale features – similar to the behavior observed in simulations with larger box sizes (*R4*). The higher-resolution simulation yields a transfer ratio of $|\langle T_{A_\parallel}\rangle_t / \langle T_\phi \rangle_t| \approx 0.86$ during the transient period, which differs from the corresponding value from the lower-resolution run (*R1*) only by about 6%.

Overall, both box-size and resolution convergence are achieved, provided that the transfer ratio r_{MR} is evaluated during the transient phase, before the Maxwell stress is strongly suppressed by the long-term growth of the large-scale zonal flows.

noise.

Chapter 4

Fluid turbulent stresses

This is what really matters... given that "really matters" is a strong word in this context.

— Robbie Ewart, Oxford plasma seminars and Vienna meetings

We have seen in previous chapters that the evolution of zonal flows is governed by the nonlinear stresses generated by the turbulence. However, the full equation (3.12) that describes this evolution is generally too complicated to reveal the underlying physics, owing to the presence of FLR effects and toroidal geometry. To facilitate a more transparent analysis of zonal-flow dynamics, we seek a self-consistent fluid model capable of describing electromagnetic ITG turbulence. Therefore, in this chapter, we formulate here a minimal local model for electromagnetic ITG turbulence in a plasma with curved equilibrium magnetic field and find numerically that transitions from zonal- to non-zonal-transport states occur at certain critical values of the plasma beta and ion temperature gradient. These values do indeed turn out to correspond to locations in parameter space where the turbulent viscosity changes sign, and it is shown that the viscosity associated with the Maxwell stress tends to be positive, i.e., it reduces zonal flow shear.

4.1 Fluid model of electromagnetic ITG – derivation

Our aim is to construct an asymptotically correct, minimal model for electromagnetic ITG turbulence that exhibits the key features of the non-zonal transitions observed in nonlinear gyrokinetic simulations. To this end, we consider a plasma consisting of electrons of mass m_e and charge $-e$ and a single ion species of mass m_i and charge Ze, immersed in a static magnetic field of constant curvature. Such a configuration, often referred to as a Z-pinch or 'curvy slab', is illustrated in the right panel of Fig. 4.1. The equilibrium magnetic field $\boldsymbol{B} = B(x)\hat{\boldsymbol{z}}$ varies in magnitude along its curvature vector with the characteristic length scale $L_B \equiv (-\mathrm{d}\ln B/\mathrm{d}x)^{-1}$. The equilibrium ion temperature T_i is also allowed to vary in x with characteristic length scale $L_T \equiv (-\mathrm{d}\ln T_i/\mathrm{d}x)^{-1}$, while both the equilibrium

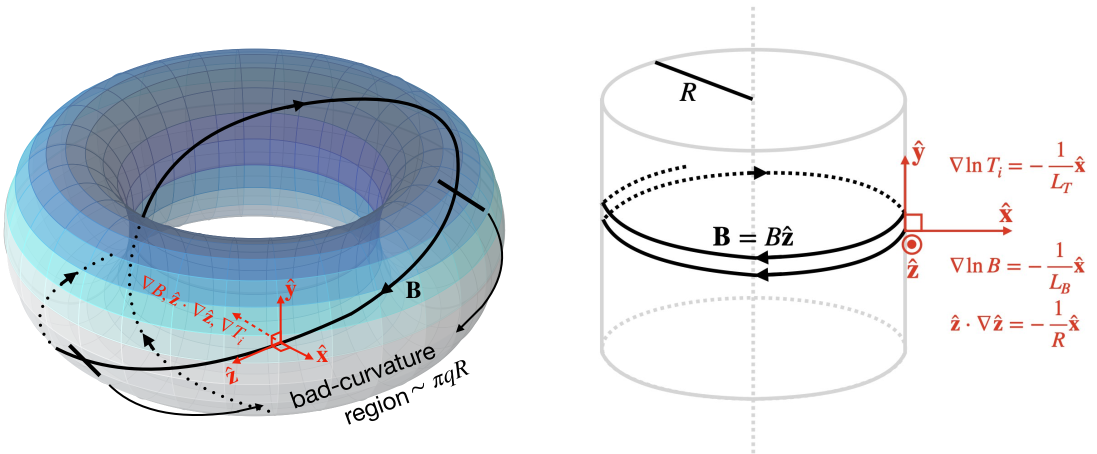

Figure 4.1: **Left panel**: An illustration of the out-board side of a tokamak, sometimes called the bad-curvature region. The length of that region is roughly $\pi q R$ where R is the major radius. Here, $\hat{\boldsymbol{z}}$ is the direction of the equilibrium magnetic field, so the equilibrium field is $\boldsymbol{B} = B\hat{\boldsymbol{z}}$ where B is the field strength, $\hat{\boldsymbol{x}}$ is the radial direction, and $\hat{\boldsymbol{y}}$ is the poloidal direction. In a general tokamak geometry $\hat{\boldsymbol{x}}$ and $\hat{\boldsymbol{y}}$ are not orthonormal, as we discussed in Subsection 1.2.4. **Right panel**: Z-pinch equilibrium. In the limit of large-aspect ratio, large q and small magnetic shear $\hat{s}$, the out-board side of the flux-surface resembles a Z-pinch geometry where $\hat{\boldsymbol{x}}$, $\hat{\boldsymbol{y}}$, and $\hat{\boldsymbol{z}}$ form an orthonormal basis; the major radius R becomes the radius of curvature of the field line.

density n and electron temperature T_e are assumed constant. Similar electromagnetic turbulence models have been studied previously for electron scale turbulence [Adkins et al., 2022]. This geometry can be viewed as a local slice taken from the out-board side of a large-aspect-ratio tokamak (see the left panel of Fig. 4.1) with nearly toroidal magnetic field (corresponding to a large safety factor, q). The out-board side of the tokamak is where the ITG instability is most unstable and is therefore the region we try to model with the Z-pinch geometry.

In the rest of the chapter, we switch to a right-handed coordinate system, i.e., $\hat{\boldsymbol{x}} \times \hat{\boldsymbol{y}} = \hat{\boldsymbol{z}}$, whereas the ones introduced in Subsection 1.2.4 are left-handed. In addition, z is defined here to represent the distance along the field line.

To derive a fluid model for the ITG turbulence, we will start from the gyrokinetic-Maxwell system of equations introduced in Section 1.3 and then carry out subsidiary expansions to achieve fluid closures. In a Z-pinch, the mirror contribution ($\propto \hat{\boldsymbol{b}}\cdot\nabla B \partial h_s/\partial v_\parallel$) in the gyrokinetic equation (1.17) vanishes since B is constant along the equilibrium field line. In addition, $\hat{\boldsymbol{b}} \cdot \nabla z = 1$ as z now measures the distance along the field line.

We now rewrite terms of (1.17) in the Z-pinch coordinates: the magnetic drift term

$$\boldsymbol{v}_{Ms} = -\frac{1}{\Omega_s}\left(\frac{v_\parallel^2}{R} + \frac{v_\perp^2}{2L_B}\right)\hat{\boldsymbol{y}}, \tag{4.1}$$

the nonlinear term

$$\langle \boldsymbol{v}_\chi \rangle_{\boldsymbol{R}_s} \cdot \nabla h_s = \frac{c}{B} \left\{ \langle \chi \rangle_{\boldsymbol{R}_s}, h_s \right\}, \tag{4.2}$$

and the energy injection term

$$\langle \boldsymbol{v}_\chi \rangle_{\boldsymbol{R}_s} \cdot \nabla F_s = \frac{c}{B} \frac{\partial \langle \chi \rangle_{\boldsymbol{R}_s}}{\partial y} \left[\frac{1}{L_{ns}} + \left(\frac{v^2}{v_{\text{th}s}^2} - \frac{3}{2} \right) \frac{1}{L_{Ts}} \right] F_s, \tag{4.3}$$

where $L_{ns} \equiv (-\mathrm{d}\ln n_s/\mathrm{d}x)^{-1}$ and $L_{Ts} \equiv (-\mathrm{d}\ln T_s/\mathrm{d}x)^{-1}$. Thus, the gyrokinetic equation (1.17) written in Z-pinch coordinates is

$$\frac{\partial h_s}{\partial t} + v_\parallel \frac{\partial h_s}{\partial z} - \frac{1}{\Omega_s} \left(\frac{v_\parallel^2}{R} + \frac{v_\perp^2}{2L_B} \right) \frac{\partial h_s}{\partial y} + \frac{c}{B} \left\{ \langle \chi \rangle_{\boldsymbol{R}_s}, h_s \right\}$$
$$+ \frac{c}{B} \frac{\partial \langle \chi \rangle_{\boldsymbol{R}_s}}{\partial y} \left(\frac{v^2}{v_{\text{th}s}^2} - \frac{3}{2} \right) \frac{F_s}{L_{Ts}} = \frac{Z_s e}{T_s} F_s \frac{\partial \langle \chi \rangle_{\boldsymbol{R}_s}}{\partial t} + \langle C[h_s] \rangle_{\boldsymbol{R}_s}, \tag{4.4}$$

where the density gradients are neglected, $1/L_{Te} = 0$ and $L_{Ti} = L_T$. In the following Subsections, we will assume the smallness of certain plasma parameters and perform the corresponding asymptotic expansions, followed by taking the fluid moments of (4.4).

4.1.1 Small mass-ratio expansion of gyrokinetics

To begin with, we exploit the smallness of the electron-ion mass ratio to derive a reduced model for electrons in which they are treated as an isothermal fluid. This is achieved by applying a subsidiary expansion in $\sqrt{m_e/m_i} \ll 1$ to the electron gyrokinetic equation [Schekochihin et al., 2009]. We focus on the ion-scale fluctuations, for which $k_\perp \rho_e \sim \sqrt{m_e/m_i} \ll 1 \sim k_\perp \rho_i$, and otherwise adopt the maximal ordering in which plasma β, ion-electron temperature ratio τ, and ion charge number Z are all of order unity. Motivated by the physics of ITG dynamics and the inclusion of electromagnetic effects, we impose the following ordering on the characteristic frequencies of the system:

$$\omega_{di} \sim \omega_{de} \sim \omega_{*T} \sim \omega \sim k_\parallel v_{\text{th}i} \sim k_\parallel v_A \sim k_\perp u_\perp \sim \nu_{ii}, \tag{4.5}$$

which includes the magnetic drift frequencies

$$\omega_{di} \equiv \frac{k_y \rho_i v_{\text{th}i}}{2L_B}, \quad \omega_{de} \equiv \frac{k_y \rho_e v_{\text{th}e}}{2L_B}, \tag{4.6}$$

the diamagnetic frequency of ions

$$\omega_{*T} \equiv \frac{k_y \rho_i v_{\text{th}i}}{2L_T}, \tag{4.7}$$

the Alfvén speed

$$v_A = \frac{B}{\sqrt{4\pi n_i m_i}} = \frac{v_{\mathrm{th}i}}{\sqrt{\beta_i}}, \tag{4.8}$$

the $\boldsymbol{E}\times\boldsymbol{B}$ advection speed

$$u_\perp = \frac{c|\nabla_\perp \phi|}{B}, \tag{4.9}$$

and ν_{ii} is the ion-ion collision frequency. The resulting equation for h_e, valid up to first order in $\sqrt{m_e/m_i}$, is

$$\begin{aligned}\underbrace{\frac{\partial h_e}{\partial t}}_{1} + \underbrace{v_\parallel \frac{\partial h_e}{\partial z}}_{0} + \underbrace{\frac{1}{\Omega_e}\left(\frac{v_\parallel^2}{R} + \frac{v_\perp^2}{2L_B}\right)\frac{\partial h_e}{\partial y}}_{1} + \frac{c}{B}\left\{\underbrace{\phi\left(\boldsymbol{R}_e\right)}_{1} - \underbrace{\frac{v_\parallel A_\parallel\left(\boldsymbol{R}_e\right)}{c}}_{0} - \underbrace{\frac{T_e v_\perp^2 B_\parallel\left(\boldsymbol{R}_e\right)}{e v_{\mathrm{th}e}^2 B}}_{1}, h_e\right\} \\ = -\frac{e}{T_e}\frac{\partial}{\partial t}\left(\underbrace{\phi\left(\boldsymbol{R}_e\right)}_{1} - \underbrace{\frac{v_\parallel A_\parallel\left(\boldsymbol{R}_e\right)}{c}}_{0} - \underbrace{\frac{T_e v_\perp^2 B_\parallel\left(\boldsymbol{R}_e\right)}{e v_{\mathrm{th}e}^2 B}}_{1}\right) F_e + \underbrace{\left\langle C\left[h_e\right]\right\rangle_{\boldsymbol{R}_e}}_{0},\end{aligned} \tag{4.10}$$

where the number below each term indicates its order in $\sqrt{m_e/m_i}$ relative to the parallel streaming term $v_\parallel \partial h_e/\partial z$, which is ordered as $(v_{\mathrm{th}e}/L_B)h_e$, and we have used the fact that $\langle\chi\rangle_{\boldsymbol{R}_e} \approx \chi(\boldsymbol{R}_e)$ to the order considered. Notice that the electron-electron collision frequency, ν_{ee}, is of order $v_{\mathrm{th}e}/L_B$. This is because, according to (4.5),

$$\frac{v_{\mathrm{th}e}}{L_B}\sqrt{\frac{m_e}{m_i}} \sim \frac{v_{\mathrm{th}i}}{L_B} \sim \nu_{ii} \sim \sqrt{\frac{m_e}{m_i}}\nu_{ee}. \tag{4.11}$$

The $A_\parallel$ contribution to $\chi(\boldsymbol{R}_e)$ is larger compared to that of ϕ since

$$\frac{v_{\mathrm{th}e}A_\parallel}{\phi c} \sim \frac{v_{\mathrm{th}i}A_\parallel}{\phi c}\sqrt{\frac{m_i}{m_e}} \sim \frac{v_{\mathrm{th}i}}{u_\perp}\frac{\delta B_\perp}{B}\sqrt{\frac{m_i}{m_e}} \sim \frac{k_\perp}{k_\parallel}\frac{\delta B_\perp}{B}\sqrt{\frac{m_i}{m_e}} \sim \sqrt{\frac{m_i}{m_e}}, \tag{4.12}$$

where we have used (4.5) and the gyrokinetic ordering (1.16). The $B_\parallel$ contribution, on the other hand, is comparable to that of ϕ:

$$\frac{B_\parallel}{B}\frac{T_e}{e\phi} \sim \frac{B_\parallel}{B}\frac{k_\perp \rho_e v_{\mathrm{th}e}}{u_\perp} \sim \frac{B_\parallel}{B}\frac{k_\perp \rho_i v_{\mathrm{th}i}}{u_\perp} \sim 1, \tag{4.13}$$

where we have again used (4.5) and (1.16).

We next expand $h_e = h_e^{(0)} + h_e^{(1)} + \cdots$, with $h_e^{(j+1)}/h_e^{(j)} \sim \sqrt{m_e/m_i}$. The lowest-order electron gyrokinetic equation is then

$$v_\parallel \frac{\partial h_e^{(0)}(\boldsymbol{r})}{\partial z} - \frac{v_\parallel}{B}\left\{A_\parallel, h_e^{(0)}\left(\boldsymbol{r}\right)\right\} = \frac{v_\parallel}{c}\frac{e}{T_e}\frac{\partial A_\parallel}{\partial t}F_e + C\left[h_e^{(0)}(\boldsymbol{r})\right]. \tag{4.14}$$

This equation constrains $h_e^{(0)}(\boldsymbol{r})$ to be a Maxwellian velocity distribution. To demonstrate this, we first note that the second term on the left-hand side of (4.14) is $v_\parallel(\delta\boldsymbol{B}_\perp/B)\cdot\nabla h_e^{(0)}(\boldsymbol{r})$, with $\nabla = \partial/\partial\boldsymbol{r} \approx \partial/\partial\boldsymbol{R}_e$. The left-hand side of (4.14) can then be written as an exact divergence:

$$\nabla\cdot\left[\tilde{\boldsymbol{B}}v_\parallel h_e^{(0)}(\boldsymbol{r})\right] = \frac{v_\parallel}{c}\frac{e}{T_e}\frac{\partial A_\parallel}{\partial t}F_e + C\left[h_e^{(0)}(\boldsymbol{r})\right], \tag{4.15}$$

where $\tilde{\boldsymbol{B}} = B\hat{\boldsymbol{z}} + \delta\boldsymbol{B}_\perp$ is the exact magnetic field, including both the equilibrium and the fluctuation, and we have used $\nabla\cdot\tilde{\boldsymbol{B}} = 0$. The divergence term is then eliminated by multiplying (4.15) by $h_e^{(0)}(\boldsymbol{r})/F_e$ and integrating over the $(\boldsymbol{r},\boldsymbol{v})$ phase space[1]. The resulting equation is

$$\frac{n_e e}{cT_e}\int \mathrm{d}^3\boldsymbol{r}\,\frac{\partial A_\parallel}{\partial t}u_{\parallel e}^{(0)} + \int \mathrm{d}^3\boldsymbol{v}d^3\boldsymbol{r}\,C\left[h_e^{(0)}(\boldsymbol{r})\right]\frac{h_e^{(0)}(\boldsymbol{r})}{F_e} = 0, \tag{4.16}$$

where $u_{\parallel e}^{(0)} = (1/n_e)\int d^3\boldsymbol{v}\,v_\parallel h_e^{(0)}(\boldsymbol{r})$ is the the lowest-order parallel flow for the electrons. The size of $u_{\parallel e}^{(0)}$ is constrained by parallel Ampère's law (1.26),

$$\nabla_\perp^2 A_\parallel = -\frac{4\pi e n_e}{c}\left(u_{\parallel i} - u_{\parallel e}\right), \tag{4.17}$$

where $u_{\parallel i} = (1/n_i)\int d^3\boldsymbol{v}\,v_\parallel\left\langle h_i\right\rangle_{\boldsymbol{r}} \sim \rho_* v_{\mathrm{th}i} \ll u_{\parallel e}^{(0)} \sim \rho_* v_{\mathrm{th}e}$, so $u_{\parallel i}$ can be dropped. So can $\nabla_\perp^2 A_\parallel$ because:

$$\frac{k_\perp^2 A_\parallel c}{4\pi e n_e u_{\parallel e}^{(0)}} \sim k_\perp\rho_i\frac{\delta B_\perp}{B\rho^*}\frac{1}{\beta_i}\sqrt{\frac{\tau m_e}{m_i}} \sim \sqrt{\frac{m_e}{m_i}}. \tag{4.18}$$

Thus, as no term in (4.17) can balance the $u_{\parallel e}$ term to lowest order, $u_{\parallel e}^{(0)} = 0$ and $u_{\parallel e} \approx u_{\parallel e}^{(1)} \sim \rho_* v_{\mathrm{th}i}$. Using this result in (4.16) gives us

$$0 = \int d^3\boldsymbol{v}\mathrm{d}^3\boldsymbol{r}\,C\left[h_e^{(0)}(\boldsymbol{r})\right]\frac{h_e^{(0)}(\boldsymbol{r})}{F_e}, \tag{4.19}$$

whence, according to Boltzmann's H-Theorem, $h_e^{(0)}(\boldsymbol{r})$ is a perturbed Maxwellian (with no mean flow to lowest order):

$$h_e^{(0)}(\boldsymbol{r}) = \left[\frac{\delta n_e}{n_e} - \frac{e\phi}{T_e} + \left(\frac{v^2}{v_{\mathrm{the}}^2} - \frac{3}{2}\right)\frac{\delta T_e}{T_e}\right]F_e, \tag{4.20}$$

where δn_e and δT_e are the electron density and temperature fluctuations, respectively.

[1] Note that the integral over the domain perpendicular to the mean magnetic field is defined so that the extent in both x and y coordinates, denoted l_x and l_y, respectively, satisfies $\rho_i \ll l_x,\, l_y \ll L$.

Substituting (4.20) back into (4.14), we obtain

$$\nabla_\parallel \left[\frac{\delta n_e}{n_e} - \frac{e\phi}{T_e} + \left(\frac{v^2}{v_{\mathrm{th}e}^2} - \frac{3}{2} \right) \frac{\delta T_e}{T_e} \right] = \frac{e}{T_e c} \frac{\partial A_\parallel}{\partial t}. \tag{4.21}$$

The operator $\nabla_\parallel(\cdots) = \partial(\cdots)/\partial z - (1/B)\left\{A_\parallel, (\cdots)\right\}$ is the derivative taken along the exact field line. Since (4.21) holds true for all v, we can split it into two separate equations:

$$\nabla_\parallel \left(\frac{\delta n_e}{n_e} - \frac{e\phi}{T_e} \right) = \frac{e}{T_e c} \frac{\partial A_\parallel}{\partial t}, \tag{4.22}$$

and

$$\nabla_\parallel \delta T_e = 0. \tag{4.23}$$

Since $\delta T_e = 0$ is a solution of (4.23), and we have assumed that there are no mean electron temperature or density gradients, δT_e will be set to zero from here onwards, i.e., the electrons are isothermal. The other equation that we have derived, (4.22), determines $A_\parallel$ via what is readily recognised as the parallel force balance between the electric field and the electron pressure gradient.

Let us now take the density moment of (4.10), working to lowest order in $\sqrt{m_e/m_i}$ (i.e., ignoring electron FLR corrections):

$$\frac{\mathrm{d}}{\mathrm{d}t} \left(\frac{\delta n_e}{n_e} - \frac{B_\parallel}{B} \right) + \nabla_\parallel u_{\parallel e} + \frac{cT_e}{Be} \left\{ \frac{\delta n_e}{n_e}, \frac{B_\parallel}{B} \right\} + \frac{\rho_e v_{\mathrm{th}e}}{2} \left(\frac{1}{L_B} + \frac{1}{R} \right) \frac{\partial}{\partial y} \left(\frac{\delta n_e}{n_e} - \frac{e\phi}{T_e} \right) = 0, \tag{4.24}$$

which is regarded as the evolution equation for δn_e. The relationship between $\delta n_e/n_e$ and ϕ is set by the quasineutrality condition (1.24), which, using (4.20), can be written as

$$\frac{\delta n_e}{n_e} = -\frac{Ze\phi}{T_i} + \frac{1}{n_i} \int d^3\boldsymbol{v} \, \langle h_i \rangle_{\boldsymbol{r}}, \tag{4.25}$$

where h_i still needs to be calculated from the ion gyrokinetic equation. Using (4.20) also for the perpendicular Ampère's law (1.28), one finds

$$\frac{B_\parallel}{B} + \frac{\beta_e}{2} \frac{\delta n_e}{n_e} - \frac{\beta_e}{2} \frac{e\phi}{T_e} = -\frac{\beta_i}{2} \sum_{\boldsymbol{k}} e^{i\boldsymbol{k}\cdot\boldsymbol{r}} \frac{1}{n_i} \int \mathrm{d}^3\boldsymbol{v} \, \frac{2v_\perp^2}{v_{\mathrm{th}i}^2} \frac{J_1(a_i)}{a_i} h_{i,\boldsymbol{k}}. \tag{4.26}$$

Equations (4.17), (4.22) and (4.24)-(4.26), together with the ion gyrokinetic equation, form a closed set of equations for the fields $u_{\parallel e}$, $A_\parallel$, δn_e, ϕ, $B_\parallel$, and h_i.

4.1.2 Fluid ion closure

Orderings

We shall now derive a set of closed equations in which the ions are treated as a cold fluid. This is achieved by performing a subsidiary expansion in $\tau = T_i/ZT_e \ll 1$ and enforcing a collisional closure on the moment hierarchy. We restrict our consideration to the long-wavelength limit $k_\perp \rho_i \ll 1$, but retain finite sound radius: $k_\perp \rho_s \sim 1 \gg \tau \sim k_\perp^2 \rho_i^2$, where $\rho_s = \rho_i/\sqrt{2\tau} \gg \rho_i$. This is necessary to capture the peak of the ITG mode growth rate.

For now, we retain finite-β_e effects by adopting the minimal ordering $\beta_e \sim 1$, which we will relax in Subsection 4.1.3. Because the ions are cold, $\beta_i = \tau\beta_e \ll 1$. For clarity, we gather the ordering assumptions here:

$$\sqrt{\frac{m_e}{m_i}} \ll \beta_i \sim k_\perp^2 \rho_i^2 \sim \tau \sim \frac{L_T}{L_B} \ll \beta_e \sim 1, \tag{4.27}$$

So our system is also strongly driven ($L_T \ll L_B$). The various frequencies present in the system are therefore ordered as

$$\frac{1}{\tau}\omega_{di} \sim \omega_{de} \sim \omega_{*T} \sim \omega \sim k_\parallel \frac{v_{\mathrm{th}i}}{\sqrt{\tau}} \sim k_\parallel v_A \sim k_\parallel c_s \sim k_\perp u_\perp \sim \nu_{ii}\tau, \tag{4.28}$$

where

$$c_s = \sqrt{\frac{ZT_e}{m_i}} = v_A\sqrt{\frac{\beta_e}{2}}, \tag{4.29}$$

and the fluctuations satisfy

$$\tau\frac{Ze\phi}{T_i} \sim \tau\frac{\delta T_i}{T_i} \sim \frac{\delta n_e}{n_e} = \frac{\delta n_i}{n_i} \sim \frac{k_\perp A_\parallel}{B} \sim \frac{B_\parallel}{B} \sim \sqrt{\tau}\frac{u_{\parallel i}}{v_{\mathrm{th}i}}, \tag{4.30}$$

where δn_i and δT_i are the ion density and temperature fluctuations, respectively. Note in (4.30) that $B_\parallel \sim k_\perp A_\parallel$, consistent with $\beta_e \sim 1$. The ordering ansatz (4.30) for the fluctuations will be verified as consistent a posteriori.

Expansion of the ion gyrokinetic equation

We now expand the ion distribution function as

$$h_i = h_i^{(-1)} + h_i^{(0)} + h_i^{(1)} + \cdots, \tag{4.31}$$

with $h_i^{j+1}/h_i^j \sim \sqrt{\tau}$, and order all terms in the ion gyrokinetic equation:

$$
\begin{aligned}
&\frac{\partial}{\partial t}\left[\underbrace{h_i^{(-1)}}_{-1}+\underbrace{h_i^{(0)}}_{0}+\underbrace{h_i^{(1)}}_{1}\right]+v_\parallel\frac{\partial}{\partial z}\left[\underbrace{h_i^{(-1)}}_{0}+\underbrace{h_i^{(0)}}_{1}\right]-\underbrace{\frac{1}{\Omega_i}\left(\frac{v_\parallel^2}{R}+\frac{v_\perp^2}{2L_B}\right)\frac{\partial h_i^{(-1)}}{\partial y}}_{1}\\
&+\frac{c}{B}\left\{\langle\phi\rangle_{\boldsymbol{R}_i},\underbrace{h_i^{(-1)}}_{-1}+\underbrace{h_i^{(0)}}_{0}+\underbrace{h_i^{(1)}}_{1}\right\}+\frac{c}{B}\left\{\left\langle\frac{-v_\parallel A_\parallel}{c}\right\rangle_{\boldsymbol{R}_i},\underbrace{h_i^{(-1)}}_{0}+\underbrace{h_i^{(0)}}_{1}\right\}\\
&+\underbrace{\frac{c}{B}\left\{\left\langle\frac{-\boldsymbol{v}_\perp\cdot\boldsymbol{A}_\perp}{c}\right\rangle_{\boldsymbol{R}_i},h_i^{(-1)}\right\}}_{1}+\left(\frac{v^2}{v_{\mathrm{th}i}^2}-\frac{3}{2}\right)\frac{c}{B}\frac{\partial}{\partial y}\left[\underbrace{\langle\phi\rangle_{\boldsymbol{R}_i}}_{-1}+\underbrace{\left\langle\frac{-v_\parallel A_\parallel}{c}\right\rangle_{\boldsymbol{R}_i}}_{0}\right.\\
&\left.+\underbrace{\left\langle\frac{-\boldsymbol{v}_\perp\cdot\boldsymbol{A}_\perp}{c}\right\rangle_{\boldsymbol{R}_i}}_{1}\right]\frac{F_i}{L_T}=\frac{Ze}{T_i}F_i\frac{\partial}{\partial t}\left[\underbrace{\langle\phi\rangle_{\boldsymbol{R}_i}}_{-1}+\underbrace{\left\langle\frac{-v_\parallel A_\parallel}{c}\right\rangle_{\boldsymbol{R}_i}}_{0}+\underbrace{\left\langle\frac{-\boldsymbol{v}_\perp\cdot\boldsymbol{A}_\perp}{c}\right\rangle_{\boldsymbol{R}_i}}_{1}\right]\\
&+\left\langle C\left[\underbrace{h_i^{(-1)}}_{-3}+\underbrace{h_i^{(0)}}_{-2}+\underbrace{h_i^{(1)}}_{-1}+\underbrace{h_i^{(2)}}_{0}+\underbrace{h_i^{(3)}}_{1}\right]\right\rangle_{\boldsymbol{R}_i}, \qquad (4.32)
\end{aligned}
$$

where the number below each term indicates its order in $\sqrt{\tau}$ relative to $v_{\mathrm{th}i}h_i^{(-1)}/L_B$. Note that the electromagnetic-field terms contain contributions at multiple different orders in $\sqrt{\tau}$ due to the presence of gyroaverages: e.g., $\langle\phi\rangle_{\boldsymbol{R}_i} = \phi(\boldsymbol{R}_i) + (\rho_i^2/2)\partial^2\phi(\boldsymbol{R}_i)/\partial\boldsymbol{R}_i^2 + \cdots = \phi(\boldsymbol{R}_i)(1+O[\tau])$. These contributions will be disentangled where necessary in the calculations that follow.

Because the collision frequency is ordered to be much larger than the fluctuation frequency ($\nu_{ii} \sim \omega\tau^{-1}$), both $h_i^{(-1)}$ and $h_i^{(0)}$ are constrained by (4.32) to be perturbed Maxwellians:

$$C\left[h_i^{(-1)}\right] = C\left[h_i^{(0)}\right] = 0, \qquad (4.33)$$

where the gyroaverages can be dropped to this order due to the fact that $k_\perp^2\rho_i^2 \sim \tau \ll 1$. It is thus useful to decompose h_i as

$$h_i = \left[\frac{Ze\phi(\boldsymbol{R}_i)}{T_i} + \frac{\delta n_i(\boldsymbol{R}_i)}{n_i} + \frac{2v_\parallel u_{\parallel i}(\boldsymbol{R}_i)}{v_{\mathrm{th}i}^2} + \left(\frac{v^2}{v_{\mathrm{th}i}^2}-\frac{3}{2}\right)\frac{\delta T_i(\boldsymbol{R}_i)}{T_i}\right]F_i(\boldsymbol{R}_i) + \cdots \qquad (4.34)$$

Using (4.30), we compare the sizes of each of the terms inside the square bracket of (4.34) to obtain expressions for $h_i^{(-1)}$, $h_i^{(0)}$ and $h_i^{(1)}$:

$$h_i^{(-1)} = \left[\frac{Ze\phi(\boldsymbol{R}_i)}{T_i} + \left(\frac{v^2}{v_{\mathrm{th}i}^2}-\frac{3}{2}\right)\frac{\delta T_i(\boldsymbol{R}_i)}{T_i}\right]F_i(\boldsymbol{R}_i), \qquad (4.35)$$

$$h_i^{(0)} = \frac{2v_\parallel u_{\parallel i}(\boldsymbol{R}_i)}{v_{\mathrm{th}i}^2}F_i(\boldsymbol{R}_i), \qquad (4.36)$$

and

$$h_i^{(1)} = \frac{\delta n_i\left(\boldsymbol{R}_i\right)}{n_i} F_i\left(\boldsymbol{R}_i\right) + \tilde{h}_i^{(1)}. \tag{4.37}$$

Note that we have included an additional contribution $\tilde{h}_i^{(1)}$ to $h_i^{(1)}$ because it is not constrained by (4.33) to be a perturbed Maxwellian.

Expansion of the field equations

We now demonstrate that the fields obtained by substituting (4.35)-(4.37) into Maxwell's equations are consistent with the ordering (4.30). We first consider the quasineutrality condition (4.25):

$$\frac{\delta n_e}{n_e} = -\frac{Ze\phi}{T_i} + \frac{1}{n_i}\int \mathrm{d}^3\boldsymbol{v}\left[1 + \frac{1}{4}\frac{v_\perp^2\rho_i^2}{v_{\mathrm{th}i}^2}\nabla_\perp^2 + O\left(\tau^2\right)\right] h_i^{(-1)}\left(\boldsymbol{r}\right) + \frac{1}{n_i}\int \mathrm{d}^3\boldsymbol{v}\, h_i^{(1)}\left(\boldsymbol{r}\right), \tag{4.38}$$

where we have expanded the Bessel function in $\left\langle h_i^{(-1)}\right\rangle_{\boldsymbol{r}}$ as follows:

$$\begin{aligned}\left\langle h_i^{(-1)}\right\rangle_{\boldsymbol{r}} &= \sum_{\boldsymbol{k}} e^{i\boldsymbol{k}\cdot\boldsymbol{r}} J_0(a_i) h_{i,\boldsymbol{k}}^{(-1)} = \left[\sum_{\boldsymbol{k}} e^{i\boldsymbol{k}\cdot\boldsymbol{r}}\left(1 - \frac{a_i^2}{4}\right) h_{i,\boldsymbol{k}}^{(-1)}\right] + O(\tau^2 h_i^{(-1)}) \\ &= \left(1 + \frac{1}{4}\frac{v_\perp^2\rho_i^2}{v_{\mathrm{th}i}^2}\nabla_\perp^2\right) h_i^{-1}(\boldsymbol{r}) + O\left(\tau^2 h_i^{(-1)}\right).\end{aligned} \tag{4.39}$$

Using expressions (4.35) and (4.37) for $h_i^{(-1)}$ and $h_i^{(1)}$ in (4.38) results in a constraint on $\tilde{h}_i^{(1)}$

$$\frac{1}{n_i}\int \mathrm{d}^3\boldsymbol{v}\,\tilde{h}_i^{(1)}\left(\boldsymbol{r}\right) = -\frac{1}{4}\rho_i^2\nabla_\perp^2\left(\frac{Ze\phi}{T_i} + \frac{\delta T_i}{T_i}\right). \tag{4.40}$$

The left-hand side of (4.40) is, according to (4.37), of size $\delta n_i/n_i$, and the right-hand side is of size $\tau(e\phi/T_i)$. This is consistent with the ordering (4.30).

Next, consider the parallel Ampère's law (4.17). Since $h_i^{(-1)}$ according to (4.35) has no $v_\parallel$ moment (to any order) and the $v_\parallel$ moment of $h_i^{(0)}$ according to (4.36) is $u_{\parallel i}$, (4.17) holds and confirms the relative ordering of $u_{\parallel i}$ and $A_\parallel$ in (4.30).

The relative size of $B_\parallel$ is determined from the perpendicular Ampère's law (4.26):

$$\begin{aligned}\frac{B_\parallel}{B} + \frac{\beta_e}{2}\frac{\delta n_e}{n_e} - \frac{\beta_e}{2}\frac{e\phi}{T_e} &= -\frac{\beta_i}{2}\sum_{\boldsymbol{k}} e^{i\boldsymbol{k}\cdot\boldsymbol{r}}\frac{1}{n_i}\int d^3\boldsymbol{v}\,\frac{2v_\perp^2}{v_{\mathrm{th}i}^2}\frac{J_1\left(a_i\right)}{a_i} h_{i\boldsymbol{k}}, \\ &\approx -\frac{\beta_i}{2}\int d^3\boldsymbol{v}\frac{v_\perp^2}{v_{\mathrm{th}i}^2} h_i^{(-1)}\left(\boldsymbol{r}\right),\end{aligned} \tag{4.41}$$

where we have used $J_1(a_i)/a_i = 1/2$ to lowest order, leading to

$$\frac{B_\parallel}{B} = -\frac{\beta_e}{2}\left(\tau\frac{\delta T_i}{T_i} + \frac{\delta n_e}{n_e}\right), \tag{4.42}$$

to lowest order in $\sqrt{\tau}$, which satisfies (4.30). This equation describes the balance between the magnetic and plasma pressure:

$$\begin{aligned}
\frac{\delta(B^2)}{8\pi} &= -\delta(n_i T_i) - \delta(n_e T_e) \\
\frac{B_\parallel}{B} &= -\frac{4\pi}{B^2}\left(\delta n_i T_i + n_i \delta T_i + \delta n_e T_e\right) \\
\frac{B_\parallel}{B} &= -\frac{\beta_i}{2}\left(\frac{\delta n_i}{n_i} + \frac{\delta T_i}{T_i}\right) - \frac{\beta_e}{2}\frac{\delta n_e}{n_e},
\end{aligned} \tag{4.43}$$

where we have used (4.23). Since the contribution from δn_i is smaller than that from δT_i by a factor of τ, this equation is reduced to (4.42).

Moments of the ion gyrokinetic equation

Let us now use (4.32) to derive the evolution equations for the moments of h_i. Consider first the density moment, i.e.,

$$\frac{1}{n_i}\int \mathrm{d}^3\boldsymbol{v}\, \langle\cdots\rangle_{\boldsymbol{r}}\,. \tag{4.44}$$

All terms in (4.32) that are odd in $v_\parallel$ will vanish upon velocity integration, so we need only consider the contributions even in $v_\parallel$:

$$\begin{aligned}
&\underbrace{\frac{\partial}{\partial t}\left[h_i^{(-1)} + h_i^{(1)}\right]}_{①} + \underbrace{v_\parallel \frac{\partial h_i^{(0)}}{\partial z}}_{②} + \underbrace{\frac{c}{B}\left\{\langle\phi\rangle_{\boldsymbol{R}_i}, h_i^{(-1)} + h_i^{(1)}\right\}}_{③} + \underbrace{\frac{c}{B}\left\{\left\langle\frac{-v_\parallel A_\parallel}{c}\right\rangle_{\boldsymbol{R}_i}, h_i^{(0)}\right\}}_{④} \\
&+ \underbrace{\frac{c}{B}\left\{\left\langle\frac{-\boldsymbol{v}_\perp\cdot\boldsymbol{A}_\perp}{c}\right\rangle_{\boldsymbol{R}_i}, h_i^{(-1)}\right\}}_{⑤} \underbrace{-\frac{1}{\Omega_i}\left(\frac{v_\parallel^2}{R} + \frac{v_\perp^2}{2L_B}\right)\frac{\partial h_i^{(-1)}}{\partial y}}_{⑥} \\
&+ \underbrace{\left(\frac{v^2}{v_{\mathrm{th}i}^2} - \frac{3}{2}\right)\frac{c}{B}\frac{\partial}{\partial y}\left[\langle\phi\rangle_{\boldsymbol{R}_i} + \left\langle\frac{-\boldsymbol{v}_\perp\cdot\boldsymbol{A}_\perp}{c}\right\rangle_{\boldsymbol{R}_i}\right]}_{⑦}\frac{F_i}{L_T} \\
&= \underbrace{\frac{Ze}{T_i}\frac{\partial}{\partial t}\left[\langle\phi\rangle_{\boldsymbol{R}_i} + \left\langle\frac{-\boldsymbol{v}_\perp\cdot\boldsymbol{A}_\perp}{c}\right\rangle_{\boldsymbol{R}_i}\right]F_i}_{⑧} + \left\langle C\left[h_i^{(-1)} + h_i^{(1)}\right]\right\rangle_{\boldsymbol{R}_i} + (\text{terms odd in } v_\parallel),
\end{aligned} \tag{4.45}$$

where we have kept the collisional term, which will contain non-zero FLR corrections to the order $\sqrt{\tau} v_{\mathrm{th}i} h_i / L_B$. The terms are of mixed orders at this point, but cancellations will occur upon taking the density moment so that all remaining terms will end up of the same order. Let us calculate the velocity integral of each term, keeping in mind that we only need to retain contributions to the lowest orders, up to first order ($\sim \sqrt{\tau} v_{\mathrm{th}i} h_i / L_B$).

Term ① :

$$\frac{\partial}{\partial t}\frac{1}{n_i}\int \mathrm{d}^3\boldsymbol{v}\,\left(h_i^{(-1)}+h_i^{(1)}\right)=\frac{\partial}{\partial t}\left(\frac{Ze\phi}{T_i}+\frac{\delta n_e}{n_e}\right), \tag{4.46}$$

which follows from (4.35), (4.37) and (4.38).

Term ② : as this term is first order in (4.32), we can safely ignore the ion FLR corrections: to lowest order,

$$\frac{\partial}{\partial z}\frac{1}{n_i}\int \mathrm{d}^3\boldsymbol{v}\,v_\parallel\left\langle h_i^{(0)}\right\rangle_{\boldsymbol{r}}=\frac{\partial}{\partial z}\frac{1}{n_i}\int \mathrm{d}^3\boldsymbol{v}\,v_\parallel h_i^{(0)}\left(\boldsymbol{r}\right)=\frac{\partial u_{\parallel i}}{\partial z}. \tag{4.47}$$

Term ③ : before calculating the velocity integral, let us write the Poisson bracket in Fourier space:

$$\begin{aligned}\left\{\langle\phi\rangle_{\boldsymbol{R}_i},h_i\right\}\approx\sum_{\boldsymbol{k},\boldsymbol{k}'}e^{i\boldsymbol{k}\cdot\boldsymbol{r}+i\boldsymbol{k}'\cdot\boldsymbol{r}}\left[-\hat{\boldsymbol{z}}\cdot\left(\boldsymbol{k}\times\boldsymbol{k}'\right)\right]\Bigg[1-\boldsymbol{k}\boldsymbol{k}':\boldsymbol{\rho}\boldsymbol{\rho}-\frac{\left(\boldsymbol{k}\cdot\boldsymbol{\rho}\right)^2}{2}-\frac{\left(\boldsymbol{k}'\cdot\boldsymbol{\rho}\right)^2}{2}\\-\frac{1}{4}\frac{v_\perp^2}{v_{\mathrm{th}i}}k_\perp^2\rho_i^2\Bigg]\phi_{\boldsymbol{k}}h_{i,\boldsymbol{k}'},\end{aligned} \tag{4.48}$$

where we have expanded $e^{i\boldsymbol{k}\cdot\boldsymbol{\rho}}$ and $J_0(a_i)$ in $k_\perp\rho_i\ll 1$ with $\boldsymbol{\rho}=\boldsymbol{r}-\boldsymbol{R}_i$. Since

$$\langle\boldsymbol{\rho}\rangle_{\boldsymbol{r}}=0,\quad \langle\boldsymbol{\rho}\boldsymbol{\rho}\rangle_{\boldsymbol{r}}=\frac{1}{2}\frac{v_\perp^2}{v_{\mathrm{th}i}^2}\rho_i^2\mathbf{I}, \tag{4.49}$$

where $\mathbf{I}$ stands for the identity matrix $\hat{\boldsymbol{x}}\hat{\boldsymbol{x}}+\hat{\boldsymbol{y}}\hat{\boldsymbol{y}}$, the gyroaverage of (4.48) at fixed $\boldsymbol{r}$ is

$$\begin{aligned}&\left\langle\left\{\langle\phi\rangle_{\boldsymbol{R}_i},h_i\right\}\right\rangle_{\boldsymbol{r}}\\&\approx\sum_{\boldsymbol{k},\boldsymbol{k}'}e^{i\boldsymbol{k}\cdot\boldsymbol{r}+i\boldsymbol{k}'\cdot\boldsymbol{r}}\left[-\hat{\boldsymbol{z}}\cdot\left(\boldsymbol{k}\times\boldsymbol{k}'\right)\right]\times\Bigg[1-\boldsymbol{k}\boldsymbol{k}':\left(\frac{1}{2}\frac{v_\perp^2}{v_{\mathrm{th}i}^2}\rho_i^2\mathbf{I}\right)-\boldsymbol{k}\boldsymbol{k}:\left(\frac{1}{4}\frac{v_\perp^2}{v_{\mathrm{th}i}^2}\rho_i^2\mathbf{I}\right)\\&-\boldsymbol{k}'\boldsymbol{k}':\left(\frac{1}{4}\frac{v_\perp^2}{v_{\mathrm{th}i}^2}\rho_i^2\mathbf{I}\right)-\frac{1}{4}\frac{v_\perp^2}{v_{\mathrm{th}i}^2}k_\perp^2\rho_i^2\Bigg]\phi_{\boldsymbol{k}}h_{i,\boldsymbol{k}'}\\&\approx\left\{\phi,h_i\left(\boldsymbol{r}\right)\right\}+\frac{1}{2}\frac{v_\perp^2}{v_{\mathrm{th}i}^2}\rho_i^2\nabla_\perp\cdot\left\{\nabla_\perp\phi,h_i\left(\boldsymbol{r}\right)\right\}+\frac{1}{4}\frac{v_\perp^2}{v_{\mathrm{th}i}^2}\rho_i^2\left\{\phi,\nabla_\perp^2h_i\left(\boldsymbol{r}\right)\right\}\\&\approx\left\{\phi,h_i^{(-1)}\left(\boldsymbol{r}\right)+h_i^{(1)}\left(\boldsymbol{r}\right)\right\}+\frac{1}{2}\frac{v_\perp^2}{v_{\mathrm{th}i}^2}\rho_i^2\nabla_\perp\cdot\left\{\nabla_\perp\phi,h_i^{(-1)}\left(\boldsymbol{r}\right)\right\}+\frac{1}{4}\frac{v_\perp^2}{v_{\mathrm{th}i}^2}\rho_i^2\left\{\phi,\nabla_\perp^2h_i^{(-1)}\left(\boldsymbol{r}\right)\right\}.\end{aligned} \tag{4.50}$$

Upon velocity integration, the first and last term of (4.50) can be combined to give

$\{\phi, \delta n_e/n_e\}$ according to (4.38). The density moment of the ϕ-nonlinearity is thus

$$\frac{1}{n_i}\int \mathrm{d}^3\boldsymbol{v} \left\langle \frac{c}{B}\left\{\langle\phi\rangle_{\boldsymbol{R}_i}, h_i^{(-1)} + h_i^{(1)}\right\}\right\rangle_{\boldsymbol{r}} \approx \frac{c}{B}\left\{\phi, \frac{\delta n_e}{n_e}\right\} + \frac{c}{B}\frac{\rho_i^2}{2}\nabla_\perp \cdot \left\{\nabla_\perp\phi, \frac{\delta T_i}{T_i}\right\} + \frac{c}{B}\frac{\rho_i^2}{2}\left\{\nabla_\perp^2\phi, \frac{Ze\phi}{T_i}\right\}. \quad (4.51)$$

Term 4 : to lowest order,

$$\frac{1}{n_i}\int \mathrm{d}^3\boldsymbol{v} \left\langle \frac{c}{B}\left\{\left\langle\frac{-v_\parallel A_\parallel}{c}\right\rangle_{\boldsymbol{R}_i}, h_i^{(0)}(\boldsymbol{r})\right\}\right\rangle_{\boldsymbol{r}} \approx -\frac{1}{B}\left\{A_\parallel, \frac{1}{n_i}\int \mathrm{d}^3\boldsymbol{v}\, v_\parallel h_i^{(0)}(\boldsymbol{r})\right\} = -\frac{1}{B}\left\{A_\parallel, u_{\parallel i}\right\}, \quad (4.52)$$

where we used $\langle A_\parallel\rangle_{\boldsymbol{R}_i} = A_\parallel$ for $k_\perp\rho_i \ll 1$.
Term 5 : to lowest order,

$$\frac{1}{n_i}\int \mathrm{d}^3\boldsymbol{v} \left\langle \frac{c}{B}\left\{\left\langle\frac{-\boldsymbol{v}_\perp\cdot\boldsymbol{A}_\perp}{c}\right\rangle_{\boldsymbol{R}_i}, h_i^{(-1)}\right\}\right\rangle_{\boldsymbol{r}} \approx \frac{c}{B}\frac{T_i}{Ze}\left\{\frac{B_\parallel}{B}, \frac{1}{n_i}\int \mathrm{d}^3\boldsymbol{v}\,\frac{v_\perp^2}{v_{\mathrm{th}i}^2} h_i^{(-1)}(\boldsymbol{r})\right\} = \frac{c}{B}\frac{T_i}{Ze}\left\{\frac{B_\parallel}{B}, \frac{Ze\phi}{T_i} + \frac{\delta T_i}{T_i}\right\}, \quad (4.53)$$

where we used (4.35) and

$$\langle\boldsymbol{v}_\perp\cdot\boldsymbol{A}_\perp\rangle_{\boldsymbol{R}_i} \approx \frac{B_\parallel}{B}\frac{v_\perp^2}{v_{\mathrm{th}i}^2}\frac{T_i}{Ze} \quad (4.54)$$

for $k_\perp\rho_i \ll 1$.
Term 6 : to lowest order,

$$\frac{1}{n_i}\int \mathrm{d}^3\boldsymbol{v} \left\langle \frac{-1}{\Omega_i}\left(\frac{v_\parallel^2}{R} + \frac{v_\perp^2}{2L_B}\right)\frac{\partial h_i^{(-1)}}{\partial y}\right\rangle_{\boldsymbol{r}} = -\frac{v_{\mathrm{th}i}^2}{2\Omega_i}\left(\frac{1}{R} + \frac{1}{L_B}\right)\frac{\partial}{\partial y}\left(\frac{Ze\phi}{T_i} + \frac{\delta T_i}{T_i}\right), \quad (4.55)$$

where we have used (4.35), $\hat{\boldsymbol{x}}\times\hat{\boldsymbol{y}} = \hat{\boldsymbol{z}}$ and the expression for the magnetic curvature $\hat{\boldsymbol{z}}\cdot\nabla\hat{\boldsymbol{z}} = -\hat{\boldsymbol{x}}/R$.
Term 7 : the lowest order expressions for $\langle\phi\rangle_{\boldsymbol{R}_i}$ and $\langle\boldsymbol{v}_\perp\cdot\boldsymbol{A}_\perp\rangle_{\boldsymbol{R}_i}$ are ϕ and (4.54), respectively. However, we have to retain the next order correction for $\langle\phi\rangle_{\boldsymbol{R}_i}$, because its lowest-order contribution vanishes upon velocity integration. To obtain this correction,

we perform the double gyroaverage:

$$\left\langle \frac{\partial \langle \phi \rangle_{\boldsymbol{R}_i}}{\partial \boldsymbol{R}_i} \right\rangle_{\boldsymbol{r}} = \left\langle \sum_{\boldsymbol{k}} i\boldsymbol{k} e^{i\boldsymbol{k}\cdot\boldsymbol{R}_i} J_0\left(k_\perp \rho_i \frac{v_\perp}{v_{\mathrm{th}i}}\right) \phi_{\boldsymbol{k}} \right\rangle_{\boldsymbol{r}}$$
$$\approx \sum_{\boldsymbol{k}} i\boldsymbol{k} \left\langle e^{i\boldsymbol{k}\cdot\boldsymbol{r}} \left(1 - i\boldsymbol{k}\cdot\boldsymbol{\rho} - \frac{1}{2}\boldsymbol{k}\boldsymbol{k} : \boldsymbol{\rho}\boldsymbol{\rho}\right) \right\rangle_{\boldsymbol{r}} \times \left(1 - \frac{k_\perp^2 \rho_i^2}{4} \frac{v_\perp^2}{v_{\mathrm{th}i}^2}\right) \phi_{\boldsymbol{k}}$$
$$\approx \nabla\phi + \frac{\rho_i^2}{2} \frac{v_\perp^2}{v_{\mathrm{th}i}^2} \nabla\nabla_\perp^2 \phi, \tag{4.56}$$

where we have expanded $e^{i\boldsymbol{k}\cdot\boldsymbol{\rho}}$ and J_0 in $k_\perp \rho_i \ll 1$ and used (4.49). The density moment of 7 is thus

$$\frac{1}{n_i} \int \mathrm{d}^3\boldsymbol{v} \left\langle 7 \right\rangle_{\boldsymbol{r}} \approx \frac{cT_i}{BZe} \frac{1}{L_T} \frac{\partial}{\partial y} \left(\frac{\rho_i^2}{2} \nabla_\perp^2 \frac{Ze\phi}{T_i} + \frac{B_\parallel}{B} \right). \tag{4.57}$$

Term 8 : the treatment of this term is analogous to that of term 7:

$$\frac{1}{n_i} \int \mathrm{d}^3\boldsymbol{v} \left\langle 8 \right\rangle_{\boldsymbol{r}} \approx \frac{1}{n_i} \int \mathrm{d}^3\boldsymbol{v} \frac{\partial}{\partial t} \left[\frac{Ze\phi}{T_i} + \frac{\rho_i^2}{2} \frac{v_\perp^2}{v_{\mathrm{th}i}^2} \nabla_\perp^2 \frac{Ze\phi}{T_i} + \frac{v_\perp^2}{v_{\mathrm{th}i}^2} \frac{B_\parallel}{B} \right] F_i$$
$$= \frac{\partial}{\partial t} \left(\frac{Ze\phi}{T_i} + \frac{\rho_i^2}{2} \nabla_\perp^2 \frac{Ze\phi}{T_i} + \frac{B_\parallel}{B} \right), \tag{4.58}$$

where the double gyroaverage has been evaluated as in (4.56).

Collecting all eight of the terms (4.46), (4.47), (4.51), (4.52), (4.53), (4.55), (4.57), and (4.58), we obtain the density moment of (4.32) to first order in $\sqrt{\tau} v_{\mathrm{th}i} h_i / L_B$:

$$\frac{\mathrm{d}}{\mathrm{d}t} \left(\frac{\delta n_e}{n_e} - \frac{B_\parallel}{B} \right) + \nabla_\parallel u_{\parallel i} - \frac{d}{dt} \frac{1}{2} \rho_i^2 \nabla_\perp^2 \frac{Ze\phi}{T_i} + \frac{1}{4} \rho_i v_{\mathrm{th}i} \rho_i^2 \nabla_\perp \cdot \left\{ \nabla_\perp \phi, \frac{\delta T_i}{T_i} \right\}$$
$$+ \frac{1}{2} \rho_i v_{\mathrm{th}i} \left\{ \frac{B_\parallel}{B}, \frac{\delta T_i}{T_i} \right\} + \frac{\rho_i v_{\mathrm{th}i}}{2L_T} \frac{\partial}{\partial y} \left(\frac{B_\parallel}{B} + \frac{1}{2} \rho_i^2 \nabla_\perp^2 \frac{Ze\phi}{T_i} \right)$$
$$- \frac{\rho_i v_{\mathrm{th}i}}{2} \left(\frac{1}{L_B} + \frac{1}{R} \right) \frac{\partial}{\partial y} \left(\frac{Ze\phi}{T_i} + \frac{\delta T_i}{T_i} \right) = -\frac{1}{2} \chi \rho_i^2 \nabla_\perp^4 \left(a \frac{Ze\phi}{T_i} - b \frac{\delta T_i}{T_i} \right), \tag{4.59}$$

where

$$\chi = \frac{8}{9} \sqrt{\frac{2}{\pi}} \nu_{ii} \rho_i^2 \tag{4.60}$$

with $a = 9/40$ and $b = 67/160$. Note that we have changed the meaning of χ. The last term is the collisional contribution calculated from the Landau collision operator [Ivanov et al., 2020, Newton et al., 2010]. Taking the difference between (4.59) and the density moment (4.24) of the electron gyrokinetic equation and using (4.17), we obtain the evolution equation for the vorticity of the $\boldsymbol{E}\times\boldsymbol{B}$ flow:

$$
\begin{aligned}
&-\frac{\mathrm{d}}{\mathrm{d}t}\frac{1}{2}\rho_i^2\nabla_\perp^2\frac{Ze\phi}{T_i}-\nabla_\parallel\frac{c}{4\pi e n_e}\nabla_\perp^2 A_\parallel+\frac{1}{4}\rho_i v_{\mathrm{th}i}\rho_i^2\nabla_\perp\cdot\left\{\nabla_\perp\phi,\frac{\delta T_i}{T_i}\right\}\\
&+\frac{\rho_i v_{\mathrm{th}i}}{2L_T}\frac{\partial}{\partial y}\left(\frac{B_\parallel}{B}+\frac{1}{2}\rho_i^2\nabla_\perp^2\frac{Ze\phi}{T_i}\right)\\
&-\frac{\rho_i v_{\mathrm{th}i}}{2}\left(\frac{1}{L_B}+\frac{1}{R}\right)\frac{\partial}{\partial y}\left(\frac{1}{\tau}\frac{\delta n_e}{n_e}+\frac{\delta T_i}{T_i}\right)=-\frac{1}{2}\chi\rho_i^2\nabla_\perp^4\left(a\frac{Ze\phi}{T_i}-b\frac{\delta T_i}{T_i}\right).
\end{aligned}
\tag{4.61}
$$

We next take the $v_\parallel$ moment of (4.32), i.e.,

$$
\frac{1}{n_i}\int \mathrm{d}^3\boldsymbol{v}\,\frac{v_\parallel}{v_{\mathrm{th}i}}\left\langle\cdots\right\rangle_{\boldsymbol{r}}.
\tag{4.62}
$$

All terms that are even in $v_\parallel$ will vanish upon velocity integration, so we only need to consider contributions odd in $v_\parallel$:

$$
\begin{aligned}
&\frac{\partial h_i^{(0)}}{\partial t}+v_\parallel\frac{\partial h_i^{(0)}}{\partial z}+\frac{c}{B}\left\{\langle\phi\rangle_{\boldsymbol{R}_i},h_i^{(0)}\right\}+\frac{c}{B}\left\{\left\langle\frac{-v_\parallel A_\parallel}{c}\right\rangle_{\boldsymbol{R}_i},h_i^{(-1)}\right\}\\
&+\left(\frac{v^2}{v_{\mathrm{th}i}^2}-\frac{3}{2}\right)\frac{c}{B}\frac{\partial}{\partial y}\left\langle\frac{-v_\parallel A_\parallel}{c}\right\rangle_{\boldsymbol{R}_i}\frac{F_i}{L_T}=\frac{Ze}{T_i}\frac{\partial}{\partial t}\left\langle\frac{-v_\parallel A_\parallel}{c}\right\rangle_{\boldsymbol{R}_i}F_i+\left\langle C\left[h_i^{(0)}\right]\right\rangle_{\boldsymbol{R}_i}\\
&+\ (\text{terms even in } v_\parallel).
\end{aligned}
\tag{4.63}
$$

All the terms here are of the same order except for the collisional term. As a result, we can ignore all FLR corrections and evaluate everything at $\boldsymbol{r}$. The $v_\parallel$ integral then is

$$
\frac{\mathrm{d}}{\mathrm{d}t}\frac{u_{\parallel i}}{v_{\mathrm{th}i}}+\frac{v_{\mathrm{th}i}}{2}\nabla_\parallel\left(\frac{1}{\tau}\frac{\delta n_e}{n_e}+\frac{\delta T_i}{T_i}\right)-\frac{v_{\mathrm{th}i}}{2B}\frac{1}{L_T}\frac{\partial A_\parallel}{\partial y}=\frac{9}{10}\chi\nabla_\perp^2\frac{u_{\parallel i}}{v_{\mathrm{th}i}},
\tag{4.64}
$$

where we used (4.35) and (4.36). Using the fact that ion-ion collisions conserve momentum of the ions, the collisional term is then obtained by calculating the next order (in τ) contribution of the gyroaveraged collisional operator.

Finally, we obtain the evolution equation for δT_i by taking the temperature moment of (4.32), i.e.,

$$
\frac{1}{n_i}\int \mathrm{d}^3\boldsymbol{v}\,\frac{v^2}{v_{\mathrm{th}i}^2}\left\langle\cdots\right\rangle_{\boldsymbol{r}}.
\tag{4.65}
$$

We only need the terms involving $h_i^{(-1)}$ since all other terms are smaller by a factor of τ:

$$
\frac{\partial h_i^{(-1)}}{\partial t}+\frac{c}{B}\left\{\langle\phi\rangle_{\boldsymbol{R}_i},h_i^{(-1)}\right\}+\left(\frac{v^2}{v_{\mathrm{th}i}^2}-\frac{3}{2}\right)\frac{c}{B}\frac{\partial\langle\phi\rangle_{\boldsymbol{R}_i}}{\partial y}\frac{F_i}{L_T}=\frac{Ze}{T_i}\frac{\partial\langle\phi\rangle_{\boldsymbol{R}_i}}{\partial t}F_i+\left\langle C\left[h_i^{(-1)}\right]\right\rangle_{\boldsymbol{R}_i}.
\tag{4.66}
$$

All terms in (4.66) except the collisional term are again of the same size, so that the FLR corrections can be neglected. The result of taking the temperature moment is then

$$\frac{\mathrm{d}}{\mathrm{d}t}\frac{\delta T_i}{T_i} + \frac{\rho_i v_{\mathrm{th}i}}{2L_T}\frac{\partial}{\partial y}\frac{Ze\phi}{T_i} = \chi\nabla_\perp^2\frac{\delta T_i}{T_i}, \tag{4.67}$$

where we have used the energy conserving property of the ion-ion collisions and expanded the gyroaveraged collision operator in τ. The collisional contribution is then obtained from taking moment of the term that is next order in τ.

Summary of the fluid equations at $\beta_e \sim 1$

In summary, the fluid model that we have derived for the electromagnetic ITG turbulence in a Z-pinch consists of the following set of equations: the parallel electron force balance (4.22):

$$\nabla_\parallel\left(\frac{\delta n_e}{n_e} - \frac{e\phi}{T_e}\right) = \frac{e}{T_e c}\frac{\partial A_\parallel}{\partial t}, \tag{4.68}$$

the electron continuity equation (4.24):

$$\begin{aligned}\frac{\mathrm{d}}{\mathrm{d}t}\left(\frac{\delta n_e}{n_e} - \frac{B_\parallel}{B}\right) + \nabla_\parallel\left(u_{\parallel i} + \frac{c}{4\pi e n_e}\nabla_\perp^2 A_\parallel\right) + \frac{cT_e}{Be}\left\{\frac{\delta n_e}{n_e}, \frac{B_\parallel}{B}\right\}&\\ + \frac{\rho_e v_{\mathrm{th}e}}{2}\left(\frac{1}{L_B} + \frac{1}{R}\right)\frac{\partial}{\partial y}\left(\frac{\delta n_e}{n_e} - \frac{e\phi}{T_e}\right) = 0,&\end{aligned} \tag{4.69}$$

where we have used (4.17) to express $u_{\parallel e}$ in terms of $u_{\parallel i}$ and $A_\parallel$, the $\boldsymbol{E}\times\boldsymbol{B}$ vorticity equation (4.61):

$$\begin{aligned}&-\frac{\mathrm{d}}{\mathrm{d}t}\frac{1}{2}\rho_i^2\nabla_\perp^2\frac{Ze\phi}{T_i} - \nabla_\parallel\frac{c}{4\pi e n_e}\nabla_\perp^2 A_\parallel + \frac{1}{4}\rho_i v_{\mathrm{th}i}\rho_i^2\nabla_\perp\cdot\left\{\nabla_\perp\phi, \frac{\delta T_i}{T_i}\right\}\\ &+\frac{\rho_i v_{\mathrm{th}i}}{2L_T}\frac{\partial}{\partial y}\left(\frac{B_\parallel}{B} + \frac{1}{2}\rho_i^2\nabla_\perp^2\frac{Ze\phi}{T_i}\right)\\ &-\frac{\rho_i v_{\mathrm{th}i}}{2}\left(\frac{1}{L_B} + \frac{1}{R}\right)\frac{\partial}{\partial y}\left(\frac{1}{\tau}\frac{\delta n_e}{n_e} + \frac{\delta T_i}{T_i}\right) = -\frac{1}{2}\chi\rho_i^2\nabla_\perp^4\left(a\frac{Ze\phi}{T_i} - b\frac{\delta T_i}{T_i}\right),\end{aligned} \tag{4.70}$$

the parallel ion momentum equation (4.64):

$$\frac{\mathrm{d}}{\mathrm{d}t}\frac{u_{\parallel i}}{v_{\mathrm{th}i}} + \frac{v_{\mathrm{th}i}}{2}\nabla_\parallel\left(\frac{1}{\tau}\frac{\delta n_e}{n_e} + \frac{\delta T_i}{T_i}\right) - \frac{v_{\mathrm{th}i}}{2B}\frac{1}{L_T}\frac{\partial A_\parallel}{\partial y} = \frac{9}{10}\chi\nabla_\perp^2\left(\frac{u_{\parallel i}}{v_{\mathrm{th}i}}\right), \tag{4.71}$$

the ion temperature equation (4.67):

$$\frac{\mathrm{d}}{\mathrm{d}t}\frac{\delta T_i}{T_i} + \frac{\rho_i v_{\mathrm{th}i}}{2L_T}\frac{\partial}{\partial y}\frac{Ze\phi}{T_i} = \chi\nabla_\perp^2\frac{\delta T_i}{T_i} \tag{4.72}$$

and the pressure balance (4.42):

$$\frac{B_\parallel}{B} = -\frac{\beta_e}{2}\left(\tau\frac{\delta T_i}{T_i} + \frac{\delta n_e}{n_e}\right). \tag{4.73}$$

In the absence of equilibrium gradients, i.e., with $\delta T_i = 0$, these equations turn into the Hall reduced MHD system considered in Schekochihin et al. [2009].

4.1.3 Low-β_e limit

Low-β_e orderings and derivation

One may simplify the fluid model even further by filtering out the ion-sound physics, which can be achieved by taking $\beta_e \to 0$. One immediately see from (4.73) that $B_\parallel$ can be neglected in (4.69) and (4.70). We feel safe in doing so as the compressible component of magnetic perturbation, $B_\parallel$, does not appear to be a necessary ingredient for the non-zonal transitions of ITG turbulence [Pueschel et al., 2013b, Rath and Peeters, 2022] and indeed will prove not to be. To keep the physics of the ITG intability intact, we take β_e and β_i to be small simultaneously while holding $k_\perp\rho_i$ and τ fixed, so $k_\perp^2\rho_i^2/\tau \sim k_\perp^2\rho_s^2 \sim 1$ still holds. Hence, the ordering assumption (4.27) in the cold-ion expansion is modified to be

$$\sqrt{\frac{m_e}{m_i}} \ll \frac{L_T}{L_B} \sim \tau \sim k_\perp^2\rho_i^2 \ll \beta_e \ll 1 \sim k_\perp\rho_s. \tag{4.74}$$

Even though now $\beta_e \ll 1$, we shall still retain both Alfvén (electromagnetic effects) and ion diamagnetic (ITG drive) frequencies, which requires $\omega \sim \omega_{*T} \sim k_\parallel v_A$ and thus

$$k_\parallel \sim \frac{\omega_{*T}}{v_A} \sim \frac{\sqrt{\beta_e}}{L_B}. \tag{4.75}$$

Physically, this means that the Alfvén waves propagate faster at lower β_e, so the ITG fluctuations must have a correspondingly longer parallel extent if the Alfvén waves were to participate dynamically. Note that the ion-sound physics has been neglected due to $c_s/v_A \sim \sqrt{\beta_e} \ll 1$. Hence, the frequency ordering (4.28) introduced in the cold-ion expansion changes to, in the limit of $\beta_e \to 0$,

$$\frac{1}{\tau}\omega_{di} \sim \omega_{de} \sim \omega_{*T} \sim \omega \sim k_\parallel v_A \sim k_\perp u_\perp \sim \nu_{ii}\tau. \tag{4.76}$$

The resulting ordering of the fluctuations is:

$$\tau\frac{Ze\phi}{T_i} \sim \tau\frac{\delta T_i}{T_i} \sim \frac{\delta n_e}{n_e} = \frac{\delta n_i}{n_i} \sim \frac{1}{\sqrt{\beta_e}}\frac{k_\perp A_\parallel}{B} \sim \frac{u_{\parallel i}}{c_s}, \tag{4.77}$$

where we have used $c_s \sim v_{\mathrm{th}i}/\sqrt{\tau}$. Compared to (4.30), the new ordering (4.77) excludes $B_\parallel$ as it decouples from the other fields. In addition, $A_\parallel$ has been scaled down by a factor of $\sqrt{\beta_e}$. This is necessary for the inclusion of Alfvénic fluctuations, which can be understood by examining the following balance in (4.68):

$$\begin{aligned} k_\parallel \frac{e\phi}{T_e} \sim \frac{e}{T_e c}\omega A_\parallel &\longrightarrow \tau \frac{Ze\phi}{T_i} \sim \frac{e v_A}{T_e c} A_\parallel \sim \frac{v_A}{c_s}\frac{k_\perp A_\parallel}{B}, \\ &\longrightarrow \tau \frac{Ze\phi}{T_i} \sim \frac{1}{\sqrt{\beta_e}}\frac{k_\perp A_\parallel}{B}, \end{aligned} \tag{4.78}$$

where we have used $\omega \sim k_\parallel v_A$. According to (4.75) and (4.78), both $k_\parallel$ and $A_\parallel$ are scaled down by a factor of $\sqrt{\beta_e}$ relative to the orderings presented in the cold-ion expansion. This ensures that the relation $\nabla_\parallel \sim k_\parallel \sim k_\perp \delta B_\perp / B$ continues to hold. As a result, the electron force balance equation (4.68) remains unchanged in the limit $\beta_e \to 0$. The ion temperature equation (4.72) also remains unchanged in that limit, as the terms have no dependence on the size of $k_\parallel$, $A_\parallel$ and $u_{\parallel i}$.

Next, we will show that the sound waves decouple from the ITG and Alfvénic dynamics. Using (4.77), let us compare the size of the $u_{\parallel i}$ term with the $\mathrm{d}/\mathrm{d}t$ term in (4.69):

$$\frac{k_\parallel u_{\parallel i}}{\omega}\frac{n_e}{\delta n_e} \sim \sqrt{\beta_e}\frac{u_{\parallel i}}{c_s}\frac{n_e}{\delta n_e} \sim \sqrt{\beta_e}. \tag{4.79}$$

So, the $u_{\parallel i}$ term can be dropped. Indeed, due to the rescaling of $k_\parallel$ and $A_\parallel$, the parallel ion momentum equation (4.71) becomes, to lowest order in $\sqrt{\beta_e}$,

$$\frac{\mathrm{d}u_{\parallel i}}{\mathrm{d}t} = \frac{9}{10}\chi \nabla_\perp^2 u_{\parallel i}, \tag{4.80}$$

of which $u_{\parallel i} = 0$ is a solution. Thus, we can safely discard $u_{\parallel i}$ everywhere. On the other hand, the parallel current term of (4.69) needs to be kept because

$$\frac{c k_\parallel k_\perp^2 A_\parallel}{e n_e \omega}\frac{n_e}{\delta n_e} \sim \frac{c k_\perp B}{e n_e v_A}\frac{k_\perp A_\parallel}{B}\frac{n_e}{\delta n_e} \sim \frac{1}{\sqrt{\beta_e}}\frac{k_\perp A_\parallel}{B}\frac{n_e}{\delta n_e} \sim 1. \tag{4.81}$$

The electron density equation (4.69) then reduces to

$$\frac{\mathrm{d}}{\mathrm{d}t}\frac{\delta n_e}{n_e} + \nabla_\parallel \frac{c}{4\pi e n_e}\nabla_\perp^2 A_\parallel + \frac{\rho_e v_{\mathrm{th}e}}{L_B}\frac{\partial}{\partial y}\left(\frac{\delta n_e}{n_e} - \frac{e\phi}{T_e}\right) = 0, \tag{4.82}$$

where we have set $L_B = R$ using the constraint from the equilibrium force balance (1.8) at low beta.

Using $\tau Ze\phi/T_i \sim \delta n_e/n_e$, we can reduce the $\mathbf{E}\times\mathbf{B}$ vorticity equation (4.70) to its low-β_e form straightforwardly, yielding

$$-\frac{\mathrm{d}}{\mathrm{d}t}\frac{1}{2}\rho_i^2\nabla_\perp^2\frac{Ze\phi}{T_i}-\nabla_\parallel\frac{c}{4\pi e n_e}\nabla_\perp^2 A_\parallel+\frac{1}{4}\rho_i v_{\mathrm{th}i}\rho_i^2\nabla_\perp\cdot\left\{\nabla_\perp\frac{Ze\phi}{T_i},\frac{\delta T_i}{T_i}\right\}$$
$$+\frac{\rho_i v_{\mathrm{th}i}}{2L_T}\frac{\partial}{\partial y}\left(\frac{1}{2}\rho_i^2\nabla_\perp^2\frac{Ze\phi}{T_i}\right)-\frac{\rho_i v_{\mathrm{th}i}}{L_B}\frac{\partial}{\partial y}\left(\frac{1}{\tau}\frac{\delta n_e}{n_e}+\frac{\delta T_i}{T_i}\right)=-\frac{1}{2}\chi\rho_i^2\nabla_\perp^4\left(a\frac{Ze\phi}{T_i}-b\frac{\delta T_i}{T_i}\right). \tag{4.83}$$

Summary of the fluid equations at low-β_e

Let us now summarise the low-β_e equations below:

$$\nabla_\parallel\left(\frac{\delta n_e}{n_e}-\frac{e\phi}{T_e}\right)=\frac{e}{T_e c}\frac{\partial A_\parallel}{\partial t}, \tag{4.84}$$

$$\frac{\mathrm{d}}{\mathrm{d}t}\frac{\delta n_e}{n_e}+\nabla_\parallel\frac{c}{4\pi e n_e}\nabla_\perp^2 A_\parallel+\frac{\rho_e v_{\mathrm{th}e}}{L_B}\frac{\partial}{\partial y}\left(\frac{\delta n_e}{n_e}-\frac{e\phi}{T_e}\right)=0, \tag{4.85}$$

$$-\frac{\mathrm{d}}{\mathrm{d}t}\frac{1}{2}\rho_i^2\nabla_\perp^2\frac{Ze\phi}{T_i}-\nabla_\parallel\frac{c}{4\pi e n_e}\nabla_\perp^2 A_\parallel+\frac{1}{4}\rho_i v_{\mathrm{th}i}\rho_i^2\nabla_\perp\cdot\left\{\nabla_\perp\frac{Ze\phi}{T_i},\frac{\delta T_i}{T_i}\right\}$$
$$+\frac{\rho_i v_{\mathrm{th}i}}{2L_T}\frac{\partial}{\partial y}\left(\frac{1}{2}\rho_i^2\nabla_\perp^2\frac{Ze\phi}{T_i}\right)-\frac{\rho_i v_{\mathrm{th}i}}{L_B}\frac{\partial}{\partial y}\left(\frac{1}{\tau}\frac{\delta n_e}{n_e}+\frac{\delta T_i}{T_i}\right)=-\frac{1}{2}\chi\rho_i^2\nabla_\perp^4\left(a\frac{Ze\phi}{T_i}-b\frac{\delta T_i}{T_i}\right), \tag{4.86}$$

$$\frac{\mathrm{d}}{\mathrm{d}t}\frac{\delta T_i}{T_i}+\frac{\rho_i v_{\mathrm{th}i}}{2L_T}\frac{\partial}{\partial y}\frac{Ze\phi}{T_i}=\chi\nabla_\perp^2\frac{\delta T_i}{T_i}. \tag{4.87}$$

(4.84)-(4.87) form a closed system describing the evolution of the four fields $A_\parallel$, δn_e, ϕ, and δT_i. These equations simplify to those of reduced MHD in the limit of a homogeneous plasma in a slab at long perpendicular wavelengths, $k_\perp\rho_s \ll 1$, and also to the electrostatic ITG equations used by Ivanov et al. [2020] in the limit of short parallel wavelengths, which turns out to be equivalent to taking $\beta_e \to 0$ (see Subsection 4.1.5). Thus, they provide the desired bridge between electrostatic and electromagnetic ('finite-beta') turbulence.

Normalised equations

Before proceeding, we simplify the form of our equations by introducing a convenient set of normalisations, given in Tab. 4.1. Upon application of these normalisations, (4.84)-(4.87) reduce to

$$\frac{\partial A}{\partial t}=\nabla_\parallel\left(n-\varphi\right), \tag{4.88}$$

$$\frac{\mathrm{d}n}{\mathrm{d}t}+\nabla_\parallel\nabla_\perp^2 A-\frac{\partial\left(\varphi-n\right)}{\partial y}=0, \tag{4.89}$$

Table 4.1: Normalisations of fields, coordinates and parameters

variable	φ	A	T	$\hat{n}$	$\hat{t}$	$\hat{x}$	$\hat{y}$	$\hat{z}$	κ_T	$\hat{\chi}$
definition	$\frac{e\phi}{T_e}\frac{L_B}{2\rho_s}$	$\frac{A_\parallel}{\rho_s B\sqrt{2\beta_e}}\frac{L_B}{\rho_s}$	$\tau\frac{\delta T_i}{T_i}\frac{L_B}{2\rho_s}$	$\frac{\delta n_e}{n_e}\frac{L_B}{2\rho_s}$	$t\frac{2c_s}{L_B}$	$\frac{x}{\rho_s}$	$\frac{y}{\rho_s}$	$\sqrt{2\beta_e}\frac{z}{L_B}$	$\frac{\tau}{2}\frac{L_B}{L_T}$	$\frac{\chi}{2\rho_s^2}\frac{L_B}{c_s}$

$$-\frac{\mathrm{d}}{\mathrm{d}t}\nabla_\perp^2\varphi - \nabla_\parallel\nabla_\perp^2 A + \nabla_\perp\cdot\{\nabla_\perp\varphi, T\} + \kappa_T\frac{\partial}{\partial y}\nabla_\perp^2\varphi - \frac{\partial\,(n+T)}{\partial y} = -\chi\nabla_\perp^4\,(a\varphi - bT)\,, \tag{4.90}$$

$$\frac{\mathrm{d}T}{\mathrm{d}t} + \kappa_T\frac{\partial\varphi}{\partial y} = \chi\nabla_\perp^2 T, \tag{4.91}$$

where

$$\frac{\mathrm{d}f}{\mathrm{d}t} = \frac{\partial f}{\partial t} + \{\varphi, f\} \quad \text{and} \quad \nabla_\parallel f = \frac{\partial f}{\partial z} - \{A, f\} \tag{4.92}$$

are now defined with respect to the normalised coordinates. For notational simplicity, we have dropped the hats on the normalised quantities introduced in Tab. 4.1. In the following sections, we use the subscript 'phys' on unnormalised versions of these quantities to avoid confusion.

4.1.4 Parameters of the model

There are effectively five free parameters in the system (4.88)-(4.91): the normalised ion temperature gradient κ_T and collisionality χ, and the box lengths in the x, y, and z directions, denoted L_x, L_y and L_z, respectively. The box lengths L_x and L_y do not matter provided they are large enough that, for a given κ_T, there are well-defined turbulence outer scales in x and y that are smaller than the corresponding box scales (the outer scales depend on κ_T, so the limits $\kappa_T \to \infty$ and L_x,$L_y \to \infty$ do not commute, but we stay at $\kappa_T \sim 1$). We thus remove these two free parameters from our study. The box scale in z can be viewed as a proxy for β_e. This is evident from the definition of the normalised z as $\sqrt{2\beta_e}z_{\mathrm{phys}}/L_B$ and is a consequence of ordering the fluctuation frequency ω_{phys} to be comparable to both the diamagnetic frequency ω_{*T} and the Alfvén frequency $k_{\parallel,\mathrm{phys}}v_A$, as discussed in Subsection 4.1.3. It is important to draw a distinction between L_z, which is the normalised simulation-box size in z, and any physical scale $L_{z,\mathrm{phys}}$ that may exist in the system under consideration. In the case of a tokamak, $L_{z,\mathrm{phys}}$ could be the length of the field line within the bad-curvature region, where $L_{z,\mathrm{phys}} \sim \pi q R$. Thus, for a system where $L_{z,\mathrm{phys}}$ is fixed, the simulation-box size L_z should be regarded as a direct proxy for β_e.

4.1.5 The role of $k_\parallel$ and recovery of the electrostatic limit

As our aim is to capture the finite-β_e modification of the electrostatic ITG turbulence, let us demonstrate that our model recovers correctly the electrostatic limit, corresponding to $\beta_e \to 0$. As explained above, in our model, this is formally equivalent to taking $k_\parallel \to \infty$. Physically, this means that Alfvén waves are assumed fast compared to the drift modes, and thus any magnetic perturbation caused by the latter will be quickly radiated away by the former (a useful analogy is pressure perturbations in 'incompressible' hydrodynamics being quickly radiated away by fast sound waves).

The induction equation (4.88) reduces in this limit to $n' = \varphi'$, where the prime denotes the difference between the un-primed quantity and its flux-surface average: e.g., $\varphi' \equiv \varphi - \langle\varphi\rangle_{yz}$, where

$$\langle\varphi\rangle_{yz} \equiv \frac{1}{L_y L_z}\int \varphi \, dydz \tag{4.93}$$

is the zonal component of φ. In a true Z-pinch, field lines close on themselves, so that a field-line average is not equivalent to a flux-surface average, but we have assumed the presence of an infinitesimal pitch angle for the magnetic field, to recover the equivalence of the two averages.

In the electrostatic limit, there is no generation of zonal density $\langle n\rangle_{yz}$ by our equations, as seen by taking the flux-surface average of (4.89):

$$\frac{\partial \langle n\rangle_{yz}}{\partial t} + \langle\{\varphi', n'\}\rangle_{yz} - \left\langle\left\{A', \nabla_\perp^2 A'\right\}\right\rangle_{yz} = 0, \tag{4.94}$$

where the nonlinear drive for $\langle n\rangle_{yz}$ vanishes as $A' \to 0$ and $n' \to \varphi'$. We thus recover the familiar modified Boltzmann response for electrons [Hammett et al., 1993, Rogers et al., 2000]:

$$n = n' = \varphi'. \tag{4.95}$$

Alert readers may wonder how the system of equations (4.88)–(4.91) self-consistently yields $A \to 0$ as $k_z \to \infty$. To see this, first note that the current terms involving A in (4.89) and (4.90) are essential for enforcing $n = \varphi'$. Without these A dependent terms, n and φ would be determined by two independent evolution equations and would therefore not be constrained to coincide. When the A-terms are retained, however, the limit $k_z \to \infty$ drives $n \to \varphi$ according to (4.88). The small correction between them generates a correspondingly A, which is then fed back into the evolution equations for n (4.89) and for φ (4.90). In this way, the system self-consistently forces n and φ to converge. Therefore, the A dependent terms are crucial and must balance with other terms in the equations, i.e., $\omega n \sim k_z k_\perp^2 A$ in (4.89). Since the balance holds as $k_z \to \infty$, A must tend to zero in this limit.

Using (4.95) and adding (4.90) to (4.89) results in a two-field set of equations for φ

and T in the electrostatic limit:

$$\frac{\mathrm{d}}{\mathrm{d}t}\left(\varphi' - \nabla_\perp^2\varphi\right) + \nabla_\perp \cdot \{\nabla_\perp\varphi, T\} + \kappa_T \frac{\partial}{\partial y}\nabla_\perp^2\varphi - \frac{\partial\left(\varphi + T\right)}{\partial y} = -\chi\nabla_\perp^4\left(a\varphi - bT\right), \quad (4.96)$$

$$\frac{\mathrm{d}T}{\mathrm{d}t} + \kappa_T\frac{\partial\varphi}{\partial y} = \chi\nabla_\perp^2 T. \quad (4.97)$$

These are the equations derived by Ivanov et al. [2020] to study two-dimensional, electrostatic ITG turbulence. The three-dimensional physics of electrostatic ITG modes described in Ivanov et al. [2022] are absent, as these require $k_{\parallel,\mathrm{phys}}L_B \sim 1$, whereas in our model, $k_{\parallel,\mathrm{phys}}L_B \sim \sqrt{\beta_e} \ll 1$. Thus, physically, the limit of two-dimensianl, electrostatic ITG turbulence corresponds to parallel wave numbers satisfying $\sqrt{\beta_e} \ll k_{\parallel,\mathrm{phys}}L_B \ll 1$. In Ivanov et al. [2020], this turbulence, and, in particular, the transition from low to high transport in it, was studied as a function of κ_T and χ. The addition of the parameter L_z in our model, as explained above, gives us the ability to study this transition as a function of β_e.

4.2 Linear instabilities

Let us first consider infinitesimal perturbations of the four fields n, T, φ, and A of the form, e.g., $n\left(\boldsymbol{r}, t\right) = \tilde{n}_{\boldsymbol{k}} \exp\left(-i\omega t + i\boldsymbol{k}\cdot\boldsymbol{r}\right)$ and neglect all nonlinear terms. Dropping tildes and subscripts on Fourier coefficients for notational simplicity, the linearised versions of (4.88)-(4.91) are

$$-i\omega A = ik_z\left(n - \varphi\right), \quad (4.98)$$

$$-i\omega n - ik_z k_\perp^2 A - ik_y\left(\varphi - n\right) = 0, \quad (4.99)$$

$$-i\omega k_\perp^2\varphi + ik_z k_\perp^2 A - i\kappa_T k_y k_\perp^2\varphi - ik_y\left(n + T\right) = -\chi k_\perp^4\left(a\varphi - bT\right), \quad (4.100)$$

$$-i\omega T + i\kappa_T k_y\varphi = -\chi k_\perp^2 T. \quad (4.101)$$

In Subsections 4.2.1-4.2.4, we consider various limits in which a relatively simple, closed-form analytical solution is obtainable. In particular, we demonstrate that our equations contain the physics needed to describe the curvature ITG instability in the electrostatic limit, its stabilisation with increasing β_e, and the excitation of unstable MHD interchange (IC) modes at high β_e. Numerical solutions of the full set of linearised equations are presented in Subsection 4.2.5.

4.2.1 Straight-field (high-frequency) limit: Alfvénic modes

Consider first the limit of straight field, usually studied in the astrophysical and space-physical contexts [Schekochihin et al., 2009]. This is formally recovered as $L_B \to \infty$, or, in terms of normalised quantities, $\omega \sim k_z \gg k_\perp \sim 1$, $\kappa_T \sim \chi \sim 1$, and $A \sim \varphi \sim n \sim T$. With these orderings, (4.98)-(4.101) reduce to

$$-i\omega A = ik_z\left(n - \varphi\right), \tag{4.102}$$

$$-i\omega n - ik_z k_\perp^2 A = 0, \tag{4.103}$$

$$-i\omega k_\perp^2 \varphi + ik_z k_\perp^2 A = 0, \tag{4.104}$$

$$-i\omega T = 0. \tag{4.105}$$

The non-zero solutions for ω are

$$\omega = \pm k_z\sqrt{1 + k_\perp^2}, \tag{4.106}$$

with corresponding eigenvectors

$$A = \pm\varphi\sqrt{1 + k_\perp^2}, \quad n = -\varphi k_\perp^2, \quad T = 0. \tag{4.107}$$

In the MHD limit $k_\perp \to 0$, we have $\omega \to \pm k_z$, and $A \to \pm\varphi$, $n = 0$, recovering the Alfvén waves:

$$\omega_{\text{phys}} = \pm k_{z,\text{phys}} v_A. \tag{4.108}$$

In the opposite limit of $k_\perp \gg 1$, we have $\omega \approx \pm k_z k_\perp$, or

$$\omega_{\text{phys}} = \pm k_{\perp,\text{phys}} \rho_s k_{z,\text{phys}} v_A, \tag{4.109}$$

which is the dispersion relation for kinetic Alfvén waves in the cold ion, low-β_e limit [Schekochihin et al., 2009]. Nonlinearly, in this limit, if energy were injected at large scales ($k_\perp \ll 1$), our equations would support a standard MHD Alfvénic cascade towards $k_\perp \sim 1$ and a kinetic Alfvénic wave cascade at $k_\perp \gtrsim 1$ [Schekochihin et al., 2009, Schekochihin et al., 2019] – a classic outcome for a low-beta solar wind. This is not a relevant limit for a fusion device.

4.2.2 Electrostatic (low-frequency) limit: curvature-ITG instability

If we allow magnetic field to be curved, but still take $k_z \gg k_\perp \sim 1$, this time as $\beta_e \to 0$, we order $\omega \sim 1$. As anticipated by the discussion at the end of Subsection 4.1.5, (4.98) then gives us the Boltzmann electron response, $n = \varphi$. We may now eliminate A (which is now a spectator quantity) by summing (4.99) and (4.100), and, together with (4.101), we obtain an electrostatic system:

$$-i\omega(1+k_\perp^2)\varphi - i\kappa_T k_y k_\perp^2\varphi - ik_y(\varphi+T) = -\chi k_\perp^4(a\varphi - bT), \tag{4.110}$$

$$-i\omega T + i\kappa_T k_y\varphi = -\chi k_\perp^2 T. \tag{4.111}$$

In the large-gradient, long-wavelength limit, $\kappa_T k_y \gg 1 \gg \kappa_T k_y k_\perp^2$, the FLR terms (those containing powers of $k_\perp^2$) are negligible and $T \gg \varphi$, so (4.110) and (4.111) reduce to

$$-i\omega\varphi - ik_y T = 0, \tag{4.112}$$

$$-i\omega T + i\kappa_T k_y\varphi = 0. \tag{4.113}$$

The resulting dispersion relation is

$$\omega = \pm ik_y\sqrt{\kappa_T}. \tag{4.114}$$

The solution with a positive imaginary part is the archetypal curvature-ITG-instability growth rate, cf. Beer et al. [1995], Ivanov et al. [2020],

$$\operatorname{Im}(\omega_{\text{phys}}) = \frac{k_{y,\text{phys}}\rho_i c_s}{\sqrt{L_B L_T}}. \tag{4.115}$$

The nonlinear version of the limit represented by (4.110) and (4.111) (with FLR terms restored to capture the short-wavelength stabilisation of the ITG modes, as well as correct zonal-flow dynamics) was studied in Ivanov et al. [2020], who proposed this as the minimal model for the Dimits transition from low to high turbulent transport. By design, this electrostatic limit is contained in our model.

4.2.3 Finite-β_e stabilisation of long-wavelength ITG modes

We can now introduce finite-β_e effects by relaxing the assumption of large k_z. Let us again take the long-wavelength limit, $k_y \ll 1$, and let $k_x = 0$ (linearly, these are always the fastest-growing modes), but leave $\kappa_T \sim 1$. The collisional terms involving χ can be neglected in this limit. From (4.98)-(4.101), we find the quartic dispersion relation

$$\omega^4 + k_y(\kappa_T - 1)\omega^3 - \left(1 - \kappa_T + k_z^2\right)\omega^2 - \left(\kappa_T + k_z^2\right)k_y\omega - k_z^2 k_y^2\kappa_T = 0. \tag{4.116}$$

Motivated by (4.114), we seek solutions to (4.116) with $\omega \sim k_y$, so the first two terms can be dropped. The remaining dispersion relation is quadratic in ω and can be easily solved. In the limit of $k_z \to \infty$ and $\kappa_T \gg 1$, we recover the ITG mode (4.114), but for

$\kappa_T \sim 1$ and $k_z \sim 1$, we find the condition of stability to be

$$(4\kappa_T - 1)\, k_z^4 + 2\kappa_T\,(1 - 2\kappa_T)\, k_z^2 - \kappa_T^2 \leq 0. \tag{4.117}$$

In the electrostatic limit, $k_z \to \infty$, this inequality is satisfied when $\kappa_T \leq 1/4$ – this critical temperature gradient also appeared in the electrostatic model of Ivanov et al. [2020]. As we are interested in the finite-β_e stabilisation of the electrostatic ITG modes, we restrict our attention to $\kappa_T > 1/4$. With this proviso, we find from (4.117) that the ITG modes are stabilised for $k_z \leq \sqrt{\kappa_T}$. This corresponds to a critical ion plasma beta

$$\beta_i = k_{z,\text{phys}}^2 L_B L_T. \tag{4.118}$$

For values of β_i in excess of this threshold, the ITG instability is quenched.

In a conventional tokamak plasma, the parallel wave number is often set by the system size: $k_{z,\text{phys}} \sim 1/qL_B$, where $\pi q L_B$ is the connection length. This implies that the long-wavelength ITG modes in a tokamak should be stabilised if

$$\beta_i \gtrsim \frac{L_T}{q^2 L_B}. \tag{4.119}$$

Note that β_i needed for stabilisation is smaller for larger temperature gradients, in agreement with previous observations [Jarmën et al., 1998, Zocco et al., 2015] from both numerical and analytical calculations. Since the stabilization of ITG modes is often followed by the onset of electromagnetic instabilities, condition (4.119) also marks the threshold for these electromagnetic modes, as noted by simple arguments from Jenko and Dorland [2001].

4.2.4 High-β_e (2D) limit: interchange modes

Finally, let us consider the high-β_e limit, for which $k_z \to 0$, so the dynamics are effectively two-dimensional. Then (4.98) gives $A \to 0$ and the remaining equations (4.99), (4.100) and (4.101) simplify to

$$-i\omega n - ik_y\,(\varphi - n) = 0, \tag{4.120}$$

$$-i\omega k_\perp^2 \varphi - i\kappa_T k_y k_\perp^2 \varphi - ik_y\,(n + T) = -\chi k_\perp^4\,(a\varphi - bT)\,, \tag{4.121}$$

$$-i\omega T + i\kappa_T k_y \varphi = -\chi k_\perp^2 T. \tag{4.122}$$

Anticipating the appearance of interchange modes, we consider perturbations with $\omega \sim 1$ and $k_\perp \ll 1$. (4.120), (4.121) and (4.122) then reduce to

$$-i\omega n - ik_y \varphi = 0, \tag{4.123}$$

$$-i\omega k_\perp^2\varphi - ik_y(n+T) = 0, \tag{4.124}$$

$$-i\omega T + i\kappa_T k_y\varphi = 0, \tag{4.125}$$

leading to the dispersion relation

$$\omega^2 = \frac{k_y^2}{k_\perp^2}(1-\kappa_T). \tag{4.126}$$

When $\kappa_T > 1$, or $L_B/L_T > 2/\tau$, there are unstable $k_x = 0$ modes with a physical growth rate in the limit of large κ_T given by

$$\mathrm{Im}(\omega_{\mathrm{phys}}) = \frac{v_{\mathrm{th}i}}{\sqrt{L_B L_T}}. \tag{4.127}$$

This mode exists at an arbitrarily large perpendicular scale, is driven by a pressure gradient in the presence of magnetic curvature and is constant on a flux surface – it is the familiar MHD (in fact, at $k_z = 0$, effectively electrostatic) interchange (IC) mode [Mercier, 1964, Freidberg, 2014]. In tokamaks, at macroscopic scales, such modes are stabilised by the magnetic shear, and generally for any viable equilibrium, MHD modes must be stabilised – this leads to the so-called beta limit [Mercier, 1964, Freidberg, 2014, Troyon et al., 1984]. Below, we will explore how close to (or far from) the MHD stability boundary the nonlinear high-beta runaway occurs.

4.2.5 Numerical calculation of linear stability

In this Subsection, we present data obtained by applying an eigenvalue solver to the linear system of equations (4.98)-(4.101). We would like to make connections with the analytical results obtained in Subsections 4.2.1-4.2.4 and to explore regions of the parameter space – in k_y, k_z (or β_e) and κ_T – where a simple analytical solution is not possible.

Growth rates from the linear solver are shown in Fig. 4.2. The results from scans in (k_z,κ_T) for the fastest growing mode and $\chi = 0.2$ show the key features obtained analytically in the long-wavelength limit: the electrostatic ITG mode is unstable when $k_z \gg 1$, with a growth rate that increases roughly as $\sqrt{\kappa_T}$; this ITG mode is partially stabilised at k_z values of order unity, with the critical k_z increasing weakly with κ_T; and MHD IC modes are driven unstable for small enough k_z. However, there are also unstable modes for small k_z and $\kappa_T < 1$, below the critical value for the onset of unstable MHD IC modes found in Subsection 4.2.4. These modes extend from $k_z = 0$ to $k_z \sim 1$, corresponding to the area between the solid yellow and dashed yellow curves in the figure. As evident from Fig. 4.2(b), these modes are a finite-k_y extension to the MHD IC modes. We thus refer to them as FLR IC modes.

Fig. 4.2 only shows the dominant instabilities, but multiple instabilities can co-exist

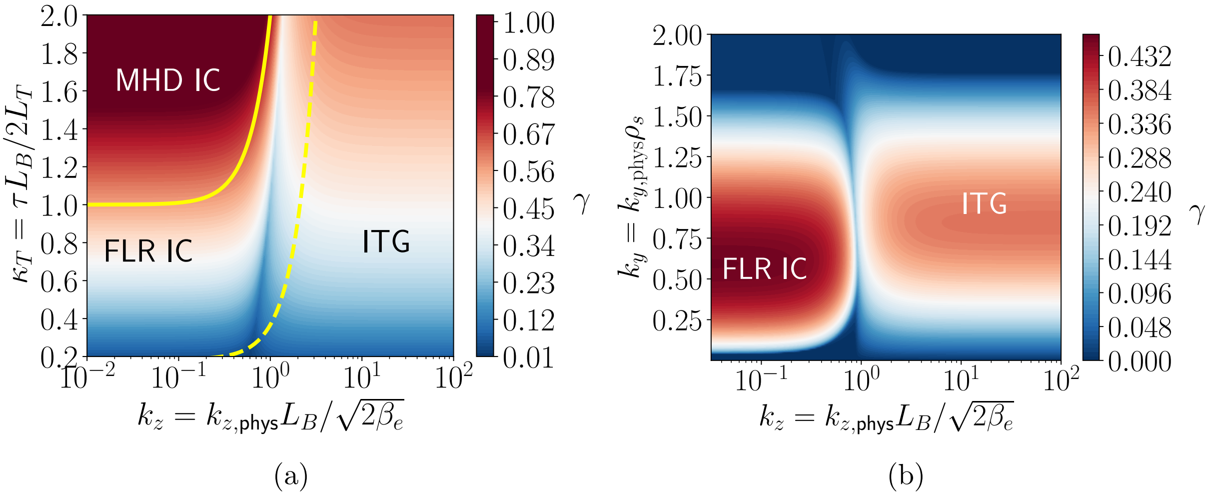

Figure 4.2: Growth-rate spectra normalised by $2c_s/L_B$ for modes with $k_x = 0$ and $\chi = 0.2$. (a): Spectrum in (k_z,κ_T) space, for the fastest growing mode. The solid yellow curve is the onset boundary for the MHD IC mode and the dashed yellow curve is the onset boundary for the FLR IC mode. The boundaries are independent of χ, and they are calculated analytically for the case with $k_y \ll 1$ (see Appendix D). (b): Spectrum in (k_z, k_y) space, for $\kappa_T = 0.8$. The MHD IC mode is stable (the growth rate at $k_y = 0$ is zero) but its finite k_y extension is unstable.

in certain parameter regimes. For $k_z \gg 1$, only the ITG mode is unstable. When k_z is decreased beyond the dashed yellow line in Fig. 4.2(a), additional modes are destabilised. Both the FLR IC mode and a collisional mode (discussed in Appendix D) are subdominant to the ITG mode near the boundary. As k_z is decreased further, the FLR IC mode becomes the dominant instability. When the solid yellow line in Fig. 4.2(a) is crossed, the MHD IC mode becomes the dominant instability and another collisional mode (also see Appendix D) is subdominant. In Subsection 4.2.3, we discovered a complete stabilisation of ITG at long wavelength. The conclusion there is that any instability whose growth rate satisfies $\gamma \sim k_y$ is stabilised above a critical β_e. In that analytical calculation, the collisional terms are ignored. It turns out that for finite χ, the growth rate at low k_y can be restored and scales like k_y^2. So, at finite χ, β_e above the critical value worked out in Subsection 4.2.3 does not completely stabilise ITG but only changes the scaling of the growth rate at low k_y. A summary plot of the instabilities (see Fig. D.5) as well as a detailed discussions of the instabilities mentioned so far can be found in Appendix D.

By using an eigenvalue solver, we find that the various instabilities that coexist at finite χ reduce to a single instability at each point in the (k_y, k_z, κ_T) parameter space when $\chi = 0$. Thus, $\chi = 0$ appears to be a singular limit of the equations.

As we have discussed, between the solid and dashed yellow curves, the FLR IC and collisional modes overlap with the ITG mode around $k_z \sim 1$, with a growth rate that is typically subdominant to that of the ITG mode near the dashed yellow line. While this complicates the interpretation of the nonlinear simulation data presented later in

Section 4.3, we will show that the appearance of these subdominant modes does not correlate well with the observed non-zonal transitions.

4.3 Nonlinear dynamics

We are interested primarily in determining how the amplitudes of the turbulent fluctuations in our model depend on β_e and κ_T. We will show in Subsection 4.3.2 that our simulations exhibit abrupt transitions from low-amplitude, zonally dominated saturated states to high-amplitude, 'streamer'-dominated turbulence once a certain critical boundary in the (β_e, κ_T) plane is crossed. These transitions are reminiscent of the 'non-zonal transitions' observed in gyrokinetic simulations of electromagnetic turbulence in tokamaks [Waltz, 2010, Rath and Peeters, 2022, Pueschel et al., 2013b] and of the 'Dimits transition' in the fluid model of electrostatic turbulence driven by the curvature-ITG instability in a Z-pinch [Ivanov et al., 2020]. Drawing inspiration from these studies, we consider in Section 4.3.3 the balance of the turbulent stresses in the evolution of the zonal flow and find that, as in Ivanov et al. [2020], the transition is correlated with a change in the sign of an effective turbulent viscosity, but this time it is aided and abetted by the Maxwell stress.

4.3.1 Numerical setup

The fluid equations (4.88)-(4.91) are solved in a triply periodic box on a single GPU by an electromagnetic version of the code described in Ivanov et al. [2020]. The Crank-Nicholson scheme is used for the time evolution of the linear terms, and the three-step Adams-Bashforth scheme is used for the time evolution of the nonlinear terms. A pseudo-spectral method with de-aliasing according to the '2/3 rule' is used to evaluate nonlinearities.

As is clear from the analysis in Section 4.2, there is no cut-off of linear growth rates at high k_z in our model, because there are no parallel heat fluxes. To avoid an accumulation of spectral energy at $k_{z,\max}$, the maximum k_z in our simulation, we include a hyper-dissipation term of the form $0.1(k_z/k_{z,\max})^4$ in all equations. This form of the hyper-dissipation ensures that, as we scan in L_z, the dissipation rate at the Nyquist scale remains fixed as long as the resolution is kept fixed. It is this scan in L_z that provides the variation in β_e: increasing L_z corresponds to increasing β_e, as explained in Subsection 4.1.5. In principle, besides L_z and κ_T, the collisionality χ is also a parameter that controls the non-zonal transition [Ivanov et al., 2020], but we shall not study this here, and fix $\chi = 0.2$ in all our nonlinear runs.

Unless stated otherwise, the perpendicular box sizes used for nonlinear simulations are $L_x = 100$ and $L_y = 150$ in units of ρ_s, with $N_{k_x} = 171$ k_x-values, $N_{k_y} = 255$ k_y-values and $N_{k_z} = 11$ k_z-values. Each simulation is initialised with low-amplitude noise and run to a normalised time $t = 10000$, with statistical quantities averaged over the time interval $t \in [5000, 10000]$. We found this duration of simulation to be sufficient in all cases to determine whether the system would saturate in a zonally dominated state.

Finally, to emulate a tokamak plasma where finite magnetic shear and the presence of good- and bad-curvature regions along the magnetic field force instabilities to have $k_z \neq 0$, we zero out the modes with $k_z = 0$ and $k_y \neq 0$ but not those with $k_z = 0$ and $k_y = 0$, $k_x \neq 0$ (the zonal modes).

4.3.2 Heat fluxes and the non-zonal transition

We characterise the saturated state of our simulations primarily via the time- and volume-averaged radial ion heat flux

$$Q \equiv \left\langle -\frac{\partial \varphi}{\partial y} T \right\rangle_{xyz} = \tau \frac{Q_{\rm phys}}{6 n_i T_i c_s} \left(\frac{L_B}{\rho_s} \right)^2, \tag{4.128}$$

where $Q_{\rm phys}$ is the dimensional ion heat flux. The variation of Q versus L_z^2 (equivalently,

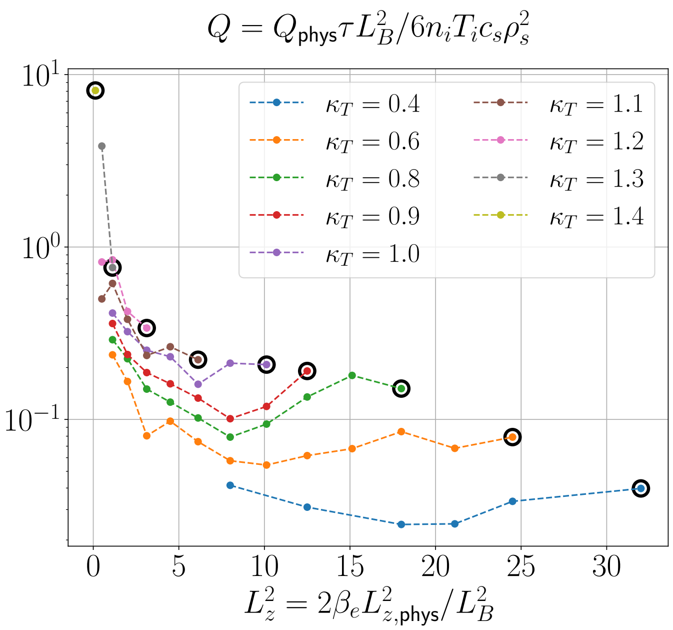

Figure 4.3: Normalized heat flux Q, defined in (4.128), versus L_z^2 (equivalently, β_e) for a sequence of values of κ_T. Black circled points denote the boundary beyond which the fluxes obtained are orders of magnitude higher than those within the boundary (see Fig. E.4 for the time trace of one such case).

β_e) for a number of values of κ_T is shown in Fig. 4.3 and corresponding examples of the heat-flux time traces are provided in Appendix E. The heat flux initially decreases with increasing L_z for small values of L_z but starts increasing again when L_z becomes sufficiently large. For each value of κ_T, there is a critical value of L_z above which the heat flux abruptly increases by several orders of magnitude. The boundary in the (L_z, κ_T)

plane where this transition occurs is indicated by black circles in Fig. 4.3. Simulations to the left of the black circles saturate with modest heat fluxes in zonal-flow-dominated states, as can be seen in the representative snapshots of the y-component of the $\boldsymbol{E} \times \boldsymbol{B}$ velocity (top right panel of Fig. 4.4) and of the non-zonal component of the ion temperature fluctuations (top left panel of Fig. 4.4). In contrast, simulations to the right of the black circles have no clear zonal structure (bottom right panel of Fig. 4.4), and the ion-temperature fluctuations take the form of box-scale 'streamers' oriented along the x-direction (bottom left panel of Fig. 4.4). These states have enormous heat fluxes and are qualitatively different from the zonally dominated states.

4.3.3 A game of stresses

Given the striking correlation between the presence (or otherwise) of a strong zonal-flow and the way in which electromagnetic turbulence saturates, let us analyse the zonal flow's evolution. The evolution equation for the zonal vorticity is obtained by applying the flux-surface average to the vorticity equation (4.90):

$$-\partial_t \partial_x^2 \left\langle \varphi \right\rangle_{yz} - \left\langle \left\{ \varphi, \nabla_\perp^2 \varphi \right\} \right\rangle_{yz} + \left\langle \left\{ A, \nabla_\perp^2 A \right\} \right\rangle_{yz} + \left\langle \partial_x \left\{ \partial_x \varphi, T \right\} \right\rangle_{yz} = -\chi \partial_x^4 \left(a \left\langle \varphi \right\rangle_{yz} - b \left\langle T \right\rangle_{yz} \right). \tag{4.129}$$

Integrating (4.129) twice in x results in an evolution equation for the zonal potential $\left\langle \varphi \right\rangle_{yz}$:[2]

$$\partial_t \left\langle \varphi \right\rangle_{yz} + \Pi_{\mathrm{turb}} + \Pi_\chi = 0, \tag{4.130}$$

where

$$\Pi_\chi \equiv \chi \partial_x^2 \left(a \left\langle \varphi \right\rangle_{yz} - b \left\langle T \right\rangle_{yz} \right) \tag{4.131}$$

is the collisional stress, and $\Pi_{\mathrm{turb}} = \Pi_\varphi + \Pi_A + \Pi_T$ is the turbulent stress, composed of the Reynolds stress

$$\Pi_\varphi \equiv - \left\langle \left(\partial_x \varphi \right) \left(\partial_y \varphi \right) \right\rangle_{yz}, \tag{4.132}$$

the Maxwell stress

$$\Pi_A \equiv \left\langle \left(\partial_x A \right) \left(\partial_y A \right) \right\rangle_{yz}, \tag{4.133}$$

and the diamagnetic stress[3]

$$\Pi_T \equiv - \left\langle \left(\partial_x \varphi \right) \left(\partial_y T \right) \right\rangle_{yz}. \tag{4.134}$$

[2]The constants of integration are of the form $f(t)x + g(t)$, where f vanishes due to the periodicity of the zonal mode and g is safely set to zero because the physical effect only comes from the flow $\partial_x \left\langle \phi \right\rangle_{yz}$.

[3]In the gyrokinetic calculations presented in Chapter 3, the Reynolds and diamagnetic stresses are both contained within the nonlinearity between ϕ and h_s, and cannot be separated into distinct contributions. Thus, when we refer to the Reynolds stress in the gyrokinetic context, we mean the entire nonlinear term. Only in the current fluid limit can the Reynolds and diamagnetic stresses be clearly distinguished and referred to separately.

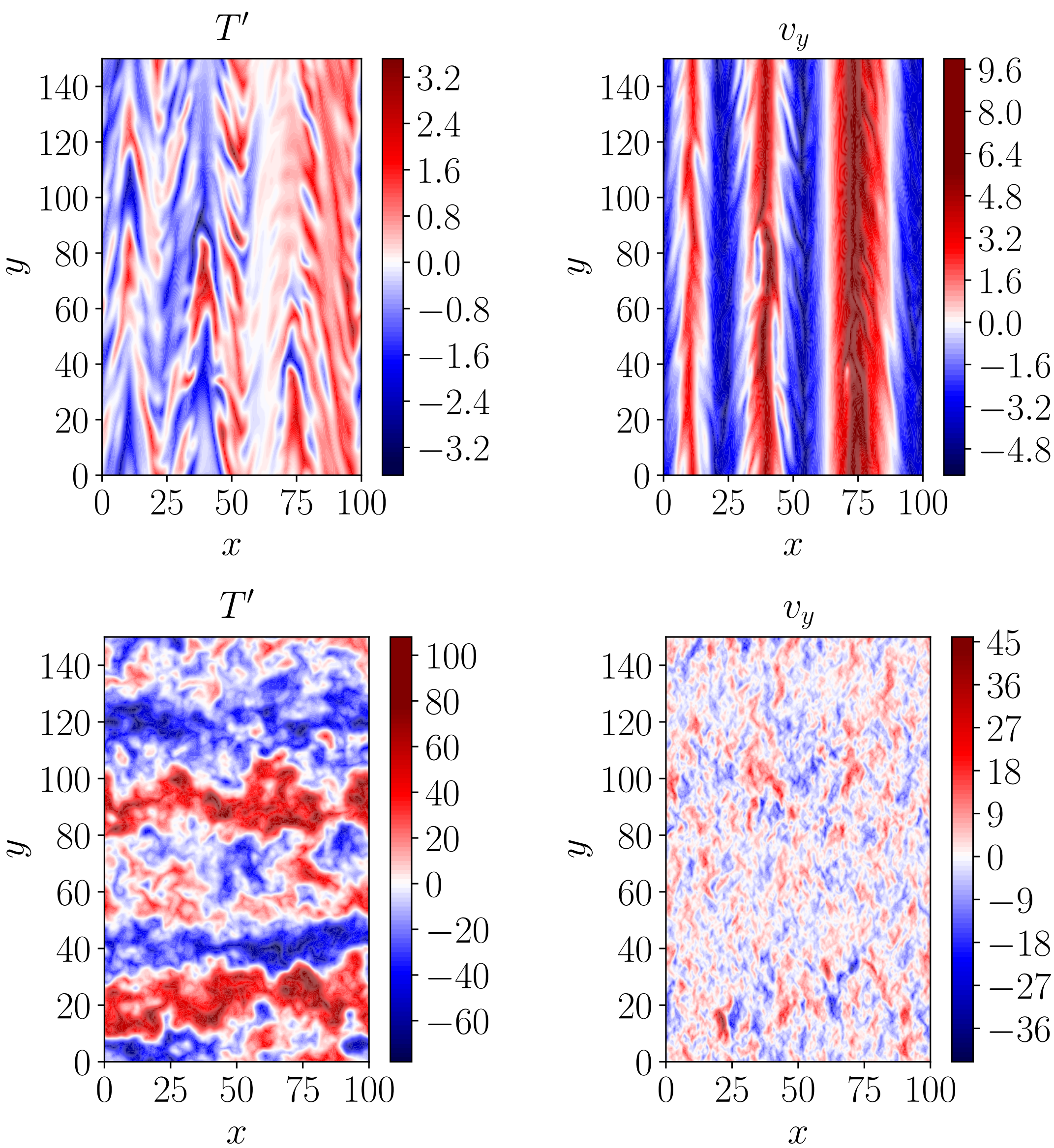

Figure 4.4: Snapshots of fields at the $z = 0$ plane for a pair of runs with $\kappa_T = 0.8$ (the green line in Fig. 4.3) and two values of L_z: $L_z^2 = 7.8$ at $t = 9000$ (top) and $L_z^2 = 19$ at $t = 450$ (bottom). The left panels show the non-zonal part of T, which indicates the level of turbulent fluctuation, and the right ones show the y-component of the $\boldsymbol{E} \times \boldsymbol{B}$ flow v_y, with a strong zonal flow manifest at the lower value of L_z^2.

We can now derive an evolution equation for the zonal flow's mean energy by multiplying both sides of (4.130) by the zonal shear $S \equiv \partial_x^2 \langle\varphi\rangle_{yz}$ and integrating over the box in x:

$$\partial_t \left\langle \frac{v_Z^2}{2} \right\rangle_x = \langle S\Pi_{\rm turb}\rangle_x + \langle S\Pi_\chi\rangle_x \,, \tag{4.135}$$

where $v_Z = \partial_x \langle\varphi\rangle_{yz}$ is the zonal flow velocity. The terms on the right-hand side of (4.135) are effectively fluid versions of the nonlinear transfer functions discussed in Chapter 3.

If a steady state with zonal flows is to be achieved, the contribution to (4.135) from the turbulent stress $\Pi_{\rm turb}$ must balance the contribution from the collisional stress Π_χ. As the latter is negative-definite, $\langle S\Pi_{\rm turb}\rangle_x > 0$ is a necessary condition for a saturated zonally dominated state. This means that, cumulatively, the three turbulent stresses must have the same sign as S – reinforcing it, rather than opposing, as conventional viscosity (exemplified by Π_χ) would do.

Previous studies of electrostatic turbulence in a fluid model [Ivanov et al., 2020, 2022] have shown that the Reynolds (Π_φ) and diamagnetic (Π_T) stresses tend to support and to oppose zonal-flow generation, respectively[4]. Indeed, Ref. Ivanov et al. [2020] argues that in the electrostatic limit, the transition from a zonally dominated, 'Dimits' state to an un-saturated, streamer state occurs when the diamagnetic stress wins the battle with the Reynolds stress, for a certain definition of 'win' that we will come to shortly. Since Π_T always grows more important as κ_T increases, the zonal-flow generation is eventually quenched after κ_T reaches a critical value. Both gyrokinetic and fluid studies of electromagnetic turbulence [Naulin et al., 2005, Scott, 2005, Anderson et al., 2011, Rath and Peeters, 2022] have shown that the Maxwell stress tends to oppose zonal-flow generation, consistent with the decrease in critical κ_T with increasing L_z demonstrated in Fig. 4.3. This is unsurprising, as the bending of magnetic field lines that accompanies a sheared zonal flow generates a restoring force due to magnetic tension that opposes the zonal flow. For purely Alfvénic fluctuations, where $\varphi = \pm A$, the Reynolds and Maxwell stresses annihilate one another due to the sign difference between (4.132) and (4.133), leaving the diamagnetic stress the sole survivor.

When interpreting numerical results, it is convenient to characterise the zonal-flow dynamics in terms of turbulent viscosity $\nu_{\rm turb}$ [Ivanov et al., 2020]. The standard definition of this quantity is in terms of an intuitively natural closure for the turbulent stress in (4.130): $\Pi_{\rm turb} = -\nu_{\rm turb} S$. A positive $\nu_{\rm turb}$ corresponds to diffusive behaviour and the erosion of zonal flow, while negative $\nu_{\rm turb}$ corresponds to anti-diffusive behaviour and the generation of zonal flow. Of course, in general, $\nu_{\rm turb} = -\Pi_{\rm turb}(x,t)/\partial_x^2 \langle\varphi\rangle_{yz}(x,t)$ is a

[4] The fact that Reynolds stress in 2D will generate zonal flows is, of course, a well-established tenet of plasma physics – this is described variously as a secondary Kelvin-Helmholtz instability of the ITG modes [Rogers et al., 2000], negative viscosity [Diamond et al., 2005], or inverse cascade [Balk et al., 1990, Diamond et al., 2005]. The latter two notions in fact originate in the theory of 2D hydrodynamic turbulence [Kraichnan, 1967, Batchelor, 1969, Kraichnan, 1976].

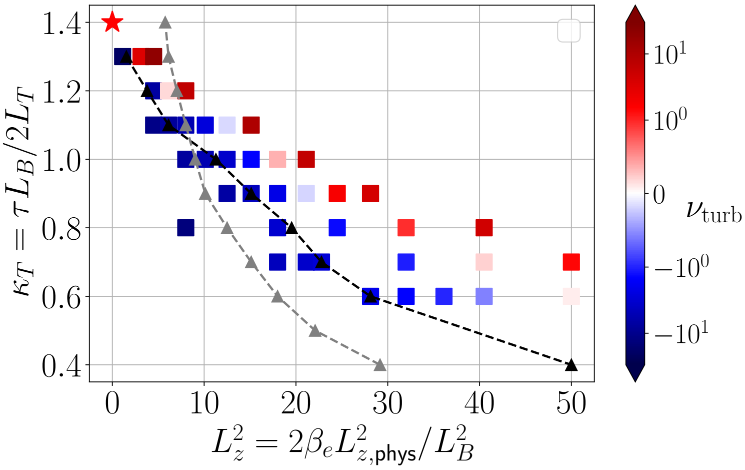

Figure 4.5: Turbulent viscosity ν_{turb} versus (κ_T, L_z^2). The values of ν_{turb} are calculated from simulations with fixed-in-time zonal flow. The black dashed line is the non-zonal transition boundary calculated from simulations with self-consistently generated zonal flows, and the grey dashed line is the onset boundary of the FLR IC and collisional modes, which is also shown as the yellow dashed line in Fig. 4.2(a). The red star is the transition threshold in the electrostatic limit [Ivanov et al., 2020].

function both of time and space, but it is useful to construct a constant proxy quantity to characterise the propensity of turbulence to amplify (or otherwise) the zonal flows. This is easiest done on the basis of the zonal-flow energy equation (4.135), where the generation term is expressed as follows:[5]

$$\partial_t \left\langle \frac{v_Z^2}{2} \right\rangle_x = -\nu_{\mathrm{turb}} \left\langle S^2 \right\rangle_x - a\chi \left\langle S^2 \right\rangle_x , \tag{4.136}$$

where we also assume that the zonal-flow evolution is much slower than the time variation of turbulent fluctuations and so define the turbulent viscosity as an average over many turnover times of the turbulence, during which the zonal flow remains approximately stationary:

$$\nu_{\mathrm{turb}} = -\left\langle \frac{\langle S\Pi_{\mathrm{turb}}\rangle_x}{\langle S^2 \rangle_x} \right\rangle_t . \tag{4.137}$$

If this quantity is negative, that means that the stress-shear correlation is on average positive and so the zonal flows are reinforced by turbulence.

The definition (4.137) makes it possible to construct a series of numerical experiments in which ν_{turb} can be measured directly as a function of κ_T and L_z^2 (i.e., β_e). In these simulations, a fixed external zonal flow was applied. The shape of the imposed zonal flow is a triangle wave whose period is L_x; there is thus a constant, positive zonal shear across half of the box and an equal and opposite zonal shear across the other half. The aim is

[5]The term $b\chi \left\langle S\partial_x^2 \langle T \rangle_{yz} \right\rangle_x$ has been neglected in (4.136). Numerically, it does indeed turn out always to be small.

to determine how well the sign of the measured turbulent viscosity correlates with the ability of the turbulence to saturate. Further details of how ν_{turb} is calculated numerically are provided in Appendix E.5.

A scatter plot of ν_{turb} obtained from these simulations is shown in Fig. 4.5. For sufficiently small values of κ_T and L_z, where the system saturates in the zonally dominated regime, ν_{turb} is negative: as expected, the turbulent stresses reinforce the imposed zonal flow. In contrast, ν_{turb} turns positive for sufficiently large κ_T and L_z. This is unsurprising because the contribution from Maxwell stress increases with L_z and the diamagnetic stress contribution increases with κ_T. The boundary in the (κ_T, L_z^2) plane where the non-zonal transition to high transport occurs is represented by black triangles in Fig. 4.5. One can see that this transition boundary, traced out by the dashed black line in the figure, coincides approximately with the line where ν_{turb} changes sign, albeit with a small offset. In contrast, the onset of linear electromagnetic instabilities does not correlate well with the transition. In Fig. 4.5, this is illustrated by the grey triangles, also connected by a dashed line, indicating the (κ_T, L_z^2) values where the FLR IC and other subdominant collisional modes first go unstable. The small offset of the transition boundary from the $\nu_{\text{turb}} = 0$ contour is likely due to the fact that ν_{turb} was measured using the imposed zonal flows described above: as these imposed flows are not precisely the same as the flows that would be set up self-consistently by the turbulence, it is reasonable to expect ν_{turb} to deviate from the true value unless ν_{turb} is exactly independent of the zonal flow itself.

As evident from (4.137), the sign of ν_{turb} is determined by the sign of Π_{turb} relative to the zonal shear. To identify the role played by each component of the turbulent stress, in Fig. 4.6 we plot indicative profiles of the time-averaged stresses and zonal shear from simulations with fixed-in-time zonal flows. As expected, the diamagnetic and Maxwell stresses both oppose the zonal flow, while the Reynolds stress supports it. As L_z increases, the Maxwell stress increases in magnitude relative to the other stresses, flipping the sign of Π_{turb} and leading to a state where zonal flows cannot be self-consistently reinforced. In Fig. 4.7, we plot the ratios

$$r_{A\varphi} = \frac{\langle|\Pi_A|\rangle_x}{\langle|\Pi_\varphi|\rangle_x}, \quad r_{T\varphi} = \frac{\langle|\Pi_T|\rangle_x}{\langle|\Pi_\varphi|\rangle_x} \tag{4.138}$$

versus L_z for a sequence of values of κ_T. One can see that the ratio between the Maxwell (Π_A) and Reynolds (Π_φ) stresses scales roughly as L_z^2 (or β_e) regardless of κ_T. Note that the scaling obtained here does not agree with the transfer scaling observed in the gyrokinetic simulations where r_{MR} was found to scale as β_e^2. Possible sources of the discrepancy include differences in magnetic geometry, the assumption of cold ions, or the FLR effects. In contrast, the ratio between the diamagnetic stress (Π_T) and Reynolds stresses increases with κ_T, but remains relatively constant as L_z is varied at a given κ_T.

Thus, the 'high-beta runaway' is brought about entirely by the hostility of the Maxwell stress to zonal-flow generation.

A simple heuristic argument can be used to explain why the Maxwell stress tends to oppose zonal flows. Consider a quasi-static zonal flow with a shearing rate S that is constant in space. The part of the turbulent viscosity due to the Maxwell stress is then

$$\nu_{t,A} = -\left\langle \frac{\langle S\Pi_A\rangle_x}{\langle S^2\rangle_x} \right\rangle_t = -\frac{1}{S}\left\langle (\partial_x A)(\partial_y A)\right\rangle_{xyzt} = -\frac{1}{S}\sum_{\boldsymbol{k}} \left\langle k_x k_y \left|A_{\boldsymbol{k}}\right|^2\right\rangle_{zt}. \tag{4.139}$$

We will next argue that the wavenumbers k_x and k_y are correlated in such a way that the sum over $\boldsymbol{k}$ produces a sign definite result. Consider a perturbation of the form $A_0 \exp(i\tilde{\boldsymbol{k}}\cdot\tilde{\boldsymbol{r}})$ growing in a background of constant zonal shear flow, where the shearing rate is S, and $\tilde{\boldsymbol{k}}$ and $\tilde{\boldsymbol{r}} = (\tilde{x}, \tilde{y}, \tilde{z})$ here are the wavenumber and position vector defined in the shearing frame, respectively. The position vector in the unsheared frame $\boldsymbol{r} = (x, y, z)$ is related to $\tilde{\boldsymbol{r}}$ through the following coordinate transformation:

$$\tilde{x} = x, \quad \tilde{y} = y - (x - x_0)St, \quad \tilde{z} = z, \tag{4.140}$$

where we have assumed that the flow velocity is zero at $x = x_0$. Next, we use (4.140) to write the wave phase $\tilde{\boldsymbol{k}}\cdot\tilde{\boldsymbol{r}}$ as

$$\tilde{\boldsymbol{k}}\cdot\tilde{\boldsymbol{r}} = \left(\tilde{k}_x - \tilde{k}_y St\right) x + \tilde{k}_y y + \tilde{k}_z z + \tilde{k}_y x_0 St. \tag{4.141}$$

Since the coordinates (x, y, z, t) are all independent, the only way for the wave phases to agree in the two frames, i.e., $\tilde{\boldsymbol{k}}\cdot\tilde{\boldsymbol{r}} = \boldsymbol{k}\cdot\boldsymbol{r}$, is when the wavenumbers are related via

$$k_x = \tilde{k}_x - \tilde{k}_y St, \quad k_y = \tilde{k}_y, \quad k_z = \tilde{k}_z. \tag{4.142}$$

Thus, the k_x of the perturbation changes with time as seen in the unsheared frame, until t reaches τ, which is the characteristic turbulence decorrelation time. If $S\tau$ is large enough, $k_x \to -\tilde{k}_y S\tau = -k_y S\tau$. Then the contribution of the Maxwell stress to the turbulent viscosity (4.139) is

$$\nu_{t,A} \sim \sum_{\boldsymbol{k}} \left\langle \tau k_y^2 \left|A_{\boldsymbol{k}}\right|^2\right\rangle_{zt} > 0. \tag{4.143}$$

All that is needed for this result is the fact that shear-induced $k_x \propto -Sk_y$ (by the same token, the Reynolds stress gives rise to negative turbulent viscosity, $\nu_{t,\varphi} < 0$).

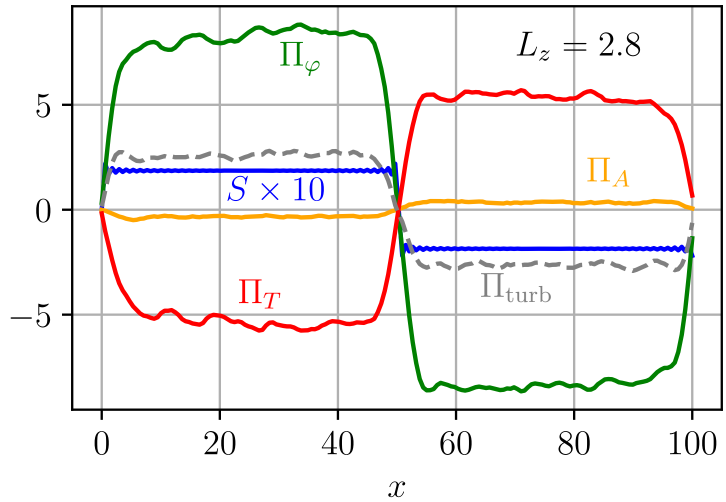

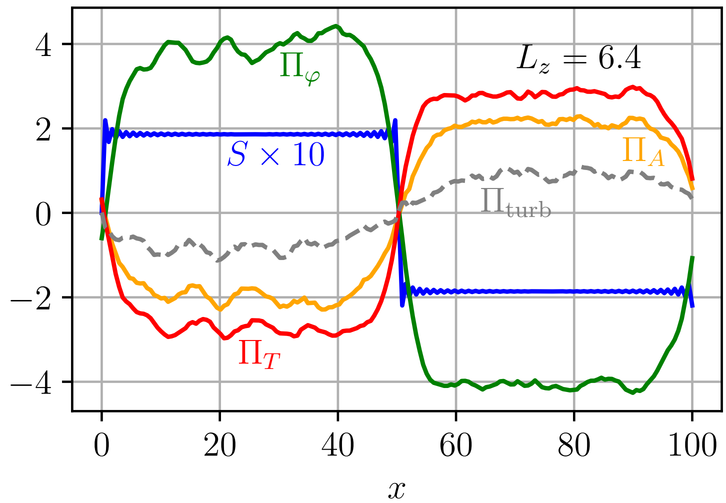

Figure 4.6: Time-averaged profiles of the zonal shear S (blue), the Reynolds stress Π_φ (green), the Maxwell stress Π_A (orange), the diamagnetic stress Π_T (red) and the net turbulent stress $\Pi_{\rm turb}$ (grey) for $\kappa_T = 0.8$ and two different values of L_z: the $L_z = 2.8$ case (top panel) corresponds to a zonal-flow-dominated state, whereas the $L_z = 6.4$ case (bottom panel) lies beyond the non-zonal transition indicated in Fig. 4.3.

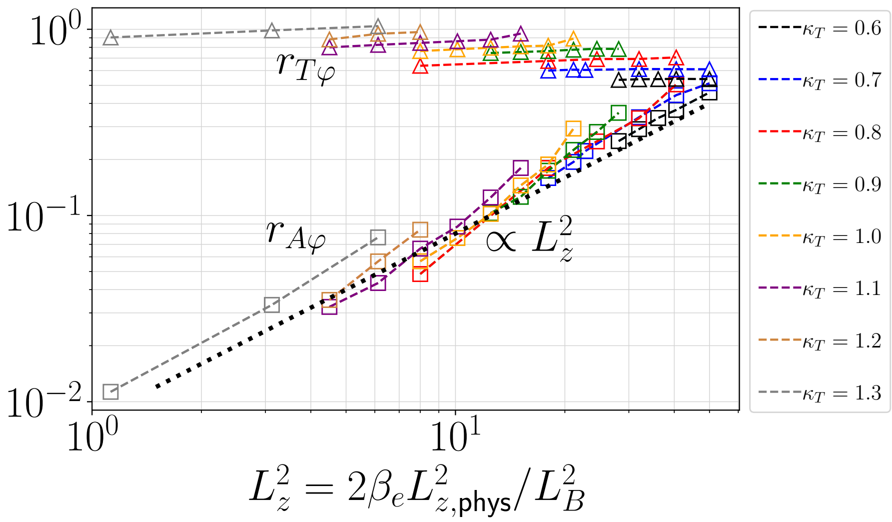

Figure 4.7: The Maxwell-Reynolds stress ratio $r_{A\varphi}$ (squares) and the diamagnetic-Reynolds stress ratio $r_{T\varphi}$ (triangles). The different colours denote different values of κ_T. The data was obtained from simulations with frozen-in-time zonal flows. The scaling $r_{A\varphi} \propto L_z^2$ is given by the dotted line, for reference.

Chapter 5

Discussion and future work

It is better to be vaguely right than exactly wrong.

— Maynard Keynes, Oxford plasma seminars and Vienna meetings

In this thesis, we examined a key physical mechanism that leads to non-zonal transition in electromagnetic cITG turbulence using gyrokinetics, and introduced a method that enables us to predict the parameters at which the non-zonal transition occurs with minimal computational effort. We then proposed a minimal fluid model for electromagnetic, cITG turbulence in a Z-pinch magnetic geometry. Despite the simplicity of our model, its numerical solution reproduces qualitatively the non-zonal transitions observed in the gyrokinetic simulations.

Summary of results from gyrokinetic simulations

The non-zonal transitions were observed in the gyrokinetics simulations with two different magnetic equilibria – one corresponding to a conventional tokamak with circular flux surfaces (the Cyclone Base Case, or CBC) and another to a spherical tokamak (ST40). The transitions occur when the effect of the Maxwell stress becomes comparable to that of the Reynolds stress; beyond this point the turbulence is characterised by weak zonal flows and extreme (or divergent) heat fluxes. The relative strengths of the Reynolds and Maxwell stresses are quantified using the time-averaged, large-scale energy-transfer functions, $\langle T_\phi \rangle_t$ and $\langle T_{A_\parallel} \rangle_t$. These transfer functions measure the rate at which turbulence transfers energy to the zonal flows through the respective nonlinear stresses. For the Reynolds stress, $\langle T_\phi \rangle_t$ is predominantly positive, indicating a net transfer of energy into the zonal flow. By contrast, $\langle T_{A_\parallel} \rangle_t$ is mostly negative, corresponding to a net extraction of energy from the zonal flow by the Maxwell stress. Non-zonal transitions are therefore expected when the magnitudes of the two stresses become comparable, i.e. when $r_{MR} = |\langle T_{A_\parallel} \rangle_t| / |\langle T_\phi \rangle_t| \approx 1$, a criterion that is indeed borne out by the simulations. Simulations also show that the non-zonal transitions occur along a boundary defined by $q^2 \beta_e = C_{\mathrm{nl}}$ in the (q,β_e) parameter space, with the CBCs exhibiting almost perfect agreement.

Nevertheless, the ST40 simulation data show noticeable deviations from the scaling law at lower q. This behaviour may be attributed to differences in the magnetic geometry, in particular the low aspect ratio characteristic of spherical tokamak equilibria. Even though the KBM and the lower IBM thresholds also seem to follow the same scaling law, i.e., $q^2\beta_e = C_{\mathrm{KBM}}$ and $q^2\beta_e = C_{\mathrm{IBM}}$, the corresponding constants are found to satisfy $C_{\mathrm{nl}} < C_{\mathrm{KBM}} < C_{\mathrm{IBM}}$. For the CBC, $C_{\mathrm{nl}} \approx 2/3C_{\mathrm{KBM}}$, and for most of the ST40 cases, $C_{\mathrm{nl}} \approx 1/2C_{\mathrm{KBM}}$. This suggests that the linear stability thresholds of electromagnetic instabilities such as KBMs do not necessarily coincide with the non-zonal transition threshold.

In addition, it was discovered that, for the CBC, the transfer ratio approximately satisfies $r_{MR} \propto (q^2\beta_e)^2$. Assuming that the empirical scaling law is universally applicable and that the non-zonal transitions occur at $r_{MR} \approx 1$, one can extrapolate the transition boundary in the (q,β_e) space from a single nonlinear simulation at low $q^2\beta_e$. This approach not only eliminates the need for an extensive parameter scan over the (q, β_e) space, but also benefits from the use of an effectively electrostatic simulation, which is typically much faster owing to a less stringent time-step constraint. An alternative strategy would be to perform a β_e scan at a single value of q to identify the non-zonal transition point and then use the relation $q^2\beta_e = C_{\mathrm{nl}}$ to extrapolate the stability boundary in (q, β_e) space. However, this is significantly more computationally expensive: multiple simulations are required to accurately locate the transition, and each simulation typically costs 2-4 times more than an effectively electrostatic simulation due to the rapid motion of electrons along perturbed field lines near the transition threshold.

Summary of results from the fluid model

In the fluid limit with cold ions, the zonal-flow drive is governed by the interplay among three nonlinear stresses – Reynolds, diamagnetic, and Maxwell stresses. While these stresses are cleanly distinguishable in the fluid description, the Reynolds and diamagnetic contributions cannot be well separated once kinetic effects are included. It was found that both diamagnetic and Maxwell stresses have a detrimental effect on the zonal-flow drive. Based on analytical calculations, we can show that, in the extreme case of Alfvénic fluctuations, the Maxwell stress contribution exactly cancels that of the Reynolds stress, eliminating the net zonal drive. Even when the linear modes are not fully Alfvénic, the Maxwell stress can still be argued to oppose the Reynolds stress whenever the fluctuations evolve on top of a background shear flow. Thus, the Maxwell stress, which arises as a result of finite plasma beta, generally acts to reduce the effectiveness of the zonal-flow generation.

To provide evidence for the stress picture, we perform simulations of the fluid model and demonstrate that, for each value of the ion temperature gradient, there is a critical value of plasma beta beyond which the system transitions abruptly from a zonal-flow-dominated state with a low heat flux to a streamer-dominated state with a much higher heat flux. It is similar to the non-zonal transition in gyrokinetic simulations and it occurs when the diamagnetic and Maxwell stresses overcome the Reynolds stress. Clear and simple scalings for the ratios of the diamagnetic and Maxwell stresses to the Reynolds stress are present in the data, with the diamagnetic-Reynolds stress ratio independent of beta and the Maxwell-Reynolds stress ratio increasing linearly with β_e. Consequently, the critical β_e at which the transition occurs can be predicted with reasonable accuracy for each κ_T using data from a single simulation at low β_e. However, although a stress-ratio scaling with β_e also appears in the gyrokinetic calculations, the scaling observed there is noticeably stronger ($r_{MR} \propto \beta_e^2$). This discrepancy may arise from differences in magnetic geometry, from the cold-ion assumption, or from FLR effects that are neglected in the fluid model.

Practical implication

From a practical standpoint, when determining the operational beta limits for a given device, it is important to account for the constraints imposed by micro-scale turbulence, rather than relying solely on linear stability boundaries. More importantly, the beta limit may be more restrictive due to the nonlinear energy transfer processes inherent to micro-scale turbulence. It is therefore essential to understand the non-zonal threshold and to identify reliable operational regimes. While performing nonlinear gyrokinetic simulations across a multi-dimensional parameter space is computationally prohibitive, our study presents a more practical alternative by using the empirical scaling law for r_{MR} combined with a relatively cheap simulation at low β_e.

That said, the linear KBM stability threshold may provide a reasonable approximation to the non-zonal transition threshold. For the CBC, the discrepancy is on the order of 50% in β_e at a given q, which may be acceptable when screening a large number of equilibria. For the ST40 cases, although the linear KBM thresholds differ substantially from the nonlinear transition points, the resulting error—particularly at low q—is comparable to the uncertainty in transition predictions based on low-β_e nonlinear transfer analysis. In such situations, the linear KBM threshold can therefore serve as a practical surrogate for identifying non-zonal transitions.

The work presented in this thesis suggests that operating in the high-beta regimes desirable for future fusion devices may require additional mechanisms – such as plasma rotation – to suppress the enhanced heat transport associated with the non-zonal transition. For devices like STEP (the Spherical Tokamak for Energy Production), which is currently under development in the UK and is expected to operate with relatively weak plasma rotation, it is therefore important to consider whether some form of rotation (or a substitute for its effects) will be necessary to maintain acceptable confinement.

Future work

The observed scaling law $r_{MR} \propto (q^2\beta_e)^2$ is not consistent with either the linear gyrokinetic arguments (presented in Appendix B) or the fluid-model prediction, both of which suggest a scaling of the form $r_{MR} \propto q^2\beta_e$. Understanding the origin of this discrepancy is therefore a direction for future work. This may involve revisiting the approximations used in the linear calculation or identifying the nonlinear physical mechanisms that lead to a deviation from the linear scaling.

Another possible direction is to apply the proposed recipe for predicting non-zonal transitions to magnetic equilibria from a range of tokamak configurations. This would help assess whether the scaling law and the associated stress-based picture of the transition are robust and broadly applicable across different devices. In principle, the non-zonal transition boundary could also be explored in other parameter spaces, such as magnetic shear $\hat{s}$ or the temperature-gradient strengths. When combined with the corresponding scaling of the transfer ratio r_{MR} with these parameters, such studies may offer a computationally efficient way to obtain a more complete picture of the operational regimes of tokamak equilibria.

Finally, the connection between the non-zonal transition and the Dimits transition is an intriguing direction for further study, as both phenomena involve qualitative changes in zonal-flow activity. In the fluid model of electrostatic ITG turbulence [Ivanov et al., 2020], it was proposed that the Dimits transition arises from a cancellation between the fluid Reynolds and diamagnetic stresses, implying that above the Dimits threshold the nonlinear drive for zonal flows should become negligible. In contrast, our results show that the nonlinear stresses continue to drive zonal flows up to the point of the non-zonal transition, at which point they finally cancel each other. This discrepancy suggests that we may need to revisit the physical picture of the Dimits transition – as a cancellation between the Reynolds and diamagnetic stresses.

Bibliography

I G Abel, G G Plunk, E Wang, M Barnes, S C Cowley, W Dorland, and A A Schekochihin. Multiscale gyrokinetics for rotating tokamak plasmas: fluctuations, transport and energy flows. *Rep. Prog. Phys.*, 76:116201, 2013.

T. Adkins, A.A. Schekochihin, P.G. Ivanov, and C.M. Roach. Electromagnetic instabilities and plasma turbulence driven by electron-temperature gradient. *J. Plasma Phys.*, 88:905880410, 2022.

Ksenia Aleynikova and Alessandro Zocco. Quantitative study of kinetic ballooning mode theory in simple geometry. *Phys. Plasmas*, 24:092106, 2017.

M S Anastopoulos Tzanis, M R Hardman, Y Zhang, X Zhang, A Sladkomedova, A Dnestrovskii, Y S Na, J H Lee, S J Park, T O'Gorman, H Lowe, M Romanelli, M Sertoli, M Gemmel, J Woods, H V Willett, and ST40 Team. Integrated modeling of st40 hot ion plasmas using the tglf transport model. *Plasma Phys. Control. Fusion*, 67:055022, 2025.

J. Anderson, H. Nordman, R. Singh, and J. Weiland. Zonal flow generation in ion temperature gradient mode turbulence. *Phys. Plasmas*, 9:4500, 2002.

Johan Anderson, Hans Nordman, Rameswar Singh, and Raghvendra Singh. Secondary instability of electromagnetic ion-temperature-gradient modes for zonal flow generation. *Phys. Plasmas*, 18:072306, 2011.

A.M. Balk, S.V. Nazarenko, and V.E. Zakharov. On the nonlocal turbulence of drift type waves. *Phys. Lett. A*, 146:217, 1990.

M. Barnes, F. I. Parra, and A. A. Schekochihin. Critically balanced ion temperature gradient turbulence in fusion plasmas. *Phys. Rev. Lett.*, 107:115003, 2011.

M. Barnes, F.I. Parra, and M. Landreman. stella: An operator-split, implicit–explicit δf-gyrokinetic code for general magnetic field configurations. *J. Comput. Phys.*, 391: 365, 2019.

G. K. Batchelor. Computation of the energy spectrum in homogeneous two-dimensional turbulence. *Phys. Fluids*, 12:II–233, 1969.

A Bañón Navarro, G Merlo, G G Plunk, P Xanthopoulos, A von Stechow, A Di Siena, M Maurer, F Hindenlang, F Wilms, and F Jenko. Global gyrokinetic simulations of itg turbulence in the magnetic configuration space of the wendelstein 7-x stellarator. *Plasma Phys. Control. Fusion*, 62:105005, 2020.

M. A. Beer, S. C. Cowley, and G. W. Hammett. Field-aligned coordinates for nonlinear simulations of tokamak turbulence. *Phys. Plasmas*, 2:2687, 1995.

R. J. Bickerton, J. W. Connor, and J. B. Taylor. Diffusion driven plasma currents and bootstrap tokamak. *Nature Phys. Sci.*, 229:110, 1971.

J. Candy, E.A. Belli, and R.V. Bravenec. A high-accuracy eulerian gyrokinetic solver for collisional plasmas. *Journal of Computational Phys.*, 324:73, 2016.

J Candy, E A Belli, and G Staebler. Spectral treatment of gyrokinetic profile curvature. *Plasma Physics and Controlled Fusion*, 62:042001, 2020.

Y. Chen, S.E. Parker, B.I. Cohen, A.M. Dimits, W.M. Nevins, D. Shumaker, V.K. Decyk, and J.N. Leboeuf. Simulations of turbulent transport with kinetic electrons and electromagnetic effects. *Nucl. Fusion*, 43:1121, 2003.

J. Citrin, F. Jenko, P. Mantica, D. Told, C. Bourdelle, J. Garcia, J. W. Haverkort, G. M. D. Hogeweij, T. Johnson, and M. J. Pueschel. Nonlinear stabilization of tokamak microturbulence by fast ions. *Phys. Rev. Lett.*, 111:155001, 2013.

J. Citrin, J. Garcia, T. Görler, F. Jenko, P. Mantica, D. Told, C. Bourdelle, D. R. Hatch, G. M. D. Hogeweij, T. Johnson, M. J. Pueschel, M. Schneider, and JET-EFDA Contributors. Electromagnetic stabilization of tokamak microturbulence in a high-beta regime. *Plasma Phys. Control. Fusion*, 57:014032, 2014.

J Citrin, H Arnichand, J Bernardo, C Bourdelle, X Garbet, F Jenko, S Hacquin, M J Pueschel, and R Sabot. Comparison between measured and predicted turbulence frequency spectra in itg and tem regimes. *Plasma Phys. Control. Fusion*, 59:064010, 2017.

J G Cordey, C D Challis, and P M Stubberfield. Bootstrap current theory and experimental evidence. *Plasma Phys. Control. Fusion*, 30:1625, 1988.

P H Diamond, S-I Itoh, K Itoh, and T S Hahm. Zonal flows in plasma—a review. *Plasma Phys. Control. Fusion*, 47:R35, 2005.

A. M. Dimits, G. Bateman, M. A. Beer, B. I. Cohen, W. Dorland, G. W. Hammett, C. Kim, J. E. Kinsey, M. Kotschenreuther, A. H. Kritz, L. L. Lao, J. Mandrekas, W. M. Nevins, S. E. Parker, A. J. Redd, D. E. Shumaker, R. Sydora, and J. Weiland. Comparisons and physics basis of tokamak transport models and turbulence simulations. *Phys. Plasmas*, 7:969, 2000.

A.M. Dimits, W.M. Nevins, D.E. Shumaker, G.W. Hammett, T. Dannert, F. Jenko, M.J. Pueschel, W. Dorland, S.C. Cowley, J.N. Leboeuf, T.L. Rhodes, J. Candy, and C. Estrada-Mila. Gyrokinetic simulations of etg and itg turbulence. *Nucl. Fusion*, 47: 817, 2007.

A V Dudkovskaia, D Li, J Candy, E A Belli, and C Yang. Dynamic mode decomposition for gyrokinetic eigenmode analysis. *Plasma Physics and Controlled Fusion*, 67:065033, 2025.

H. T. Evensen, R. J. Fonck, S. F. Paul, G. Rewoldt, S. D. Scott, W. M. Tang, and M. C. Zarnstorff. Measurements of ion temperature fluctuations in the tokamak fusion test reactor. *Nucl. Fusion*, 38:237, 1998.

Jeffrey P. Freidberg. *Ideal MHD.* Cambridge University Press, 2014.

{E. A.} Frieman and Liu Chen. Nonlinear gyrokinetic equations for low-frequency electromagnetic waves in general plasma equilibria. *Phys. Fluids*, 25:502, 1982.

M. Giacomin, D. Kennedy, F. J. Casson, Ajay C. J., D. Dickinson, B. S. Patel, and C. M. Roach. On electromagnetic turbulence and transport in step. *Plasma Phys. Control. Fusion*, 66:055010, 2024.

A. Gibson and the JET Team. Deuterium–tritium plasmas in the joint european torus (jet): Behavior and implications. *Phys. Plasmas*, 5:1839, 1998.

H Grad and H Rubin. Hydromagnetic equilibria and force-free fields. Technical report, New York Univ., New York. Inst. of Mathematical Sciences, 1958.

B. A. Grierson, W. X. Wang, S. Ethier, G. M. Staebler, D. J. Battaglia, J. A. Boedo, J. S. deGrassie, and W. M. Solomon. Main-ion intrinsic toroidal rotation profile driven by residual stress torque from ion temperature gradient turbulence in the diii-d tokamak. *Phys. Rev. Lett.*, 118:015002, 2017.

G W Hammett, M A Beer, W Dorland, S C Cowley, and S A Smith. Developments in the gyrofluid approach to tokamak turbulence simulations. *Plasma Phys. Control. Fusion*, 35:973, 1993.

E. G. Highcock. Ph.D. Thesis,, 2012. University of Oxford.

W. Horton, D. I. Choi, and W. M. Tang. Toroidal drift modes driven by ion pressure gradients. *Phys. Fluids*, 24:1077, 1981.

Plamen G. Ivanov, A. A. Schekochihin, W. Dorland, A. R. Field, and F. I. Parra. Zonally dominated dynamics and dimits threshold in curvature-driven itg turbulence. *J. Plasma Phys.*, 86:855860502, 2020.

Plamen G. Ivanov, A.A. Schekochihin, and W. Dorland. Dimits transition in three-dimensional ion-temperature-gradient turbulence. *J. Plasma Phys.*, 88:905880506, 2022.

A Jarmën, P Malinov, and H Nordman. Itg modes with finite-β effects and the upper η_i stability regime. *Plasma Phys. Control. Fusion*, 40:2041, 1998.

F Jenko and W Dorland. Nonlinear electromagnetic gyrokinetic simulations of tokamak plasmas. *Plasma Phys. Control. Fusion*, 43:A141, 2001.

F. Jenko, W. Dorland, M. Kotschenreuther, and B. N. Rogers. Electron temperature gradient driven turbulence. *Phys. Plasmas*, 7:1904, 2000.

D. Kennedy, M. Giacomin, F.J. Casson, D. Dickinson, W.A. Hornsby, B.S. Patel, and C.M. Roach. Electromagnetic gyrokinetic instabilities in step. *Nucl. Fusion*, 63, 2023.

J. Y. Kim, W. Horton, and J. Q. Dong. Electromagnetic effect on the toroidal ion temperature gradient mode. *Phys. Fluids B*, 5:4030, 1993.

J.Y. Kim and H.S. Han. Enhanced stiffness weakening and confinement improvement by the linear electromagnetic effect in relatively high-q and low magnetic-shear plasmas. *Nucl. Fusion*, 59:056021, 2019.

Sumire Kobayashi and Barrett N. Rogers. The quench rule, dimits shift, and eigenmode localization by small-scale zonal flows. *Phys. Plasmas*, 19:012315, 2012.

M. Kotschenreuther, W. Dorland, M. A. Beer, and G. W. Hammett. Quantitative predictions of tokamak energy confinement from first-principles simulations with kinetic effects. *Phys. Plasmas*, 2:2381, 1995a.

Mike Kotschenreuther, G. Rewoldt, and W.M. Tang. Comparison of initial value and eigenvalue codes for kinetic toroidal plasma instabilities. *Comput. Phys. Commun.*, 88: 128, 1995b.

R. H. Kraichnan. Eddy viscosity in two and three dimensions. *J. Atmos. Sci.*, 33:1521, 1976.

Robert H. Kraichnan. Inertial ranges in two-dimensional turbulence. *Phys. Fluids*, 10: 1417, 1967.

N. Kumar, Y. Camenen, S. Benkadda, C. Bourdelle, A. Loarte, A.R. Polevoi, F. Widmer, and JET contributors. Turbulent transport driven by kinetic ballooning modes in the inner core of jet hybrid h-modes. *Nucl. Fusion*, 61:036005, 2021.

S. Maeyama, A. Ishizawa, T.-H. Watanabe, M. Nakata, N. Miyato, M. Yagi, and Y. Idomura. Comparison between kinetic-ballooning-mode-driven turbulence and ion-temperature-gradient-driven turbulence. *Phys. Plasmas*, 21:052301, 2014.

N.R. Mandell, W. Dorland, I. Abel, R. Gaur, P. Kim, M. Martin, and T. Qian. Gx: a gpu-native gyrokinetic turbulence code for tokamak and stellarator design. *J. Plasma Phys.*, 90:905900402, 2024.

S. Mazzi, Y. Camenen, J. Garcia, D. Zarzoso, D. Frigione, L. Garzotti, F. Rimini, D. Van Eester, and JET Contributors. Effects of the parallel flow shear on the itg-driven turbulent transport in tokamak plasmas. *Nucl. Fusion*, 62:096024, 2022.

I.J. McKinney, M.J. Pueschel, B.J. Faber, C.C. Hegna, A. Ishizawa, and P.W. Terry. Kinetic-ballooning-mode turbulence in low-average-magnetic-shear equilibria. *Journal of Plasma Physics*, 87:905870311, 2021.

Claude Mercier. Equilibrium and stability of a toroidal magnetohydrodynamic system in the neighbourhood of a magnetic axis. *Nucl. Fusion*, 4:213, 1964.

R. L. Miller, M. S. Chu, J. M. Greene, Y. R. Lin-Liu, and R. E. Waltz. Noncircular, finite aspect ratio, local equilibrium model. *Phys. Plasmas*, 5:973, 1998.

P. Mulholland, M.J. Pueschel, J.H.E. Proll, K. Aleynikova, B.J. Faber, P.W. Terry, C.C. Hegna, and C. Nührenberg. Finite-β turbulence in wendelstein 7-x enhanced by sub-threshold kinetic ballooning modes. *Nucl. Fusion*, 65:016022, 2024.

A Najlaoui, Y Camenen, C Bourdelle, and A Loarte. Verifying turbulence model reduction in high tokamak plasmas. *Plasma Physics and Controlled Fusion*, 67:045016, 2025.

V. Naulin, A. Kendl, O. E. Garcia, A. H. Nielsen, and J. Juul Rasmussen. Shear flow generation and energetics in electromagnetic turbulence. *Phys. Plasmas*, 12:052515, 2005.

W. M. Nevins, E. Wang, and J. Candy. Magnetic stochasticity in gyrokinetic simulations of plasma microturbulence. *Phys. Rev. Lett.*, 106:065003, 2011.

S L Newton, S C Cowley, and N F Loureiro. Understanding the effect of sheared flow on microinstabilities. *Plasma Phys. Control. Fusion*, 52:125001, 2010.

Richard Nies, Felix Parra, Michael Barnes, Noah Mandell, and William Dorland. Saturation of magnetised plasma turbulence by propagating zonal flows, 2024.

Felix I Parra and Michael Barnes. Intrinsic rotation in tokamaks: theory. *Plasma Phys. Control. Fusion*, 57:045002, 2015.

M. J. Pueschel and F. Jenko. Transport properties of finite-beta microturbulence. *Phys. Plasmas*, 17:062307, 2010.

M. J. Pueschel, M. Kammerer, and F. Jenko. Gyrokinetic turbulence simulations at high plasma beta. *Phys. Plasmas*, 15:102310, 2008.

M. J. Pueschel, T. Görler, F. Jenko, D. R. Hatch, and A. J. Cianciara. On secondary and tertiary instability in electromagnetic plasma microturbulence. *Phys. Plasmas*, 20: 102308, 2013a.

M. J. Pueschel, D. R. Hatch, T. Görler, W. M. Nevins, F. Jenko, P. W. Terry, and D. Told. Properties of high-β microturbulence and the non-zonal transition. *Phys. Plasmas*, 20:102301, 2013b.

M. J. Pueschel, P. W. Terry, F. Jenko, D. R. Hatch, W. M. Nevins, T. Görler, and D. Told. Extreme heat fluxes in gyrokinetic simulations: A new critical β. *Phys. Rev. Lett.*, 110:155005, 2013c.

M. J. Pueschel, P. W. Terry, and D. R. Hatch. Aspects of the non-zonal transition). *Phys. Plasmas*, 21:055901, 2014.

F. Rath and A. G. Peeters. Transport hysteresis in electromagnetic microturbulence caused by mesoscale zonal flow pattern-induced mitigation of high beta turbulence runaways. *Phys. Plasmas*, 29:042305, 2022.

Paolo Ricci, B. N. Rogers, and W. Dorland. Small-scale turbulence in a closed-field-line geometry. *Phys. Rev. Lett.*, 97:245001, 2006.

J. E. Rice, E. S. Marmar, P. T. Bonoli, R. S. Granetz, M. J. Greenwald, A. E. Hubbard, J. W. Hughes, I. H. Hutchinson, J. H. Irby, B. LaBombard, W. D. Lee, Y. Lin, D. Mossessian, J. A. Snipes, S. M. Wolfe, and S. J. Wukitch. Spontaneous toroidal rotation in alcator c-mod plasmas with no momentum input. *Fusion Sci. Technol*, 51: 288, 2007.

B. N. Rogers, W. Dorland, and M. Kotschenreuther. Generation and stability of zonal flows in ion-temperature-gradient mode turbulence. *Phys. Rev. Lett.*, 85:5336, 2000.

F. Romanelli. Ion temperature-gradient-driven modes and anomalous ion transport in tokamaks. *Phys. Fluids B*, 1:1018, 1989.

S Saarelma, P Hill, A Bottino, G Colyer, A R Field, B McMillan, A Peeters, C M Roach, and the MAST team. Global gyrokinetic turbulence simulations of mast plasmas. *Plasma Phys. Control. Fusion*, 54:085012, 2012.

J. N. Sama, A. Biancalani, A. Bottino, D. Del Sarto, R. J. Dumont, G. Di Giannatale, A. Ghizzo, T. Hayward-Schneider, Ph. Lauber, B. McMillan, A. Mishchenko, M. Muruggapan, B. Rettino, B. Rofman, F. Vannini, L. Villard, and X. Wang. Ion temperature gradient mode mitigation by energetic particles, mediated by forced-driven zonal flows. *Phys. Plasmas*, 31:112503, 2024.

A. A. Schekochihin, S. C. Cowley, W. Dorland, G. W. Hammett, G. G. Howes, E. Quataert, and T. Tatsuno. Astrophysical Gyrokinetics: Kinetic and Fluid Turbulent Cascades in Magnetized Weakly Collisional Plasmas. *Astrophys. Suppl.*, 182: 310, 2009.

A. A. Schekochihin, Y. Kawazura, and M. A. Barnes. Constraints on ion versus electron heating by plasma turbulence at low beta. *J. Plasma Phys.*, 85:905850303, 2019.

B. D. Scott. Energetics of the interaction between electromagnetic exb turbulence and zonal flows. *New J. Phys.*, 7:92, 2005.

Bruce D Scott. Computation of turbulence in magnetically confined plasmas. *Plasma Phys. Control. Fusion*, 48:B277, 2006.

V. D. Shafranov. Plasma Equilibrium in a Magnetic Field. *Rev. Plasma Phys.*, 2, 1966.

P. B. Snyder. Ph.D. Thesis,, 1999. Princeton University.

W. M. Stacey. Applications of the miller equilibrium to extend tokamak computational models. *Phys. Plasmas*, 15:122505, 2008.

T H Stix. Heating of toroidal plasmas by neutral injection. *Plasma Phys.*, 14:367, 1972.

Tokamak Energy Ltd. St40 spherical tokamak. https://www.tokamakenergy.co.uk, 2025.

F Troyon, R Gruber, H Saurenmann, S Semenzato, and S Succi. Mhd-limits to plasma confinement. *Plasma Phys. Control. Fusion*, 26:209, 1984.

F Van Wyk, E G Highcock, A R Field, C M Roach, A A Schekochihin, F I Parra, and W Dorland. Ion-scale turbulence in mast: anomalous transport, subcritical transitions, and comparison to bes measurements. *Plasma Phys. Control. Fusion*, 59:114003, 2017.

R. E. Waltz. Three-dimensional global numerical simulation of ion temperature gradient mode turbulence. *Phys. Fluids*, 31:1962, 1988.

R. E. Waltz. Nonlinear subcritical magnetohydrodynamic beta limit. *Phys. Plasmas*, 17: 072501, 2010.

John Wesson. *Tokamaks.* Oxford University Press, Oxford, 4 edition, 2011.

G. G. Whelan, M. J. Pueschel, and P. W. Terry. Nonlinear electromagnetic stabilization of plasma microturbulence. *Phys. Rev. Lett.*, 120:175002, 2018.

A Zocco, P Helander, and J W Connor. Magnetic compressibility and ion-temperature-gradient-driven microinstabilities in magnetically confined plasmas. *Plasma Phys. Control. Fusion*, 57:085003, 2015.

A. Zocco, P. Xanthopoulos, H. Doerk, J. W. Connor, and P. Helander. Threshold for the destabilisation of the ion-temperature-gradient mode in magnetically confined toroidal plasmas. *J. Plasma Phys.*, 84:715840101, 2018.

Appendix A

Benchmark between `stella`, `CGYRO` and `GENE`

In this Appendix, we present benchmark results obtained by comparing the turbulent heat fluxes calculated with three gyrokinetic codes: `stella`, `CGYRO`, and `GENE`.

A.0.1 Definition of heat fluxes

In `stella`, the turbulent heat flux averaged over the flux-tube volume due to a particular species is defined as

$$\begin{aligned} Q_s &= \frac{1}{V_\rho} \int \mathrm{d}^3\boldsymbol{r} \int \mathrm{d}^3\boldsymbol{v}\, \frac{m_s v^2}{2} \left(\boldsymbol{v}_\chi \cdot \nabla\rho\right) \delta f_s \\ &= \frac{1}{V_\rho} \int \mathrm{d}z\, J \frac{c}{B} \left(\hat{\boldsymbol{b}} \times \nabla y \cdot \nabla\rho\right) \int \mathrm{d}x\mathrm{d}y \int \mathrm{d}^3\boldsymbol{v}\, \frac{m_s v^2}{2} \frac{\partial\chi}{\partial y} \left\langle \delta f_s \right\rangle_{\boldsymbol{r}}, \end{aligned} \tag{A.1}$$

where we have written $\int \mathrm{d}^3\boldsymbol{r}$ in the flux tube coordinates. $\nabla\rho$ is the gradient of the flux surface label and

$$V_\rho = L_x L_y \int \mathrm{d}z\, J|\nabla\rho|. \tag{A.2}$$

Since `stella` solves for the Fourier transformed kinetic equations, it is more convenient to write Q_s in terms of the Fourier components of the distribution function and fields:

$$Q_s = \frac{1}{\int \mathrm{d}z J|\nabla\rho|} \int \mathrm{d}z\, J \frac{c}{B} \left(\hat{\boldsymbol{b}} \times \nabla y \cdot \nabla\rho\right) \sum_{\boldsymbol{k}} i k_y \int \mathrm{d}^3\boldsymbol{v}\, \frac{m_s v^2}{2} \chi_{\boldsymbol{k}} \left\langle \delta f^*_{s,\boldsymbol{k}} \right\rangle_{\boldsymbol{r}}, \tag{A.3}$$

where we have used the fact that fluctuating quantities are real and periodic in (x, y). With `stella` normalisations listed in Tab. 4.1, we can write the normalised heat flux $\tilde{Q}$ as

$$\tilde{Q}_s = \frac{Q_s}{Q_{gB}} = \hat{H}\left(\tilde{\chi}_{\boldsymbol{k}} \left\langle \delta \tilde{f}^*_{s,\boldsymbol{k}} \right\rangle_{\boldsymbol{r}}\right), \tag{A.4}$$

where $Q_{gB} = n_r T_r v_r \rho_r^2/a^2$ and $\hat{H}$ is an integral operator defined as

$$\hat{H} = \frac{\tilde{n}_s \tilde{T}_s}{2\sqrt{\pi}} \frac{1}{\int \mathrm{d}z\, J|\nabla\rho|} \int \mathrm{d}z\, J \left(\hat{\boldsymbol{b}} \times \nabla y \cdot \nabla \rho\right) \sum_{\boldsymbol{k}} i k_y \rho_r \int \mathrm{d}\tilde{\mu} \int \mathrm{d}\tilde{v}_\parallel\, \tilde{v}^2. \tag{A.5}$$

As $\tilde{\chi}_{\boldsymbol{k}} = \tilde{\phi}_{\boldsymbol{k}} - 2\tilde{v}_\parallel v_{\mathrm{th}s} \tilde{A}_{\parallel,\boldsymbol{k}}/v_r + 4\tilde{\mu}\tilde{T}_s \tilde{B}_{\parallel,\boldsymbol{k}}/Z_s$, we can extract different contributions to the total heat flux that come from different fields. The electrostatic heat flux is

$$\tilde{Q}_{s,\mathrm{es}} = \hat{H}\left(\tilde{\phi}_{\boldsymbol{k}} \left\langle \delta \tilde{f}^*_{s,\boldsymbol{k}} \right\rangle_{\boldsymbol{r}}\right). \tag{A.6}$$

When there is magnetic perturbation perpendicular to the equilibrium field line, particles streaming along the exact field line causes radial heat transport ('flutter' transport), which is given by

$$\tilde{Q}_{s,A_\parallel} = -2\frac{v_{\mathrm{th}s}}{v_r} \hat{H}\left(\tilde{v}_\parallel \tilde{A}_{\parallel,\boldsymbol{k}} \left\langle \delta \tilde{f}^*_{s,\boldsymbol{k}} \right\rangle_{\boldsymbol{r}}\right) \tag{A.7}$$

and is typically dominated by the electrons. If, in addition, $B_\parallel \neq 0$, the perturbed field can cause magnetic drift in the radial direction. With a particular phase relationship between $B_\parallel$ and perpendicular temperature, this radial magnetic drift can give rise to a net heat transport given by

$$\hat{Q}_{s,B_\parallel} = 4\frac{\tilde{T}_s}{Z_s} \hat{H}\left(\tilde{\mu} \tilde{B}_{\parallel,\boldsymbol{k}} \left\langle \delta \tilde{f}^*_{s,\boldsymbol{k}} \right\rangle_{\boldsymbol{r}}\right). \tag{A.8}$$

A.0.2 Numerical setup of the gyrokinetic codes

For the CBC benchmark, we choose the same set of parameters as in Tab. 4.1, with the addition of $\delta B_\parallel$ and a consistent β'. In `stella`, the perpendicular box sizes are $L_x = L_y = 126\rho_r$, and the numerical resolutions are $N_{v_\parallel} = 48$, $N_\mu = 12$, $N_z = 32$, $N_x = 171$ and $N_y = 22$. The value of electron beta is set to $\beta_e = 0.006$. In `GENE`, the same wavenumber resolution and box-sizes in x and y are used. The velocity-space domain extends to $l_v = 3.0$ in normalised parallel velocity and $l_w = 9.0$ in normalised magnetic moment. The corresponding velocity-space resolutions are $n_{v0} = 64$ grid points in parallel velocity and $n_{w0} = 24$ grid points in magnetic moment. The number of grid points along the equilibrium field line is set to $n_{z0} = 32$. In `CGYRO`, N_ENERGY $= 12$, E_MAX $= 8$, N_XI $= 32$, N_THETA $= 32$.

A.0.3 Results of Heat flux benchmark

Fig. A.1 shows the comparison of heat flux data between three codes for the electrostatic heat fluxes (the top panel) and the electromagnetic heat fluxes (the bottom panel). Note that, to facilitate the comparison between the codes, we have chosen to plot the total electromagnetic heat flux $\tilde{Q}_{s,\mathrm{em}} = \tilde{Q}_{s,\mathrm{A}_\parallel} + \tilde{Q}_{s,\mathrm{B}_\parallel}$. The time traces show good agreement

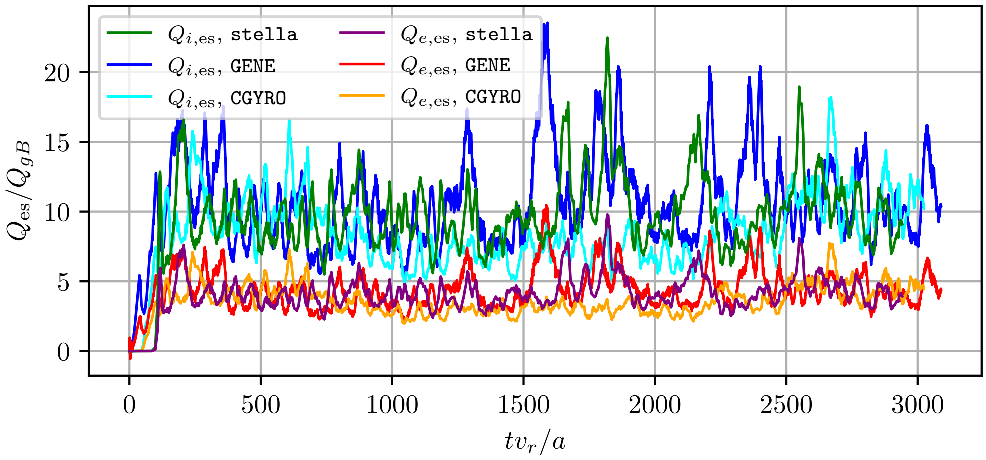

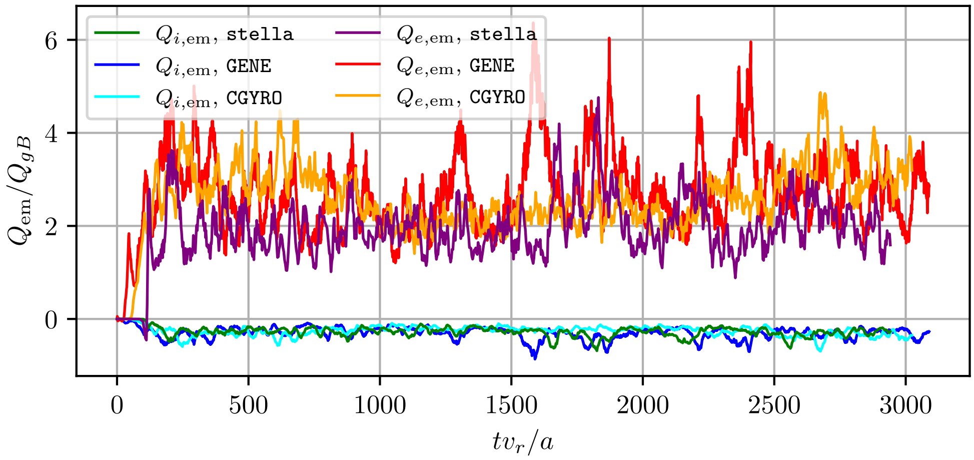

Figure A.1: Time traces of heat fluxes normalised by $Q_{gB} = n_r T_r v_r \rho_r^2/a^2$. The data is from a CBC simulation using `stella`, `CGYRO` and `GENE`. The CBC parameters listed in Tab. 4.1 are used, with $\beta_e = 0.006$ and a consistent β'. Both panels show time traces of the different heat flux components, with the top panel for the electrostatic heat fluxes and the bottom panel for the electromagnetic heat fluxes.

between the codes. The time-averaged heat fluxes over the saturated period are also listed in Tab. A.1.

Heat fluxes/Q_{gB}	$Q_{i,\mathrm{es}}$	$Q_{e,\mathrm{es}}$	$Q_{i,\mathrm{em}}$	$Q_{e,\mathrm{em}}$
`stella`	9.92	4.25	-0.283	1.99
`CGYRO`	8.57	3.62	-0.259	2.62
`GENE`	10.8	4.46	-0.308	2.75

Table A.1: Time-averaged, normalised heat fluxes for each of the codes included in the benchmark.

Appendix B

Heuristic scaling of the transfer ratio

In this Appendix, we estimate the (q, β_e) scaling of the transfer ratio. This ratio is essentially determined by the stress ratio, and thus by the ratio between fields:

$$\frac{T_{A_\parallel}}{T_\phi} \sim \frac{\left\langle \left\langle A_\parallel \right\rangle_{\boldsymbol{R}_s} \sum_s Z_s \int \mathrm{d}^3\boldsymbol{v} v_\parallel h_s \right\rangle_{\boldsymbol{r}}}{c \left\langle \left\langle \phi \right\rangle_{\boldsymbol{R}_s} \sum_s Z_s \int \mathrm{d}^3\boldsymbol{v} h_s \right\rangle_{\boldsymbol{r}}} \sim \frac{1}{\beta_e} \frac{(A_\parallel/\rho_i B)^2}{(e\phi/T_e)^2}, \tag{B.1}$$

where we have used (1.24), (1.26), (3.14), (3.15). We have also assumed that $k_\perp \rho_i \sim 1$ and that all the species have comparable equilibrium densities and temperatures. Next, we estimate the size of $(A_\parallel/\phi)$ by coming up with a condition by which the electrostatic limit can be approached. In the electrostatic limit, the electrons follow the Boltzmann response $\delta n_e/n_e = e\phi/T_e$. Therefore, at small β_e, we expect $\delta n_e/n_e \sim e\phi/T_e$. From the density moment of the electron gyrokinetic equation, we obtain an evolution equation for the electron density:

$$\omega \delta n_e + k_\parallel \int \mathrm{d}^3\boldsymbol{v}\, v_\parallel \left\langle h_e \right\rangle_{\boldsymbol{r}} + \cdots = 0. \tag{B.2}$$

However, there is a separate evolution equation for ϕ (the vorticity equation), which is in general different from the evolution of δn_e. As a result, in order for electrons to become Boltzmann as $\beta_e \to 0$ while ensuring consistency between (B.2) and the vorticity equation, we need the parallel flow $\int \mathrm{d}^3\boldsymbol{v}\, v_\parallel \left\langle h_e \right\rangle_{\boldsymbol{r}}$ to regulate the size of δn_e. Thus, the electrostatic limit exists if, at moderate β_e, we require

$$\begin{aligned} &\omega \frac{\delta n_e}{n_e} \sim k_\parallel \frac{1}{n_e} \int \mathrm{d}^3\boldsymbol{v}\, v_\parallel \left\langle h_e \right\rangle_{\boldsymbol{r}}, \\ &\longrightarrow \omega \frac{e\phi}{T_e} \sim k_\parallel \frac{A_\parallel c}{e n_e \rho_i^2}, \\ &\longrightarrow \frac{(A_\parallel/\rho_i B)}{(e\phi/T)} \sim \frac{R}{L_{T_i}} q \beta_e, \end{aligned} \tag{B.3}$$

where we have used $k_y \rho_i \sim k_\perp \rho_i \sim 1$, $k_\parallel \sim 1/qR$, (1.26), and $\omega \sim k_y \rho_i v_{\mathrm{th}i}/L_{T_i}$ for ITG instabilities. Plugging (B.3) into (B.1), we obtain

$$\frac{T_{A_\parallel}}{T_\phi} \sim \left(\frac{R}{L_{T_i}} \right)^2 (q^2 \beta_e). \tag{B.4}$$

It is (B.4) that initially motivated the search for non-zonal transition boundaries in the (q,β_e) parameter space, even though the $q^2\beta_e$ scaling turns out to disagree with the nonlinear simulation results.

Appendix C

$\tau \sim 1$ equations

In this Appendix we derive a set of fluid equations for warm ions with $\tau \sim 1$. We start with the set of equations derived for isothermal electrons in Subsection 4.1.1 and impose the warm-ion ordering

$$k_\perp^2 \rho_i^2 \sim \beta_i \sim \beta_e \sim \frac{L_T}{L_B} \ll 1, \; \tau \sim 1. \tag{C.1}$$

The orderings we employ are similar to the 'high-β' ordering used by Aleynikova and Zocco [2017] in studying kinetic ballooning mode (KBM) instabilities. The frequencies are ordered as

$$\frac{k_\parallel c_s}{\sqrt{\beta_i}} \sim \omega \sim k_\parallel v_A \sim k_\perp u_\perp \sim \omega_{*T} \sim \frac{\omega_{di}}{\beta_i} \sim \nu_{ii}\beta_i, \tag{C.2}$$

and the perturbations are ordered as:

$$\frac{Ze\phi}{T_i} \sim \frac{\delta T_i}{T_i} \sim \frac{1}{\beta_i}\frac{\delta n_e}{n_e} \sim \frac{1}{\beta_i}\frac{B_\parallel}{B} \sim \frac{1}{\beta_i}\frac{\delta B_\perp}{B}. \tag{C.3}$$

Notice that although $Ze\phi/T_i$ is much larger than $\delta B_\perp/B$, $A_\parallel$ is still dynamically important. To see this, we write $\delta B_\perp$ as $k_\perp A_\parallel$ and calculate the ratio between $Ze\phi/T_i$ and $\delta B_\perp/B$:

$$1 \sim \frac{Ze\phi}{T_i}\frac{B\beta_i}{k_\perp A_\parallel} \sim \frac{Ze\phi}{T_i}\frac{Bk_\perp \rho_i \sqrt{\beta_i}}{k_\perp A_\parallel} \sim \frac{\phi c}{v_A A_\parallel}. \tag{C.4}$$

Using the ordering for ω, we get

$$\frac{k_\parallel \phi c}{\omega A_\parallel} \sim 1. \tag{C.5}$$

Thus, the effect of $A_\parallel$ field is still retained, as the $A_\parallel$ and ϕ terms are balanced in (4.22). However, $B_\parallel$ is indeed ordered out by (C.3).

Unlike the case of electromagnetic ITG, now $\delta n_e/n_e$ has been ordered small compared to $Ze\phi/T_i$. The current set of equations is thus incompatible with a Boltzmann electron response and so is unable to capture correctly the electrostatic limit for ITG. Using the new orderings above, we take the fluid moments of the ion gyrokinetic equation, obtaining the following set of equations: parallel electric force balance (the same as (4.22)):

$$\frac{e}{T_e c}\frac{\partial A_\parallel}{\partial t} = -\nabla_\parallel \frac{e\phi}{T_e}, \tag{C.6}$$

the vorticity of the $\boldsymbol{E}\times\boldsymbol{B}$ flow (derived in the same way as (4.61)):

$$\begin{aligned}&-\frac{\mathrm{d}}{\mathrm{d}t}\frac{1}{2}\rho_i^2\nabla_\perp^2\frac{Ze\phi}{T_i} - \nabla_\parallel\frac{c}{4\pi e n_e}\nabla_\perp^2 A_\parallel + \frac{1}{4}\rho_i v_{\mathrm{th}i}\rho_i^2\nabla_\perp\cdot\left\{\nabla_\perp\phi, \frac{\delta T_i}{T_i}\right\}\\ &+\frac{\rho_i v_{\mathrm{th}i}}{2L_T}\frac{\partial}{\partial y}\left(\frac{1}{2}\rho_i^2\nabla_\perp^2\frac{Ze\phi}{T_i}\right) - \frac{\rho_i v_{\mathrm{th}i}}{L_B}\frac{\partial}{\partial y}\frac{\delta T_i}{T_i} = -\frac{1}{2}\chi\rho_i^2\nabla_\perp^4\left(a\frac{Ze\phi}{T_i} - b\frac{\delta T_i}{T_i}\right),\end{aligned} \tag{C.7}$$

the ion temperature equation (derived by taking the temperature moment of the ion gyrokinetic equation and retaining only the lowest order contributions):

$$\frac{\mathrm{d}}{\mathrm{d}t}\frac{\delta T_i}{T_i} + \frac{\rho_i v_{\mathrm{th}i}}{2L_T}\frac{\partial}{\partial y}\frac{Ze\phi}{T_i} = \chi\nabla_\perp^2\frac{\delta T_i}{T_i}. \tag{C.8}$$

(C.6), (C.7) and (C.8) constitute a three-field model for an electromagnetic turbulence driven by the ion temperature gradient.

To understand the underlying linear instability that drives the turbulence, consider only the linear terms in (C.6)-(C.8) and ignore collisions. The equations are reduced to

$$\frac{e}{T_e c}\frac{\partial A_\parallel}{\partial t} = -\frac{\partial}{\partial z}\frac{e\phi}{T_e}, \tag{C.9}$$

$$-\frac{\partial}{\partial t}\frac{1}{2}\rho_i^2\nabla_\perp^2\frac{Ze\phi}{T_i} - \frac{\partial}{\partial z}\frac{c}{4\pi e n_e}\nabla_\perp^2 A_\parallel + \frac{\rho_i v_{\mathrm{th}i}}{2L_T}\frac{\partial}{\partial y}\left(\frac{1}{2}\rho_i^2\nabla_\perp^2\frac{Ze\phi}{T_i}\right) - \frac{\rho_i v_{\mathrm{th}i}}{L_B}\frac{\partial}{\partial y}\frac{\delta T_i}{T_i} = 0, \tag{C.10}$$

$$\frac{\partial}{\partial t}\frac{\delta T_i}{T_i} + \frac{\rho_i v_{\mathrm{th}i}}{2L_T}\frac{\partial}{\partial y}\frac{Ze\phi}{T_i} = 0. \tag{C.11}$$

Performing a Fourier decomposition of (C.9)-(C.11) results in the dispersion relation

$$k_\perp^2\rho_i^2\omega^2 + \frac{k_y\rho_i v_{\mathrm{th}i}}{2L_T}k_\perp^2\rho_i^2\omega + k_\perp^2\rho_i^2\frac{v_{\mathrm{th}i}^2}{L_B L_T} - \frac{1}{\beta_i}k_z^2 k_\perp^2\rho_i^2 v_{\mathrm{th}i}^2 = 0. \tag{C.12}$$

This agrees with the large-η_i, Z-pinch limit of the ideal-ballooning equation with a diamagnetic correction [Aleynikova and Zocco, 2017], which serves as an approximation of the KBM at large temperature-gradient.

Restricting attention to modes with $k_x = 0$, the growth rate γ is

$$\gamma = \frac{1}{2}\sqrt{\frac{4v_{\mathrm{th}i}^2}{L_B L_T} - \frac{4k_z^2 v_{\mathrm{th}i}^2}{\beta_i} - \frac{k_y^2\rho_i^2 v_{\mathrm{th}i}^2}{4L_{Ti}^2}}. \tag{C.13}$$

We note that the maximum growth rate occurs at $k_y = 0 = k_z$, and its value is $v_{\mathrm{th}i}/\sqrt{L_B L_T}$: the same as the MHD IC instability obtained from the cold-ion model.

Consequently, we conjecture that the bad-curvature region of KBM found in tokamaks manifests as the MHD IC instability in the Z-pinch model.

Appendix D

The effect of finite χ on the linear stability

Here, we provide a broader perspective on the linear instabilities that arise in the fluid model. In particular, we highlight the role of retaining a finite χ even in the low-wavenumber limit. Analytical calculations of the linear instabilities without neglecting the χ terms will be presented in Subsection D.0.1. We will discover the MHD IC mode, the low k_y continuation of the FLR IC and ITG modes, as well as two additional instabilities named C and D modes.

D.0.1 Analytical investigation

We focus on modes with $k_x = 0$ and assume κ_T, k_z, $\chi \sim 1$. The resulting dispersion relation, obtained from (4.99)-(4.101), is

$$\begin{aligned}\omega^4 + \omega^3 \left(i\chi k_y^2 - k_y + k_y\kappa_T + ia\chi k_y^2\right) + \omega^2(-k_z^2k_y^2 - i\chi k_y^3 - k_z^2 - 1 + \kappa_T + i\chi\kappa_T k_y^3 \\ -\kappa_T k_y^2 - a\chi^2 k_y^4 - ia\chi k_y^3 - ib\chi\kappa_T k_y^3) + \omega(-i\chi k_z^2 k_y^4 - i\chi k_z^2 k_y^2 - k_z^2 k_y - i\chi k_y^2 \\ -\kappa_T k_y - \kappa_T k_z^2 k_y^3 - i\chi\kappa_T k_y^4 - ia\chi k_z^2 k_y^4 + a\chi^2 k_y^5 + ib\chi\kappa_T k_y^4) \\ -i\chi k_z^2 k_y^3 - \kappa_T k_z^2 k_y^2 - i\chi\kappa_T k_z^2 k_y^5 + a\chi^2 k_z^2 k_y^6 + ib\chi\kappa_T k_z^2 k_y^5 = 0.\end{aligned} \quad \text{(D.1)}$$

We express $\omega = \omega_r + i\gamma$ and seek solutions for the frequency ω_r and growth rate γ. We consider initially the long-wavelength limit, and look for solutions satisfying $\gamma \sim k_y^2$. This is motivated by numerical observations, which we present in Subsection D.0.2. We will find two distinct unstable modes: one with $\omega_r \sim 1$ and another with $\omega_r \sim k_y$. First, consider the case with $\omega_r \sim 1$. Using the fact that $\gamma \ll \omega_r$, we can expand the terms in (D.1) of the form ω^m as

$$\omega^m \approx \omega_r^m \left(1 + im\frac{\gamma}{\omega_r}\right), \quad \text{(D.2)}$$

where $m \leq 4$ is an integer. The real part of (D.1) gives

$$\omega_r = \pm\sqrt{1 + k_z^2 - \kappa_T} \tag{D.3}$$

to lowest order in k_y. We will refer to the '+' solution as a C mode and to the '$-$' solution as an FLR IC mode. To lowest order in k_y, the imaginary part of (D.1) gives

$$\gamma = \frac{\kappa_T - a\omega_r^2}{2\omega_r^2}\chi k_y^2. \tag{D.4}$$

Note that (D.3) and (D.4) are consistent with our ansatz of $\omega_r \sim 1$ and $\gamma \sim k_y^2$. Hence, the modes are unstable if

$$\kappa_T > \frac{a\left(1 + k_z^2\right)}{1 + a}. \tag{D.5}$$

Together with the condition $\omega_r^2 = 1 + k_z^2 - \kappa_T > 0$, we obtain the unstable region for the instabilities:

$$\kappa_T > \frac{a\left(1 + k_z^2\right)}{1 + a} \approx 0.184 \times \left(1 + k_z^2\right) \quad \text{and} \quad \kappa_T < 1 + k_z^2. \tag{D.6}$$

Let us try to understand the nature of these instabilities. One notice that the instabilities can exist when $k_z = 0 = k_x = a = b$ and $k_y \ll 1$. Thus, (4.99)-(4.101) can be simplified accordingly to give

$$-i\omega n - ik_y\left(\varphi - n\right) = 0, \tag{D.7}$$

$$-i\omega k_y^2\varphi - ik_y\left(n + T\right) = 0, \tag{D.8}$$

$$-i\omega T + i\kappa_T k_y \varphi = -\chi k_y^2 T. \tag{D.9}$$

Since the energy injection is due to the κ_T term in (D.9), and T couples to φ in (D.8), we must have that $T \sim k_y\varphi$ (the real part of $\omega \sim 1$). In order for n to matter, we also need $n \sim T \sim k_y\phi$. Hence, in the second term of (D.7), n can be neglected, leading to $n = -k_y\varphi/\omega$. From (D.9), we get $T = i\kappa_T k_y\varphi/(i\omega - \chi k_y^2)$. Plugging the expression for n and T into (D.8), we obtain

$$\omega^2 = 1 - \frac{i\kappa_T\omega}{i\omega - \chi k_y^2}. \tag{D.10}$$

We consider first the collisionless case $\chi = 0$. If $\kappa_T > 1$, we recover the dispersion relation for the MHD IC instability with $k_x = 0$ (see (4.126)). If $\kappa_T < 1$, there is a curvature drift wave since the first term on the right hand side of (D.10) comes from the curvature term in (D.7). If collisions are added, we can solve (D.10) to obtain the frequency and growth rate given by (D.3) and (D.4), respectively, in the case of $k_z = 0$ and $a = 0$. The physical picture of the C mode and the low-k_y FLR IC modes is as follows. Consider a blob of plasma being carried by the drift wave. This blob oscillates between the hot and cold regions. In the presence of collisions, part of the heat carried from the hot region is dissipated locally when the blob reaches the cold region. As a consequence, when the blob is carried back toward the hot region, its temperature is lower than when it started. This process results in net temperature mixing between the hot and cold regions, reinforced by the combined action of drift-wave advection and collisional diffusion. Nevertheless, if the wave frequencies were too fast compared with the diffusion rate, the curvature drift wave, together with AWs, would provide a stabilising mechanism for the C and FLR IC modes, as seen from (D.3) and (D.4). If κ_T becomes so large that ω_r in (D.3) becomes imaginary, the FLR IC modes will switch to MHD IC modes. The appearance of MHD IC modes can be expected from the dispersion relation (D.1): we know that the MHD IC modes have γ independent of k_y in the limit of $k_y \to 0$. If $\omega \sim 1$ and $k_y \ll 1$, the only terms that survive in (D.1) are

$$\omega^4 + \omega^2 \left(-k_z^2 - 1 + \kappa_T\right) = 0 \tag{D.11}$$

which gives $\omega^2 = 1 + k_z^2 - \kappa_T$. So the MHD IC modes are unstable if $\kappa_T > 1 + k_z^2$. This is the same as the stability criteria of the C and FLR IC modes (The C modes are much less important based on the numerical results in Subsection D.0.2.), which shows that $\kappa_T = 1 + k_z^2$ is the transition boundary for the FLR and MHD IC modes.

Now consider the case where $\omega_r \sim k_y$. As $k_y \to 0$, since $\gamma/\omega_r \sim k_y \ll 1$, (D.2) is still valid and can be plugged into (D.1). After that, to lowest order in k_y, the real part of (D.1) gives

$$\omega_r = \frac{k_y}{2\left(1 + k_z^2 - \kappa_T\right)} \times \left[-\left(k_z^2 + \kappa_T\right) \pm \sqrt{\left(k_z^2 + \kappa_T\right)^2 - 4\left(1 + k_z^2 - \kappa_T\right)\kappa_T k_z^2} \right]. \tag{D.12}$$

We will refer to the $\omega_r > 0$ solution as a D mode. As for the $\omega_r < 0$ solution, we show later in Subsection D.0.2 that it is simply a collisional, low k_y extension of the ITG mode. At sufficiently large k_z (electrostatic limit), the ITG modes exhibit the scaling $\gamma \propto k_y$ for $k_y \ll 1$. As k_z is decreased, the low k_y modes become modified and eventually transition to a regime in which $\gamma \propto \chi k_y^2$ for $k_y \ll 1$. We will refer to modes in this regime as χITG. To lowest order in k_y, the imaginary part of (D.1) gives

$$\gamma = \frac{\left(1 + k_z^2\right)\omega_r + k_z^2 k_y}{\left(-2k_z^2 - 2 + 2\kappa_T\right)\omega_r - k_z^2 k_y - \kappa_T k_y} \chi k_y^2. \tag{D.13}$$

Note that (D.12) and (D.13) are consistent with our ordering anstaz $\omega_r \sim k_y$ and $\gamma \sim k_y^2$. Numerically, one finds that the unstable region for the D modes is very close to $\kappa_T > 1+k_z^2$ (the same as that of MHD IC modes), and the unstable region for the χITG modes is close to $\kappa_T > k_z^2$ (See Fig. D.1).

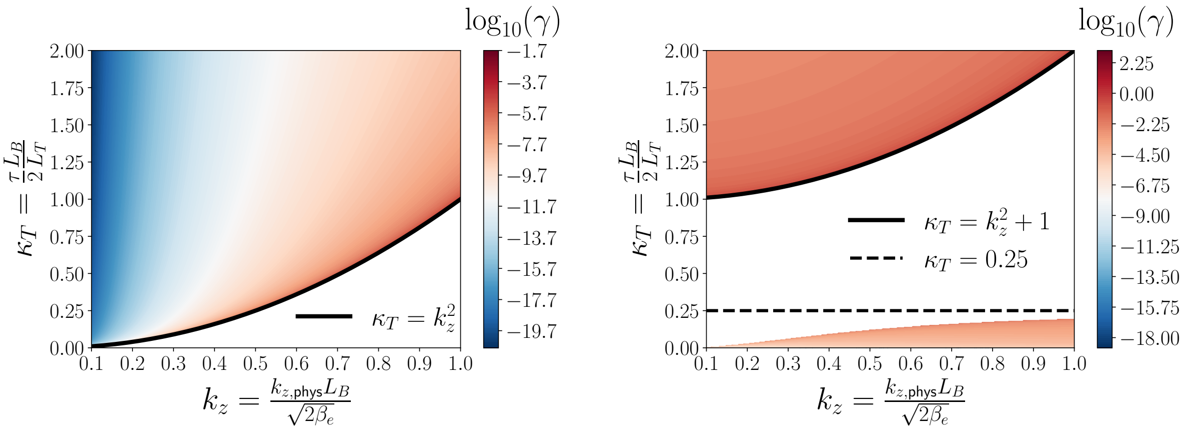

Figure D.1: Analytical growth rate γ given by (D.13), plotted in (k_z, κ_T) space for the χITG (left panel) and D (right panel) modes with $k_y = 0.1$, $k_x = 0$ and $\chi = 0.2$. The blank space corresponds to the stable regions, and the black solid lines are the stability boundaries. Notice that for D modes there is a separate unstable region below $\kappa_T = 0.25$ marked by the dashed black line.

D.0.2 Numerical investigation

In this Subsection, we present a numerical study of the linear instabilities discussed in Subsection D.0.1.

We consider the effect of β_e on the finite-χ growth rate spectrum for two different values of κ_T in Fig. D.2. The corresponding eigenvalue solves kept $k_x = 0$ and $\chi = 0.2$ fixed, while varying the box size L_z to scan in k_z. As discussed in Subsection 4.1.3, $k_z \propto \beta_e^{-1/2}$, so this is equivalent to a scan in β_e. The behaviour at low β_e (high k_z) is qualitatively similar for both κ_T values: There is a single peak in k_y, and the growth rate goes to zero at $k_y = 0$. As β_e is increased (k_z decreased), a second peak appears at low k_y and grows in amplitude with β_e. For the $\kappa_T = 0.8$ case, this second bump corresponds to the FLR IC mode. With $\kappa_T = 2.0$, the growth rate of the second bump extends all the way to $k_y = 0$: This is the MHD IC mode, which is absent for $\kappa_T < 1$, as in Fig. D.2(a).

We will now calculate all subdominant modes. There are two additional subdominant modes, the C and D modes, that can coexist with the ITG (or χITG, if $k_z < \sqrt{\kappa_T}$) and FLR IC modes. This is demonstrated in Figs. D.3 and D.4, where the growth rate and frequency spectra of all unstable modes are plotted for two different sets of κ_T and k_z values. The data in Figs. D.3 and D.4 are obtained at ($k_z = 0.8$, $\kappa_T = 0.8$) and ($k_z = 0.4$, $\kappa_T = 2.0$), respectively, corresponding to β_e and κ_T values beyond the threshold where the interchange modes dominate over χITG modes. We identify the mode type by comparing their stability boundaries and the k_y-scalings of their growth rates and frequencies with the analytical expressions derived in Subsection D.0.1.

Plotting all the subdominant instabilities at $k_z = 0.8$ in Fig. D.3, one can see that

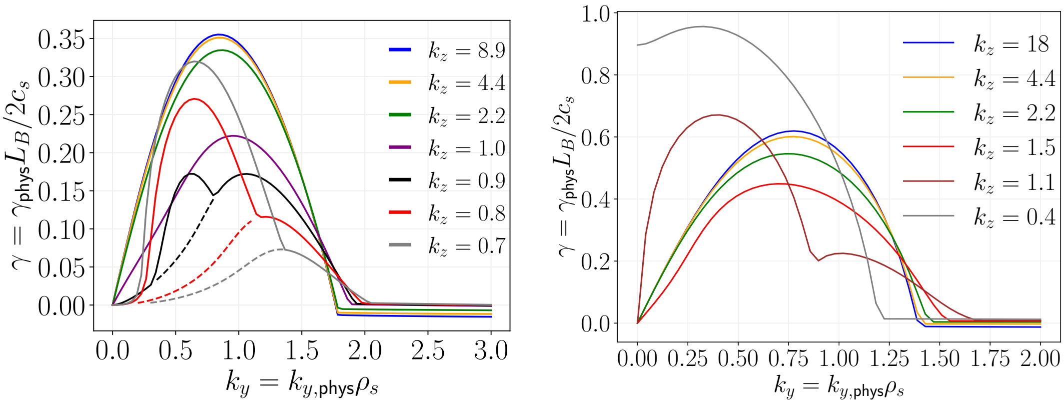

(a) (b)

Figure D.2: Growth rate γ versus k_y for $k_x = 0$, $\chi = 0.2$ and several different values of k_z. The left panel has $\kappa_T = 0.8$, and the right panel has $\kappa_T = 2.0$. The k_z scan was performed by changing the box size L_z and examining box-scale modes. The dashed lines in the left panel are the subdominant ITG modes.

there co-exist three different modes. The numerical solutions show that the FLR IC mode has surpassed ITG and become the dominant instability. However, there is also a third instability. To understand them better, we investigate their frequency spectra. As shown in Fig. D.3(b), the mode with the second largest growth rate at $k_y \approx 0.5$ has its frequency spectrum pretty much overlaps with the spectrum at $k_z = 8.9$ where only ITG is unstable. The real frequency of this mode also satisfies $\omega_r \propto k_y$ and it agrees with the analytical expression (D.12) at low k_y. Therefore, we can identify this subdominant mode as the χITG mode.

When $\kappa_T = 2.0$, there is also transition from ITG to MHD modes shown by Fig. D.4. The subdominant modes corresponding to the $k_z = 0.4$ case are plotted in the figure. One find that three instabilities coexist — MHD IC, χITG and D modes. This is expected since $\kappa_T > 1 + k_z^2$.

A summary plot indicating the region of instability for each mode in the $(\kappa_T,\, k_z)$ plane is given in Fig D.5.

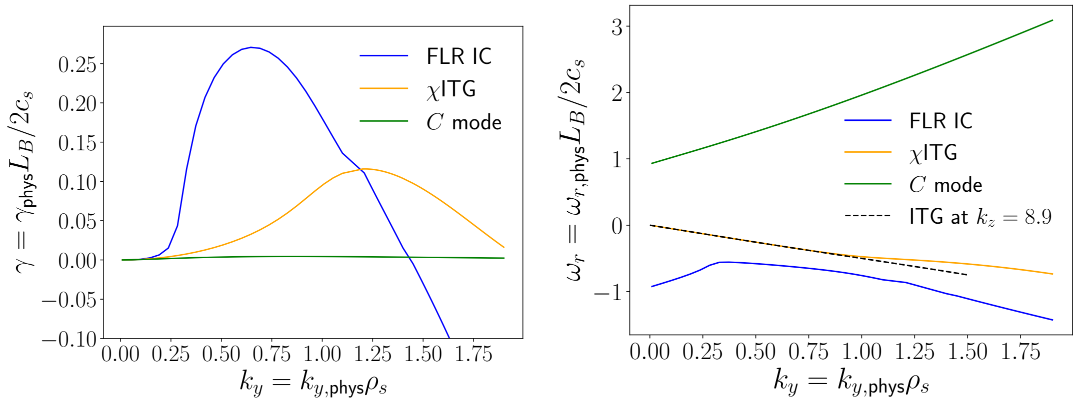

(a) (b)

Figure D.3: Growth rate (a) and frequency (b) spectra corresponding to the $k_z = 0.8$ case in Fig. D.2(a). The dashed black line is the frequency spectrum taken from the $k_z = 8.9$ case where χITG is the only instability.

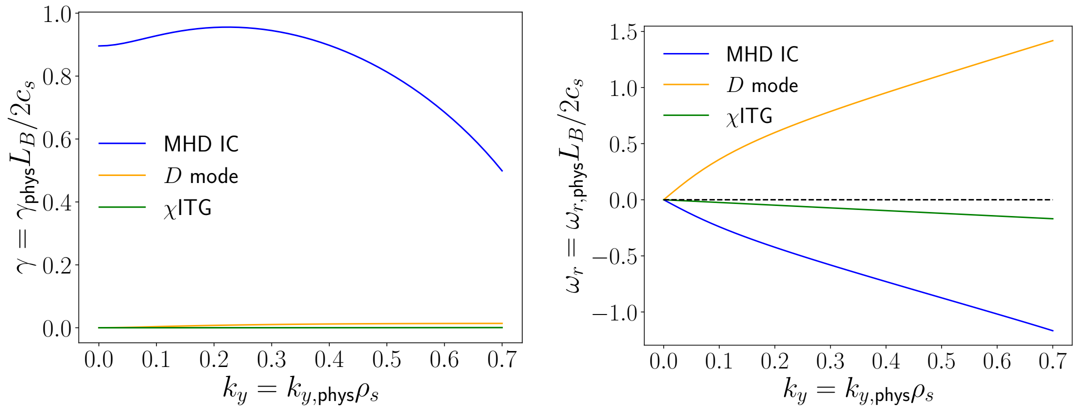

(a) (b)

Figure D.4: Growth rate (a) and frequency (b) spectra corresponding to the $k_z = 0.4$ case in Fig. D.2(b). The D and χITG modes have much smaller growth rates than the MHD IC modes at this value of k_z. The D mode has positive frequency so it is easily identifiable. The χITG frequency spectrum is less steep compared to the MHD IC frequency spectrum.

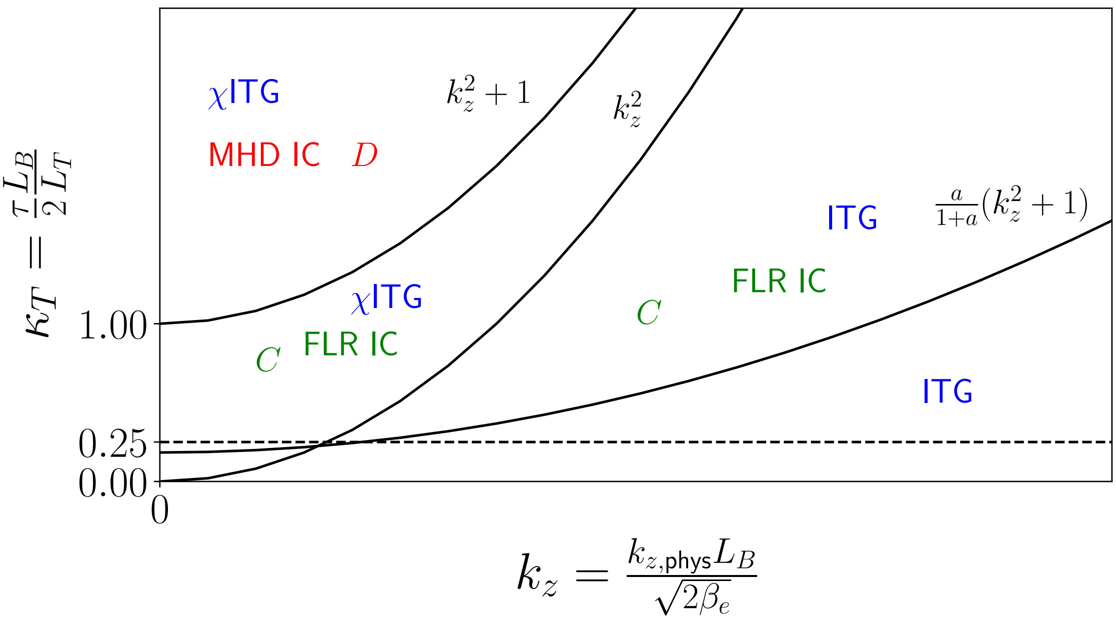

Figure D.5: Regions of instability at $k_y \ll 1$ for each of the modes identified in Subsection D.0.1. The stability boundaries $\kappa_T = k_z^2 + 1$ and $\kappa_T = a(k_z^2+1)/(1+a)$ come from the stability criteria given by (D.6). The boundary $\kappa_T = k_z^2$ is plotted according to the results in Fig. D.1(b). To the left of the curve $\kappa_T = k_z^2$, ITG modes with $\gamma \sim k_y$ at $k_y \ll 1$ are stabilized and replaced by χITG modes with $\gamma \sim k_y^2$. The MHD IC modes are found on the top left of the plot where the temperature gradients and β_e are high. The C and D modes have much smaller growth rates and positive frequencies which are opposite to all other modes.

Appendix E

Time traces

In this Appendix we provide indicative time traces for the heat flux and for the electromagnetic field fluctuations corresponding to the simulations presented in Section 4.3. A typical 'early' time trace used to obtain time-averaged fluxes is shown in Fig. E.1. The heat flux and virtually all field components reach an apparent steady state but the zonal component of A is slowly evolving throughout. When the simulation is extended by an order of magnitude in time (Fig. E.2(c)) the zonal A continues to evolve still. Another example of the long-time evolution of zonal A disrupting the turbulent steady-state if provided in Fig. E.3. There, the slow growth of zonal A eventually triggers a transition to a state with very large heat flux. The small secular growth rate is eliminated by including a resistivity term in (4.88), which is formally absent in our model due to the ordering we impose. However, this long-time behaviour is not a problem in practice when identifying the non-zonal transition on which this study is focused. This is because simulations that exhibit a non-zonal transition do so at much earlier times, as exhibited in the time traces of Fig. E.4.

E.1 Time traces for $\kappa_T = 0.8$, $L_z = 2.8$ and $\chi = 0.2$ (up to $t = 10000$)

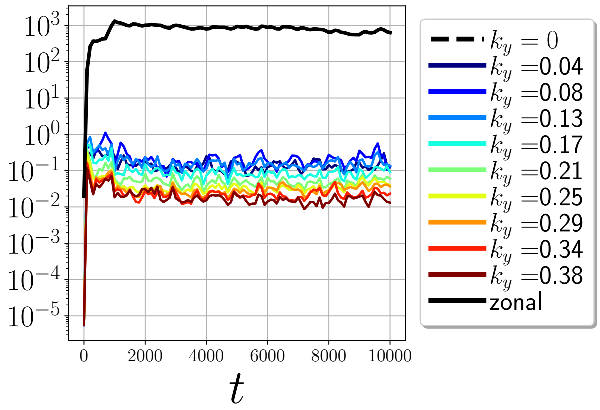

(a) $\sum_{k_x,k_z} |\varphi_{\boldsymbol{k}}|^2$

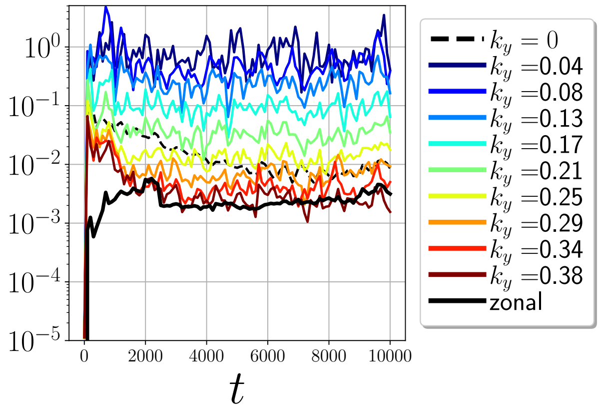

(b) $\sum_{k_x,k_z} |A_{\boldsymbol{k}}|^2$

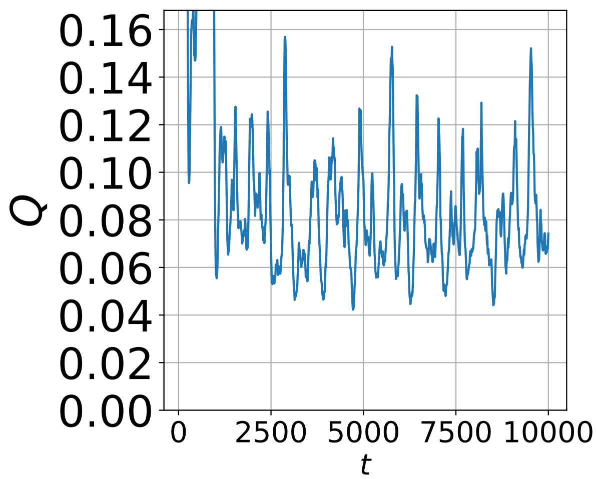

(c) $Q(t)$

Figure E.1: **(a)(b)**: Time traces of the perturbations. Only the first 10 k_y modes are plotted. **(c)**: Q versus t.

E.2 Time traces for $\kappa_T = 0.8$, $L_z = 2.8$ and $\chi = 0.2$ (up to $t = 100000$)

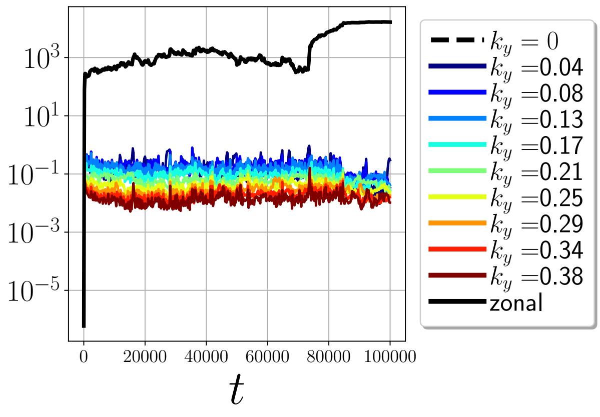

(a) $\sum_{k_x,k_z} |\varphi_{\boldsymbol{k}}|^2$

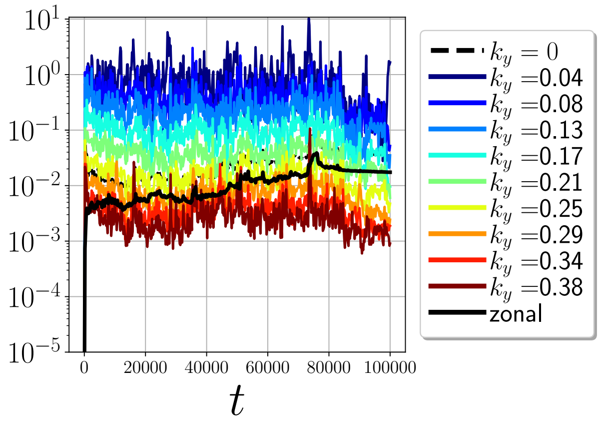

(b) $\sum_{k_x,k_z} |A_{\boldsymbol{k}}|^2$

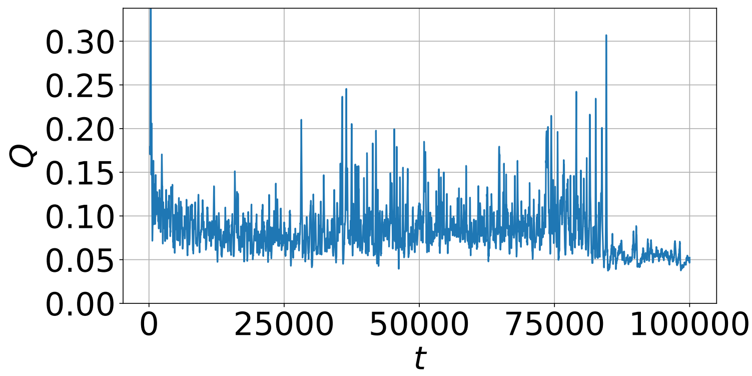

(c) $Q(t)$

Figure E.2: **(a)(b)**: Time traces of the perturbations. Only the first 10 k_y modes are plotted. **(c)**: Q versus t.

E.3 Time traces for $\kappa_T = 0.8$, $L_z = 4.2$ and $\chi = 0.2$

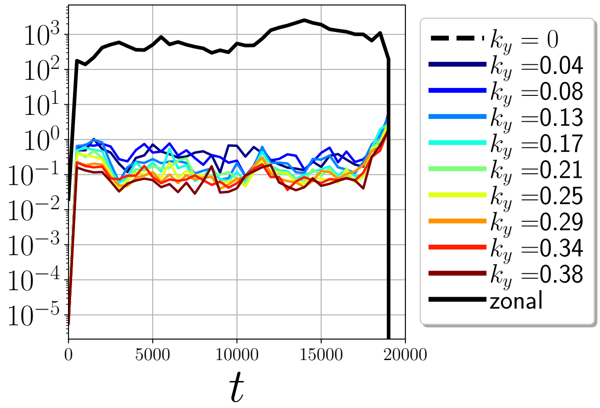

(a) $\sum_{k_x,k_z} |\varphi_{\boldsymbol{k}}|^2$

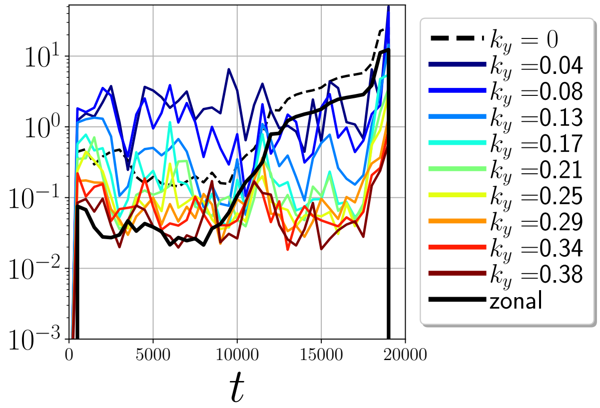

(b) $\sum_{k_x,k_z} |A_{\boldsymbol{k}}|^2$

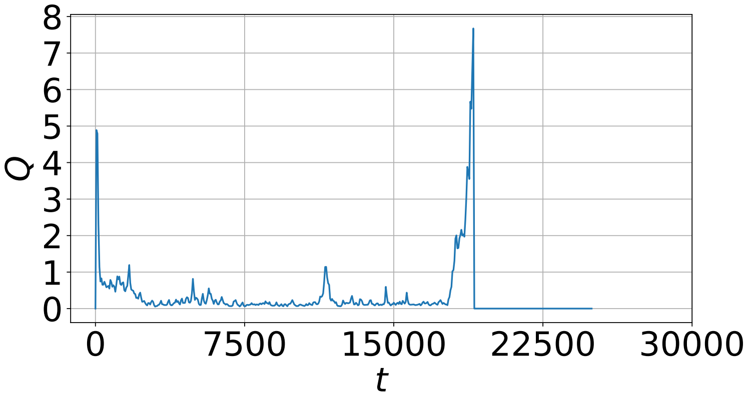

(c) $Q(t)$

Figure E.3: **(a)(b)**: Time traces of the perturbations. Only the first 10 k_y modes are plotted. **(c)**: Q versus t. If the simulation was run only up to $t = 10000$, then one might think that it has saturated. However, running it for longer reveals the slow growth of zonal A which eventually breaks the convergence, leading to large heat fluxes. The simulation was stopped at about $t = 19000$ due to the timestep becoming too small.

E.4 Time traces for $\kappa_T = 0.8$, $L_z = 4.4$ and $\chi = 0.2$

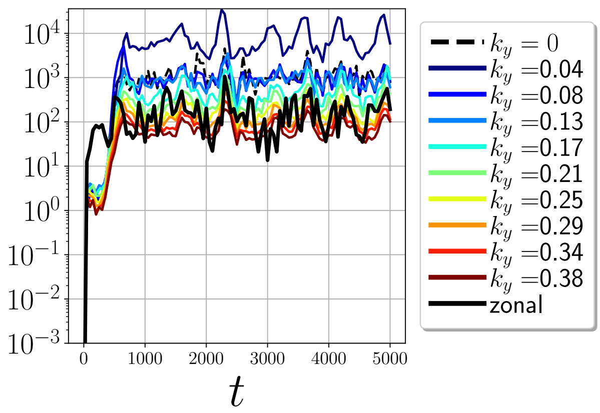

(a) $\sum_{k_x,k_z} |\varphi_{\boldsymbol{k}}|^2$

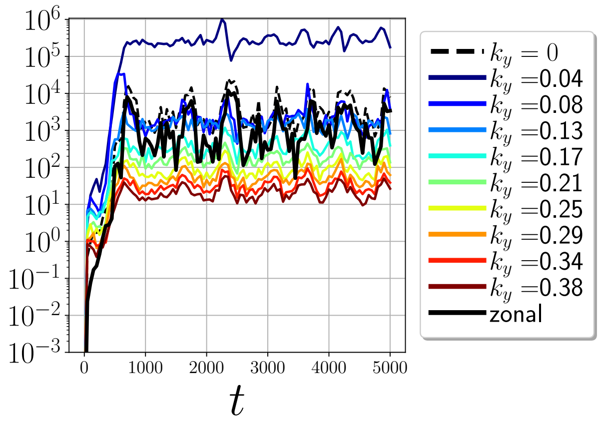

(b) $\sum_{k_x,k_z} |A_{\boldsymbol{k}}|^2$

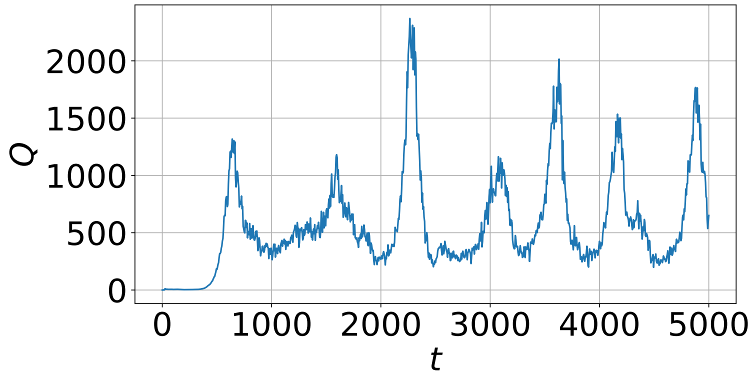

(c) $Q(t)$

Figure E.4: **(a)(b)**: Time traces of the perturbations. Only the first 10 k_y modes are plotted. **(c)**: Q versus t. In this case the zonal flow is not strong enough to suppress the turbulence so the system enters a non-zonal regime where the heat flux is orders of magnitude larger than cases with smaller L_z. Since there are always only box scale streamers, this should not be treated as well-converged turbulence.

E.5 Frozen-zonal-flow simulations

Here we illustrate the calculation of ν_{turb} using the time trace data of the fluctuations. Take the case with $\kappa_T = 0.8$ and $L_z = 6.4$ as an example (one beyond the non-zonal transition). After an initial triangular zonal flow is set up, all other modes are evolved in time. However, the ultimate saturation is difficult due to the growing zonal A (see Fig. E.5(c)). What's more, when zonal A is large enough, the stresses start to correlate worse with the zonal shear (see Fig. E.5(d)). This might explain why sometimes it leads to a transition to a non-zonal state after a very long time. However, as we have noted before, zonal A does not play any roles in the non-zonal transition shortly after the initial transient. Thus, the fixed-in-time zonal flow simulations are run up to a time when the stresses have been well correlated with the zonal shear while zonal A still has a small impact.

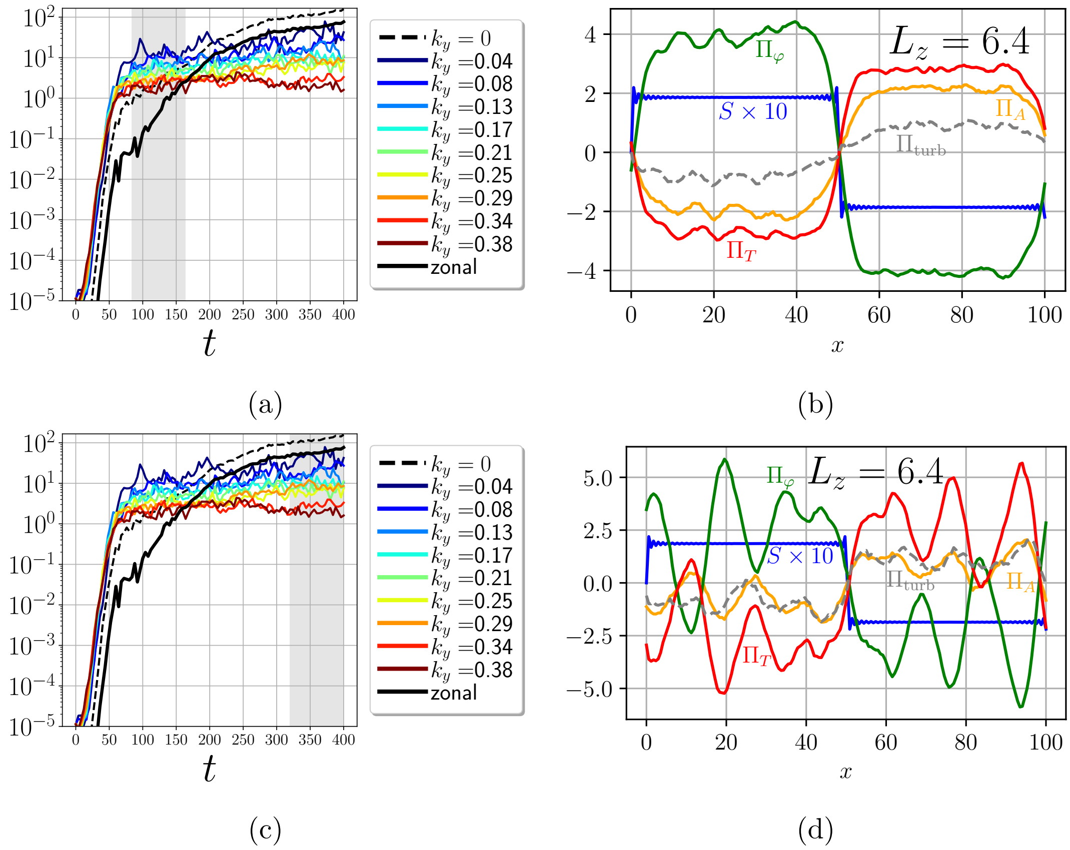

Figure E.5: Time traces of A and stresses plotted along x. **(a)** and **(c)**: Time trace of A summed over all k_z and k_x as a function of k_y. Only the smallest 10 k_y modes are plotted. The shaded area stands for the period during which the stresses are averaged over. **(b)** and **(d)**: Zonal shear and various stresses plotted along x.